International Committee for Future Accelerators

Sponsored by the Particles and Fields Commission of IUPAP

Beam Dynamics Newsletter

No. 44

Issue Editor:
A. Ghodke

Editor in Chief:
W. Chou

December 2007

Contents

4

1   Foreword

1.1   From the Chair

Weiren Chou, Fermilab
Mail to: chou@fnal.gov

The International Committee for Future Accelerators (ICFA) met on August 15, 2007 at Daegu, South Korea during the *LP07* Conference. The meeting approved a new member of the ICFA Beam Dynamics Panel: Marica Biagini from Frascati National Laboratories (LNF-INFN), Italy. She replaces Caterina Biscari, who stepped down after a number of years of great service on the panel. Turnover of panel membership is important for the healthy growth of the panel and was encouraged at the panel's meeting in June (see p.133 of Newsletter no. 43).

ICFA approved the 42nd ICFA Advanced Beam Dynamics Workshop: *HB2008*, a continuation of the High Intensity High Brightness Hadron Beams workshop series. This workshop will take place from August 24 to 29, 2008 in Nashville, Tennessee, U.S.A., and will be hosted by Oak Ridge National Laboratory. (Note: *HB2002* was hosted by Fermilab, *HB2004* by GSI, and *HB2006* by KEK.)

ICFA also issued a statement on Open Access (OA) Publishing, which aims at making particle physics publications available free to everyone while at the same time retaining the peer review process. A major beneficiary of the new publishing model will be to researchers in developing countries. The proposal will apply to worldwide journals in English, but not to local journals or those in other languages. For a journal that contains other physics fields in addition to particle physics (such as *Physical Review Letters*), the cost sharing arrangement will depend on the fraction of articles published in the journal on particle physics. This statement is published on the web: http://www.fnal.gov/directorate/icfa/statements.html.

ICFA approved the ILC *Reference Design Report* (RDR) submitted by Barry Barish. They also appointed Enzo Iarocci as the next ILC Steering Committee (ILCSC) Chair, replacing Shin-ichi Kurokawa, whose term has expired.

The Second International Accelerator School for Linear Colliders took place at the Ettore Majorana Center, Erice (Sicily), Italy from October 1 to 10, 2007. Fifty-seven students from 18 countries attended. A detailed report can be found in Section 2.2. The venue and dates of the third school have been decided. It will be held from October 19 to 29, 2008 at the Oak Brook Hills Marriott Hotel near Chicago, U.S.A. Fermilab will be the host institution. Registration will begin in January. More information will be available on the school web site: http://www.linearcollider.org/school/2008/.

The editor of this issue is Dr. Ajay Ghodke, a panel member and a senior scientist from the Raja Ramanna Centre for Advanced Technology (RRCAT) in Indore, India. Dr. Ghodke collected a number of very interesting articles for this issue. The total page count reaches 230 making this the largest single volume of this newsletter that has been assembled. I congratulate Dr. Ghodke for this remarkable editorial success and express my sincere thanks to him for producing a fine Newsletter on schedule.

1.2   From the Editor

Ajay Ghodke

Raja Ramanna Centre for Advanced Technology, Indore, India

Mail to: ghodke@cat.ernet.in

The theme section of this issue is dedicated to the subject of LOCO (Linear Optics from Closed Orbits). During the commissioning and understanding of an accelerator or storage ring, one of the important tasks for an accelerator physicist is to check the first-order optics of the ring and beam lines and to look for errors in the system. Thus measurement and optimization of the storage ring linear optics are essential commissioning tasks. Nowadays the LOCO program has become a standard tool to characterize, and correct as required, real normal and skew quadrupole gradient errors, BPM and corrector gains, insertion device gap compensations, betatron coupling, local chromaticities and transverse impedance distributions. This is done based on a fit of measured and model orbit response matrices. After optics correction, the measured values are very close to designed values. As a result of this study, the storage-ring operation becomes well controlled. LOCO can be a valuable tool for maximizing storage ring performance.

This theme section includes seven well-prepared articles. I am grateful to the contributors to this section, especially to James Safranek for his support and for generating an interesting theme article on LOCO.

In the ILC section, there are three articles: an article discussing in detail about beam dynamics challenges for the ILC, a report from a recent superconducting RF workshop held in Beijing, China, and a report of the Second International Accelerator School for Linear Colliders.

I have received a number of activity reports. Two of them are on the storage ring commissioning. One is contributed by Greg LeBlanc on the Australian synchrotron in which there is a comprehensive summary of the Australian Light Source commissioning and another by J M Filhol on the SOLEIL [*French for sun*] storage ring. There are also reports from the CANDLE Light Source in Armenia, ALBA Storage Ring in Spain, and two beam dynamics articles: one from LBNL, another from Northern Illinois University (U.S.A.). A summary report from the LARP Beam-Beam Compensation 2007 Workshop is also included.

There are also three workshop announcements: e^+e^- Factories 2008, Nanobeam 2008 and an ICFA mini-workshop on deflecting/crabbing RF cavity.

Editing of this issue has been a pleasant experience and I am thankful to all the contributors for providing good quality material on schedule.

2 International Linear Collider (ILC)

2.1 Beam Dynamics Challenges for the ILC

Kiyoshi Kubo, KEK, 1-1 Oho, Tsukuba, Ibaraki 305-0801 Japan
Mail to: kiyoshi.kubo@kek.jp

Andrei Seryi, SLAC, 2575 Sand Hill Road, Menlo Park, CA 94025 USA
Mail to: seryi@slac.stanford.edu

Nicholas Walker, DESY, Notkestrasse 85, 22607 Hamburg, Germany
Mail to: nicholas.walker@desy.de

Andy Wolski, The Cockcroft Institute, Daresbury, Warrington WA4 4AD, UK
Mail to: a.wolski@dl.ac.uk

2.1.1 Introduction

The International Linear Collider (ILC) is a proposal for 500 GeV centre-of-mass electron-positron collider, with a possible upgrade to ~1 TeV centre-of-mass. At the heart of the ILC are the two ~12 km 1.3 GHz superconducting RF (SCRF) linacs which will accelerate the electron and positron beams to an initial maximum energy of 250 GeV each. The Global Design Effort (GDE) – responsible for the world-wide coordination of this uniquely international project – published the ILC Reference Design Report in August of 2007 [1].

The ILC outlined in the RDR design stands on a legacy of over fifteen-years of R&D. The GDE is currently beginning the next step in this ambitious project, namely an Engineering Design phase, which will culminate with the publication of an Engineering Design Report (EDR) in mid-2010.

Throughout the history of linear collider development, beam dynamics has played an essential role. In particular, the need for complex computer simulations to predict the performance of the machine has always been crucial, not least because the parameters of the ILC represent in general a large extrapolation from where current machines operate today; many of the critical beam-dynamics features planned for the ILC can ultimately only be truly tested once the ILC has been constructed. It is for this reason that beam dynamics activities will continue to be crucial during the Engineering Design phase, as the available computer power and software techniques allow ever-more complex and realistic models of the machine to be developed. Complementary to the computer simulation efforts are the need for well-designed experiments at beam-test facilities, which – while not necessarily producing a direct demonstration of the ILC-like parameters for the reasons mentioned above – can provide important input and benchmarking for the computer models.

The fundamental challenge for the ILC beam dynamicists is the production and preservation of the ultra-small emittance beams required for the ambitious luminosity goal of $\sim2\times10^{34}$ cm^{-2}s^{-1}. A general scaling law for the luminosity for a fixed centre-of-mass energy can be written as

$$L \propto P_{beam} \sqrt{\frac{\delta_{RMS}}{\varepsilon_y}} \, , \tag{1}$$

where P_{beam} is the average beam power, δ_{RMS} is the RMS energy loss of the beams during the collision (beamstrahlung), and ε_y is the normalized vertical emittance. Implicit in the scaling law are the assumptions of a flat beam ($\varepsilon_x \gg \varepsilon_y$) and that the vertical beta-function at the interaction point (β_y^*) is constrained by the bunch length (σ_z) such that $\beta_y^* \geq \sigma_z$ to avoid the so-called "hour-glass" effect leading to a loss of luminosity. Assuming that we constrain the beamstrahlung to a fixed few percent[1], achieving a high luminosity requires high beam powers (current), ultra-small vertical emittance beams, short bunch lengths and very strong focusing at the interaction point. Some examples of the nominal ILC parameters are given in Table 1.

Table 1: Typical key parameter ranges for the 500 GeV centre-of-mass ILC

	min.	*nominal*	*max.*	
Bunch population	1	2	2	$\times 10^{10}$
Number of bunches	1260	2670	5340	
Linac bunch interval	180	369	500	Ns
RMS bunch length at IP	200	300	500	μm
Normalized horizontal emittance at IP	10	10	12	mm·mrad
Normalized vertical emittance at IP	0.02	0.04	0.08	mm·mrad
Horizontal beta function at IP	10	20	20	Mm
Vertical beta function at IP	0.2	0.4	0.6	Mm
RMS horizontal beam size at IP	474	640	640	Nm
RMS vertical beam size at IP	3.5	5.7	9.9	Nm
Vertical disruption parameter	14	19.4	26.1	
Fractional RMS energy loss to beamstrahlung	1.7	2.4	5.5	%

Achieving these ambitious parameters requires pushing the envelope in every sub-system of the ILC. Figure 1 shows the layout (footprint) of the machine, indicating the main sub-systems:

- The electron and positron sources must produce the necessary bunch charge and train structure (2670 bunches in a ~950 μs pulse). The electron source must produce a high (~90%) level of polarisation, using a laser-driven photo-injector and a GaAs cathode. Positrons are produced by using an undulator magnet in the main electron linac to produce high energy photons (gammas), which then impact a thin Ti-alloy target to produce electron positron pairs. This positron source can also be used to generate polarized beams. In both cases, the beams must be efficiently captured and accelerated to 5 GeV before being injected into the damping rings.
- The electron and positron damping rings are centrally located. The two 6.7 km circumference storage rings are responsible for producing the high-

---

[1] For both physics reasons and suppression of beam-beam backgrounds

quality ultra-small emittance beams required by the luminosity: achieving the required 2 pm vertical emittance is the primary challenge. To do so they must damp the vertical emittances by (in the case of the positrons) approximately eight orders-of-magnitude in the 200 ms storage time. Many of the fundamental beam dynamics challenges for the ILC are associated with the damping rings, particularly collective effects, both classical and in particular electron-cloud and fast-ion instability effects.

- The Ring to Main Linac section (RTML) must transport the ejected beams from the damping rings, along the entire length of the main linacs, where they are turned around and injected into the bunch compressors, and simultaneously accelerated from 5 GeV to ~15 GeV before being injected into the main linacs. Bunch compression by a factor of ~30 is achieved in two stages by rotating the longitudinal phase space. SCRF linacs are used to introduce a strong energy correlation along the bunches, which enable non-isochronous magnetic chicanes to compress the bunch longitudinally. The primary beam dynamics concern here is the preservation of the tiny vertical emittance during transport and bunch compression. Many of the fundamental problems of wakefields and chromatic effects are essentially the same as in the main linacs (see below), but are exacerbated by the very long bunch before and the large energy spread after compression.

- The Main Linac is essentially a repetitive system of SCRF accelerating structures with focusing provided by a simply FODO lattice structure. As with the RTML, the primary beam dynamics issues related to emittance preservation. Suppression of higher-order modes (HOMs, or long-range wakefields) is achieved by random cavity detuning of the HOMs and by HOM-couplers and absorbers mounted in the accelerating units (cryomodules). Short range (single-bunch) wakefields of the large-iris superconducting cavities are relatively weak, and so the primary emittance growth arises from chromatic effects and cross-plane coupling arising from the alignment errors of the quadrupole lattice.

- The Beam Delivery System (BDS) is responsible for transporting the high-energy beams from the linacs to the interaction region, where they are strongly focused to the required nanometer-size beams at the collision point. This challenges the optics of the Final Focus system, which requires careful cancellation of second- and higher-order chromatic and geometric aberrations. In addition, the strong focusing (small β_y^*) places extremely tight component alignment and field-quality tolerances on the magnets. Magnet vibration and slow ground motion issues must be considered, and keeping the tiny beams in collision at the IP will require fast beam-based feedback systems.

Each sub-system has its unique set of beam dynamics issues. For the remainder of this report, we will focus specifically on a summary of the issues in the Damping Ring, the RTML and Main Linac and in the final section the BDS. For more detailed and comprehensive list of beam dynamics challenges for the ILC (including the sources), the reader is referred to the RDR and the references therein [1].
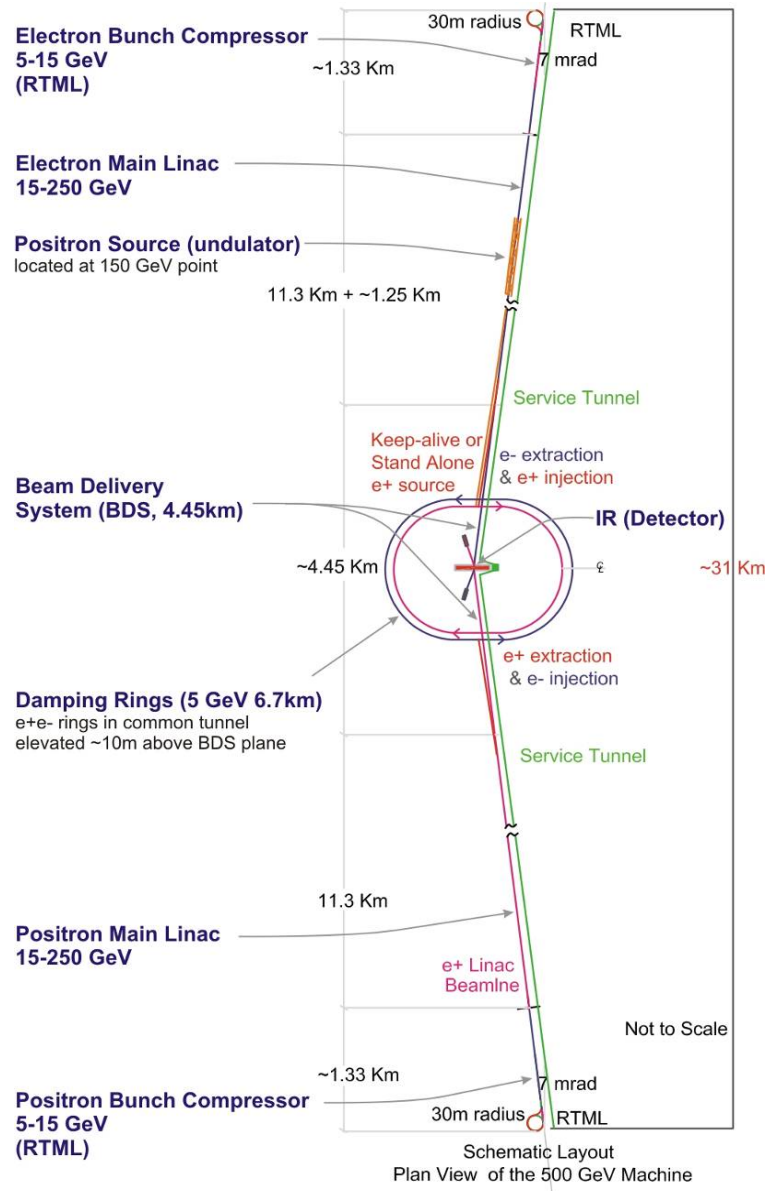
Figure 1: Schematic layout of the 500 GeV centre-of-mass ILC.

2.1.2 Damping Rings

Generation of luminosity in the ILC will depend on colliding beams with emittances much smaller than can be produced directly from particle sources. In the case of the positron beam, the vertical emittance must be reduced by five orders of magnitude between the source and the interaction point. Emittance reduction is achieved by radiation damping, with each beam remaining in a synchrotron storage ring (damping ring) for 200 ms between machine pulses. The principal parameters of the damping rings must be chosen to provide a balance between competing requirements. For example, the circumference must be large enough to accommodate a full train of up to

around 6000 bunches, with sufficient spacing between bunches to fire the injection and extraction kickers; however, increasing the circumference leads to longer damping times, increases the impact of some beam dynamics effects such as space charge, and increases the costs of the rings. The higher the energy of the stored beam, the shorter the damping times and the more robust the beam will be against various collective effects; however, raising the beam energy also increases the equilibrium emittances, and increases the cost of the damping rings. An analysis [2] taking into account a range of considerations has led to the present damping ring design having circumference of about 6.5 km, and beam energy of 5 GeV.

The principal beam dynamics issues in the damping rings are: achieving high injection efficiency of the large-emittance positron beam (with average injection power 225 kW); tuning for ultra-low vertical emittance; and maintaining beam quality and at high bunch charges and average currents. Regarding injection efficiency, the dynamical effects of intrinsic nonlinearities in the field of the damping wigglers are a concern, and have been the subject of detailed study. The present belief is that sufficiently good field quality can be achieved in the wigglers such that limitations on dynamic aperture will come from other sources. Some of the techniques applied in the studies leading to this conclusion have been described previously [3], and we do not elaborate further here. In this article, we discuss briefly the issues associated with achieving vertical emittance of less than 2 pm, and some of the many effects that threaten to impact beam stability.

While the horizontal emittance in a storage ring is generally determined by the lattice design, the vertical emittance is usually limited by magnet alignment and tuning errors that generate vertical dispersion and betatron coupling. The non-zero opening angle of the synchrotron radiation in a storage ring imposes a fundamental lower limit on the vertical emittance, since there is some vertical momentum recoil when particles in the beam emit photons. Neglecting other effects (dispersion and betatron coupling) that generate vertical emittance, the equilibrium emittance determined from the opening angle of the synchrotron radiation can be calculated for a given lattice using the formula:

$$\varepsilon_y = \frac{13}{55} \frac{C_q}{j_y} \frac{\oint \beta_y / |\rho|^3 \, ds}{\oint 1/\rho^2 \, ds} \tag{2}$$

where C_q is the quantum constant ($\approx 3.832 \times 10^{-13}$ m), j_y is the vertical damping partition number, β_y is the vertical beta function, and $1/\rho$ is the curvature of the reference trajectory. Note that this expression is independent of beam energy: although higher-energy particles emit photons with higher momenta for a given bending radius, the opening angle of the radiation is reduced at higher beam energy. Generally, one finds for damping ring designs that the vertical emittance given by Eq. (2) is of order 0.1 pm, while the specified equilibrium vertical emittance is 2 pm: we expect that in practice, the vertical emittance will be dominated by magnet alignment errors.

In the ILC damping rings, the target vertical emittance of 2 pm is about 0.25% of the specified horizontal emittance; correction of betatron coupling at this level has been demonstrated at existing storage rings. However, the contribution of vertical dispersion to the vertical emittance is likely to be as important as that from betatron coupling. If the vertical dispersion is generated by random, uncorrelated errors around a storage ring, then the contribution of the vertical dispersion to the vertical emittance can be estimated from:

$$\varepsilon_y \approx 2 j_z \left\langle \frac{\eta_y^2}{\beta_y} \right\rangle \sigma_\delta^2 \tag{3}$$

where j_z is the longitudinal damping partition number, η_y is the vertical dispersion, σ_δ is the rms energy spread, and the brackets $\langle \rangle$ indicate an average around the ring. Applied to the ILC damping rings, we find that the rms vertical dispersion in the damping rings needs to be less than 3 mm, without any allowance for betatron coupling. Assuming that at the specified vertical emittance betatron coupling and vertical dispersion make roughly equal contributions to the vertical emittance (as suggested by simulations), the betatron coupling must be less than about 0.1%, and the rms vertical dispersion must be less than about 1.5 mm. Based on experience at operating storage rings, these figures indicate that the goal of 2 pm vertical emittance in the ILC damping rings is realistic; however, the lowest vertical emittance demonstrated to date is about a factor of two larger than this [4]. Further studies are needed to demonstrate tuning techniques that are sufficiently effective and can be applied quickly in a machine of the size and complexity of the damping rings. Initial alignment of magnets, functionality and performance of diagnostics (particularly beam position and beam size monitors), and application of beam-based alignment techniques will all be critical. Once achieved, the vertical emittance will be sensitive to motion of the sextupoles at the level of tens of microns; so mechanical and thermal stability of the damping ring components and their environment will also be critical issues.

One feature that will distinguish the ILC damping rings from most storage rings built to date is that around 80% of the synchrotron radiation will come from the damping wiggler: in third generation synchrotron light sources, insertion devices typically account for around 20% of the radiation. The present design of the ILC damping rings includes about 140 m of wiggler with peak field 1.6 T, so as to achieve damping times of less than 25 ms. One consequence of the fact that the wigglers dominate the radiation loss is that for tuning the vertical emittance, particular attention must be paid to correction of dispersion and local betatron coupling in the wiggler sections. This may allow some improvements in speed and efficiency of low-emittance tuning if global correction strategies (for example, orbit response matrix analysis) are modified to act locally.

Correction of errors at the level necessary to achieve 2 pm vertical emittance is essentially an issue of single-particle dynamics. However, the damping rings will need to operate with average currents of 400 mA, and bunch charges of up to 3 nC; with these parameters, a range of collective effects threaten to limit beam quality and stability. Effects that are of concern include: space-charge tune shifts; intrabeam scattering; impedance; ion instabilities (in the electron damping ring); and electron cloud effects (in the positron damping ring). Coherent synchrotron radiation has also been considered, but is not thought likely to have a significant impact with the present configuration. The effect causing most concern, based on present understanding and experience from other facilities, is electron cloud [5].

Instabilities associated with electron cloud have been observed in a number of proton and positron storage rings. A key mechanism associated with the build-up of electrons in the vacuum chamber of a proton or positron ring is the release of secondary electrons from the impact of primary electrons on the chamber wall. Although the secondary electrons are at low energy, a positively charged beam can accelerate them to energies where they can themselves release multiple secondary electrons on striking the

wall. Depending on the beam parameters, properties of the vacuum chamber surface, and presence of external electromagnetic fields, multipacting can lead to a rapid increase in the density of electrons in the chamber, with saturation occurring when the charge on the beam is effectively neutralized by the charge on the electrons in the cloud. Figure 2 shows the results of a simulation of the variation in density of the electron cloud in the wiggler of the positron damping ring, during the passage of three bunches of positrons. As a bunch passes, electrons in the cloud are accelerated and hit the wall with high energy, releasing showers of secondary electrons, and resulting in an increase in the cloud density; between bunches, the cloud dissipates. At sufficiently high electron densities, interactions between the cloud and the beam can lead to a variety of undesirable effects, including incoherent tune shifts, emittance growth, and instabilities. Figure 2 shows the results of a simulation of the vertical beam size in the positron damping ring, over 1000 turns, starting from the nominal beam parameters, and with various densities of electron cloud (averaged around the ring). Up to densities of around 1.2×10^{11} m^{-3}, there is no significant increase in the beam size; above densities of 1.4×10^{11} m^{-3}, the interaction between the cloud and the beam drives a weak instability that increases the beam emittance.
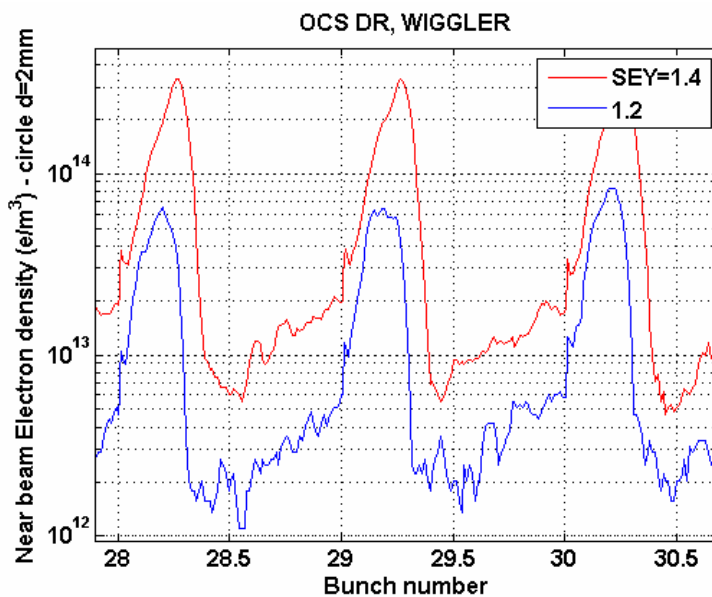
Figure 2: (M. Pivi, SLAC) Variation of near-beam electron cloud density in the wiggler section of the ILC positron damping ring. Cases with peak secondary electron yield 1.2 (blue line) and 1.4 (red line) are shown.

The electron cloud research program for the ILC damping rings has two goals: first, to determine the maximum density of electrons in the chamber before there is an adverse impact on the beam quality and stability; and second, to demonstrate effective and practical techniques for suppressing the development of electron cloud, so that the electron density stays at safe levels. Figure 3 compares the predicted instability threshold, with the expected cloud density under various conditions. While it seems likely that conditions can be found to avoid any effects from electron cloud, the significant uncertainty in the simulation results makes it desirable to aim for a significant margin of safety.
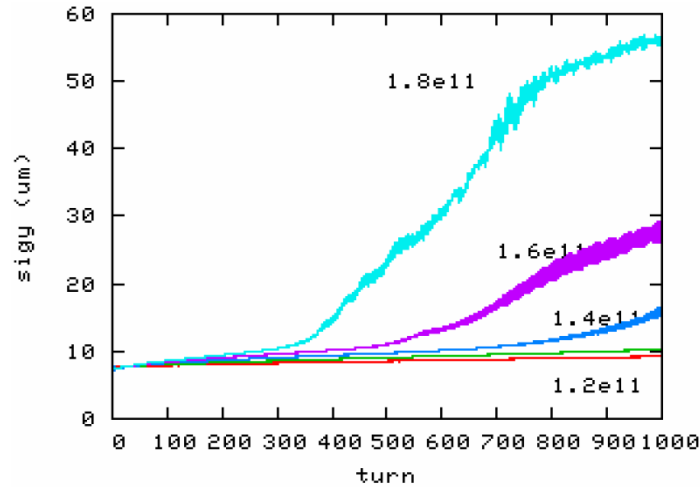
Figure 3: (K. Ohmi, KEK) Evolution of vertical positron beam size over 1000 turns in the ILC damping ring, for various densities of electron cloud. An instability threshold occurs for a cloud density between 1.2 and 1.4×10^{11} m^{-3}.
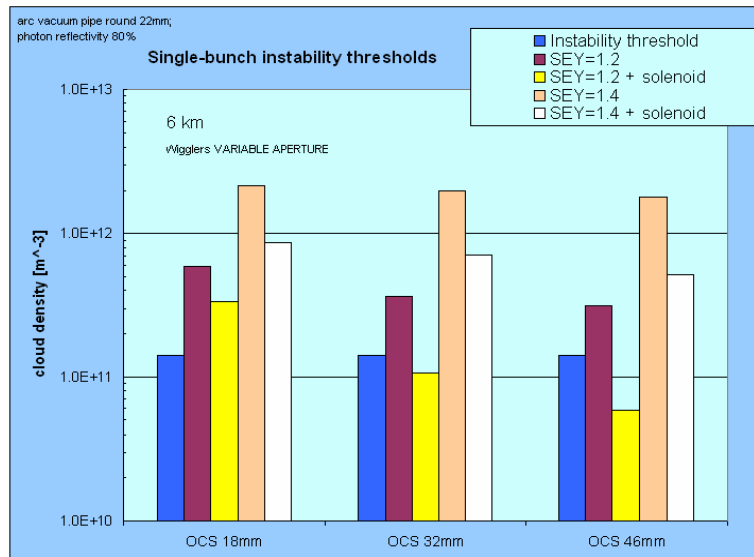
Figure 4: (M. Pivi, SLAC) Electron cloud density threshold (blue bar), compared with predicted average density under various conditions. The three groups show different wiggler apertures: 18 mm, 32 mm and 46 mm (left to right).

In the B-factories, solenoid windings around the vacuum chamber were effective at suppressing build-up of electron cloud in field-free regions. This technique may also be used in the ILC damping rings; however, the damping rings will have a relatively large proportion of their circumference within wiggler and dipole fields, so that even with all straight sections covered by solenoids there could remain enough electron cloud to drive instabilities in the beam. Other techniques being considered for suppression of electron cloud build-up in the damping rings include: coating the chamber surface with a material having a low secondary electron yield (such as titanium nitride, or titanium zirconium vanadium); shaping the surface with grooves to "trap" and re-absorb

secondary electrons before they can be accelerated by the beam; use of clearing electrodes. All these techniques show promising results in simulation; coatings and grooved surfaces have also been shown to reduce the effective secondary electron yield (SEY) in measurements performed in specialized apparatus. Experiments are underway to investigate the properties of low-SEY coatings and grooved surfaces in an accelerator environment at PEP-II [6] and initial results appear promising.

Predictions of the build-up of electron cloud and its impact on the performance of the damping rings are based on simulations. However, although the simulation codes have been benchmarked against data collected from existing machines, there remain significant extrapolations in the beam parameters from any existing storage ring to the ILC damping rings. For example, the vertical emittance specified for the damping rings is three orders of magnitude lower than that achieved in the B-factories. There are concerns that effects that could significantly limit the performance of the damping rings may not even be observable in machines with relatively much larger emittances. Therefore, a priority for the R&D program is to collect data at a facility that will: provide beam parameters (particularly, bunch charge, bunch spacing and emittances) and environment (vacuum chamber, wiggler fields) as close as possible to those specified for the damping rings; allow detailed measurements of cloud build-up and its impact on the beam; allow tests of a variety of mitigation techniques. Possibilities being considered for test facilities include CesrTA at Cornell University, and, on a longer timescale, KEKB.

While effects ascribed to electron cloud have been observed in electron machines, electron cloud is not expected to have a significant impact on performance of the electron damping ring. However, there are concerns that beam instabilities could be caused by accumulation of ions from residual gas in the vacuum chamber. At equilibrium, the small size of the beam means that only light ions can be trapped; however, the injected beam size is much larger, and even heavy ions can be trapped during the early stages of the damping process. Including regular gaps in the fill can prevent long-term ion trapping (though the gaps must be positioned so as to be consistent with the overall timing scheme of the ILC), but it is possible that sufficient ions can accumulate during the passage of even a small number of bunches to cause observable instabilities. Effects consistent with such a "fast ion" instability have been observed at the ALS [7], the PLS [8] and the ATF [9], though quantitative data are still lacking: fast ion effects are expected to become stronger as the beam size is reduced, and achieving the low-emittance regime specified for the damping rings is challenging. A theory to describe the fast ion instability has been developed by Raubenheimer and Zimmermann [10]; applied to the ILC damping rings, the theory predicts instability growth times of a few tens of turns, depending on the vacuum pressure. Modern bunch-by-bunch feedback systems are capable of suppressing instabilities with growth times of 20 turns or so, and recent simulation studies 11 suggest that a combination of a fast feedback system and low vacuum pressure (below 1 ntorr in the straights) will allow the damping rings to avoid limitations from ion effects.

Some other dynamics effects more usually associated with relatively low energy beams or hadron storage rings are of potential concern in the ILC damping rings because of the very low emittance regime in which the damping rings will operate. However, estimates made for the present design of the damping rings indicate that such effects should not limit performance. For example, the increase in horizontal emittance from intrabeam scattering will likely be of order 20%, which can easily be

accommodated by providing an appropriate margin in the lattice design. While it is still desirable to confirm predictions of collective effects such as space charge and intrabeam scattering by performing studies in machines operating as close as possible to the parameter regime of the damping rings, the top priorities for the ILC damping rings remain electron cloud and ion effects.

2.1.3 Preservation of Small Emittance in the RTML and Main Linacs

There are two main sources of emittance growth:
- wakefield effects, primarily in the superconducting linacs, but also from other apertures such as collimators;
- Chromatic (i.e. dispersive) effects, arising from magnet misalignment and beam trajectory errors.

One of the advantages of using superconducting RF is the relatively low cavity wakefields. The expected mechanically alignment accuracy of the accelerating cavities (a few hundred microns RMS) is good enough for suppressing single-bunch wakefield effect to acceptable levels. Multi-bunch wakefields are handled by random detuning (by fabrication errors) of the higher-order modes (HOM) in cavities at the 0.1% level, and by special purpose HOM couplers and absorbers.

Chromatic effects, however, require a typical quadrupole alignment accuracy which is one to two order-of-magnitude better than can be achieved with state-of-the-art mechanical alignment techniques. Beam-based alignment algorithms become mandatory to achieve the required emittance preservation (emittance growth budgets).

The two main sources of spurious dispersion are offset errors of quadrupole magnets and tilt errors of accelerating cavities, both of which effectively give a dispersive (i.e. energy-dependent) kick to the particles in a bunch. The kicks introduce a linear energy correlation in the transverse beam phase space (dispersion) resulting in a larger *projected* emittance, which if left locally uncorrected filaments as the beam is transported (accelerated in the linacs) down the machine. The focus of the single-bunch beam dynamics studies in these sections of the machine are primarily aimed at determining beam-based alignment techniques which achieve the required alignment accuracy (tolerable spurious dispersion). These techniques are generally based on measurements of the beam trajectory using Beam Position Monitors (BPMS). Additional 'global' tuning techniques, such as the application of closed-trajectory dispersive bumps or adjustment of combinations of quadrupoles to fine-tune the remaining linear aberrations require either a direct and accurate measurement of the beam emittance, or ultimately the luminosity itself.

Beam Based Alignment Techniques

There are several methods of beam-based alignment (correction) for suppressing dispersive effects which cause emittance growth. Here we discuss two examples: kick minimization steering (KMS) and dispersion free steering (DFS).

In KMS, we assume every quadrupole magnet has attached dipole correctors (one horizontal and one vertical) and an attached BPM. The sum of squares of total kick at the quadrupole-dipole,

$$\sum_i r^2 (y_i \pm \theta_i / k_i)^2 + \sum_i y_i^2 \,, \tag{4}$$

is minimized. The sign + is for horizontal and − for vertical plane. i is index of quad-dipole-BPM set, y_i the beam position (BPM reading), θ_i the kick angle of the dipole corrector, k_i the integrated normalized strength (inverse of the focal length) of the quadrupole magnet. Note that $\pm k_i y_i$ is the horizontal or vertical kick angle produced by the quadrupole magnet if there is no relative offset between the quadrupole magnetic field center and the BPM electrical center. The second term is necessary to *constrain* the absolute trajectory, preventing it from becoming too large (a general result in the presence of measurement errors); r is a weighting factor, which should be approximately equal to the ratio of the expected typical quadrupole misalignment and quadrupole-to-BPM offset error, the latter of which should be small for the algorithm to be effective. Accurate determination of the quad-to-BPM offset requires beam measurement, using a technique known as "quad shunting". In quad shunting, the strength of quadrupole magnets is changed one by one and the resulting difference in the downstream beam trajectory is measured. The difference trajectory is proportional to the strength of the quadrupole field and the beam offset with respect to the quadrupole field center.

DFS functions somewhat differently. The actual dispersive trajectory is measured directly by varying the beam energy. A corrected trajectory is found which minimizes the difference measured, and hence the dispersion. Usually, a long beam line is divided into several sections and the correction is done section by section starting at the upstream end of the machine and moving systematically down. The beam energy is modified by typically tens of percent by adjusting the accelerating RF. The dipole correctors are then adjusted to minimize

$$\sum_i w^2 (y_i - y_{0,i})^2 + \sum_i y_{0,i}^2 \tag{5}$$

where $y_{0,i}$ and y_i are beam position at i-th BPM for the on-energy (nominal) and off-energy beam trajectories respectively. As for KMS, the second term is again necessary to avoid large absolute trajectory displacements in the presence of measurement errors. For DFS, the weighting factor w is approximately the ratio of typical expected RMS BPM misalignment and BPM resolution.

Examples of Simulated Performance: Long Return Line (RTML)

The ~11 km long return line, which transports the 5 GeV beam from the Damping Ring to the end of the accelerator complex will require beam-based alignment. Simulations of KMS, assuming quadrupole RMS offset error of 300 μm, quadrupole RMS roll error of 300 μrad and BPM-to-Quad RMS offset error of 30 μm show that a normalized vertical emittance growth of about 2nm, (10% of the nominal emittance) can be achieved [12]. Figure 5 shows sensitivity to the BPM-to-Quad RMS error. The results indicate that an BPM-to-Quad offset of typically <50 μm is required. The residual (minimum) emittance growth is due to *x-y* coupling from the rolled quadrupoles.
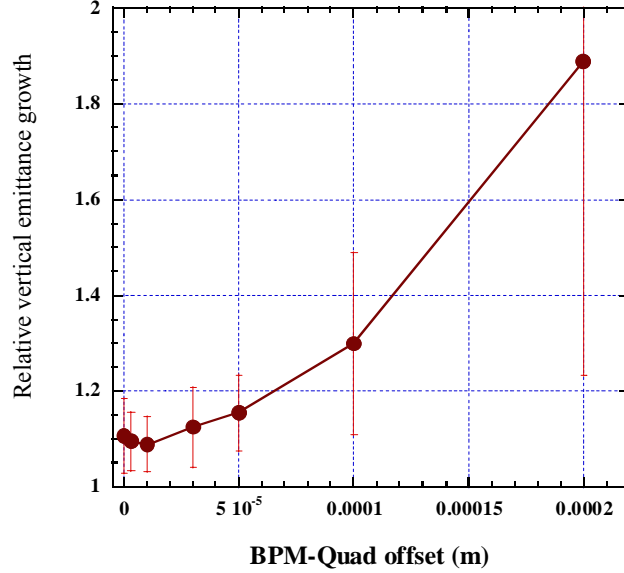
Figure 5: Vertical emittance at the end of the long RTML return line after KMS. as a function of BPM-to-quad offset error. (Averaged results over 100 random seeds.)

Examples of Simulated Performance: Turn around (RTML)

The 5 GeV 180° turn-around at the end of the return line has much stronger focusing to keep the horizontal dispersion small and hence reduce the effect of synchrotron radiation on the horizontal emittance. As a result, alignment tolerances are much tighter than in the turn-around. Preliminary simulations of KMS resulted in more than 20 nm expected vertical emittance growth (>100%). Adding 'global corrections' using dispersion bumps and coupling bumps have reduced this to ~4 nm, or 20%. These initial result are still not satisfactory and further studies are on going [13,14,15].

Examples of Simulated Performance: Bunch Compressors

The two bunch compressor sections required to reduce the bunch length by a factor of 30 may eventually prove to be the largest challenge for emittance preservation in the ILC. The long bunch lengths in the compressor linacs (9 mm in the first stage, 1 mm in the second stage) make increase the sensitivity to the expected random cavity tilts and wakefield effects. The large energy spread generated by the compressor RF (2.5% and 1.5% in the first and second compressor stages respectively) significantly increases the chromatic effects and hence tighten the required alignment tolerances.

One candidate tuning method in the bunch compressors is DFS. Since the beam is far from the crest of the RF (close to the zero-crossing in the first-stage compressor), it is particularly convenient to use a phase of adjustment to produce the required change in beam energy. The result of a simulation study is shown in Figure 6. In this simulation, beam trajectories were recorded at three RF phase settings: nominal phase ϕ_0, $\phi_0 + \Delta\phi$ and $\phi_0 - \Delta\phi$. The figure of merit to be minimized is now (see equation 4):

$$\sum_i w^2 (y_{+\Delta\phi,i} - y_{-\Delta\phi,i})^2 + \sum_i y_{0,i}^2 \tag{6}$$

where $y_{\pm\Delta\phi,i}$ denote i-th BPM reading with phase setting of $\phi_0 \pm \Delta\phi$. The method was applied simultaneously to both the first- and second-stage compressors. This minimum result of 4 nm increase (20%) is good but still requires improvement [16, 17].
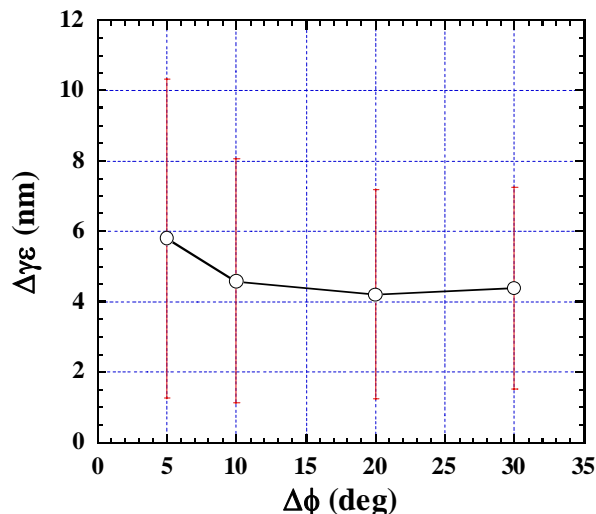
Figure 6: Vertical normalized emittance growth as function of phase change of DFS in the bunch compressors. Average of 50 random seeds (circles) and standard deviation (error bars) are shown. (The following random RMS errors were used; quad and bend magnet offset 150 μm, BPM-to-quad offset 7 μm, BPM resolution 1 μm, cavity offset 300 μm and cavity tilt 300 μr.)

Examples of Simulated Performance: 15-250 GeV 1.3 GHz Superconducting Main Linac

Low emittance preservation tuning in Main Linac has been intensely studied over the past decade by many people using many different computer codes. DFS is the most popular tuning method [18, 19, 20, 21, 22]. Results of DFS have been cross checked using various simulation codes [24]. KMS with an additional correction for cavity tilts has also been studied (although less extensively than DFS) with similar performance [25]. Here, we show example of DFS tuning studies [23].

Table 2: RMS alignment errors assumed for the Main Linac simulations. These values are considered as 'installation' alignment tolerances.

	Vertical	*Horizontal*
Quad offset w.r.t. design	0.36 mm	1.08 mm
Cavity offset w.r.t. design	0.64 mm	1.92 mm
BPM offset w.r.t. design	0.36 mm	1.08 mm
Quad roll w.r.t. design	0.3 mrad	
Cavity tilt w.r.t. design	0.3 mrad (pitch)	0.9 mrad (yaw)
BPM resolution	1 μm	1 μm

Table 2 shows the vertical and horizontal alignment errors assumed in the simulations. Figure 7 shows the resulting normalized vertical emittance along the Main Linac after DFS (assuming the errors in Table 2), averaged over 50 seeds.
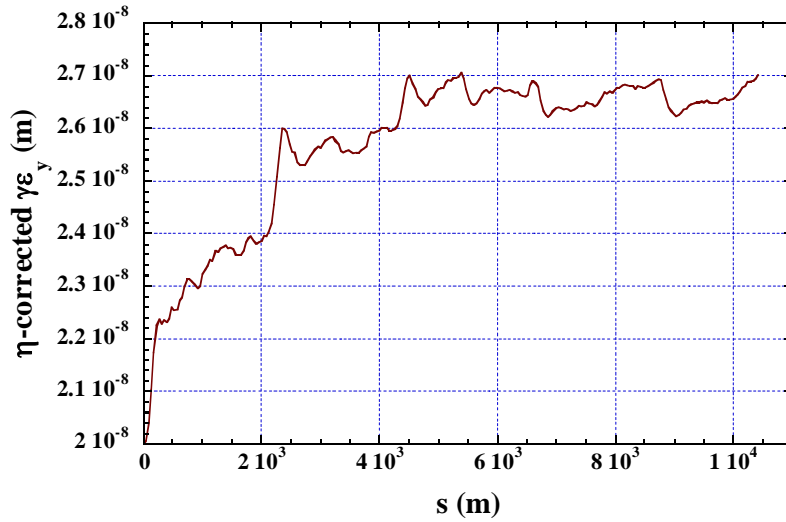
Figure 7: Normalized vertical emittance along Main Linac after DFS with the "standard" set of errors. Average of 50 random seeds.
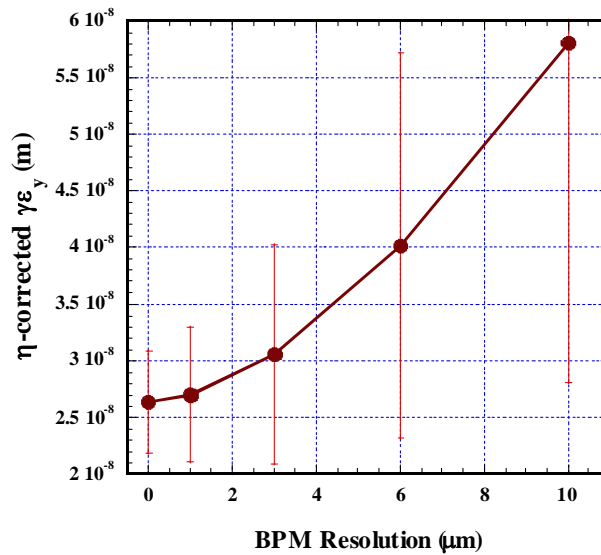
Figure 8: Effect of BPM resolution on the average vertical emittance after applying of DFS. (Data points are averaged over 40 seeds.)

The achievable performance for DFS is set by the BPM resolution. Figure 8 shows the effect of the BPM resolution (random noise) on the DFS performance. To keep the emittance growth below ~50% in the Main Linac would require a BPM resolution of ~3 μm or less (based on this simulation.) Note the residual emittance growth at zero resolution (~6 nm) is attributed to the remaining non-zero errors in Table 2.

The results shown in the above figures assume a linac which follows the curvature of the earth ($r \sim 6000$ km). This results in a small but nevertheless non-zero *design* vertical dispersion along the entire linac. The DFS algorithm was developed for 'laser-

straight' beamlines, where the design dispersion is zero (hence dispersion *free* steering). For the curved linac, the goal is to achieve the non-zero design dispersion: in this case we tend to refer to the modified algorithm as dispersion *matched* steering (DFM).

For the most part, the impact of the non-zero dispersion is negligible (providing it is correctly matched at the entrance and exit of the linac and that it is accounted for in the algorithm). One particular consequence is an increased sensitivity to the linear slope (or calibration) error of the BPMs. Figure 9 shows the influence of random BPM scale errors on DMS performance. Clearly a calibration better than ~10% is required, which is quite challenging. This effect can be easily understood. DFS is essentially a nulling technique: we simply do not want the beam to move when we change the energy. Here the scale errors only play a role in how fast the algorithm converges (i.e. the number of times we need to iterate). For DFM the beam moves with energy *by design*, and this motion must be accurately determined, and hence the scale error plays a significant role.
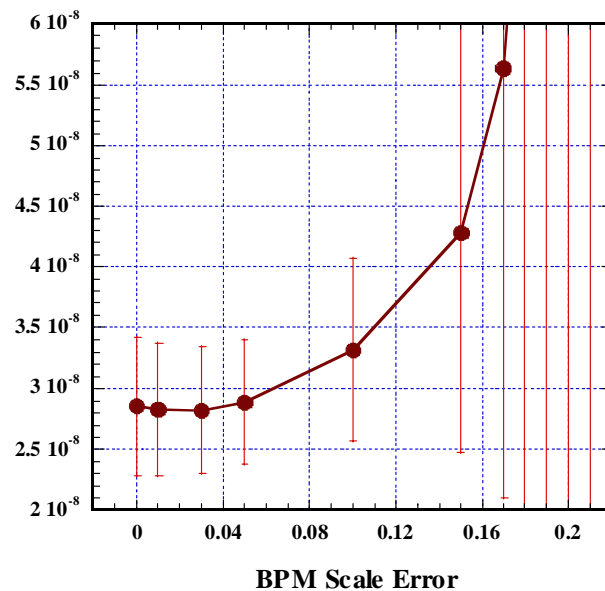
Figure 9: Impact of BPM linear scale error on DFS performance.
(Date points are averaged over 40 seeds).

Dynamic effects

KMS, DFS and DMS are all beam-based alignment techniques which have been developed to achieve the *static* alignment tolerances required for emittance preservation. The sensitivity to (predominantly) quadrupole motion due to vibration or slow ground motion drifts (or indeed other environmental effects such as temperature) requires attention to trajectory correction and almost constant beam tuning.

Both quadrupole vibration and power supply ripple will cause "beam jitter" (fast random transverse motion of the beam). In the Main Linac, a vertical quadrupole vibration of 100 nm cause approximately one beam sigma of vertical motion of the linac (entrance to the BDS), and scales linearly with the vibration amplitude. The emittance growth "jitter" associated with this amplitude of motion is negligible, but scales quadratically with the quadrupole vibration amplitude; an amplitude of ~200 nm begins to have a significant effect. Fortunately, we do not expect the quadrupoles to vibrate more than 100 nm inside the cryostats.

The beam motion would significant impact on the luminosity, however, if it were not for the use of fast intra-train beam feedback.

Apart from quadrupole vibration, there are other potential sources of potentially damaging beam jitter. One concern in the long transport line (return line) in the RTML, where time-dependent stray magnetic at the nTesla level may be an issue.

Again the ILC makes use of the long 1 ms ~3000 bunch train to correct an induced jitter. A feed-forward system utilizing the turnaround (monitoring orbit of each bunch before the turnaround and correct the orbit of that bunch after the turnaround), will mitigate most of accumulated beam jitter from the damping ring to the entrance of the bunch compressors. The remaining uncorrected effect is then the emittance growth. This is especially a problem for the jitter in the turn-around itself, where the strong focusing leads to a large chromaticity, and hence tight tolerances on both magnet position and beam stability (jitter).

One study has showed that vertical orbit jitter of one-sigma of the beam size in the turnaround causes emittance growth of about 1.6 nm, or 8% of nominal emittance. A random time-dependent stray magnetic field of 2 nTesla in the long transport line can induce such orbit jitter [26]. (Note this is only for fast variation which cannot be corrected by trajectory feedback leading into the turn-around.) Fortunately measurements of stray fields inside accelerating housings have shown weaker time-dependent amplitudes [27]. However, for confirmation, measurements at different places under similar conditions to the ILC beam tunnel are needed.

2.1.4 Beam Delivery System

Producing ILC luminosity requires colliding beams with nanometer scale sizes, which is the primary goal of Beam Delivery System. Consequent beam dynamics challenges include the need for strong focusing in the Final Focus part of BDS, compensation of chromaticity in the FF, careful compensation of nonlinear aberration in FF lattice and overcoming synchrotron radiation driven emittance growth arising in the bends, quadrupoles and other magnets of BDS. The small beam sizes at the interaction point (IP) and small beam emittance produce particular requirements on stability of the elements and on the design of feedback systems and tuning methods. The Beam Delivery must also provide acceptable background conditions for the experimental detectors, the innermost vertex detector of which has a radius of only 1.2-1.5 cm. Providing acceptable background would require avoiding even a single particle of the beam hitting any apertures in the Interaction Region (IR), requiring high-efficiency collimation of the unavoidable beam halo which accompanies the beam core at large apertures. The relatively small gaps of spoilers and absorbers of the collimation system may create wake-fields and an emittance growth for off-centered beam; use of non-linear magnets (such as octupoles) to effectively fold in the high-amplitude tails of the halo may allow the widening of the spoiler gaps in the collimation sections, thus alleviating the wake-field effects.

Addressing stability of the BDS beamline would require constant tuning of various knobs, to prevent decay of the luminosity, and also requires careful measurement of the beam properties (phase space) as it comes out of the linac. The current 14 mrad crossing-angle at the IP needs to be compensated with use of crab-cavities, which rotate the beam before collision but must not perturb the beam quality due to various beam-induced parasitic modes excited in the cavities themselves. The solenoid field of the

experimental detector, which overlaps with quadrupole field of the final focusing magnets, produces anomalously large coupling of the beam, which must be compensated. As a final example, the resistive wall wake-fields of the vacuum chamber are capable of deteriorating the beam emittance, if the chamber is not accurately aligned to the beam. There are many other challenges in the design of Beam Delivery system, related to extracting highly disrupted beam, providing machine protection functions, arranging Interaction Region configuration for two push-pull detectors, providing precise beam energy and polarization measurements *etc.*, which are beyond the scope of this beam dynamics focused article.

The Beam Delivery design and beam dynamics challenges mentioned above are addressed in the system outlined in Figure 10, where the optics and functions of BDS are shown. The main subsystems of the Beam Delivery starting from the exit of the main linac are the diagnostics region, betatron and energy collimation, final focus, interaction region (IR) and extraction line. The initial part of the BDS is responsible for measuring and correcting the properties of the beam before it enters the collimation and FF. The skew correction section and the emittance diagnostic section contain four skew quadrupoles and also four laser wires which are capable of measuring horizontal and vertical RMS beam sizes down to 1 micrometer. Such system allows a complete measurement of 2D transverse phase space and determination of the projected horizontal and vertical emittances and correction of any arbitrary linearly coupled beam. Particles in the beam halo are removed in the BDS collimation system consisting of betatron collimation section followed by energy collimators. The collimators are arranged in spoiler-absorber pairs where the spoilers have typical full gap of about 1mm, and are tapered, to reduce wake-fields. Electromagnetic showers created by primary beam particles in the collimators produce penetrating muons which can easily reach the collider hall. The muon flux through the detector is reduced by five-meter-long tunnel-filling magnetized iron shield located several hundred meters upstream of the collision point. The Final Focus system de-magnifies the beam to the required size and provides local chromaticity correction using sextupoles next to the final doublets [28]. The final focus includes two superconducting octupole doublets which use nonlinear focusing to reduce the amplitudes of beam halo particles while leaving the beam core untouched. This "tail-folding" would permit larger collimation aperture that in turn would reduce the amount of beam power intercepted in the collimators and the unwanted wakefields [29]. The Beam Delivery system is designed for 500 GeV CM and can reach up to 1 TeV CM in the same layout, with additional magnets installed in the provided gaps. Below we will review some of the design features and associated beam dynamics challenges in more detail.
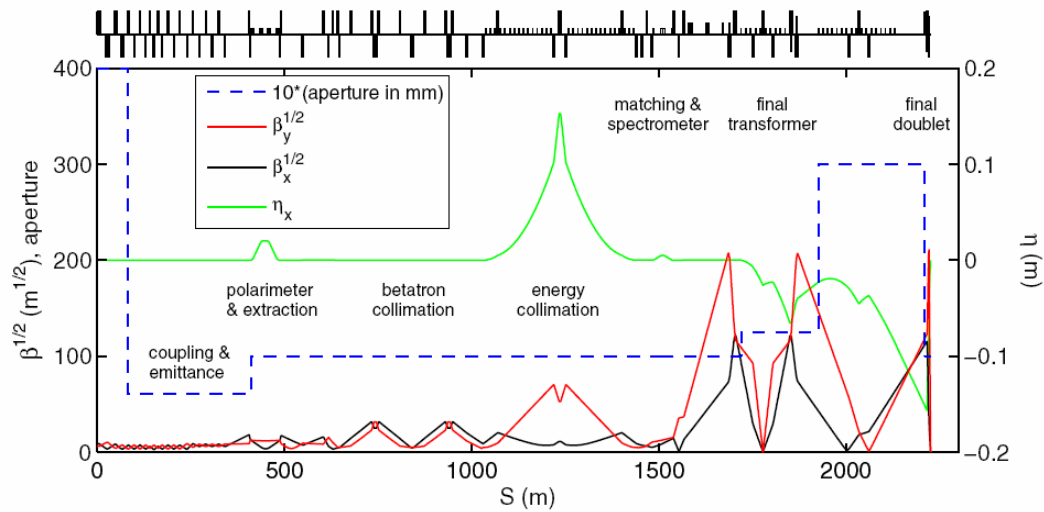
Figure 10: Beam Delivery optics and subsystems. The system is designed to work up to the energy of 1 TeV in the center of mass in the same layout.

The layout of magnets in the Final Doublet of the Interaction Region of the BDS is shown in Figure 11. The 14 mrad crossing angle dictates the use of compact design of the superconducting magnets. The local compensation of chromaticity is done with sextupoles SD0 and SF1 embedded in the Final Doublet. The first quadrupoles in the FD are built with use of active shielding design – a negative polarity quadrupole coil compensates the fringe field outside of the magnet, thus reducing cross-talk between the incoming and outgoing beamlines. The magnets of the Final Doublet are arranged in two independent cryostats, with warm space in between – this is the area where beampipe will be disconnected in the push-pull operation foreseen for the two detectors.
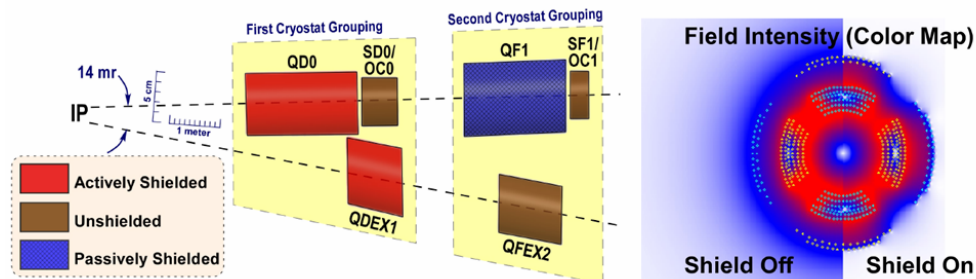
Figure 11: Layout of the BDS Interaction Region magnets, quadrupoles QD0 and QF1 and sextupole-octupole packages SD0/OC0 and SF1/OC1 for the incoming beam and quadrupoles QDEX1/2 for the outgoing beam. Active shielded quadrupoles is illustrated on the right. The passively shielded quadrupoles use iron layer for the shielding.

The design and beam dynamics of the Interaction Region is complicated by the presence of the detector's 3-5 Tesla solenoid field, which overlaps with the Final Doublets, in particular the QD0 quadrupole. The overlap of the solenoid and quadrupole field breaks the symmetry of the solenoid field and create anomalously large coupling of the beam, which is many tens of times larger than the same solenoid would produce

if there would be no overlap with quadrupoles. Such coupling could be compensated efficiently and locally with use of a weak antisolenoid, with optimized field shape [30]. The antisolenoid is weak in the sense that it compensates only the part of detector solenoid field which overlaps with the FD, and not the full integral. Such compensation is illustrated in Figure 12. An interesting and helpful feature of such local compensation is that it practically independent on beam energy or optics settings, and therefore would not require retuning in normal operation. In the most recent design of the FD, the antisolenoid is incorporated into the QD0 cryostat in a force-neutral double solenoid configuration [31], which eliminates the force acting on the compensating solenoid from the main solenoid of the detector.
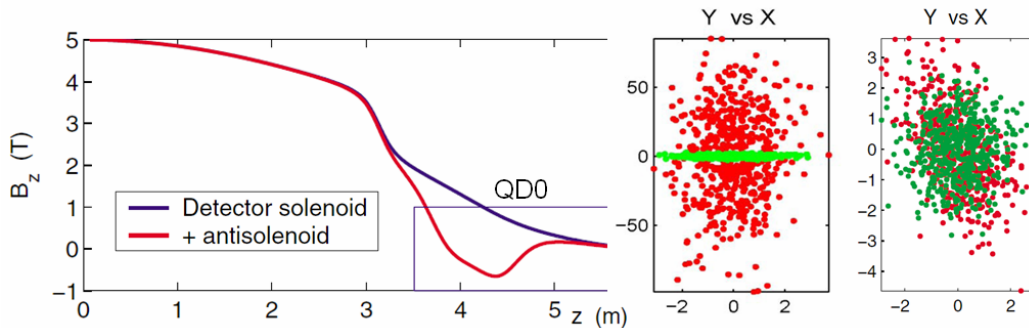
Figure 12: Example of the overlap of detector solenoid field with Final Doublet quadrupole QD0. The field overlap produces the anomalously large beam coupling illustrated in the middle picture, in normalized X-Y plane. Green and red dots show the tracked beam, without and with the solenoid effects. Coupling can be compensated locally, with use of antisolenoid, which removes major part of the coupling as shown on the right picture.

The Beam Delivery collimation system must collimate the beam tails outside of 8-10 sigma in horizontal and 60-80 sigma in the vertical plane, in order to protect IR apertures from hits by any beam particles, or any synchrotron radiation photons generated by the beam halo. The beam sizes in the location of spoilers are enlarged to provide survival of spoilers after an accidental hit by a bunch, which determines the size of the gaps of the spoilers to be about a millimeter. Geometric and resistive wake-fields from narrow collimators are one of the challenges of the design not only because they create single bunch emittance growth for off-centered bunch and amplify beam jitter, but also due to challenges of accurate predictions of these effects. Computation of wakefields from shallow angle tapered collimators represent significant challenge, both for analytical and computer models, which is one of the reason for ongoing experimental program to measure collimation wakes for spoilers of various shapes and materials [32]. With the present design of the collimation system, ~0.5σ vertical beam jitter would result in approximately 5% emittance growth due to collimation wakefields. One of the possible ways to open the gaps of spoilers and reduce the effect of collimation wakefields is the use of so called octupole doublets to fold the tails of the beam halo [29]. These doublets apply nonlinear focusing, affecting the beam halo at large amplitudes, while leaving the beam core untouched. Two opposite polarity octupoles are arranged in pairs such that their overall combined effect gives focusing in all directions as illustrated in Figure 13. Two superconducting octupole doublets are installed in the beginning of Final Focus to allow folding of tails by a factor of three, in

terms of particle amplitudes in the Final Doublet, and thus provide an additional safety factor for collimation system.
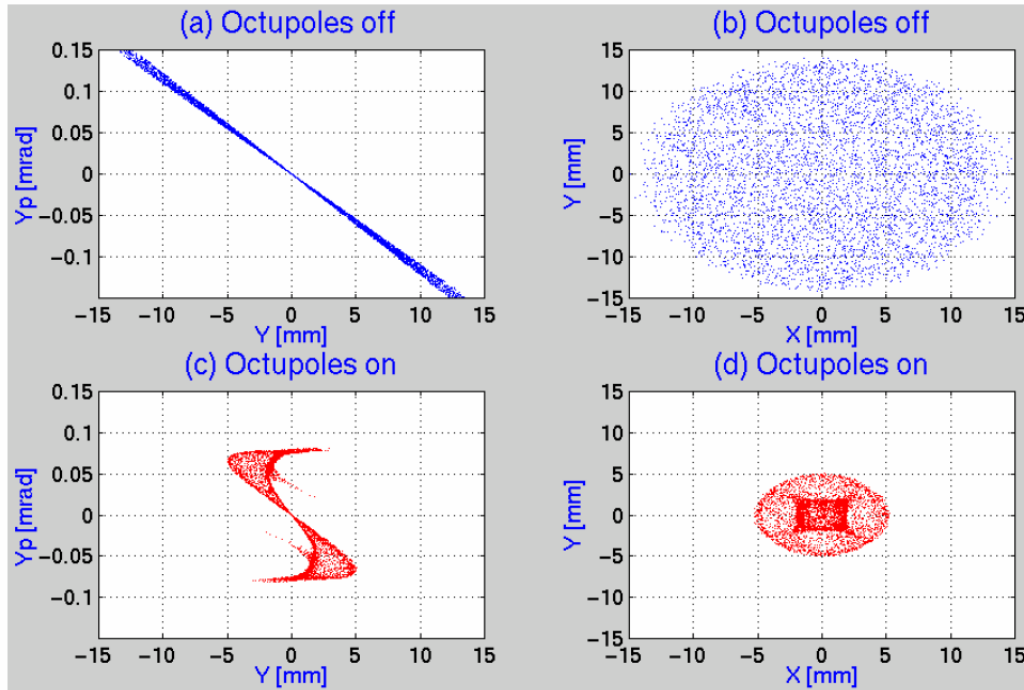
Figure 13: Tail folding effect of the octupole doublets on beam halo, as illustrated by the beam distribution at a beta-function maximum point in the Final Focus after the octupole doublets.

Maintaining the stability of the BDS is an essential prerequisite to producing luminosity. Since the beams have RMS vertical sizes of 5.7 nm at the IP, vertical offsets of about 1 nm will noticeably reduce the luminosity. In addition, especially for parameter sets with higher disruption, the beam-beam interaction is so strong that the luminosity is extremely sensitive to small variations in the longitudinal shape of the bunch caused by short-range wakefields. Beam-based orbit feedback loops are used to maintain the size and position of the beam at the IP. All of the feedback loops use beam position monitors with at least micron-level (and in some cases sub-micron) resolution to detect the beam position, and dipole magnets or stripline kickers to detect the beam. There are two basic forms of feedback in the BDS: train-by-train feedbacks, which operate at the 5 Hz repetition rate of the ILC, and intra-train feedbacks, which can apply a correction to the beam between bunches of a single train. A train-by-train feedback with several correctors controls the orbit through the sextupoles in the horizontal and vertical planes, where the optical tolerances are tightest. Additional correctors throughout the BDS help reduce long-term beam size growth. The orbit control feedback can maintain the required beam sizes at the IP over periods from a few hours to several days depending on details of the environment. On longer timescales, IP dispersion and coupling knobs need to be applied. The intra-train feedbacks use the signals detected on early bunches in the train to correct the IP position and angle of subsequent bunches. The offset of the beams at the IP is determined by measuring the deflections from the beam-beam interaction; this interaction is so strong that nm-level offsets generate deflections of tens of microradians, and thus BPMs with micron-level

resolution can be used to detect offsets at the level of a fraction of a nanometer. Corrections are applied with a stripline kicker located in the incoming beamline between SD0 and QF1.

The challenge of tuning the Beam Delivery system and maintaining the very small beam size reliably and for a long time is one of the motivations for creating the Beam Delivery test facility ATF2 at KEK, Japan [33]. The ATF2 is a small scaled down version of the ILC Beam Delivery system which will use 1.28 GeV beam extracted from ATF damping ring and focus it into 35-40 nm beam size. Layout of the ATF2 facility is shown in Figure 14.
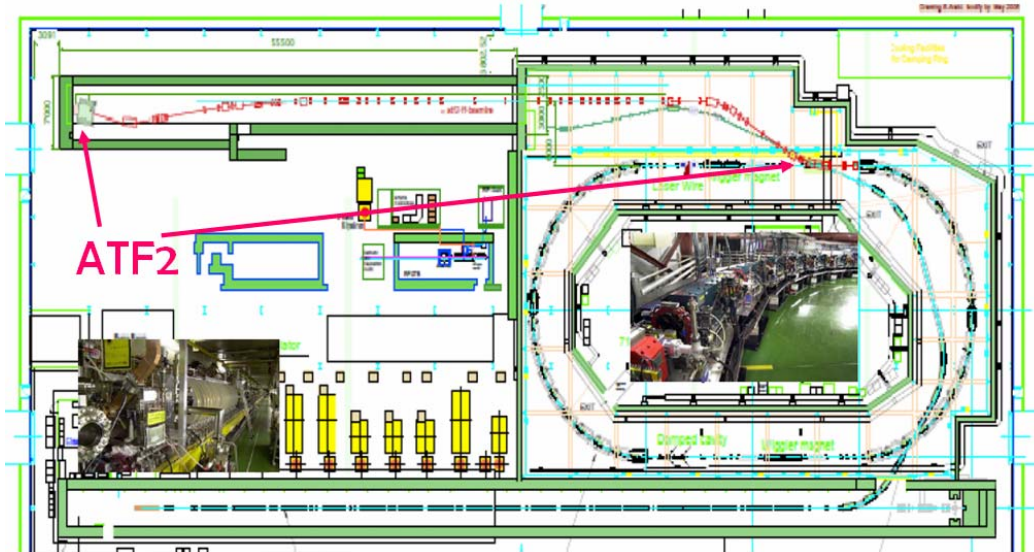
Figure 14: Layout of the ATF facility at KEK, Japan, where the ATF2 beam delivery test facility (shown by red) is being constructed

Maintaining the stability of ATF2 beam size will be done in a very similar way as is foreseen for the ILC BDS, with application of orbit feedbacks and sextupole tuning knobs. However an obvious complication is the absence of the opposite beam which provides IP beam position signal based on beam-beam effects and also the absence of a fast luminosity monitor. Those essential functions will be provided by nanometer resolution beam position monitor and a Shintake beam size monitor [34]. The large number of pulses required to obtain statistically significant measurement of the beam size is one of the challenges which makes tuning of the ATF2 beamline at least of the same complexity as ILC BDS. The intra-train feedback will also be studied in ATF2, when the multi-bunch mode (about sixty bunches) will become available.
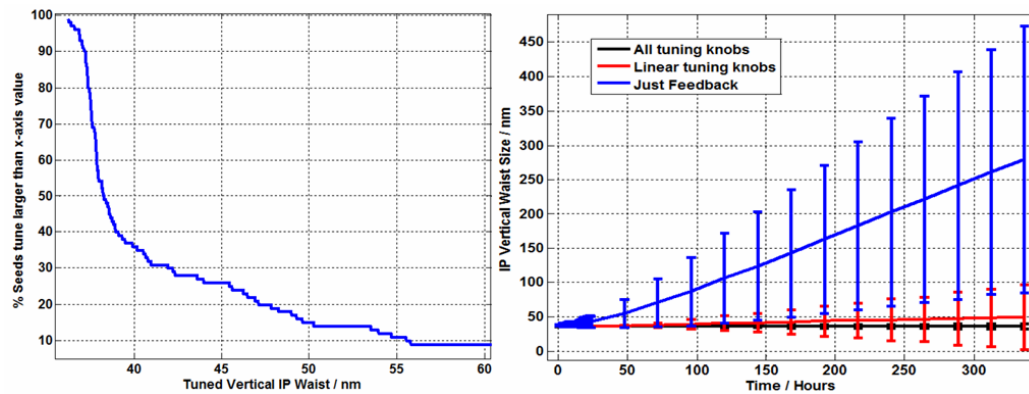
Figure 15: (Glen White, SLAC) Illustration to the working progress for the tuning study of ATF2 beamline. On the left, the histogram which shows the number of cases that achieved certain vertical beam size. For example, 65% of the cases reach beam size smaller than 40nm. The expected errors of magnets, position, beam position and energy jitter, resolution of instrumentation, etc. are taken into account. On the right, behaviour of the IP beam sizes is shown for the case of orbit feedback only and also for the case when linear and second order knobs are applied, which then able to keep the beam size constant for long time.

Extensive studies of ATF2 tuning are being conducted now. The studies (simulations) currently being implemented for ATF2 are now including 'real-world' practical details (by necessity) that have hitherto not been included in the ILC simulations. For example the limits of the movers, beamline apertures and radiation conditions caused by loss of a fraction of the beam during tuning. An example of tuning studies for ATF2 is shown in Figure 15. Commissioning of the ATF2 is planned to start in autumn of 2008.

2.1.5 References

1. The ILC Reference Design Report: http://www.linearcollider.org/cms/?pid=1000437 (2007)
2. A. Wolski, J. Gao, S. Guiducci (editors), "Configuration Studies and Recommendations for the ILC Damping Rings," LBNL-59449 (February, 2006).
3. C.E. Mitchell and A. J. Dragt, "Computation of Transfer Maps from Magnetic Field Data in Wigglers and Undulators," ICFA Beam Dynamics Newsletter, No. 42, pages 65-70 (April, 2007).
4. Y. Honda et al, "Achievement of Ultralow Emittance Beam in the Accelerator Test Facility Damping Ring," Phys. Rev. Lett. 92, 054802-1 (2004).
5. For reviews of some recent work on electron cloud effects, including studies related to the ILC damping rings, see the proceedings of ECLOUD 2007, Daegu, Korea (April, 2007). http://chep.knu.ac.kr/ecloud07/
6. M. Pivi, "Clearing Electrodes and Groove Tests Planned for the ILC DR Magnet Regions," proceedings of ECLOUD 2007, Daegu, Korea (April, 2007).
7. J. Byrd et al, "First Observations of a Fast Beam-Ion Instability," Phys. Rev. Lett. 79, 79-82 (1997).
8. J.Y. Huang et al, "Direct Observation of the Fast Beam-Ion Instability," Phys. Rev. Lett. 81, 4388-4391 (1998).
9. Y. Honda, "Pressure Dependence Studies of Multi-Bunch Beam," presented at ISG XI, KEK (December 2003). http://lcdev.kek.jp/ISG/ISG11/DR/FI_Honda.pdf

10. T.O. Raubenheimer and F. Zimmermann, "Fast Beam Ion Instability: Linear Theory and Simulations," Phys. Rev. E 52, 5487-5498 (1995).
11. E.-S. Kim, "Simulations of Fast Ion Instability in the ILC Electron Damping Ring," ICFA Beam Dynamics Newsletter, No. 43, pages 14-18 (August 2007).
12. K. Kubo, "Simulation of Low Emittance Transport in Long Straight Line of ILC RTML," ILC-NOTE-2007-008 (2006)
13. J. Smith, "Coupling Correction in the ILC Ring to Main Linac," ILC-NOTE-2007-006 (2007)
14. P. Tenenbaum, "Application of Kick Minimization to the RTML `Front End'," SLACTN-07-002 (2007).
15. P. Tenenbaum et.al., "Emittance Preservation in the International Linear Collider Ring to Main Linac Transfer Line." Contributed to Particle Accelerator Conference (PAC 07), Albuquerque, New Mexico, 25-29 Jun 2007.
16. P. Tenenbaum, "Emittance Studies in the 2006 Bunch Compressor," ILC-NOTE-2007-003 (2007)
17. Andrea Latina, to be published.
18. N. Walker, EUROTeV-Report-2005-017 (2005).
19. A. Latina et al., EUROTeV-Report-2006-050 (2006).
20. K. Ranjan et al., MOP064, LINAC 2006(2006).
21. K. Kubo, ILC-Asia Note 2005-25, ILC-Asia Note 2005-23 (2005).
22. Eliasson and D. Schulte, EUROTeV-Report-2005-021 (2005). (bumps in ML)
23. Kubo, ILC-Asia Note 2006-04 (2006)
24. J. Smith et.al., "Comparison of Tracking Codes for the International Linear Collider" Contributed to Particle Accelerator Conference (PAC 07), Albuquerque, New Mexico, 25-29 Jun 2007.
25. K. Kubo, ILC-Asia Note 2005-18, ILC-Asia Note 2005-17 (2005).
26. K. Kubo, "Rough Estimation of Fast-Changing Stray Field in Long Transport of RTML," ILC-NOTE-2007-007 (2006).
27. J. Frisch et al., SLAC-TN-04-041 (2004).
28. P. Raimondi and A. Seryi, ``A novel final focus design for future linear colliders," Phys. Rev. Lett. 86, 3779 (2001).
29. R. Brinkmann, P. Raimondi, A. Seryi, ``Halo reduction by means of nonlinear optical elements in the NLC final focus system," SLAC-PUB-8896, PAC 2001.
30. Y. Nosochkov and A. Seryi, ``Compensation of detector solenoid effects on the beam size in linear collider", Phys. Rev. ST Accel. Beams 8, 021001 (2005).
31. B.Parker, et al., ``The Superconducting Magnets of the ILC Beam Delivery System," SLAC-PUB-12832, also PAC 2007.
32. N.K. Watson, et al., ``Direct measurement of geometric and resistive wakefields in tapered collimators for the International Linear Collider," EUROTEV-REPORT-2006-059.
33. ATF2 proposal, vol. 1 and 2, SLAC-R-771, SLAC-R-796, KEK-REPORT-2005-2, KEK-REPORT-2005-9.

2.2   The 13th International Workshop on RF Superconductivity

Chen Jia-er, Hao Jian-kui, Zhao Kui
Institute of Heavy Ion Physics, Peking University, Beijing 100871, China
Mail to: chenje@pku.edu.cn

2.2.1   Introduction

The 13th International Workshop on RF Superconductivity was held from 15th to 19th October 2007 at Peking University. More than 270 participants attended the meeting, among them 190 are from abroad. Responsible representatives from the Ministry of Education, Ministry of Science and Technology and the National Natural Science Foundation of China were also among the distinguished guests at the Opening Ceremony. The audience was warmly welcomed by the conference chair and the Executive vice chairman of the University Council of Peking University. Dr. Wang Jie, the vice president of NSFC and Professor Hasan Padamsee of Cornell University gave the congratulatory speeches at the Opening session Chaired by Professor Dieter Proch of DESY. There are totally 36 invited talks given in 11 sessions by scientists and engineers from national laboratories and universities all over the world. Two hot topics were discussed at the plenary session of the workshop chaired by professors Padamsee and Proch. In addition, 11 oral contributions are presented by students and young researchers. Prior to the workshop, 10 tutorial lectures had already been given to students and scientists new to this field. Two afternoon sessions were specially arranged for 170 posters and 14 industrial exhibitions. In the closing session awards for young researchers sponsored by Heraeus and Wah Chang Co. were conferred to Dr. A. Neumann of BESSY and N. Ptron of INFN-LNL. Finally, according to the decision of International Program Committee, the next workshop will be held in Berlin jointly hosted by BESSY and FZD-Rossendorf Laboratory.

2.2.2   Main Topics of Invited Talks

2.2.2.1   *Progress Reports of Existing Projects*

Fifteen progress reports on existing main projects were presented in four sessions of the first day. For SRF Linac-based advanced light sources, the main progress and the challenging issues were presented for FLASH and X-FEL of DESY, ERLP and 4GLS at Daresbury, ERL prototype and ERL light source of Cornell University as well as the growth of SRF in China. A nice overview on SRF linac-based FELs as fourth generation light source was given by J. Knobloch of BESSY. It is indicated by Dr. E. Vogel of DESY that as an user facility FLASH provided high brilliant VUV and EUV light with beam delivery in 70% scheduled time for user experiments and so far the world's shortest wavelength of FEL has reached 6.5 nm in SASE performance. The average gradient of the cryomodules was more than 25 MV/m, while the highest record was 40MV/m. SRF application in the domain of light and heavy ions were also well presented, for instance SRF Linac for SNS at ORNL, ISAC of TRIUMF, Coupled Cyclotron Facility at NSCL of MSU, SC Linac driver of GANIL and IUAC at New Delhi etc. It is noticed that for the ISACII/TRIUMF, the average E_{acc} for low-beta particles reached 7.5 MV/m, and for a 19-cell CH structure at Frankfurt University, a gradient of 7 MV/m was achieved.

2.2.2.2   *Basic SRF Topics*

J. Sethna tried to predict behaviour of ideal, clean SC surface exposed to large, slowly varying magnetic fields. He showed the preliminary new calculation from basic

superconductivity Eilenberger equations, which gives $H_{sh} = 0.84 \ H_c$ at $T = 0$ K and $H_{sh} = 0.745 \ H_c$ at $T = Tc$. It is 13% larger than GL (Ginzburg-Landau) estimate at $T=0$ and in agreement with GL near $T = Tc$. According to Eilenberger E_{acc} might reach 120 MV/m for perfect Nb and 200 MV/m for perfect MgB_2 respectively.

G. Ciovati and A. Romanenko reported developments on analysis and measurements of Q slope since SRF2005. Experimental results on Nb cavities showed that mm-scale surface roughness, Nb_2O_5 oxide layer and Grain boundaries do not play a dominant role in causing the Q-drop. Q-drop and baking effect are related to changes up to a depth ~ 20 nm from the outer surface. Q-drop is driven by high magnetic field. Surface treatments which affect the energy gap also affect the Q-drop onset and the quench field after baking. To study the effect of baking in improving the Q slope, cavity surfaces are examined by a number of analysis with AFM, OP, Magneto-optical imaging, XPS, SIMS, ToF-SIMS, 3DAP, EBSD, etc. It turned out that crystalline defect structure within penetration depth may play a substantial role for the effect.

New possibilities to improve the cavity performance by reducing vortex dissipation were presented by A. Gurevich. It includes RF annealing of R_s by the rf field cycling: non-monotonic hysteretic field dependence of R_s (H) at $H \ll H_c$; Eliminating vortex hotspots by external thermal gradients; Multilayer S-I-S-I-S coating may break the Nb monopoly taking advantage of superconductors with much higher H_c without the penalty of lower H_{c1}; Strong reduction of the BCS resistance because of using SC layers with higher Δ (Nb_3Sn, NbN, etc).

2.2.2.3 Advances in SRF Technology

Twelve invited talks were presented during 3 sessions of Advances in SRF Technology. The topics consists of the frontier aspects in SRF fields: Advances in Electropolishing / Rinsing and Assembly Techniques to Reduce Field Emission; Gradient Yield Improvement Efforts for Single and Multi-Cells and Progress for very high gradient cavities; Prospects for higher Tc superconductors for SRF application; Progress in Seamless Cavities and SC Spoke Cavity Development; New Designs for tuners and HOM couplers and broadband absorbers; Developments of Input Power Coupler; Developments on Superconducting RF Photo-injectors; Progress on Large Grain and Single crystal Niobium Cavities; etc.

Gradient scatter in 9-cell cavity is a most concerned issue for ILC specification. K. Saito reviewed history of the high gradient improvement in the last 15 years. He showed that new cavity shapes have made a remarkable breakthrough to push gradient since the SRF 2005. Now the gradient for a single cell cavity is closing to 60MV/m. The best Eacc of 59 MV/m was recorded by Cornell/KEK collaboration of a re-entrant cavity. W. Singer presented the progresses on seamless cavities. The best Q (Eacc) result of hydro-formed single cell cavity is 43 MV/m. Proof of principle of seamless 9-cell cavity is done. New ideas of hydro-forming or spinning of single crystal cavities are developing. Large grain/single crystal technology has been a topic at every conference and workshop since SRF2005, P. Kneisel reported the recent progresses on large grain and single crystal niobium cavities after carrying out about 100 tests. It turned out that the performances of single crystal or large grain Nb are comparable with that of fine grain Nb, but does not need electro-polishing, BCP only is fine and very smooth surfaces can be achieved. The potential benefit is lower costs at comparable performance. More experience and confidence is needed for large scale application, e.g. 8x9 cell cryomodule. S. Belomestnykh gave the review talk on input power coupler

developments. Several new input coupler designs, both pulsed and CW, have been tested recently with very good results. SRF photoinjectors are essential for generating low emittance beam. J. Sekutowicz gave an overview by comparing the performances of 3 types of injectors: NC cathode plus SRF cavity, NC cathode in DC gun plus SRF booster cavity and SC cathode plus SRF cavity. Greater efforts to improve the performance of all 3 types of SRF photoinjector are well on the way.

X. Xi reported that MgB2 films prepared by reacting CVD boron films with Mg vapour show good properties. The technique is compatible to coating of cavities. G. Wu and V. Palmieri gave Reviews on SRF Materials Workshop and Thin Film Workshop respectively.

2.2.2.4 *Hot Topics Discussions and Industrialization on SRF Accelerators*

To meet the needs of the construction of X-FEL and future ILC projects, two hot topics were raised for discussion: "Is large grain/single crystal Nb an alternative material to polycrystalline niobium?" and "Is 35 MV/m still a good choice for ILC?" As the cost of a 9-cell cavity is still as high as US $ 90,000, people do hope to simplify the process of fabrication and treatment to reduce the effective cost of the cavity. The large grain/single crystal niobium has showed some potential merits in this direction and thus might lower the cost at comparable performances. Though a number of participants thought large grain/single crystal niobium might be a way to high gradient cavities, great efforts are to be further performed, from the improvement of material properties, the processing and handling of niobium sheets and cavities as well as the reduction of scatter of performance before one can assure large grain/single crystal niobium is a viable alternative to polycrystalline niobium for multi-cell cavities. For this purpose coordination of activities in various laboratories round the world is needed.

So far the best Eacc of ~40 MV/m was achieved by both seamless and welded versions of 9-cell cavities. During the workshop KEK reported their recent results of 42 MV/m for an Ichiro type 9-cell cavity at 2K. However, the yield rate of stable and reliable gradient of 35MV/m for vertical tests is still a difficult issue; the scatter of the cavity performance is still large. The gradient is limited by field emission and quench as well as quality assurance of preparation and diagnostics. More efforts are anticipated to produce stable and reliable gradient 35MV/m cavities with reasonable yield rate at the industrial level.

Talks on the industrialization on SRF Accelerators were given both by B. Petersen and D. Moeller. The experience in constructing cryomodules of FLASH provides a sound base for industrial production of cryomodules for Euro-XFEL. The general goal is to order XFEL-modules by the end of 2008. For this purpose, participation of industry for cryomodule prototypes at DESY, first results of industrial cryomodule assembly studies, prototype test facility in operation as well as prototype and cold masses' for tender are scheduled and going on well. In addition, as there will be 800 power couplers for X-FEL and 16000 for ILC, the industrial study for power coupler production is also an important issue. Three contracts have already placed at the industry under the supervision of LAL of Orsay. For further development, testing and conditioning of power couplers, a collaboration is working between LAL and DESY since 2004.

2.2.2.5   Future Projects and New Ideas

Ilan Ben-zvi talked on SRF Linac based electron cooling and electron-ion collider at BNL. Two 5nC electron bunches accelerated from 5 MeV to 54 MeV by a three passes SRF ERL for electron cooling of high energy hadron beams and a 20 GeV 260 mA e-beam generated by a 4 passes ERL system for electron-nuclear collider were described. Issues of generating high currents of polarized or high-brightness unpolarized electrons, high charge per bunch and high currents and associated issue of high order modes generation and damping were discussed. G. Neil gave an over view on high average power ERL FEL. The SRF Linac based IR FEL at JLab achieved the world's highest average CW light power of 14.2 KW at 1.6 µm with a 160 MeV beam of 9.1 mA average current. The application of ERLs at Novosibirsk high power THz FEL and ERL FEL at JAERI were also described. Scheme of future ERL light source projects like IR & VUV FEL and XUV amplifier of 4GLS at Daresbury, high power FEL at KAERI and Big Light FEL for NHMFL as well as ERL prototypes and test facilities at a number of laboratories were presented too. Common issues for further development ERL based light source were discussed. An over view of planned high-intensity proton accelerators with linac-based low-energy (<8 GeV) section for Spallation source, ADS, and various neutrino applications was given by F. Gerigk of CERN. The advancement of SC RF technology makes it now possible to build multi-GV linacs with a reasonable footprint (several 100 m), even for low beam power. Considering the upgrade potential for the future Physics needs, CERN and FNAL chose linac designs over RCS solutions despite the 30% cost difference. CEBAF is to upgrade to 12 GeV. J. Preble reported the program including the new cryomodule appropriate for upgrading. For this purpose prototype components and assemblies have been built and tested. The performance requirements of all system have been met. After completion of the RDR in spring 2007, ILC enters the engineering design phase. H. Hayano of KEK talked on the engineering design of SRF technology which is divided into cavity & cavity package, cryomodules, cryogenics, high-level RF and main linac integration. The goal of task S0 is to achieve ILC baseline qualification gradient of $35MV/m@Q_0=1x10^{10}$ with 95% yield and for task S1 to achieve 31.5MV/m operational gradient in cryomodules.

2.2.3   Concluding Remarks and Acknowledgements

Thanks to the joint efforts of all participants and working staffs, especially the excellent contributions of invited speakers, tutorial lecturers and poster authors who made the 13th workshop a great success. Moreover, the considerate design of the program by IPC, headed by the past and elected Chair Prof. Hasan Padamsee and Prof. Dieter Proch, enabled us to have a very fruitful and enjoyable time during the workshop. Owing to the great efforts of working staffs, including two specialists from KEK, the Power Point version of all talks can be downloaded now from the website http://www.pku.edu.cn/academic/srf2007/home.html. With the help of Prof. J. Delayen the proceedings of the whole workshop will be presented for the first time in JACoW and can be found from the related website. Limited by our experience some important contributions may not included in this short report, and for this we must apologize. Finally let us express our very best wishes to the 14th SRF workshop in Berlin.

2.2.4   References

1. Proceedings of 13th International Workshop on RF Superconductivity, to be published

2.3   Second International Accelerator School for Linear Colliders

Barry Barish, Weiren Chou and Shin-ichi Kurokawa
Mail to: barish@ligo.caltech.edu, chou@fnal.gov, shin-ichi.kurokawa@kek.jp

The Second International Accelerator School for Linear Colliders took place October 1-10, 2007 at Erice (Sicily), Italy (http://www.linearcollider.org/school/2007/). It was a continuation of the first international LC accelerator school held in 2006 in Japan. This year's school was jointly organized by the ILC GDE, the International Linear Collider Steering Committee (ILCSC) and the ICFA Beam Dynamics Panel.

The school was aimed at PhD students, postdocs and young researchers, especially young experimentalists. The response to the school was overwhelming. We received 243 applications from 31 countries and most of the candidates presented strong credentials. However, the school could only accommodate a maximum of 70 students. Through a difficult and rigorous selection process, the Curriculum Committee accepted 69 students from 18 countries. These committee members read the CV and recommendation letter of each applicant carefully and discussed among themselves before making the decision to admit or reject an applicant. For various reasons (personal or a problem obtaining a visa) twelve admitted students unfortunately could not come. The fifty seven students who attended the school were a talented and highly motivated group. They successfully met the challenge of an intensive 8-day lecture program and did very well in the final examination.

The curriculum consisted of 12 lectures, homework assignments and a final exam. The lectures covered both basic and advanced topics in linear colliders and were given by a group of accomplished accelerator physicists, many of whom are GDE members. These lecturers not only gave lectures during the day, but also gave tutorials and helped students with their homework in the evenings. They also created the examination problems and graded them. The final on the last day lasted 4-1/2 hours. All 57 students took the final exam. The lecture slides, homework problems, exam problems with their solutions can all be found on the school web site.

The exam problems were challenging but the students did well as shown in the figure of exam scores. The top 10 students were honored at the banquet and each was awarded a certificate and a book (*Handbook of Accelerator Physics and Engineering*, edited by A. Chao and M. Tigner, and published by World Scientific). The best student scored 94.5 points, a remarkable achievement.

In addition to studying, the students were encouraged to make new friends. This was a once-in-a-lifetime opportunity to meet with many other young talented people from different origins who shared the same interest (accelerators) and career goals (ILC). Some of the friendships nurtured at the school will last a lifetime.

Because the workload was heavy, the school organized an excursion to give the students a well-deserved break. They visited Segesta, a place famed for an old Temple and a Theatre. The Temple was built 3,200 years ago and is well maintained.

The venue of the school, Erice in Sicily, Italy, is a wonderland. It is extremely beautiful and also ideal for a school because of its isolation from the rest of the world. Our host, the Ettore Majorana Center, is famous for its southern Italian hospitality. Ms. Fiorella Ruggiu and her staff arranged everything for our school: student visa

applications, airport pickup, housing assignments, meals, coffee breaks, reception, banquet, photos, excursions, printing of lecture notes and homework. These logistics were so well taken care of that the teachers could concentrate on teaching and the students could focus on studying and learning. We were impressed by the talent and dedication of the Center staff. The facilities at the Center were equally impressive. The San Domenico Lecture Hall was well equipped with modern A/V equipment and Internet connection. The view from the Discussion Hall during coffee breaks was magnificent and breathe taking. The San Francesco study rooms were perfect for working on homework. We were amazed by how well the Center brought in modern technology while retaining the medieval beauty of its buildings.

Throughout the organization of this school, Fermilab's Cynthia Sazama and Suzanne Weber did an enormous amount of hard work over many months to make the school a success. We greatly appreciate all of their efforts.

The school received generous sponsorship from a number of funding agencies and institutions all over the world: U.S. DOE, NSF, Fermilab, SLAC, BNL, LBNL, TRIUMF, CERN, DESY, IN2P3, INFN, CARE/ELAN, Oxford University, Cockcroft Institute, University of London, Ettore Majorana Center, Tomsk Polytechnic University, KEK, KNU (South Korea), PAL, Tsinghua University (Beijing), National Tsinghua University (Taipei), NSRRC (Taiwan) and Australian Synchrotron Laboratory.

Based on the interest, demand and success of the first two schools, it was decided to have a third school. This one will be in the United States and will take place from October 19 to 29, 2008 at the Oak Brook Hills Marriott Hotel near Chicago. Fermilab will be the host institution.

Table 1: Lectures of the 2007 LC Accelerator School

Lecture	Topic	Lecturer
1	Introduction	Nick Walker (DESY)
2	Sources & bunch compressors	Masao Kuriki (KEK)
3	Damping ring	Andy Wolski (U. Liverpool)
4	Linac	Peter Tenenbaum (SLAC)
5	LLRF & high power RF	Stefan Simrock (DESY)
6	Superconducting RF	Kenji Saito (KEK)
7	Beam delivery & beam-beam	Andrei Seryi (SLAC)
8	Instrumentation & control	Marc Ross (Fermilab)
9	Operations	Marc Ross (Fermilab)
10	CLIC	Frank Tecker (CERN)
11	Conventional facilities	Atsushi Enomoto (KEK)
12	Physics & detectors	Jim Brau (U. Oregon)

Second International Accelerator School For Linear Colliders
October 1-10, 2007
Erice (Sicily), Italy
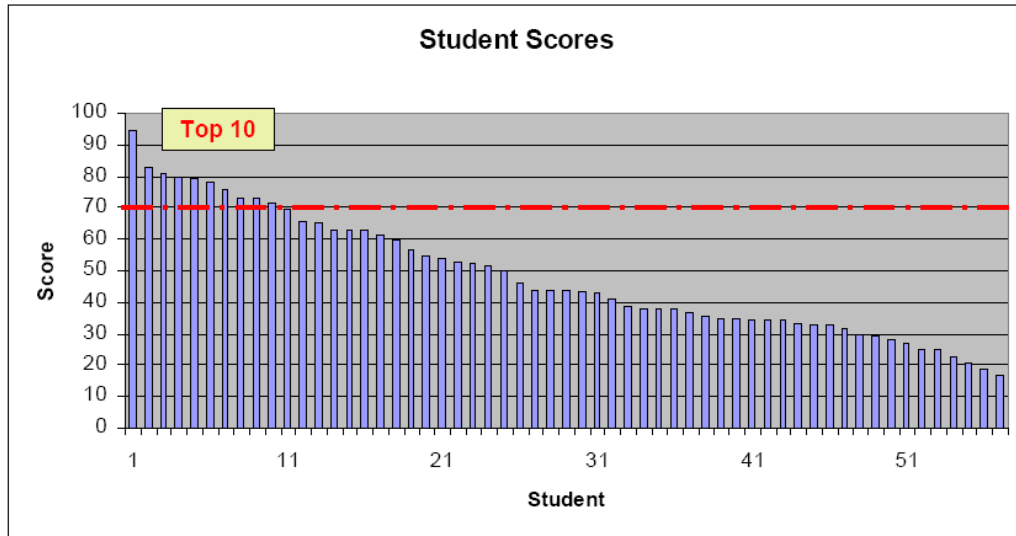
3 Theme Section – LOCO

3.1 Linear Optics from Closed Orbits (LOCO) – An Introduction

James Safranek, SLAC, 2575 Sand Hill Road, Menlo Park, CA 94025
Mail to: safranek@slac.stanford.edu

3.1.1 Introduction

The LOCO code is used to find and correct errors in the linear optics of storage rings. The original FORTRAN code was written to correct the optics of the NSLS X-Ray ring [1], and was applied soon thereafter to debug problems with the ALS optics [2]. The ideas used in the code were developed from previous work at SLAC [3, 4]. Several years ago, LOCO was rewritten in MATLAB [5]. As described in this newsletter [6], the MATLAB version includes a user-friendly interface, with many useful fitting and analysis options.

LOCO has been used at many accelerators. Presently, a search for LOCO in the text of papers on the Joint Accelerator Conferences Website yields 107 papers. A comprehensive survey of applications will not be included here. Details of recent results at a few light sources are included in this newsletter [7-10].

In the past, the quality of LOCO fitting results varied significantly, depending on the storage ring. In particular, the results were mixed for colliding beam facilities, where there tend to be fewer BPMs that in light sources. Fitting rings with less BPM data to constrain the fit optics parameters often led to unreasonably large fit quadrupole gradient variations. Recently, modifications have been made to the LOCO fitting algorithm which leads to much better results when the BPM data does not tightly constrain the fit parameters. The modifications are described in this newsletter [11], and an example of results with this new algorithm is included [7].

3.1.2 Basic LOCO Algorithm

If the linear optics in a storage ring is known, then the closed orbit response matrix can be easily calculated. The LOCO algorithm reverses this process. Given the (measured) orbit response matrix, the code divines the actual linear optics of the ring, including the errors in the optics. The quadrupole strengths can then be adjusted to correct the errors.

The closed orbit response matrix is defined as

$$\begin{bmatrix} \bar{x} \\ \bar{y} \end{bmatrix} = M \begin{bmatrix} \bar{\theta}_x \\ \bar{\theta}_y \end{bmatrix}, \tag{1}$$

where (x, y) is the horizontal and vertical shift in closed orbit at all the BPMs for a change in strength of the steering magnets of (θ_x, θ_y). The size of the orbit response matrix is the number of BPMs times the number of steering magnets, so the measured orbit response matrix typically contains thousands or tens of thousands of data points.

The measurement accuracy of the closed orbit is usually much better than 1 micron, so the orbit response matrix contains a huge number of data points reflecting the optics of the ring.

The best way to find the optics model that best fits the data is to minimize the chi-squared difference between the measured data and the model.

$$\chi^2 = \sum_{i,j} \frac{(M_{\text{mod},ij} - M_{\text{meas},ij})^2}{\sigma_i^2} \equiv \sum_{k=i,j} E_k^2 \, , \tag{2}$$

where σ_i is the measured noise level on the ith BPM, and E_k is the error vector. Minimizing the length of the vector $\vec{E}$ is equivalent to minimizing chi-squared.

Finding the best fit optics model simply requires minimizing single function, χ^2. The algorithm used in LOCO is Gauss-Newton minimization. Model parameters are adjusted to generate a $\Delta \vec{E}$ such that

$$\vec{E} + \Delta \vec{E} = \vec{E} + \frac{\partial \vec{E}}{\partial K_l} \Delta K_l = 0 \, , \tag{3}$$

where K_l are the parameters varied to fit the response matrix, and each column of the matrix $\partial \vec{E}/\partial K_l$ corresponds to the change in the orbit response matrix error vector with some fit parameter K_l. Depending on the fit parameter, the LOCO code uses an analytical calculation of $\partial \vec{E}/\partial K_l$ or uses AT [12] to numerically calculate the derivative.

The model fitting is now a linear algebra problem,

$$\frac{\partial \vec{E}}{\partial K_l} \Delta K_l = -\vec{E} \, , \tag{4}$$

where the matrix $\partial \vec{E}/\partial K_l$ is inverted to find the ΔK_l that best cancels the difference between the measured and model response matrices. There are far more data points in the response matrix then there are fit parameters, so the equation is over-constrained. LOCO uses SVD [13] to invert the response matrix.

The change in the response matrix with quadrupole gradients is not entirely linear, so the fitting must be iterated a few times to converge to the best solution. If the initial model is far from the actual ring optics, the problem may be sufficiently nonlinear that the iterations do not converge. In the past, such problems were addressed (with varying results) by reducing the number of singular values used in SVD and/or reducing the number of fit parameters in initial iterations. More recently, Levenberg-Marquadt minimization has been added as a fitting option in LOCO when the problem is too nonlinear for Gauss-Newton minimization [11].

3.1.3   Fit Parameters

The standard parameters varied when fitting the orbit response matrix are:

quadrupole gradients
BPM gains
steering magnet calibrations
skew quadrupole gradients
BPM x-to-y and y-to-x coupling
Steering magnet rolls

The parameters in blue are primarily associated with the uncoupled quadrants of the response matrix, M, in equation 1 (i.e. the diagonal quadrants giving the horizontal shift at BPMs from changing horizontal steering magnets and the vertical shift when changing vertical steerers). The parameters in red are associated with the coupled, off-diagonal, quadrants of M. The red parameters only need to be included when the coupled parts of the response matrix are included in the fit.

Often times, the main goal of LOCO is to debug and correct linear optics (quadrupole gradient) errors. Nonetheless, the BPM gains and steering magnet calibrations should still be included in the fit. Often, the calibrations of these parameters are not accurately known. The calibration errors contribute significantly to the error in the measured response matrix. If the calibrations were not included in the fit, then the fit quadrupole gradients would be adjusted to best compensate for the errors they generate in the measured response matrix. This would cause systematic error in the fit quadrupole gradients.

Depending on the desired results or error sources, other parameters that are sometimes fit include: normal and skew gradients in sextupoles or insertion devices, steering magnet or BPM longitudinal positions, and steering magnet energy shifts.

3.1.4   LOCO Application Examples

3.1.4.1   *Finding Optics Errors*

Figure 1 shows an example from ALS in which LOCO was used to identify gradient errors in quadrupoles [2]. In this case it was known from other measurements that there was a large distortion in the vertical betatron function. The LOCO analysis indicated that the source of the problem was large strength variations in the QD magnets. Subsequent current measurements confirmed that the individual power supplies for the QD magnets were poorly calibrated. In this analysis, the fit parameters were quadrupole gradients, BPM gains, and steering magnet strengths.
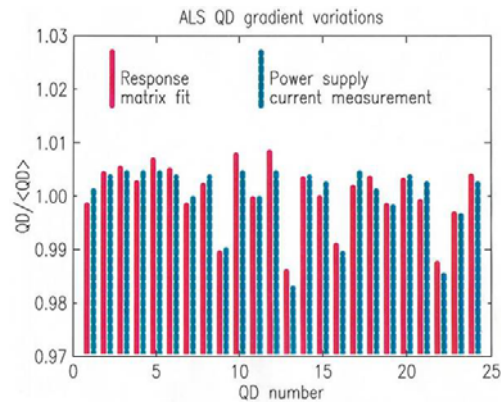
Figure 1: ALS QD calibration

Often this kind of analysis reveals BPM gain or steering magnet mis-calibrations as well as optics issues. Figure 2 shows an example of BPM gain correction factors for SPEAR3. A gain correction factor of 1.0 would mean the gain is correct. We were surprised by the 30% error in our BPM gains as well as the large variation from BPM to BPM. Subsequent direct measurements of the electronics verified these calibration errors.
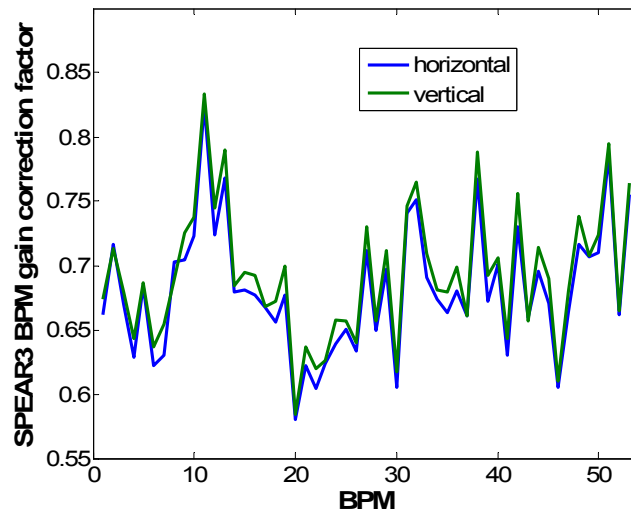
Figure 2: SPEAR3 BPM gain correction factors.

3.1.4.2 *Fixing Optics Errors*

Figure 3 shows an example from the NSLS VUV ring, in which LOCO was used to fix optics distortion. In this analysis it was discovered that the quadrupole gradients had been incorrectly adjusted to compensate for insertion device (ID) focusing. In analyses such as this, when optics correction is the goal, the quadrupole gradients are grouped in the fitting, so all quadrupoles on a single power supply are fit as a single parameter. Quadrupoles strung together on a single power supply are varied together, and quadrupoles on individual supplies are varied independently. In this way the fit parameters from LOCO can be applied directly to the ring to give the best optics

correction possible given the available power supplies. The quadrupole power supply currents are changed such that

$$\frac{\Delta I}{I} = -\frac{\Delta K}{K},$$

(5)

where ΔK is the difference between the fit and ideal quadrupole gradients.
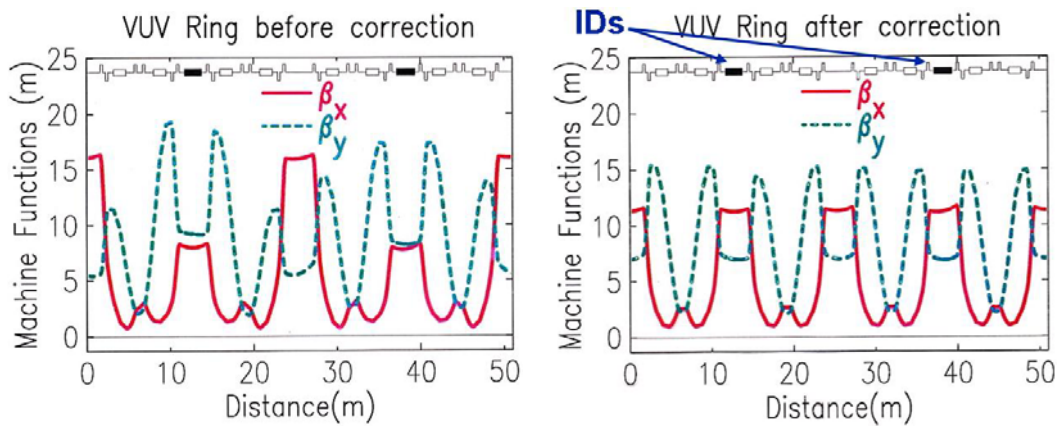
Figure 3: VUV ring optics correction (left=before, right=after).

This kind of correction can be used to correct for quadrupole gradient errors, or gradient errors from sextupoles, insertion devices or some other magnet. Figure 4 shows an example in which the skew gradient in an elliptically polarized undulator (EPU) at SPEAR3 is corrected as a function of the ID gap with a local skew quadrupole corrector. The orbit response matrix was measured for various EPU gaps. A full analysis of on of the orbit response matrices was made, varying all 15 skew quadrupole correctors in the ring. Then, starting from the model determined by this first analysis, all of the response matrices were analyzed with the only skew gradient the local skew corrector at the EPU. The fit values were used to determine the skew corrector excitation curve vs. gap.
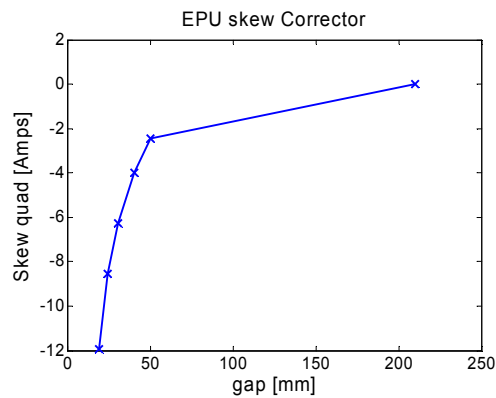
Figure 4: SPEAR3 EPU coupling correction.

3.1.4.3   *Dispersion Correction*

The horizontal dispersion, η_x, is automatically corrected to a certain extent in a LOCO optics correction, because η_x is part of the response matrix. When a horizontal steering magnet j is changed by $\theta_{x,j}$, the orbit shift at BPM i is

$$\frac{\Delta x_i}{\theta_j} = \frac{\sqrt{\beta_i \beta_j}}{2 \sin \pi \nu} \cos(|\phi_i - \phi_j| - \pi \nu) + \frac{\eta_i \eta_j}{\alpha L} , \qquad (6)$$

where α is the momentum compaction, and L is the ring circumference. The second term, which includes η, cancels the path length increase of the first term. Thus the closed orbit shift maintains constant path length, and stays in synchronism with the RF.

The second term in equation 6 shows that the horizontal dispersion is implicitly corrected in LOCO. LOCO also has the option of including η_x explicitly as an additional column in the response matrix. In this way the change in RF frequency used to measure the dispersion is treated like one more horizontal steering magnet. This has two benefits: it can be used to add additional weight to dispersion correction, and it constrains the BPM gain and steering magnet calibration factors.

Controlling dispersion is particularly important for achieving design emittance, so it is worthwhile putting additional weight on the dispersion correction.

Without dispersion explicitly included there is an overall scaling uncertainty in the BPM and corrector calibrations. In equation 6 BPM gain changes Δx_i, and steering magnet calibration changes θ_j, but changing them both equally leaves the ratio unchanged. So the response matrix data from steering magnets alone does not constrain the overall scaling of the steering magnet calibrations vs. the BPM gains. Adding the dispersion as an additional column in the response matrix removes this problem. The change in RF frequency used to measure the dispersion is well known, so this column does not have a calibration factor to be fit.

Figure 5 shows an example of fitting the dispersion at the NSLS X-Ray ring. Before LOCO fitting, the measured dispersion differed greatly from the measurements. After fitting, the agreement is quite good. The fit quadrupole gradients were then used to correct the optics, as with equation 5.
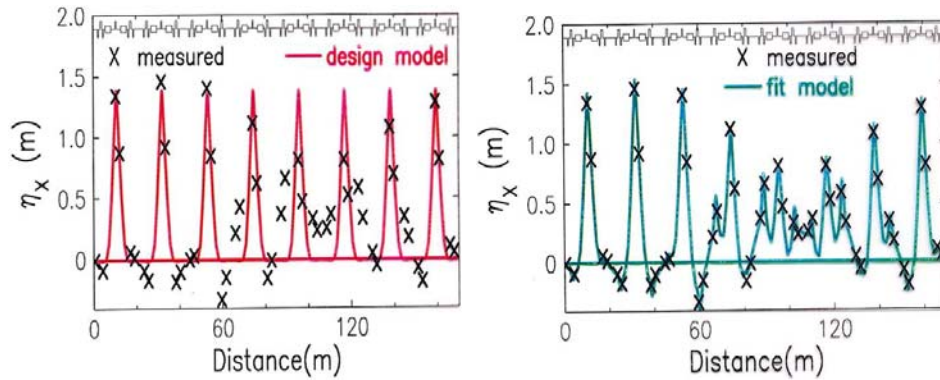
Figure 5: NSLS X-Ray ring dispersion fitting.

3.1.4.4   Other Applications

The above examples show some of the most common LOCO applications. Another common application is coupling and vertical dispersion correction. Coupling correction is discussed elsewhere in this newsletter [9].

LOCO can also be used for various other applications, such as beam-based alignment of sextupoles (fitting normal and skew gradients in sextupoles), local chromaticity calibration (fitting response matrices measured at varying RF frequencies), and local transverse impedance measurements (see article in this newsletter [10]).

3.1.5   LOCO Code Availability

The latest version of the LOCO code is available on the web [14].

3.1.6   References

1. J. Safranek, "Experimental determination of storage ring optics using closed orbit response measurements", Nucl. Inst. and Meth. A388, (1997), pg. 27.
2. D. Robin, J. Safranek, G. Portmann and H. Nishimura, "Model calibration and symmetry restoration of the Advanced Light Source," proceedings of the 1996 European Particle Accelerator Conference (1996).
3. W.J. Corbett, M.J. Lee, and V. Ziemann, "A fast model calibration procedure for storage rings," SLAC-PUB-6111, May, 1993.
4. M.J. Lee, Y. Zambre and W.J. Corbett, "Accelerator simulation using computers," SLAC-PUB-5701A, January, 1992.
5. J. Safranek, G. Portmann, A. Terebilo, C. Steier, "MATLAB-based LOCO", proceedings of the 2002 European Particle Accelerator Conference, Paris, France (2002).
6. G. Portmann et al., "MATLAB based LOCO", these proceedings.
7. L. Nadolski, "LOCO fitting challenges and results for SOLEIL", these proceedings.
8. M. Spencer, "LOCO at the Australian Synchrotron", these proceedings.
9. C. Steier et al., "Linear Lattice Calibration for Frequency Map Analysis and Low Emittance Tuning using Orbit Response Matrix Analysis at the ALS", these proceedings.
10. V. Sajaev, "Transverse impedance distribution measurements using the response matrix fit method at APS", these proceedings.
11. X. Huang, et al., "LOCO with constraints and improved fitting technique", these proceedings.
12. A. Terebilo, "Accelerator Toolbox (AT)", http://www.slac.stanford.edu/~terebilo/at/.
13. Numerical Recipes, Cambridge University Press.
14. http://als.lbl.gov/als_physics/portmann/MiddleLayer/Release/applications/loco/

3.2   Matlab Based LOCO

Greg Portmann, Lawrence Berkeley National Lab, Berkeley, CA 94720, USA
Mail to: gregportmann@lbl.gov

James Safranek and Xiaobiao Huang, SLAC, Menlo Park, CA 94025, USA

3.2.1   Introduction

The LOCO algorithm has been used by many accelerators around the world. Although the uses for LOCO vary, the most common use has been to find calibration errors and correct the optics functions. The light source community in particular has made extensive use of the LOCO algorithms to tightly control the beta function and coupling. Maintaining high quality beam parameters requires constant attention so a relatively large effort was put into software development for the LOCO application.

The LOCO code was originally written in FORTRAN. This code worked fine but it was somewhat awkward to use. For instance, the FORTRAN code itself did not calculate the model response matrix. It required a separate modeling code such as MAD to calculate the model matrix then one manually loads the data into the LOCO code. As the number of people interested in LOCO grew, it required making it easier to use.

The decision to port LOCO to Matlab was relatively easy. It's best to use a matrix programming language with good graphics capability; Matlab was also being used for high level machine control; and the accelerator modeling code AT, [5], was already developed for Matlab. Since LOCO requires collecting and processing a relative large amount of data, it is very helpful to have the LOCO code compatible with the high level machine control, [3]. A number of new features were added while porting the code from FORTRAN and new methods continue to evolve, [7][9]. Although Matlab LOCO was written with AT as the underlying tracking code, a mechanism to connect to other modeling codes has been provided.

3.2.2   The Matlab Code and Functionality

3.2.2.1   Graphical User Interface (GUI)

Figure 1 shows the Matlab-LOCO GUI. The GUI was the most time consuming part the coding process but without a GUI it would be much more difficult to follow, understand, and direct what is going on during a LOCO run.
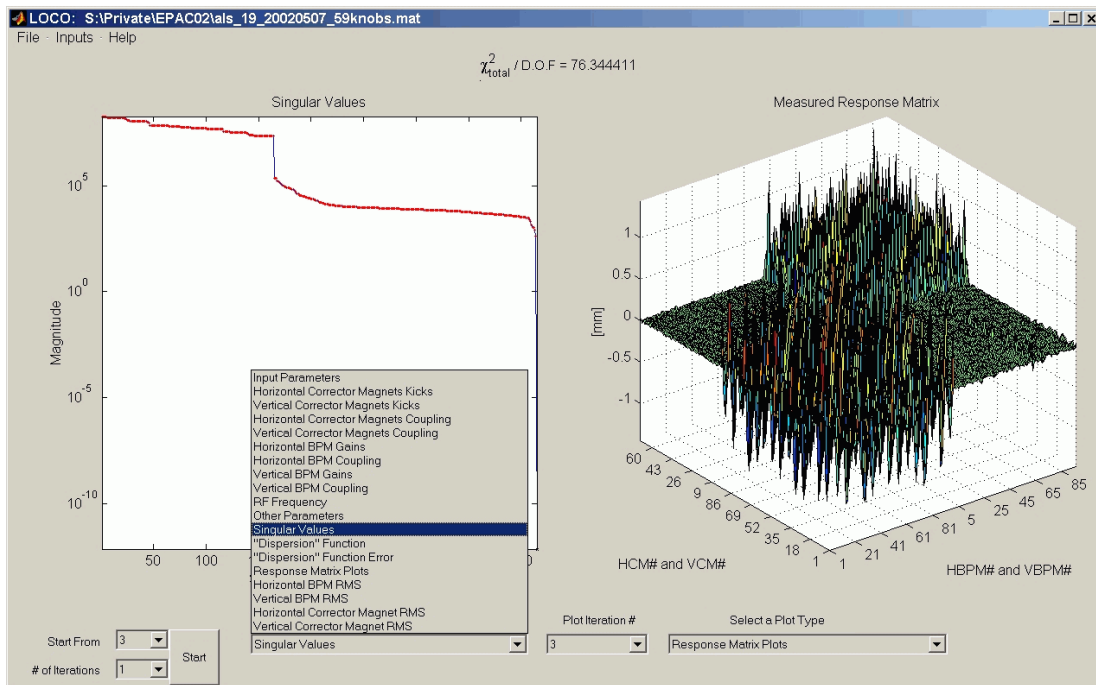
Figure 1: Matlab LOCO GUI.

LOCO uses an iterative method to converge to the minimum χ^2. The process is initiated using the "Start" button in the bottom left of Figure 1 and the "# of Iterations" pull-down menu selects the iterations. The information displayed on each plot is selectable from the plot selection menu shown expanded in the figure. It's common to go back to a previous iteration with the "Start From" pull-down menu, change an input, and rerun the iteration. The ability to quickly experiment with different LOCO setups and view the results is quite useful. The "Inputs" menu is used to make choices concerning the fitting for each iteration. The "Inputs" menu is shown below and many of the options are discussed in the following sections.

Input Menu
└Minimization Algorithm
       Gauss-Newton
       Gauss-Newton (with parameter costs)
       Levenberg-Marquardt
       Scaled Levenberg-Marquardt
└Fit BPM Coupling
└Edit BPM List
└Fit Corrector Magnet Kicks
└Fit Corrector Magnet Coupling
└Edit Corrector Magnet List
└Include Off-Diagonal Response Matrix Terms
└Fit Energy Shifts at the Horizontal Corrector Magnets
└Fit Energy Shifts at the Vertical Corrector Magnets
└Response Matrix Calculator
       Linear or Full Response Matrix Calculator
       Fixed Path Length or Fixed Momentum
└Response Matrix Measurement Method (Bi-directional or uni-directional)

└Include "Dispersion" as part of the Response Matrix
        Weight for horizontal dispersion
        Weight for vertical dispersion
└Fit the RF Frequency for Measured Dispersion
└Dispersion Measurement Method (Bi-directional or uni-directional)
└Auto-Correct Deltas
└Singular Value Selection Method
└Normalize (column weights)
└Outlier Rejection
└Calculator Error Bars
└Single or Double Precision

No information is saved in the GUI. All information is contained in the Matlab data file which is saved after each iteration. Hence, if the computer crashes or runs out of memory on the sixth iteration, the last five will have already been saved.

3.2.2.2 The Minimization Algorithm

The algorithm is discussed in detail in a number of references so it will not be discussed here. The original Gauss-Newton search LOCO algorithm can be found in Reference [1] and [6]. Reference [7] discusses a weighted version of the Gauss-Newton method as well as the Levenberg-Marquadt method, [9]. All methods are selectable from the GUI.

3.2.2.3 Orbit Response Matrix Calculation

There are a couple options for computing the model response matrix. A linear approximation option was introduced for calculation time reasons. The linear method orbit response matrix computation is based on the numerically obtained 4-by-4 transfer matrixes at each corrector and BPM, the model dispersion function, and model momentum compaction factor. The nonlinear method iteratively searches for a closed orbit in the presence of the corrector magnet kick. For many accelerators the time spent computing a full nonlinear model is not necessary on the first couple iterations if at all. The nonlinear methods are slower but include the non-linear effects due to sextupoles and other non-linear elements.

The second option is to choose whether to hold the path length fixed or the momentum fixed. How these options are implemented in AT is shown in Table 1.

Table 1: Response Matrix Calculation Methods

	Constant Momentum	*Constant Path Length*
Linear	Transfer Matrix	Transfer Matrix + Dispersion Term
Full NonLinear	findorbit4	findsynorbit

The response matrix calculation method can change more than just how the response matrix is numerically generated. The merit function minimized in LOCO is

just the difference between the model and measured response matrix. However, when using the constant momentum method, model response matrix is modified by the fit energy change at the corrector magnets.

$$M_{model} = (\Delta p/p)_{fit}\, \eta_{measured} + M_{AT\,model}$$

where $\eta_{measured} = -\alpha * RF * \Delta Orbit / \Delta RF$, $\Delta p/p$ is the energy change due to that corrector when generating the response matrix. The constant momentum method was developed to tackle the problem that orbit errors in the quadrupoles and sextupoles cause dispersion errors which are not accounted for in the model. To correct this, the energy shift at the correctors are fit and the model is altered by the energy shift times the actual dispersion in the machine. Hence, even with a perfect fit of all LOCO parameters the model and measured dispersion will not be forced to match. Note that the model response matrix has been changed by a term proportional to the measured dispersion which means measurement errors have been added to the model. Although it is a little odd to introduce measurement errors to a model, this method was chosen since changing the measured response matrix introduces other logical problems. In general, one would not include the dispersion as a column of the response matrix or fit the RF frequency when using the constant momentum method. This method was developed to zero the weighted dispersion in the least squares algorithm.

When using LOCO to correct the optics, localizing the source of the error is not important. All the calibration and magnet feeddown errors need to be corrected with the available power supplies. The constant path length response matrix is preferred for this case.

3.2.2.4   *Dispersion Fitting*

Since the dispersion function is relatively fast and easy to measure, there is an option to include it in the fit as an additional column in the response matrix – much like including another horizontal steering magnet.

Fitting the response to steering magnets alone usually gives a model with the correct tunes and beta functions, but does not always reproduce the dispersion as accurately. This can happen because the beta functions do not vary much with dipole magnet errors around the ring, while the dispersion does. Or it can happen when fitting a subset of the actual gradient errors in order to find the best correction as opposed to looking for the source of the error. The non-local gradient corrections can correct beta function distortion associated with the gradient error, but not necessarily the dispersion distortion. Including dispersion explicitly as a column of the response matrix forces LOCO to generate a model that accurately reflects both the beta functions and the dispersion of the real storage ring. The dispersion fitting option can be useful for controlling dispersion to achieve low emittance.

Including the dispersion in the fit can also provide an absolute calibration of the BPMs and correctors magnets. Without the dispersion there is always a degeneracy between the scaling of the BPMs and corrector magnets. This will create a small singular value per plane which needs to be removed. If dispersion is included and the RF frequency is not fit (which is often the case since the accuracy of RF changes is usually very good) then the horizontal degeneracy should disappear. If there is

substantial vertical dispersion then the vertical degeneracy will also disappear. To force this, the coupling is sometimes increased just to obtain a good vertical BPM calibration.

3.2.2.5 BPM and Corrector Magnet Calibration

There is an option to compute the BPM and corrector magnet gain and coupling corrections. Basically the BPM corrections are applied to the model response matrix to best match the measurement using the following equation.

$$\begin{pmatrix} x_{meas} \\ y_{meas} \end{pmatrix} = \begin{pmatrix} g_{x,loco} & c_{x,loco} \\ c_{y,loco} & g_{y,loco} \end{pmatrix} \begin{pmatrix} x_{model} \\ y_{model} \end{pmatrix}$$

There are also conversion functions to gain-crunch-roll format that was used in the FORTRAN LOCO code.

$$\begin{pmatrix} x_{meas} \\ y_{meas} \end{pmatrix} = \frac{1}{\sqrt{1-C^2}} \begin{pmatrix} \cos\theta & \sin\theta \\ -\sin\theta & \cos\theta \end{pmatrix} \begin{pmatrix} 1 & C \\ C & 1 \end{pmatrix} \begin{pmatrix} g_x x_{model} \\ g_y y_{model} \end{pmatrix}$$

It is also possible to include single view BPMs.

For corrector magnets LOCO computes the gain and coupling terms which relate the kick applied to the accelerator (measured) to fit value of the kick (actual). These values are often converted to gain and roll coordinates (horizontal corrector shown below).

$$\begin{pmatrix} \delta_{x,Actual} \\ \delta_{y,Actual} \end{pmatrix} = \begin{pmatrix} g_{loco} \\ c_{loco} \end{pmatrix} \delta_{x,meas} = \begin{pmatrix} \cos(\theta) \\ \sin(\theta) \end{pmatrix} * gain * \delta_{x,meas}$$

where δ refers to the steering magnet kick angle. Including BPM and steering magnet calibrations in LOCO fitting is nearly always the best choice.

3.2.2.6 Error Bar Propagation

Matlab LOCO includes an analytical calculation of the error bars on the fit parameters associated with BPM random measurement noise. This calculation gives a lower bound on the error bars, because is does not include systematic errors. The calculated error bars, however, are still useful as a guide to the relative accuracy with which the parameters can be fit. Fit parameter error bars can also be determined empirically by analyzing multiple response matrices and calculating the rms variation in the fit parameters over the different fit models.

Since the error bar calculation takes computer time there is an option to turn it off. The calculation gets particularly lengthy if the dispersion function is used without unity weights. For instance, in the typical least square equations, $y = Ab + e$, the assumed variance of input error is $\text{var}(e) = \sigma I$ and the variance of the least squares estimate $\hat{b} = (A'A)^{-1}A'y$ is $\text{var}(\hat{b}) = \sigma(A'A)^{-1}$. If all the input error variances are not equal then a row weight is used to force them to be so. This is done in LOCO with the BPM sigma. However, if a non-unity weight is put on the dispersion then the simple variance calculation cannot be used. The new one is $\text{var}(\hat{b}) = (A'A)^{-1}A'\Sigma A(A'A)^{-1}$ where Σ is the

covariance matrix of the input error. (Note: $\hat{b}$ is no longer an unbiased estimator.) The default in LOCO is to output only the diagonal of the covariance matrix of $\hat{b}$, but there is an option in the GUI to output the full covariance matrix.

When singular values are removed from the gradient matrix, A, interpreting the error bar is more difficult. Basically, removing a singular value removes a dimension so it reduces the ability of the least squares algorithm to find the best minimum and it reduces a way for the input error to project onto the estimates $\hat{y}$ and $\hat{b}$. The net effect is to increase the residual error, $y - \hat{y}$, but decrease the variance of the fit, $var(\hat{y})$. Usually only very small singular values are removed. Very small singular values corrupt the numerical inverse and removing them usually has very little impact on the residual error or the variance.

3.2.2.7 Outlier Data Rejection

There is also an option to reject outlier data based a user defined threshold. Before each iteration, the rms difference between the model and measured response matrices is calculated. This difference for each point is compared against the threshold times the total rms. The calculation is done twice. The first test will remove very large outliers, if they exist, so that second test has a more accurate rms calculation. Using outlier data rejection is usually the best choice.

3.2.2.8 Numerical Derivative Calculation

The χ^2 minimization routine requires the numerical derivatives of the model response matrix with respect to each of the fit parameters. In order to numerically compute the gradient w.r.t. each parameter being fit a reasonable delta change in each parameter needs to be found. The user can determine the appropriate step sizes by trial and error or the code will automatically determine the appropriate step sizes. This is the "Auto-Correct Deltas" input. The deltas are chosen to keep the RMS change in the response matrix equal to one micron when calculating numerical derivatives. Including auto-correct deltas is usually the best choice.

3.2.2.9 Normalization

Nomalization refers to column weighting of the gradient matrix in the least squares problem, min|Ab - y|. (Row weighting of this matrix was discussed in the Error Bar Propagation section above.) Normalization can be switch on or off. Normalization is used to help with potential numerical precision issues. If the columns of the A-matrix have very different relative scaling, then the SVD calculation could run into numerical problems. Column weight is the same as changing the units of the parameter fits. Normalization also affects the size of the singular values. The effect of normalization when singular values are removed has not been studied. Using normalization is usually the best choice.

3.2.2.10 Memory Requirements and Speed

The memory requirement is usually driven by the size the response matrix and the number of parameters to be estimated. Matlab uses 8-byte precision for matrices, so the numerical derivative of the model response matrices requires 8 × no. of parameters ×

no. of BPMs × no. of steerers bytes of memory for the fully coupled case. A rough estimate of the memory required for the LOCO subroutine is 2.5 times this number.

There is a single precise option to reduce the required memory but there have been cases where single precision produced incorrect results. With 64-bit operating systems now widely available, the memory issue is not the problem it once was.

The LOCO code converges on the order of three times faster than the original FORTRAN code. The time required for a particular storage ring depends strongly on the size of the response matrix and number of fit parameters. To give an example, it takes about 15 minutes to converge to a solution for the Advanced Light Source without coupling, when running on a CPU with speed equivalent to about 2 GHz.

3.2.3 Data Flow

The LOCO algorithm requires a lot of data. A great attempt was made to come up with sensible method for data handling which makes calling LOCO recursively relatively easy. That said, it's still a lot of data to organize. There are seven data structures based on the model, measurements, fit parameters (BPMs, corrector magnets, and other parameters), LOCO setup variable, and LOCO outputs. For accelerators that use the Matlab Middlelayer (MML) for high level control, this process has been automated to a large extent.

The most complicated data structure is the one that specifies which parameters in the model to fit. It needed to be very flexible so that anything can be varied. There is a function (mkparamgroup) to help build this structure for the most common parameters, like normal and skew quadrupole gradient. A fit parameter can be linked one element in the model, like a magnet, or effect many elements in the model, like a power supply connected to a series of magnets.

3.2.4 LOCO Output and Plotting Options

Many papers have been written showing successful applications of the LOCO algorithm, [1, 6-9] to name a few. This section will show some of the plotting options available in the LOCO GUI, using examples from various applications.

3.2.4.1 *Goodness of Fit*

There are a number of quick checks often made after completing a LOCO run. Figure 2 shows the singular values and a "chi-by-eye" check on the accuracy of the fit. Problems with individual corrector magnets or BPMs often are very apparent in the response matrix error plot. Figure 3 shows a histogram of the initial response matrix error and fourth iteration. Note that the BPM errors are usually rather small compared with the systematic errors, so a χ^2 per degree of freedom of 23 (or greater) is often still a usable fit.
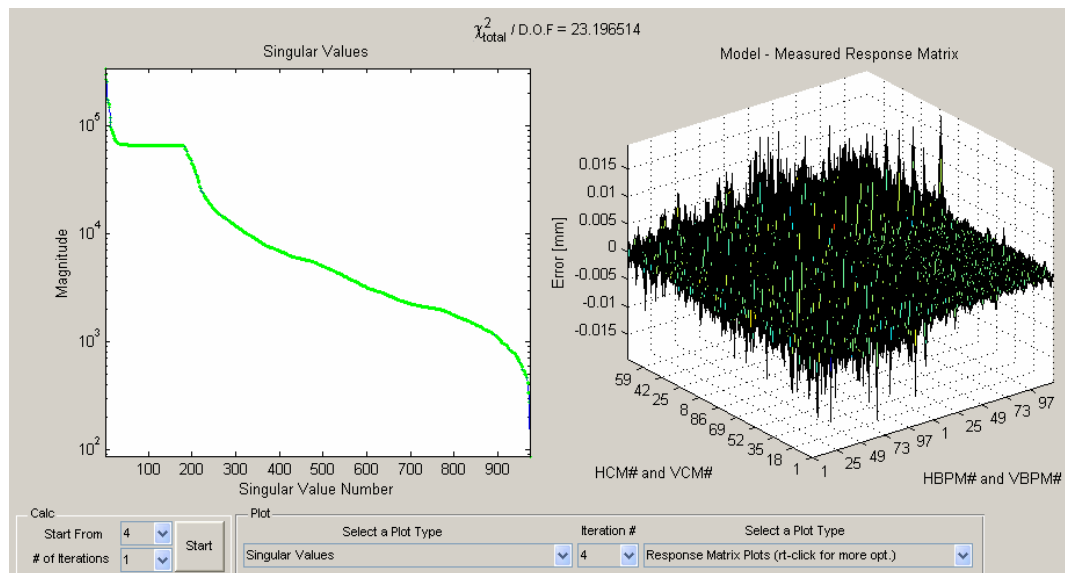
Figure 2: Singular Values and Response Matrix Error.
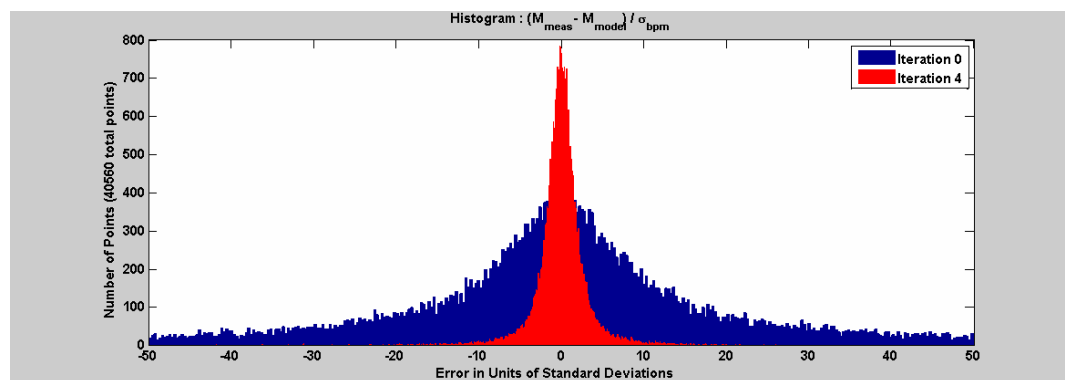
Figure 3: Histogram of the Response Matrix Error.

The dispersion function really needs to be inspected manually. The dispersion is a relatively small part of the response matrix, so it's possible to have a reasonably small χ^2 and still have a fitting problem with the dispersion, depending on the weight applied to the dispersion fit. Figure 4 shows a reasonably good fit for this ALS example. Note that when fitting energy shifts at the correctors, the model and measured dispersion may not match. The beta beat plot reflects how well the accelerator is calibrated to model.
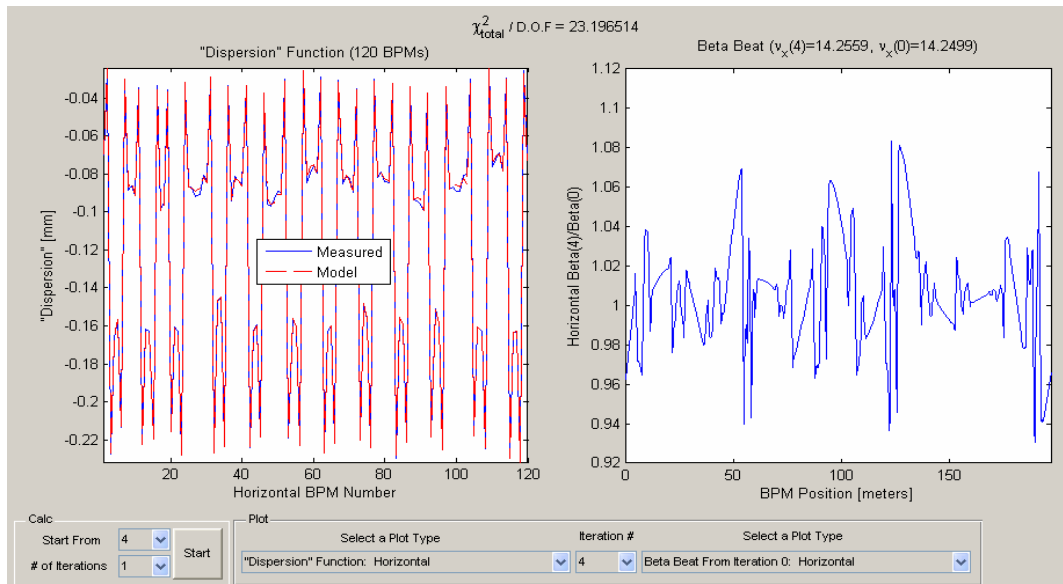
Figure 4: Dispersion and Beta Functions.

3.2.4.2   *BPM Gain and Coupling*

Figure 5 shows the vertical BPM gain and coupling fits for the ALS. A 10% gain error seems to be quite common at light sources. The coupling error of -.7 on BPM(78) is horrible. The cause was later discovered to be an attenuation problem with one of the BPM buttons.
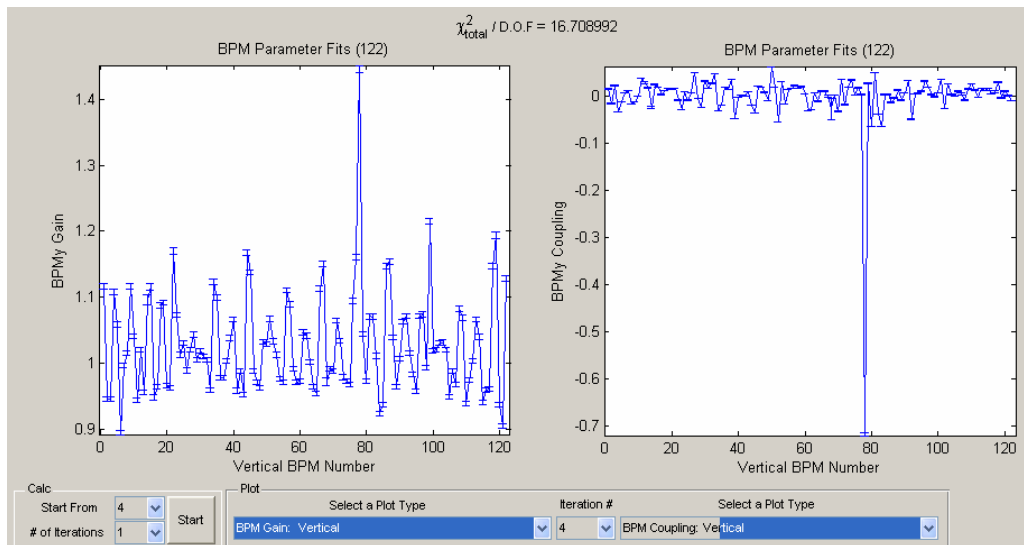
Figure 5: BPM Problem.

3.2.4.3 χ^2 *Change vs. Fit Parameter*

Figure 6 shows the change in χ^2 for each fit parameter and groups of parameters for the first iteration of a Gauss-Newton and Levenberg-Marquardt run (same measurement

data). If the χ^2 is not converging this plot can be helpful for locating the source of the problem. The basic idea is that if a particular fit parameter makes a large change in χ^2, then it could be projecting the fit into a nonlinear region and should be reduced. Adding a parameter cost or using the Levenberg-Marquardt method is a way to accomplish that goal, [7-9].
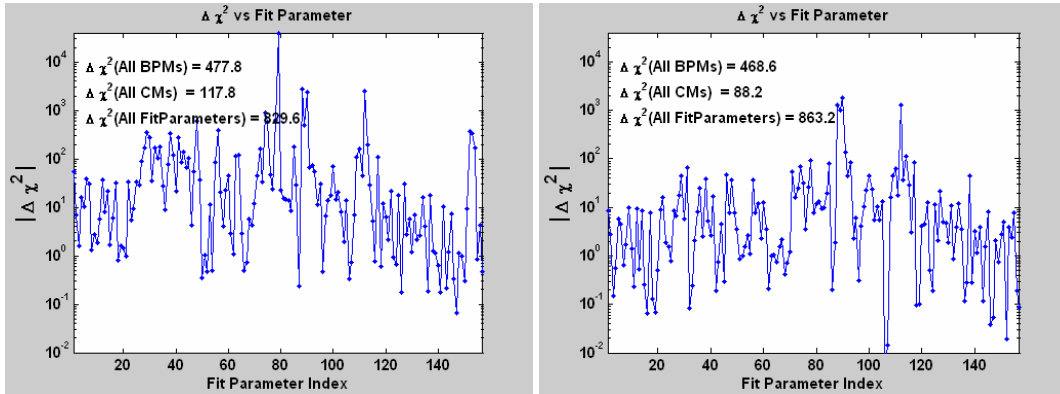
Figure 6: Gauss-Newton (Left), Levenberg-Marquardt (Right).

To gain more insight into the Levenberg-Marquardt method the equivalent parameter cost can be plotted, Figure 7. Inspecting the partial of χ^2 w.r.t. fit parameter might also be useful when debugging problems. The cost function is flat for parameters 649 to 973 due to normalization.
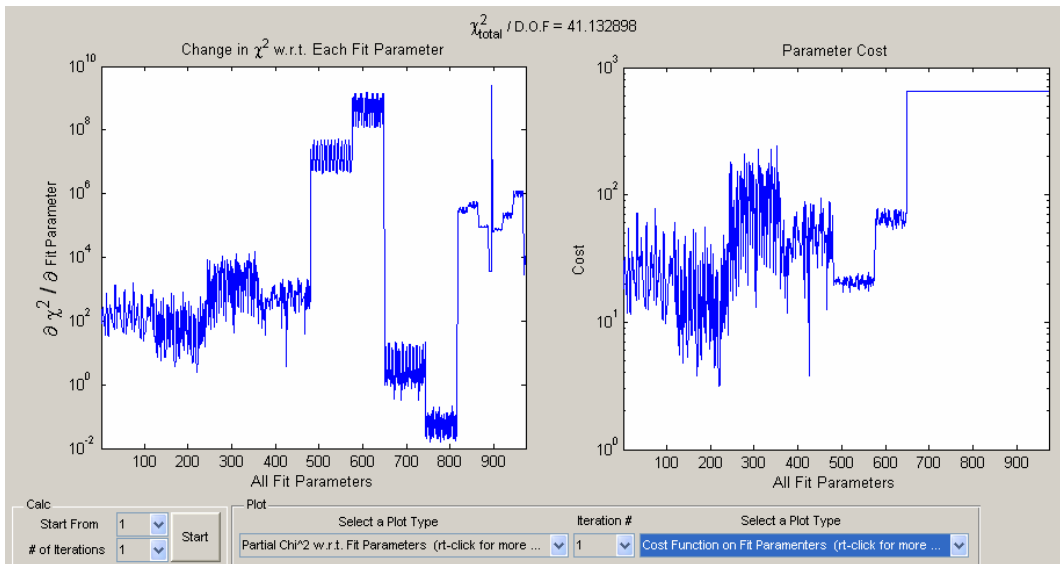
Figure 7: Partial of χ^2 w.r.t. Fit Parameter and the Equivalent Cost Function.

3.2.5 Code availability

The MATLAB LOCO is available on the web or contact:
    safranek@slac.stanford.edu or gjportmann@lbl.gov. A web search on "portmann loco" also seems to find the right place.

3.2.6 Acknowledgments

The author thanks A. Terebilo, C. Steier, L. Nadolski, W. Wittmer, D. Robin, J. Corbett, and M. Spencer for the many important discussions over many years.

3.2.7 References

1. J. Safranek, "Experimental Determination of Storage ring Optics using Orbit Response Measurements", Nucl. Inst. And Meth. A388, 27 (1997).
2. J. Safranek, G. Portmann, A. Terebilo, and C. Steier, "Matlab-based LOCO", EPAC'02, Paris, June 2002, pp. 1184-1186.
3. J. Corbett, G. Portmann, and A. Terebilo, "Accelerator Control Middle Layer", PAC'03, May 2003, Portland, pp. 2369-2371.
4. L. Nadolski et al., "Control Applications for SOLEIL Commissioning and Operation", EPAC'06, Edinburgh, July 2006, pp. 3056-3058.
5. A. Terebilo, "Accelerator Toolbox for Matlab", SLAC-PUB8732, May 2001, http://www-ssrl.slac.standford.edu/at.
6. See contribution by J. Safranek in this ICFA beam dynamics newsletter.
7. See contribution by X. Huang in this ICFA beam dynamics newsletter.
8. See contribution by L. Nadolski in this ICFA beam dynamics newsletter.
9. L. Yang, et al, "A new code for orbit response matrix analysis", Proceedings of PAC07, Albuquerque, NM.

3.3 LOCO with Constraints and Improved Fitting Technique

Xiaobiao Huang, James Safranek, SLAC, Menlo Park, CA 94025, USA
Mail to: xiahuang@slac.stanford.edu

Greg Portmann, Lawrence Berkeley National Lab, Berkeley, CA 94720, USA

3.3.1 Introduction

LOCO has been a powerful beam-based diagnostics and optics control method for storage rings and synchrotrons worldwide ever since it was established at NSLS by J. Safranek [1]. This method measures the orbit response matrix and optionally the dispersion function of the machine. The data are then fitted to a lattice model by adjusting parameters such as quadrupole and skew quadrupole strengths in the model, BPM gains and rolls, corrector gains and rolls of the measurement system. Any abnormality of the machine that affects the machine optics can then be identified. The resulting lattice model is equivalent to the real machine lattice as seen by the BPMs. Since there are usually two or more BPMs per betatron period in modern circular accelerators, the model is often a very accurate representation of the real machine. According to the fitting result, one can correct the machine lattice to the design lattice by changing the quadrupole and skew quadrupole strengths. LOCO is so important that it is routinely performed at many electron storage rings to guarantee machine performance, especially after the Matlab-based LOCO code [2] became available.

However, for some machines, LOCO is not easy to carry out. In some cases, LOCO fitting converges to an unrealistic solution with large changes to the quadrupole strengths ΔK. The quadrupole gradient changes can be so large that the resulting lattice

model fails to find a closed orbit and subsequent iterations become impossible. In cases when LOCO converges, the solution can have ΔK that is larger than realistic and often along with a spurious zigzag pattern between adjacent quadrupoles. This degeneracy behavior of LOCO is due to the correlation between the fitting parameters – usually between neighboring quadrupoles. The fitting scheme is therefore less restrictive over certain patterns of changes to these quadrupoles with which the correlated quadrupoles fight each other and the net effect is very inefficient χ^2 reduction, i.e., small χ^2 reduction with large changes of ΔK. Under effects of random noise, the fitting solution tends to crawl toward these patterns and ends up with unrealistically large ΔK. Such a solution is not very useful in optics correction because after the solution is dialed in, the quadrupoles will not respond as predicted by the lattice model due to magnet hysteresis. We will show that adding constraints to the fitting parameters is an effective way to combat this problem of LOCO [3-4]. In fact, it improves optics calibration precision even for machines that don't show severe degeneracy behavior.

LOCO fitting is essentially to solve a nonlinear least square problem with an iterative approach. The linear least square technique is applied in each iteration to move the solution toward the minimum. This approach is commonly referred to as the Gauss-Newton method. By using singular value decomposition (SVD) to invert the Jacobian matrix, this method has generally been very successful for LOCO. However, this method is based on a linear expansion of the residual vector over the fitting parameters which is valid only when the starting solution is sufficiently close to the real minimum. The fitting algorithm can have difficulties to converge when the initial guess is too far off. For example, it's possible for the χ^2 merit function to increase after an iteration instead of decrease. This situation can be improved by using more robust nonlinear least square fitting algorithms, such as the Levenberg-Marquardt method [7].

We will discuss the degeneracy problem in section 2 and then show how the constrained fitting can help in section 3. The application of Levenberg-Marquadt method to LOCO is shown in section 4. A summary is given in section 5.

3.3.2 The Degeneracy Problem

A general nonlinear least-square problem is to minimize the merit function

$$f(\mathbf{p}) = \chi^2 = \sum \left[y_i - y(x_i;\mathbf{p}) \right]^2 \tag{1}$$

where $\mathbf{p}$ is a vector of the fitting parameters, (x_i, y_i) are measured data and $y(x;\mathbf{p})$ is a nonlinear model function. The residual vector is a column vector $\mathbf{r}$ whose components are $r_i = y_i - y(x_i;\mathbf{p})$, with $i = 1,2,\cdots,N$ and N is the number of data points. The Jacobian matrix $\mathbf{J}$ is defined as,

$$J_{ij} = \frac{\partial r_i}{\partial p_j} . \tag{2}$$

Each column of the Jacobian matrix is the derivative of the residual vector over one fitting parameter. In the Gauss-Newton method, the solution is advanced toward the minimum at each iteration by $\Delta \mathbf{p}$, which is determined by

$$\mathbf{J}^T\mathbf{J}\Delta\mathbf{p} = -\mathbf{J}^T\mathbf{r}_0, \tag{3}$$

where $\mathbf{r}_0$ is the residual vector of the previous iteration. This is essentially the method adopted by the original LOCO, although where the equation was $\mathbf{J}\Delta\mathbf{p} = -\mathbf{r}_0$. However, it is much faster to do SVD on matrix $\mathbf{J}^T\mathbf{J}$ than on $\mathbf{J}$ since the latter has tens of times more rows [3].

In a fitting problem, two parameters can be deeply coupled such that their contributions to the merit function are very difficult to separate. In an extreme case, for example, it is impossible to determine the two fitting parameters p_1 and p_2 in the problem defined by $\chi^2 = \sum[y_i - y(x_i, p_1 - p_2)]^2$ because the merit function has no dependence on $p_1 + p_2$. The corresponding columns of the Jacobian matrix for the two parameters differ by only a scaling constant. Therefore, the Jacobian matrix is rank deficient. In a less severe case, the merit function may have weak dependence over $p_1 + p_2$ so that in principle it can be determined. But it is susceptible to noise in the experimental data and tends to have large error bar. Consequently the two parameters p_1 and p_2 both have larger error bars. The coupling of adjacent quadrupole gradient parameters in LOCO is very similar to the above case. If two quadrupoles are placed next to each other without much space between, they perturb the linear optics of the machine in essentially the same manner.
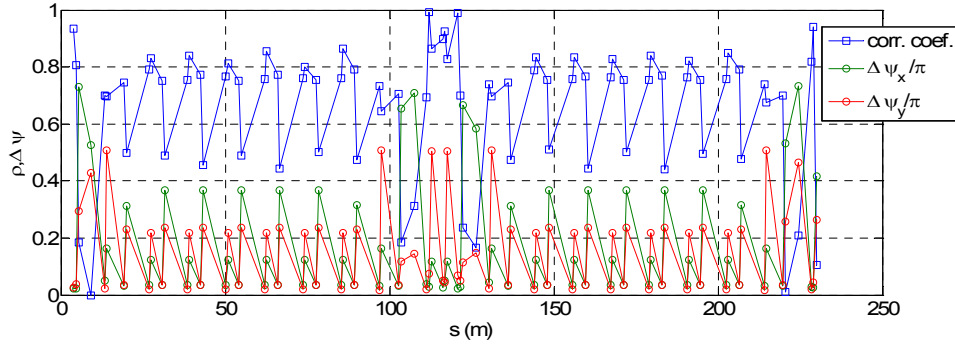
Figure 1: the correlation coefficients and betatron phase advances between neighboring quadrupoles (excluding QFC) in SPEAR3.

LOCO may be able to accurately fit the combined integrated gradient of the two magnets but it would not be able to distinguish the individual contributions. When quadrupoles are separated with drift spaces or other components, the coupling between their gradients gets weaker but remains existent. Detailed analysis shows that it is the betatron phase advances between two quadrupoles that determine their coupling strength. Adding BPMs in the vicinity can alleviate the problem to some extent, but cannot eliminate it.

The coupling between fitting parameters is reflected in the similarity of their corresponding columns in the Jacobian matrix, which may be characterized by their correlation coefficient,

$$\rho_{12} = \frac{\mathbf{J}_1^T\mathbf{J}_2}{\|\mathbf{J}_1\|\|\mathbf{J}_2\|}, \tag{4}$$

where $\mathbf{J}_{1,2}$ are corresponding columns of the parameters p_1 and p_2, and $\|\bullet\|$ stands for the 2-norm of its argument. Fig. 1 shows the correlation coefficients between neighboring quadrupoles in SPEAR3. The horizontal and vertical betatron phase advances ($\mathrm{mod}\,2\pi$) between these quadrupoles are also plotted. The correlation coefficients between neighboring QF, QD magnets in a DBA cell are around 0.8. Quadrupole magnets in the double waist straight section (in the center of the plot), [6], have even stronger correlation between their neighbors. Clearly, strong correlation is the result of small betatron phase advances between them. Stronger correlation can occur between two quadrupoles that are physically set apart but both betatron phase advances between them are close to a multiple of π. One may calculate a correlation matrix and examine the coupling relations between the fitted quadrupole gradients.

Because of the coupling between quadrupoles, some patterns of changes of the quadrupole gradients are much less restricted by LOCO fitting. If these patterns form a null-space in the parameter space, meaning that they correspond to singular values considerably smaller than others, then they can be simply removed by proper selection of singular values. However, the less restrictive patterns have various severities
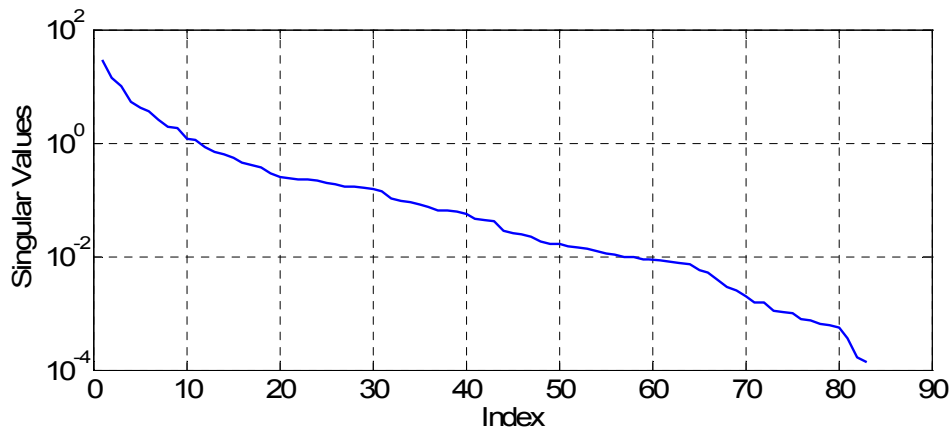
Figure 2: singular values of the correlation matrix of SPEAR3 quadrupoles.

and are rarely orthogonal. The patterns through SVD have to be orthogonal to each other. Consequently the singular value spectrum is usually a smooth curve without a clear cut. For example, the singular values for the correlation matrix in the SPEAR3 example are shown in Fig. 2. The less restrictive patterns tend to be clustered toward the lower end of the spectrum. When degeneracy becomes a problem, removing some of the very low singular value modes is justifiable. However, completely removing any mode is a loss of information and thus would reduce the fitting accuracy to some level. It often takes much work to find an optimal threshold. And our experience shows that some less restrictive patterns still leak into the solution even if a seemingly optimal threshold is applied. It seems not possible to retain good accuracy of fitting and keep the quadrupole strength changes reasonably low at the same time by merely selecting the singular values. This has also been the observation at Soleil, [10].

The response matrix measurement always has errors because of random BPM noises and random machine fluctuation. There are also systematic errors due to, for example, nonlinearity of the machine. The solution may drift along a less restrictive direction by a large step to gain a small reduction of χ^2 that is under the error level. Since the fitting algorithm does its best to find a minimum, the final solution tends to acquire large

excursions toward the less restrictive directions. Such excursions are not necessarily reflected in the standard error bar calculation of LOCO because there only random BPM noises are considered.

The degeneracy caused by coupling between the fitting parameters is intrinsic to the problem. Strictly speaking, there is no single "best solution". Instead, any solution whose χ^2 differs from the global minimum by less than a certain amount determined by the noise level is a valid, equivalent solution. These solutions should in principle give the same machine lattice. We should pick the reasonable ones from this set of equivalent solutions. In the next section, we will show how this can be done by the constrained fitting method.

3.3.3 LOCO Fitting with Constraints

Since coupling between LOCO fit parameters can cause excursions of the solution in unconstrained directions, it is natural to put a penalty on such excursions. This can be done by modifying the merit function with additional penalty terms. Ideally we would like the penalty terms to represent the unconstrained patterns as was done in Ref. [3-4]. However, it is not easy and also not necessary to identify these patterns. A much simpler approach is to put penalty on the change of gradient ΔK of each quadrupole directly. Therefore the least-square problem now reads,

$$\chi^2 = \sum_{i,j} \frac{(M_{\text{mod},ij} - M_{\text{meas},ij})^2}{\sigma_i^2} + \frac{1}{\sigma_{\Delta K}^2} \sum_k w_k^2 \Delta K_k^2 \,, \tag{5}$$

where $\sigma_{\Delta K}$ is an overall normalization constant and w_k^2 are individual weighting factors that represent the needs to constrain their corresponding quadrupoles. The weighting factors should be adjusted according to the performance on a trial and error basis. But once a suitable set of weighting factor is found for one lattice, there is usually no need to change it later on. Removing singular values is equivalent to put infinite penalty weight on the corresponding patterns. This extreme measure seems to work less efficiently than the more "gentle" approach here.

It is straightforward to implement this modified LOCO fitting scheme. The input and output are the same data as the original LOCO. Only the minimization algorithm needs a slight modification. The additional terms in χ^2 amount to simultaneous linear equations, $\Delta K_k = 0$, $k = 1, 2, \cdots, N_q$, each with a weight $w_k^2 / \sigma_{\Delta K}^2$, where N_q is the number of constrained quadrupoles. Consequently the residual vector and the Jacobian matrix are extended. Suppose the original Jacobian matrix has N rows (i.e., N data points). The Jacobian matrix will have N_q more rows with nonzero elements $J_{N+k,k} = w_k / \sigma_{\Delta K}$ and the corresponding additional elements of the previous residual vector $\mathbf{r}_0$ are zeros. Then Eq. (3) is applied as usual to find the step to the next solution.

The additional constraint terms changes the solution to the linear problem of each iteration. However, since only the gradient changes between successive iterations are constrained with a cost, the global minimum of the original problem remains the same. What has been changed is the convergence path. Fig. 3 serves as an illustration of this picture, where point 0 represents the initial guessed solution; point M is the global minimum within a sea of equivalent solutions under the noise level. The unconstrained

path (solid arrows) takes large excursions and reaches the global minimum quickly, while the constrained path (dashed arrows) touches the nearest edge of the noise sea and slows down.

Fig. 4 is an example of real LOCO data at SPEAR3 fitted for 12 iterations with both algorithms. Here 12 iterations are run just to show the behavior of the fitting methods. We usually run two or three iterations and apply the solution for optics correction. The convergence paths are shown on an rms relative gradient change vs. residual χ^2 (normalized by degree of freedom) plot. The unconstrained algorithm converges in three iterations but ends with a 2.1% rms relative gradient change. The constrained algorithm brings χ^2 down to the same level in three steps with an rms relative gradient change of only 0.6%. The additional gradient changes of the unconstrained algorithm do not result in a very different lattice. In fact, the rms relative differences of horizontal and vertical beta functions between the two lattices at point 3 and point 3' are only 1% and 0.3%, respectively. Most of the additional gradient changes are cancelled by fighting each other. The lattice difference would be far larger if the gradient changes were random.
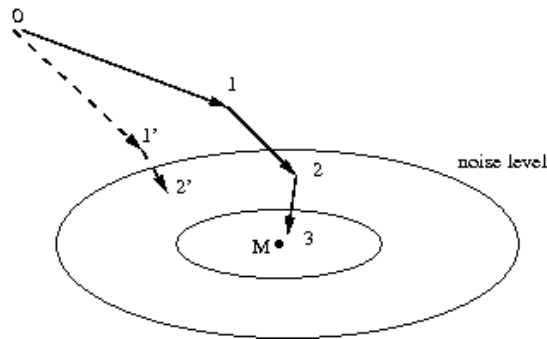
Figure 3: An illustration of the changes to the convergence path with or without constraints. Solid: no constraints; Dashed: with constraints.
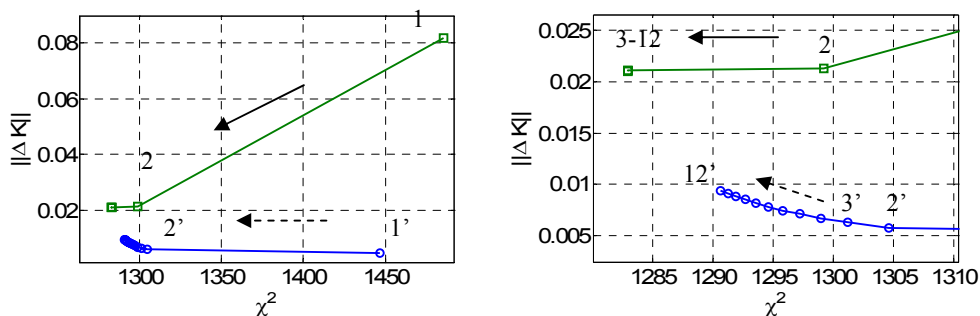
Figure 4: The rms relative change of gradients vs. the residual χ^2 for a SPEAR3 data set. Green: no constraints; Blue: with constraints. Point 0 is located at (2.0×10^6, 0). The right plot is a blowup show of the left plot.

A LOCO solution with smaller gradient changes is preferred for optics control. When quadrupole setting corrections are dialed in according to the solution, it is

assumed that the magnets respond with a linear field-current relation. This assumption holds only when the current changes are sufficiently small because of magnet saturation and hysteresis. Therefore, a solution with large changes of gradients may not produce the expected lattice in reality. For the nominal SPEAR3 lattice the coupling problem is not severe. A beta beating under 1% rms was achieved with proper selection of singular values using the original LOCO method. The constrained fitting, however, still proves to be a valuable tool by improving the precision of optics control. Presently, the machine optics are corrected to a beta beat less than 0.2% beta beating without special care to singular value selections. For the low alpha lattice, [5], this tool is indispensable because the lattice couldn't be calibrated without it. For one LOCO data set from the low alpha lattice, the rms relative ΔK change is fitted to be 14.5% by keeping 530 out of 542 singular values and larger if more singular values are kept with the unconstrained method. The constrained method finds a solution with only 3.5% rms relative ΔK change and the rms relative beta function difference between the two resulted lattices is only 2.0% horizontal and 0.7% vertical. After correction, the beta beat was reduced to 0.5% horizontal and 0.3% vertical.

It is worth noting that the ability of LOCO to identify large gradient errors is not sacrificed by adding constraints. The constraints endanger primarily the existence of the less restrictive patterns in the solution because they are "cheap" in terms of χ^2. Real gradient errors usually cause large χ^2 contributions and they rarely form a less restrictive pattern. For example, during the 2007 shutdown of SPEAR3, an insertion device was moved to a new location. The perturbation to the lattice corresponds to normalized χ^2 contributions over 8×10^4. The nearby quadrupole magnets stand out in the fitting solution to account for the change, even if we put 20 times more weight on these quadrupoles than we normally do.

The penalty terms, the costs, are essential to the improved performance of LOCO. It is important to set the cost factors properly. If the penalty is too high, the solution would converge too slowly. If the penalty is too low, the benefit of constraints would not be seen. The average cost may be a good indicator of the choice of weighting factors. In Fig. 5 we plot the average cost for each iteration for the example shown in Fig. 4. For SPEAR3, equal weighting factors were initially chosen for all quadrupoles and then adjustments are made as needed. The more sensitive a parameter is to coupling issues, the more weight gets added. The proper overall weighting factor may be found by adjusting it to produce an average cost at the first iteration that is comparable to the normalized residual χ^2. The correlation coefficient plot (Fig. 1) could be useful in identifying the sensitive quadrupoles. However, a more straightforward and easier method is to study the individual χ^2 contribution of the fitting parameters, [3]. The χ^2 contribution of a fitting parameter is defined as the increase to χ^2 if we set this parameter to its initial value at iteration 0 and keep all other parameters unchanged. We can define the contribution of a group of parameters in the same manner. Ideally, if there is no correlation between the fitting parameters so they don't fight each other, then the sum of their individual contributions should be nearly equal to their group contribution, assuming a linear expansion is valid. In contrast, if a parameter drifts along a less restrictive direction by a large amount from iteration 0, then it will cause a sizable χ^2 contribution because the other parameters are not present to cancel its effect in this calculation. This is what was observed in the same SPEAR3 data set. Fig. 6

shows the χ^2 contribution after three iterations with or without constraints. Because quadrupoles that share the same power supply are combined as one fitting parameter, there are 72 quadrupole fit parameters. Also shown in Fig. 6 are contributions of the 14 skew quadrupoles. It is first noted that the group contribution of all fitting parameters for the two cases are about the same ($\Delta\chi^2 \approx 3600$).This is not surprising because the two resulting model lattices are nearly the same (see discussion before Fig. 3). However, for the unconstrained case, the individual contributions are considerably higher, especially for a few quadrupole magnets. It is reasonable to assign more weights to these parameters. These magnets turn out to be located around the double waist straight section, where the coupling between magnets is stronger. The constrained solution has small individual χ^2 contribution for the fitting parameters and their sum is on the same order as their group contribution.
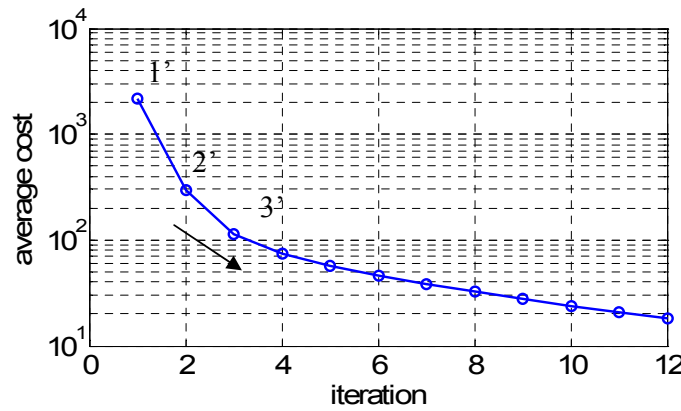
Figure 5: the average cost for the SPEAR3 example shown in Fig. 4
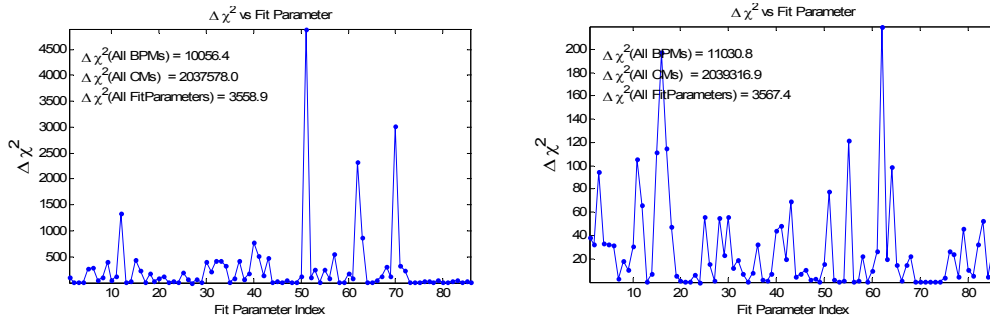
Figure 6: χ^2 contribution for individual fitting parameters at point 3 (left) and point 3' (right) for the SPEAR3 example shown in Fig. 4. The first 72 parameters are quadrupoles. The last 14 are skew quadrupoles.

Constraints can be easily applied to other parameters such as BPM gains and rolls, corrector gains and rolls but this is not necessary for the case of SPEAR3.

3.3.4   The Levenberg-Marquadt Fitting Algorithm

The Gauss-Newton method that is adopted by the original LOCO converges quickly if the initial solution is close to the minimum. But there are situations when a good initial guess is not available. In those situations, the fitting algorithm may behave

unexpectedly, for example, an increased χ^2 or one that oscillates around the minimum. In such cases the steepest descent is more suitable because it can move the solution toward the minimum. The Levenberg-Marquadt algorithm combines the two methods in an elegant way so that either one is selected in its applicable region [7]. This is achieved by replacing Eq. (3) with

$$(\mathbf{J}^T\mathbf{J} + \lambda\mathbf{D}^T\mathbf{D})\Delta\mathbf{p} = -\mathbf{J}^T\mathbf{r}_0, \tag{6}$$

where $\mathbf{D} = \mathrm{diag}(\|\mathbf{J}_1\|,\|\mathbf{J}_2\|,\cdots,\|\mathbf{J}_{NP}\|)$, NP is the number of columns of the Jacobian matrix and $\lambda > 0$ is a scaling constant. In other words, the diagonal elements of the matrix $\mathbf{J}^T\mathbf{J}$ are scaled up by $1+\lambda$. The constant λ controls the behavior of the algorithm. If λ is very small (much less unity), it is the same as the Gauss-Newton method. If λ is much larger than unity, it becomes the steepest descent method. Usually λ is set to a small value initially, for example $\lambda = 0.001$. Then after every iteration it is adjusted, depending on the result of the solution found in that iteration. A simple way is to scale it down by a factor of 10 if the solution reduces χ^2 and update the Jacobian matrix; and if χ^2 is increased then scale λ up by a factor of 10 until a solution is found to reduce χ^2. In this way χ^2 is guaranteed to decrease after every iteration. The application of the Levenberg-Marquadt method to LOCO has been suggested in Ref. [3-4].

It is interesting that the fitting with constraints scheme can be cast into the same framework as the Levenberg-Marquadt algorithm. In fact, Eq. (6) applies to the former case with $\lambda = 1$ fixed and $\mathbf{D} = \mathrm{diag}(0,\cdots,0,w_1,w_2,\cdots,w_{N_q})/\sigma_{\Delta K}$, where the 0's are for non-constrained parameters. This is not surprising because both methods want to limit the step sizes toward the next solution, but for different reasons! For the Levenberg-Marquadt method, the goal is to find the global minimum reliably. But the constrained fitting actually wants to avoid the global minimum by going with slower paces.

A recent report [8] indicates that a more delicate form of the Levenberg-Marquadt algorithm [9] could have better performance for LOCO. This algorithm is based on explicit control of a trust-region: it finds the best solution for the iteration within the region specified by

$$\|\mathbf{D}\Delta\mathbf{p}\| \leq \Delta, \tag{7}$$

where Δ on the right hand side represents the size of the trust region and it is adjusted according to the efficiency of χ^2 reduction after every iteration.

3.3.5 Summary

Two ways to improve the LOCO technique have been discussed – the constrained fitting method and the Levenberg-Marquadt algorithm. The constrained fitting is introduced to cure the degeneracy problem caused by the coupling between fitting parameters (mainly the neighboring quadrupoles). This is a common problem that occurs to many machines in different severity. The constraints are implemented by putting penalties for the step sizes between the solutions of successive iterations. It has

shown to be an efficient way to remove the less restrictive patterns from the solution and it results in fitted lattices with small changes from the starting point. This enables precise control over the machine optics, even for machines where the degeneracy problem has made the original form of LOCO not useful.

The Levenberg-Marquadt algorithm is a robust solver for general nonlinear least square problems. It is useful for LOCO in cases when the initial guessed solution is not close enough to the minimum. In such cases the Gauss-Newton solver may fail because the solution it finds could lie outside of the region where linearization of the model is valid. The Levenberg-Marquadt algorithm is based on the trust-region strategy – the solution it finds is confined in a region where the linear model is valid. The size of the trust region is controlled implicitly or explicitly and is adjusted after every iteration.

3.3.6 References

1. J. Safranek, "Experimental determination of storage ring optics using orbit response measurements", Nucl. Instr. and Methods, A 388 (1997) 27-36
2. J. Safranek, et al, "Matlab-based LOCO", Proceedings of EPAC02, Paris, France
3. X. Huang, Indiana University PhD thesis (unpublished), 2005
4. X. Huang, et al, "Fitting the fully coupled ORM for the Fermilab Booster", Proceedings of PAC05, Knoxville, TN
5. X. Huang, et al, "Low alpha mode for SPEAR3", Proceedings of PAC07, Albuquerque, NM
6. J. Corbett, "Implementation of the double-waist chicane optics in SPEAR3", Proceedings of EPAC06, Edinburgh, Scotland
7. W. H. Press, et al, "Numerical recipes in C", 2nd Ed. Cambridge University Press.
8. L. Yang, et al, "A new code for orbit response matrix analysis", Proceedings of PAC07, Albuquerque, NM
9. J. J. More, "The Levenberg-Marquadt algorithm: implementation and theory", Lecture Notes in Mathematics (G. Wastson ed.), vol 630, Springer, 1978, p. 105
10. See contribution by L. Nadolski in this ICFA beam dynamics newsletter.

3.4 LOCO Fitting Challenges and Results for SOLEIL

Laurent S. Nadolski

Saint Aubin BP 48, Gif-sur-Yvette, France, http://www.synchrotron-soleil.fr
Mail to: nadolski@synchrotron-soleil.fr

3.4.1 Introduction

SOLEIL is a 354 m long third generation light source delivering photons to beam-lines since January 2007. Already 13 beam-lines from infrared to hard X-rays take beam in November 2007. The standard performance given to the beam-lines consist on a multi-bunch filling pattern (312 out of 416 filled RF-buckets), a 200 mA stored beam current with 0.4% of coupling and 15 hours of beam lifetime (2 MV RF-voltage and 1.2×10^{-10} mbar average pressure).

Operating at 2.75 GeV, the 3.7 nm.rad storage ring lattice is based on a modified Chasman-Green optics with dispersion distributed all around the ring [1]. Typically the straight sections accommodate a 15 to 20 cm horizontal dispersion with a maximum value of 25 cm in the arcs (see Figure 1). The aftermaths of the breaking the fourfold

symmetry leads to a reduction of the injection efficiency and of the beam lifetime since the on- and off-dynamics apertures are reduced *via* resonance excitations [2-3].
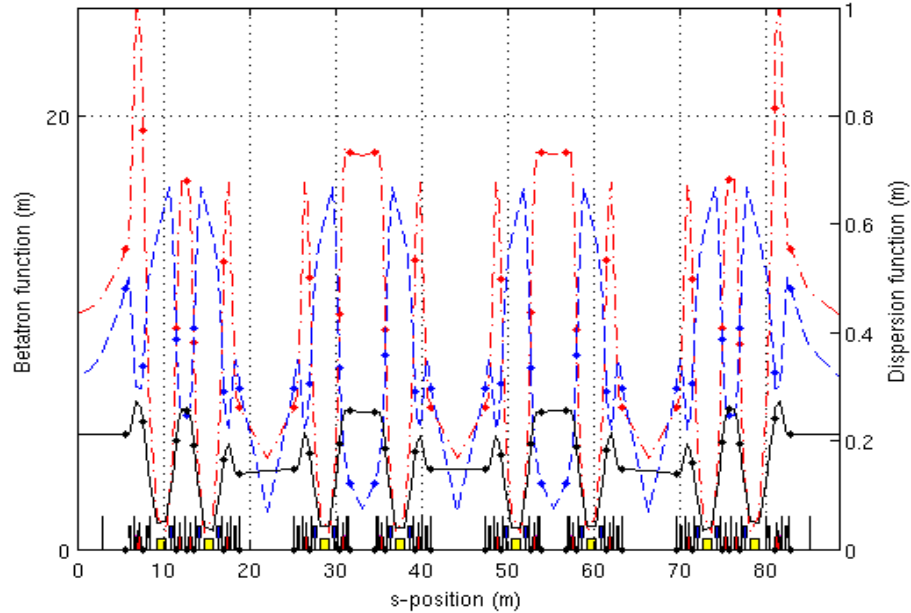
Figure 1: SOLEIL modified Chasman-Green optics for 1 of the 4 super-periods: horizontal (red dotted-dashed line), vertical (blue dashed line) betatron functions and horizontal dispersion function (black solid line). Dots are BPM locations.

Strong focusing optics is a key factor in new light sources such as SOLEIL. A total of 160 quadrupoles divided in ten families are set all around the storage ring. Each quadrupole magnet is individually powered by a 18 bit numerically regulated power supply. This is necessary due to the extreme sensitivity of the transverse beam dynamics: beam lifetime, injection efficiency, effects of insertion devices, on- and off-momentum apertures are very sensitive to quadrupole errors.

Due to this high sensitivity a peculiar attention was given to the magnetic measurements and the alignment processes of these multipole magnets. RMS magnetic center alignments are 8.4 and 7.5 µm respectively in H- and V-planes with a RMS tilt error of 40 µrad [4]. The total alignment precisions, magnets together with their girders, are around 60 µm RMS in both planes. The RMS gradient identity from one quadrupole to the other is 10^{-3}.

A schematic of 16 cells is given by Figure 2. Besides dipole, quadrupole and sextupole magnets, correctors and beam position monitors (BPMs) are displayed as well. The horizontal and vertical closed orbit correctors and the skew quadrupoles are secondary coils included inside the main sextupole magnets. Each cell accommodates a total of 7 to 8 BPMs and 10 quadrupoles. It is worthwhile noting that the ratio of the number of quadrupoles over the number of BPMs is larger than a unit in a machine such as SOLEIL. This will strongly impact the LOCO analysis.

This paper will discuss in details the first attempts using LOCO and the problems encountered. Then first cures will be described. In the last section, examples using LOCO as a diagnostics and very valuable tool will be given.
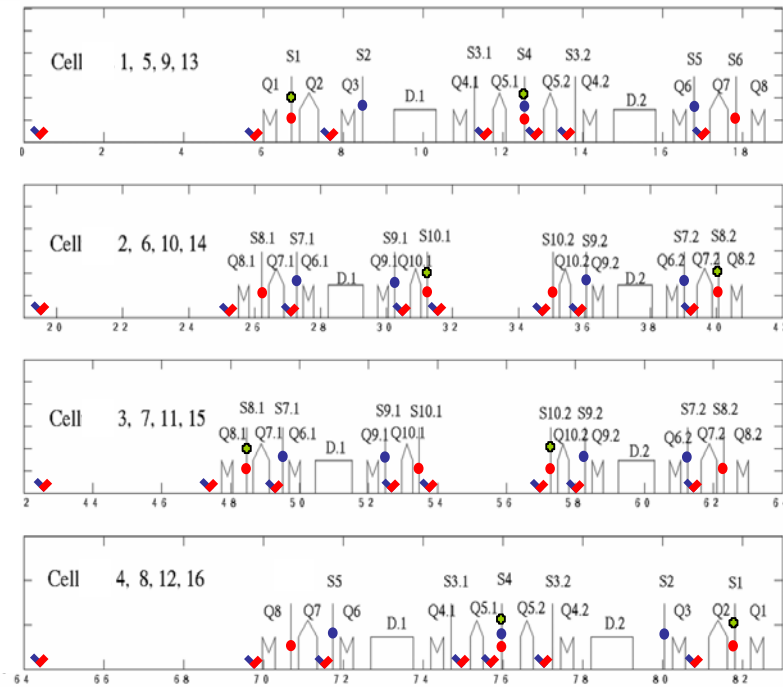
Figure 2: Schematic of the storage ring cells: BPMs (blue & red "v"), H-correctors (red dots), V-correctors (blue dots) and skew quadrupoles (green crosses).

3.4.2 First Attempts using LOCO for the SOLEIL Storage Ring

3.4.2.1 Tools for doing the LOCO Analysis

The SOLEIL high level control framework in the control-room is based on the Matlab Middle Layer (MML [5]) which was extended and integrated to the TANGO control system [6]. As an online simulator, the Accelerator Toolbox (AT) is used [7]. Dipole fringe field has been taken into account giving an additional vertical focusing term in the lattice. The LOCO code is fully integrated in Matlab together with AT and MML. It is based on the early Fortran version written by J. Safranek [8] and ported into Matlab language [9]. Two versions of the code have been used for the present analysis: the standard version with no constraints on the quadrupole gradient variations and a new version with constraints integrated into the code during the spring of year 2007 [10].

3.4.2.2 Typical Data Sets used for doing the LOCO Analysis

For doing the LOCO analysis a standard set of input data is required: a measured dispersion function, a BPM noise measurement and an orbit response matrix. A short description of each of them will be given with SOLEIL specificities. All this work has been done after a careful beam based alignment: the closed orbit goes through the

quadrupole centers with a RMS value of 40 to 50 micrometers in both planes after orbit correction.

The Figure 3 displays a typical BPM noise measurement: data are acquired at a 2 Hz rate during 180 seconds. RMS noise values of 220 nm in horizontal and 60 nm in vertical are daily measured after optimization of the Libera electronics of the BPMs by the diagnostics group. This noise level includes all together contributions from the beam, the cables and the electronics. In the horizontal plane, the dispersion pattern is clearly showing up. It may be related to the analogical loop on the RF phase keeping the phase within a range of $\pm 0.1°$.
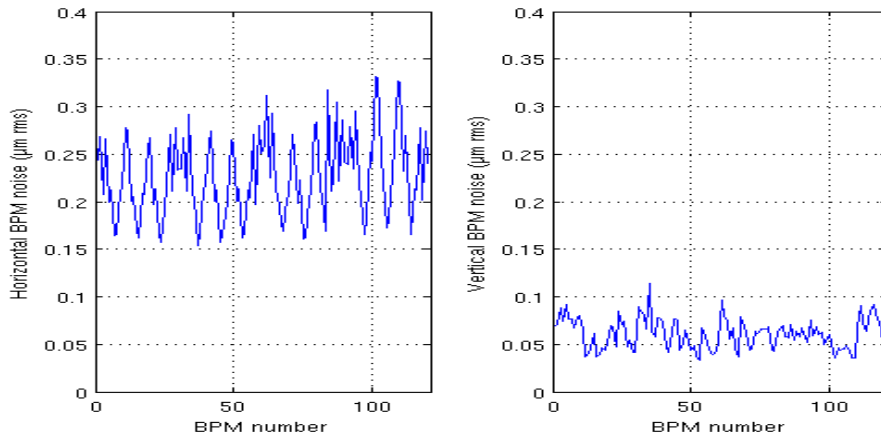
Figure 3: Typical RMS (BPM+beam) noise for averaged data during a 180 s time span. Data are expressed in micrometers for each of the 120 BPMs in both planes.

The dispersion function is measured by varying the RF frequency by steps of $\pm$ 50 Hz, corresponding to an average horizontal orbit distortion of $\pm$ 50 μm in average.

The orbit response matrix measurement is acquired using a bipolar method, stepping the corrector magnet setpoint values by +/- 5 μrad in H-plane and +/-10 μrad in V-plane (equivalent to a closed orbit distortion of 100 μm peak). The corrector power supplies have a 20 bit DAC/ADC and a full dynamic range allowing a kick of 0.9 and 0.7 mrad respectively in H- and V-planes. The total measurement lasts for 15 minutes for 56 correctors in both planes and 120 BPMs. Typically the full orbit response matrix is analyzed including the off-diagonal blocks describing the coupling.

The LOCO algorithm has been extensively described in the present beam dynamics newsletter issue. In the following sections, focus will be given on its application to SOLEIL. The fitting parameters are summarized into the Table 1 with a total number of 896 parameters for the full coupled matrix. Thanks to today computers inverting such a large matrix is not anymore a show-stopper. Performing the inversion requires around 512 Mo of RAM memory and one minute of computational time.

Table 1: Parameters used by the LOCO code to fit the model response matrix to the experimental one at Synchrotron SOLEIL.

Parameter types	Number of elements
BPM gains	240
BPM coupling factors	240
Corrector strengths	112
Corrector tilts	112
Skew quadrupole strengths	32
Quadrupole gradients	160
Total	**896**

3.4.2.3   First Results and Discussion

The first use of LOCO has a twofold conclusion. A first sight, it restored back most of the symmetry of the dispersion (Figure 4) and betatron functions (Figure 5) but at the same time it was unfruitful since the gradient variations given by the code were too large, with values of a few percents. This section is devoted for discussing these very results.

Several difficulties were experienced:

1. The spectrum of singular values was extremely flat with no clear cut (Figure 6). Choosing the number of singular values to be used was not a trivial task. Too few singular values gave no correction at all. Too many gave more than 10% of relative gradient variations. At the end the right number was obtained painfully by tries and errors: 410 singular values happened to be the best solution.
2. It is worth saying that the BPM and corrector settings were almost independent on the number of singular values.
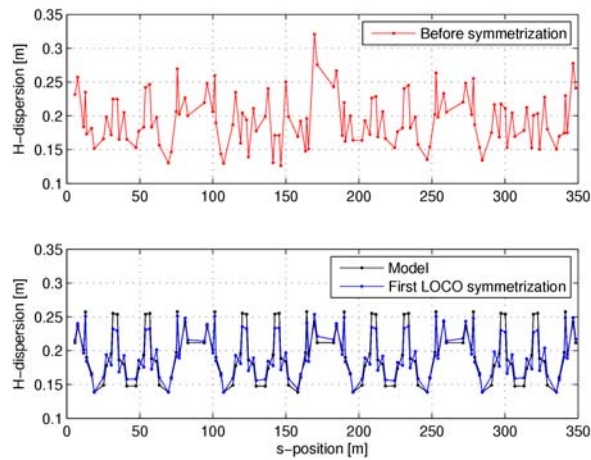
Figure 4: Horizontal dispersion before (red) and after (blue) the first LOCO symmetrization and comparison with the model (black).
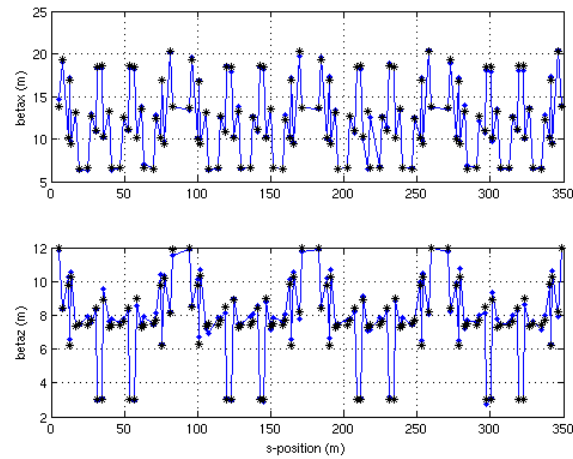
Figure 5: Comparison of betatron functions after applying LOCO with the AT model. Blue dots are experimental date obtained from turn by turn measurements and black stars, the values deduced from AT model.

3. Each LOCO solution was working in the simulator. Basically, the LOCO code is fitting the betatron functions at the position of the BPMs but the solution is not unique. The ring symmetry and global parameters such as betatron tunes are then restored.

4. At SOLEIL, it is not possible to store the beam with the sextupoles turned off. For off-axis beam, the 10 sextupole families give a quadrupole component which could be integrated in theory. Several analyses have been performed with a reduction of 50% of the sextupole strengths. No significant variations of the gradient distributions have been observed. Consequently, sextupole contribution to beta beating is considered to be negligible.

5. The gradient distribution restoring back the symmetry is given by Figure 7. This set of values is reached with 3 iterations of the LOCO code but variation values are very large: a few percents, up to 5 to 6 percent for the Q3 quadrupole family.
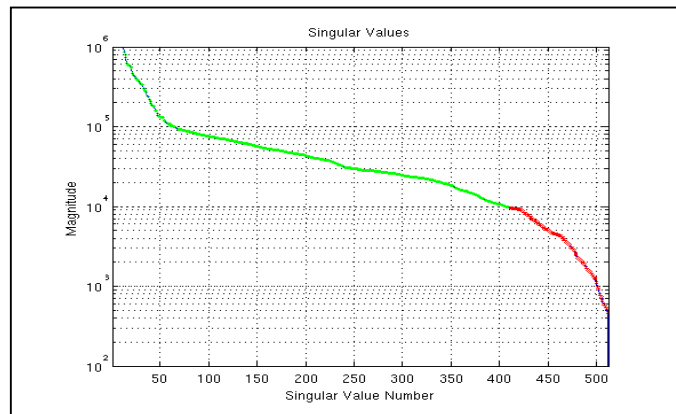
Figure 6: Singular value spectrum: for an uncoupled orbit response matrix the maximum number of singular values is 512. The green part corresponds to the values used by LOCO

These values were not acceptable for several reasons. Firstly as discussed in the introduction, the magnetic measurements of the quadrupoles showed an excellent magnetic quality and all the magnets had been aligned onto the storage ring girders using state of the art methods. Secondly, a value of a few percents would have result as huge beam disturbances (focusing and orbit) which were not observed during the early storage ring commissioning phase. Thirdly gradient variations corresponding to the measured beta-beatings (10 % peak) are expected to be only a few thousandths.

Another possibility would have been problems with the 160 individual power supplies. Nevertheless significant efforts had been put on the settings and calibrations of theses power supplies. Each of their internal DCCT had been carefully calibrated with the same external reference DCCT.
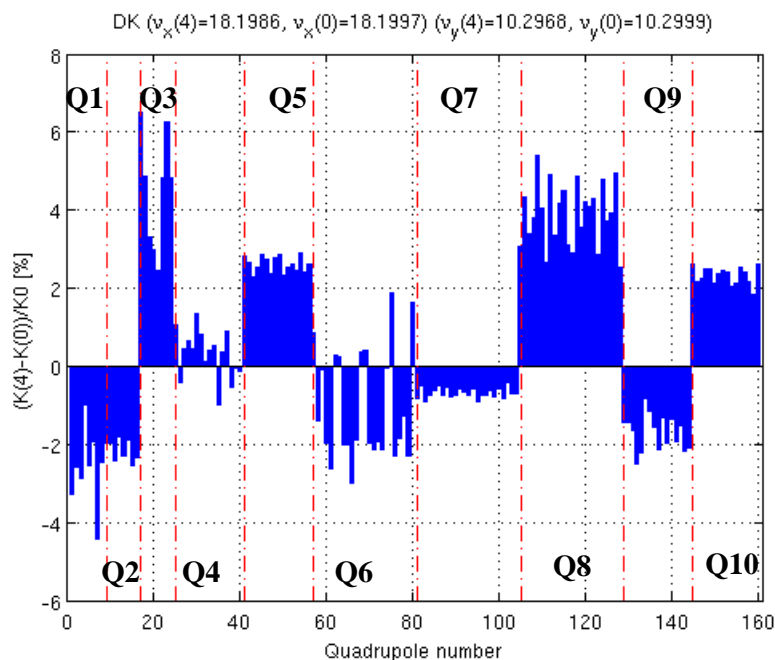
Figure 7: Relative quadrupole gradient variation given by LOCO to symmetrize the ring. Vertical red dashed lines delimit the 10 different quadrupole families (Q1 to Q10).

3.4.3   New Philosophy and First Solutions

In the previous section, the LOCO solution applied to the machine was not fully satisfactory since the gradient variations were by far too large. The difficulty to find a clear cut in the singular value spectrum has been identified to be a result of the compactness of the SOLEIL lattice. In fact after discussion with SPEAR3 colleagues, it appeared that this issue may be common to new light sources such as DIAMOND, CLS, Australian Synchrotron and ALBA.

In these machines the ratio of the number of quadrupoles over the number of BPMs is more than one. As a result the LOCO code encounters difficulties to disentangle the effect of adjacent quadrupoles. For example at SOLEIL, if one quadrupole is next to another one without BPM in between, the code will try to compensate the focusing effect of the latter by the defocusing effect of the former and *vice versa*. This can give

large gradient variations and local beta function mismatch even if the tunes or betatron functions at the BPM position keep the same. Therefore solutions are not unique and depend strongly on the arbitrary choice of singular values.

The LOCO code was then modified to include a weighting factor to constrain the gradient variations in addition to the other minimization parameters. One could still argue that this is a bit artificial but improvements are dramatic at SOLEIL.

Results are displayed by Figures 8 to 10: two successive iterations are shown; ieration 0 correspond to the bare machine (*i.e.* before LOCO symmetrization). Keeping the same betatron function beatings as found with the previous code version (previous section), *viz*. 5% RMS in both planes, the quadrupole gradient variations are now just a few in-a-thousand. There is one exception around the center of the storage ring where variations can reach up to 1.2%. This feature is not fully understood yet but appears clearly in the natural orbit (closed orbit with all correctors turned off) and in the dispersion function. After two successive symmetrizations of the machine, the betatron and dispersion function beatings are below 0.5 % RMS at the BPM positions.
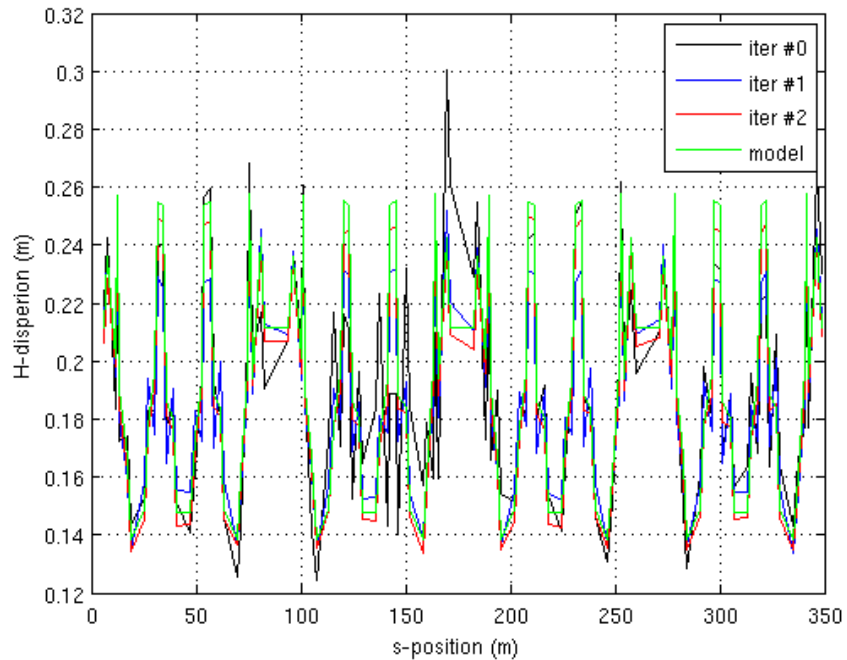
Figure 8: Horizontal dispersion evolution between two LOCO symmetrizations. The last iteration is closed to the modelled dispersion (green curve).
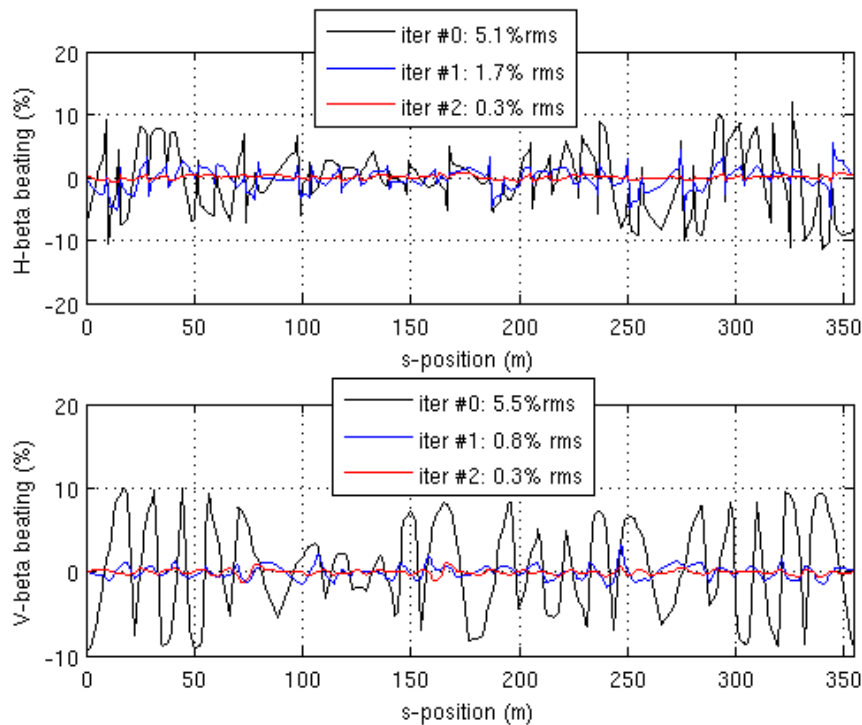
Figure 9: Beta-beating reduction from there bare lattice (black) after two successive symmetrizations of the optics using LOCO (curve blue and red).

These results are satisfactory at several levels:

1. All the singular values but one are used for the fitting. Indeed due to almost zero vertical dispersion, it is equivalent to increase all the corrector efficiencies and decrease all the BPM gains in the vertical plane. Therefore one singular value has to be removed.
2. The gradient errors are now fully compatible with the errors of alignment and the magnetic measurements.
3. The BPM gains are found to be within a range of 1 to 2 %, which is in agreement with the sorting performed on the capacities of the buttons for all BPM blocks during their installation in the machine.
4. Improvements of a few percents are observed on the injection efficiency. Effects of insertion devices on the injection performance are improved. This is especially true for one APPLE II type insertion device with an improvement of 40% of the injection efficiency when closed to its minimum gap of 15.5 mm.
5. By fitting the off-diagonal terms of the orbit response matrix using the 32 installed skew quadrupole, the global coupling of the machine can be reduced from 0.3% down to 0.08%. This value is deduced from beam size measurements with the pinhole system.
6. Lastly, the internal coupling of the BPMs can be deduced. At SOLEIL Libera RF front-ends suffer from a cross talk up to 5% between RF channels. These values have been measured in the laboratory during a 2 week shutdown period for all the 120 BPM modules. Figure 11 gives a comparison between those measurements and the BPM coupling factors output from LOCO. A strong

correlation is observed for most cells (measurement bench resolution is less than beam based measurements measurement).
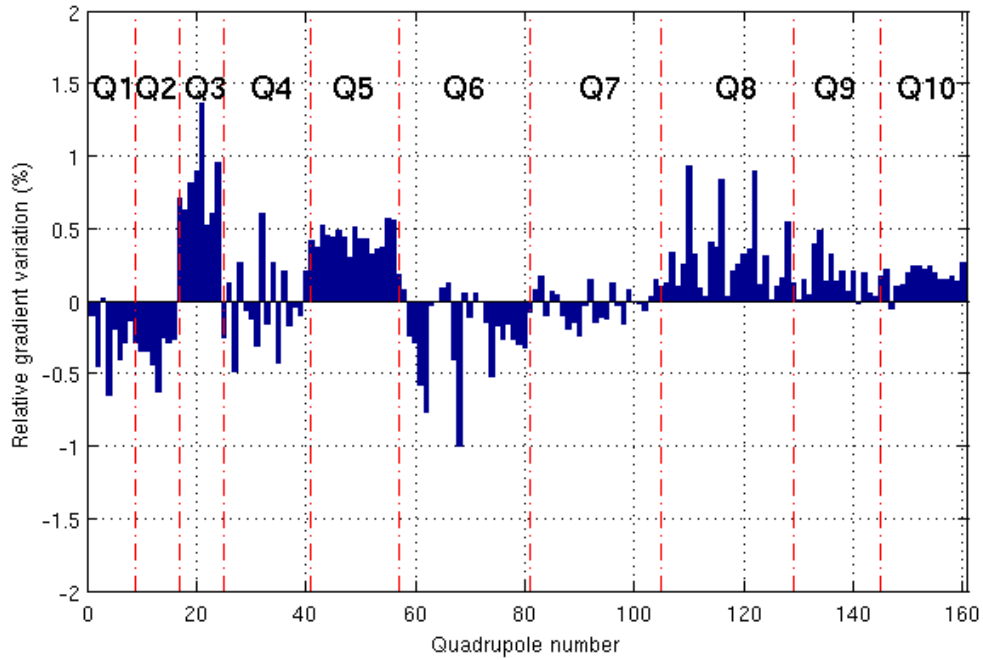
Figure 10: Total relative gradient variations after two iterations of the LOCO code. The values are sorted by quadrupole families.

To end, it should be stressed that these results can still be improved. The author is strongly convinced that the final resolution of the method has not been reached yet. The main issue remains that between successive lattice symmetrizations the gradient values found out by the code oscillate instead of converging to zero. This might be still correlated to the additional constraint introduced on the variation of the quadrupole gradients. Further investigations are still under way.
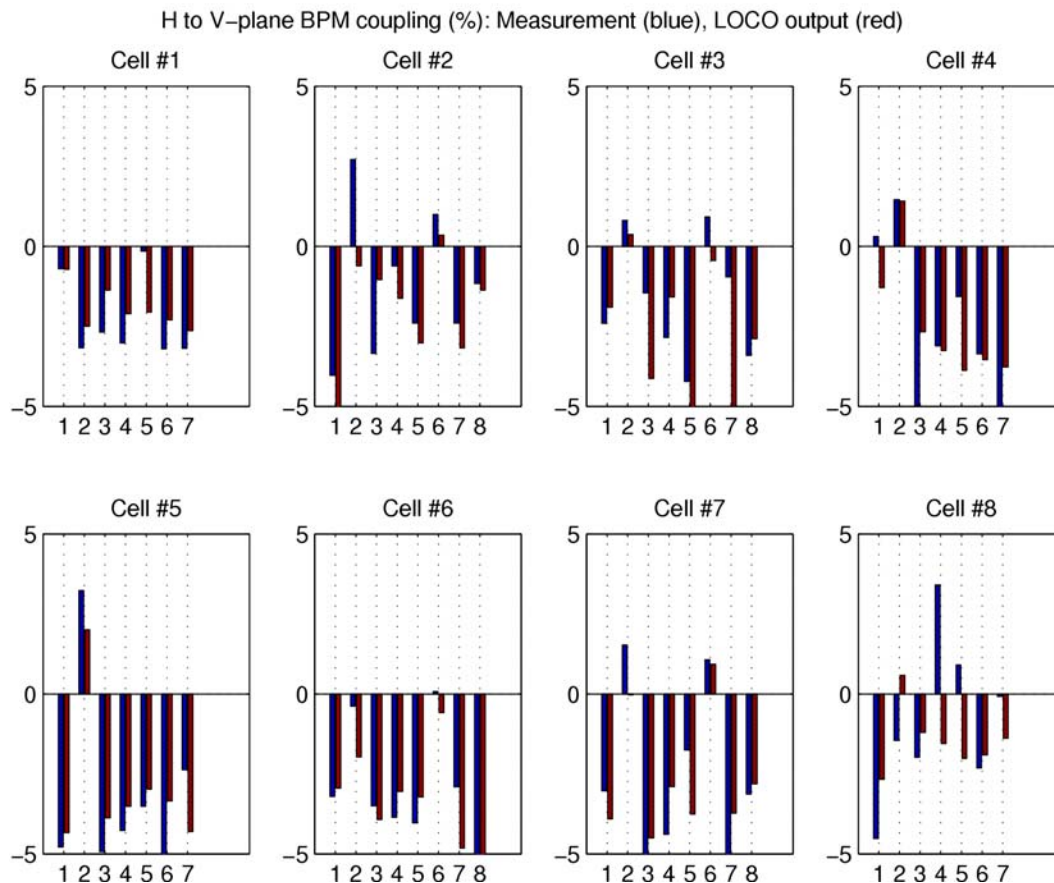
Figure 11: BPM coupling factor (cross talk of the BPM RF channels in cell 1 to 8) in percent from the horizontal plane to the vertical plane. The results from LOCO analysis (red) compare well with directly measurements done on a diagnostic bench (blue).

3.4.4   LOCO intensively used as a Diagnostics Tool

In this last section the author wishes to emphasize other useful and very valuable aspects of LOCO. Indeed the information gathered into an orbit matrix response is extremely rich and can reveal quickly problems with equipments (BPMs, orbit correctors, coupling, focusing defects). A few of them are listed thereafter, using real life cases encountered during the first year of operation of SOLEIL.

1. After each shut-down period an orbit response matrix is measured (15 min) and analyzed (5min). It enables us to quickly identify problems with BPMs, correctors and even quadrupoles. Frequently some BPMs and correctors are disconnected for maintenance or installation of new equipments. This is done either within the storage ring tunnel or within the technical gallery where racks house their electronics. With a total of 120 BPMs and 112 correctors the probability to get every component without errors is not fully zero. Hopefully using a good methodology and cable labelling following the nomenclature defined for the control, error level is very low.

2. BPM and corrector inversions have been observed using LOCO and fixed within minutes (several of them are housed in the same electronics racks).
3. Recently 4 BPMs have been identified with the wrong longitudinal position in the lattice model. These errors of a few centimetres have been seen only by looking at residual errors when comparing measured and LOCO fitted orbit response matrices. The task was not eased by the fact that around this location, betatron and dispersion functions are very flat in both planes.
4. Analysing the corrector tilts and efficiencies, LOCO gives hints about loose connections of the cables on magnet coils.
5. As discussed earlier analysis of the BPM coupling factor gives valuable information about the cross talk of the Libera module and saves a lot of time (with a better precision) in comparison with measurements done in the laboratory.

3.4.5 Conclusions

The use of the LOCO code has been more painful than expected due to the SOLEIL lattice compactness. The introduction into the code of constraints on the quadrupole gradients gave tremendous improvements. The convergence is satisfactory, beta – beatings are reduced from 5 to below 1 % RMS in both planes. Restoring the symmetry of the lattice enhanced the performance of the storage ring.

In parallel due to the high number of insertion devices at SOLEIL, 10 already installed, 11 to come next year, a programme to compensate individual focusing term may be launch using LOCO data.

Besides improving the LOCO code performance, a next step will be to make LOCO usable directly by operators in the control room.

3.4.6 Acknowledgments

The author thanks X. Huang, J. Safranek and, J. Corbett for key discussions during a visit at SSRL in May 2007.

He is very thankful to G. Portmann for integrating the new LOCO version with constraints in the Matlab Middle Layer and many rich interactions.

Finally the author is very grateful to the SOLEIL Beam Diagnostics and Machine Physics groups for intense and very helpful discussions.

3.4.7 References

1. A. Nadji et al., "A modified lattice for SOLEIL with a larger number of straight sections", SSILS, Shanghai, September 2001.
2. D. Robin, J. Safranek, and W. Decking, "Realizing the benefits of restored periodicity in the Advanced Light Source", Phys. Rev. ST Accel. Beams 2, 044001.
3. See contribution by C. Steier in this ICFA beam dynamics newsletter.
4. P. Brunelle et al., "Magnetic Measurement Results of the Dipoles, Quadrupoles and Sextupoles of the SOLEIL Storage Ring". EPAC'06, Edinburgh, July 2006, pp. 3278-3280.
5. J. Corbett, G. Portmann, and A. Terebilo, "Accelerator Control Middle Layer", PAC'03, May 2003, Portland, pp. 2369-2371.
6. L. Nadolski et al., "Control Applications for SOLEIL Commissioning and Operation",

EPAC'06, Edinburgh, July 2006, pp. 3056-3058.

7. A. Terebilo, "Accelerator Toolbox for Matlab", SLAC-PUB8732, May 2001, http://www-ssrl.slac.standford.edu/at.

8. J. Safranek, "Experimental Determination of Storage ring Optics using Orbit Response Measurements", Nucl. Inst. And Meth. A388, 27 (1997).

9. J. Safranek, G. Portmann, A. Terebilo, and C. Steier, "Matlab-based LOCO", EPAC'02, Paris, June 2006, pp. 1184-1186.

10. See contribution by X. Huang in this ICFA beam dynamics newsletter.

3.5   LOCO at the Australian Synchrotron

Martin Spencer

Australian Synchrotron, 800 Blackburn Rd, Clayton Victoria 3168, Australia

Mail to: martin.spencer@synchrotron.vic.gov.au

3.5.1   Introduction

3.5.1.1   *Australian Synchrotron Lattice*

The Australian Synchrotron is a 3 GeV, 3rd generation facility which achieved first stored beam in July 2006 [1,2].

The ring is a double bend achromat with 14 sectors [3] (see Figures 1 and 2 and Tables 1 and 2). The corrector magnets and skew quadrupoles exist as extra windings on the sextupole magnets, with independent power supplies.

Table 1: Storage ring components

Dipoles	*28; each with a significant QD component*
Quadrupoles	28 QFAs, 28 QDAs, and 28 QFBs
Sextupoles	28 SFAs, 28 SDAs, 28 SFBs and 28 SDBs
Horizontal correctors	42 (3 in each sector)
Vertical correctors	56 (4 in each sector)
BPMs	98 (7 in each sector)
Skew quadrupoles	28

Table 2: Key lattice parameters of the Australian Synchrotron storage ring

Parameter	*Value*	
Energy	3 GeV	
Circumference	216 m	
Harmonic Number	360	
Periodicity	14	
Emittance	15.8 nmrad at 0 dispersion in the straights	
Tune	Horizontal: 13.29	Vertical: 5.216
Natural Chromaticity	Horizontal: -30	Vertical: -27
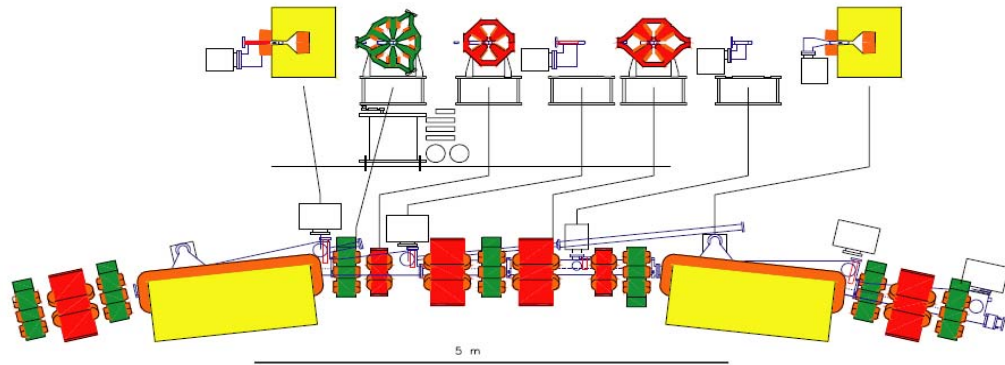
Figure 1: The Australian Synchrotron's double bend achromat arc structure. This arc section is repeated 14 times around the ring. Note that the correctors and skew quadrupoles are implemented as extra windings on the skew quadrupole magnets.
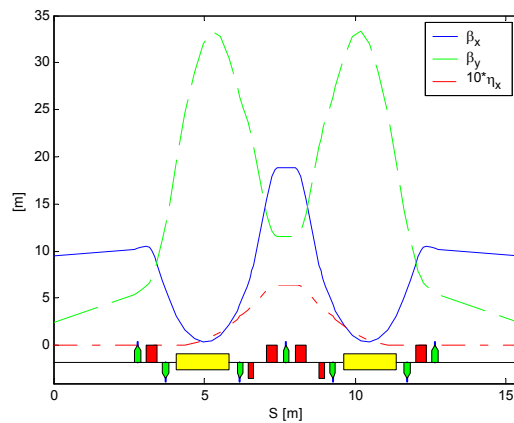
Figure 2: Model machine functions (zero dispersion in the straights).

3.5.1.2   *LOCO use at the Australian Synchrotron*

LOCO has been an extremely useful tool at the Australian Synchrotron. It is used in the following ways:

- To restore the lattice symmetry and establish the correct tune working point.
- Establish the desired dispersion.
- To predict appropriate settings for the skew quadrupole magnets, in order to reduce or increase the ring's coupling.
- To 'measure' an insertion device's contribution to horizontal and vertical focusing.
- 'Measure' the real beta functions at beamline source points.

3.5.2   Method used at the Australian Synchrotron

LOCO works by varying certain fit parameters in the model in order to minimise the difference between the model and machine's response matrices. The initial model is set up to have the desired beam qualities. The changes made to calibrate this ideal model can then be applied to the machine in reverse. Once the changes are made, the quadrupoles are cycled, and the process is repeated. We have found that this is enough to reliably optimise the machine. This approach requires that you chose fit parameters which are also easily varied in the real machine. Typically, the parameters used to calibrate the model are:

- BPM gains and coupling
- Corrector magnet gains and coupling
- Quadrupole strengths
- Skew quadrupole strengths

We include dispersion in the response matrix giving a weighting of: 10 to the horizontal and 1 to the vertical. 3 iterations of LOCO seem to always be the optimum number. After 3 iterations, very little improvement is made to the calibration of the model.

An alternative approach requires that a large range of fit parameters are chosen. In addition to those listed above, we might also choose to include:

- Quadrupole rotations and translations
- Dipole rotations and translations

An algorithm is then developed to restore the symmetry, tunes and dispersion of the model. These same changes can then be applied to the machine. This method has yet to be attempted in full at the Australian Synchrotron.

3.5.3   BPMs and Correctors

3.5.3.1   *Gains*

The LOCO calibrated model shows a 4% variation in the BPM gains (Figure 3). This is most likely caused by differences in the electrical characteristics of the BPM buttons and cables.
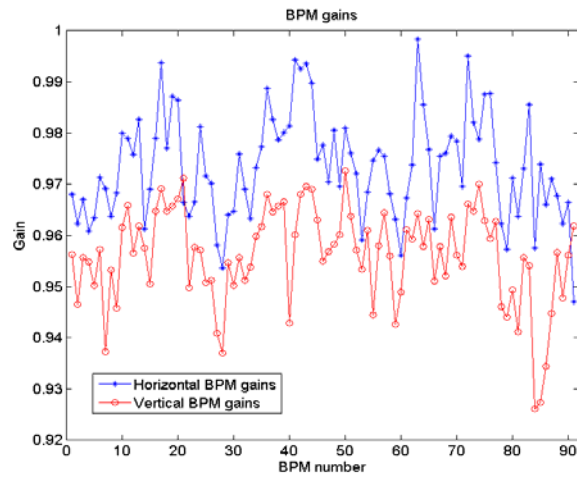
Figure 3: BPM gains

There is a 1-2% variation in the horizontal corrector magnet strengths, and a 3-4% variation in the vertical magnet strengths (Figure 4). The regular pattern seen in the corrector gains might be due to regular errors in the longitudinal positions of the correctors in the model. The remaining small variation could be attributed to irregularities in the sextupole windings or differences in the power supplies.
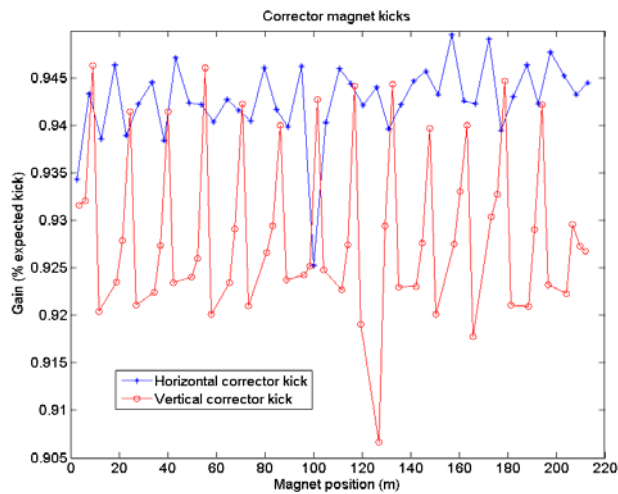
Figure 4: Corrector magnet kicks as a fraction of the intended kick.

3.5.3.2 *Coupling*

LOCO gives two coupling values for each BPM block (Figure 5). These are measured as the fraction of pure vertical movement seen as horizontal movement, and vice-versa; 'x-coupling' and 'y-coupling'.
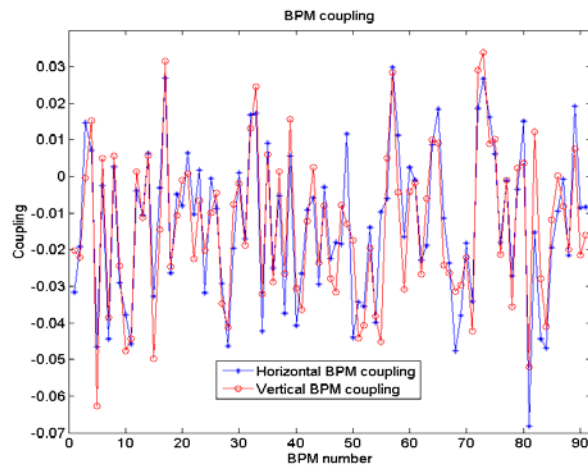
Figure 5: BPM coupling.

The BPM coupling appears to be less than 4% on average but up to 6% in some cases. It was confirmed that the block itself is not rotated by this much. Measurements of the cable attenuation showed that the coupling is indeed due to electronics [4]. If the coupling was due to BPM block rotation then the ratio of the two coupling values (x and y) should be -1.

Figure 6 shows that the corrector magnet coupling peaks at 1.5% but averages less than 0.5%. These values may be attributable to geometric variations in the corrector magnets (which exist as windings on the sextupole magnets).
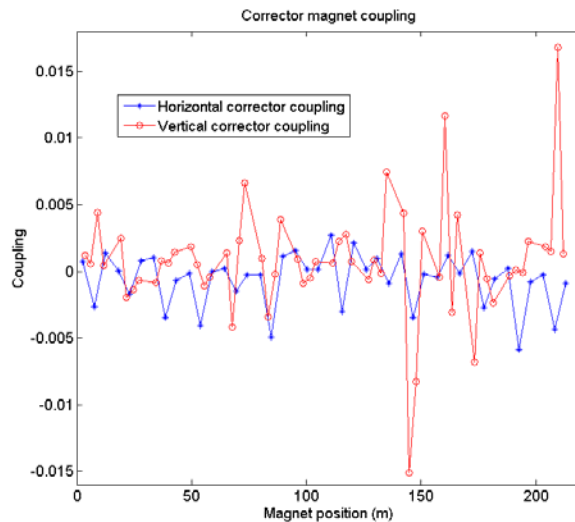
Figure 6: Corrector coupling.

3.5.4   Quadrupole Strengths, Tunes, Beta Functions and Dispersion

The beta functions of the calibrated model of the uncorrected machine show a significant level of beta beating; around 10% horizontally and 25% vertically (Figure 7).
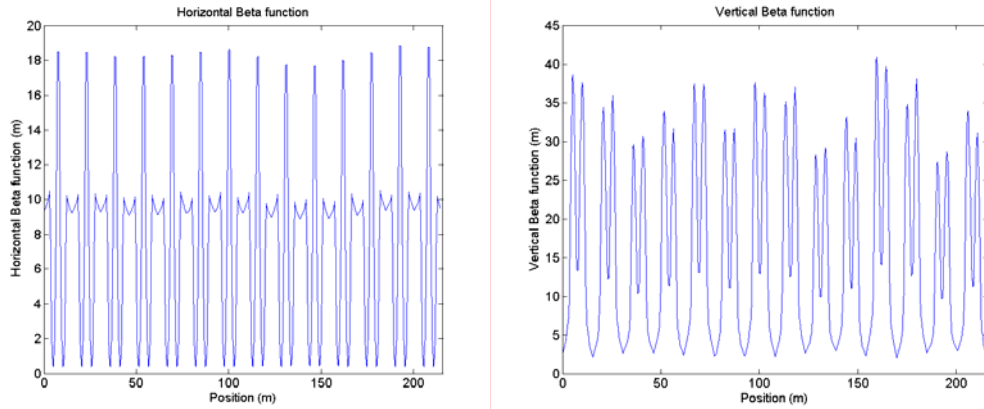
Figure 7: Beta functions of the calibrated model before the machine is corrected.

The quadrupole changes used to calibrate the ideal model are applied in reverse to the machine. These changes lead to the settings shown in Figure 8. It was possible to apply these changes while retaining stored beam. It is intended in the future to pair QFBs as single fit parameters to avoid the splitting seen in the 3rd graph of Figure 8.
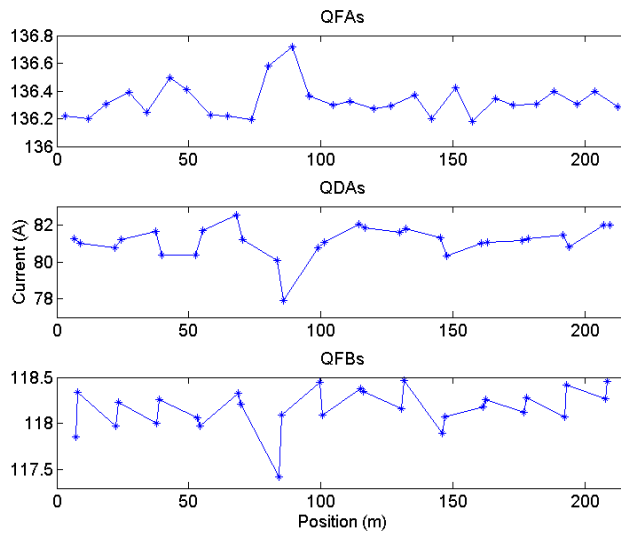
Figure 8: Quadrupole settings used to restore symmetry to the machine.

A new calibrated model is created from the corrected machine with the settings shown in Figure 8 and this model shows very low beta beating; 0.5% horizontally and 0.3% vertically (Figure 9).
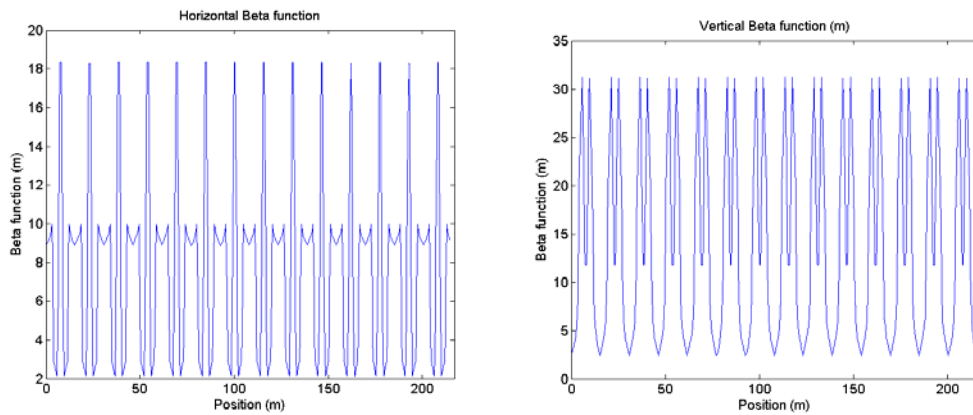
Figure 9: Beta functions of the calibrated model after the corrections shown in Figure 8.

By beginning with a model with distributed dispersion it was possible to establish a corresponding lattice in the real machine. Figure 10 shows the dispersion measurement made.
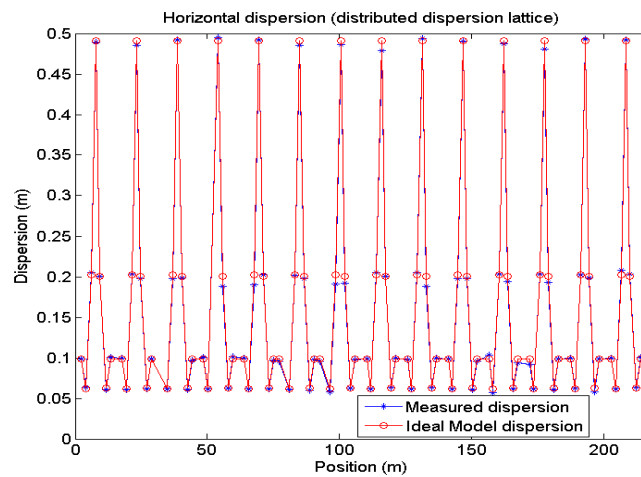
Figure 10: Dispersion measurement of the corrected lattice.

3.5.5 Emittance Coupling and Skew Quadrupoles

Figure 11 shows the settings for the skew quadrupoles that LOCO predicts will remove all coupling from the lattice. The coupling of the calibrated model was calculated for a number of difference skew quadrupole configurations (Table 2).
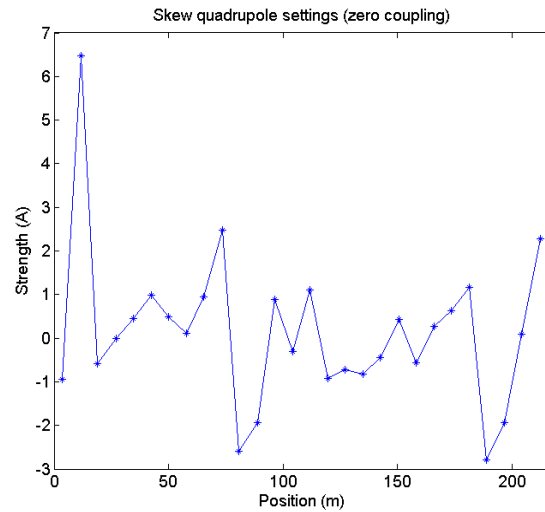
Figure 11: Skew quadrupole settings predicted by LOCO to remove coupling.

The coupling of the lattice is measured by using a model which includes a number of non-existent (or ghost) skew quadrupoles. The ghost skew quadrupoles are included to ensure that the calibrated model reflects as much as possible of the coupling of the real machine [5]. This lattice is calibrated to the machine, and the coupling of this calibrated model is calculated. Table 3 shows the effect of adding more ghost skew quadrupoles on the calculated coupling. As more skew quadrupoles were added, the emittance coupling began to increase and converge to its final value.

Table 3: Coupling achieved using LOCO predicted skew set-points. Note that the settings used for the skew quadrupoles to reduce the coupling to 0 are by no means optimised.

Conditions	Emittance coupling calculated from a calibrated model with only real skew quadrupoles. (vertical emittance)	Measurement calculated from a calibrated model with 'ghost' quadrupoles in all quadrupole and sextupole magnets. (vertical emittance)
Natural (skews at 0A)	0.19% (20 pm rads)	-
Skews set for 0 coupling	0.018% (1.9 pm rads)	0.043% (4.3 pm rads)
Skews set to opposite of 0 coupling	0.74% (78 pm rads)	-
Skews at their maximum (5A) same direction as natural coupling.	1.8% (190 pm rads)	-

3.5.6   Insertion Device Compensation

A wiggler was installed in December 2006 (Table 4) [6].

Table 4: Wiggler parameters

Parameter	Value
Length	2 m
Field Strength	1.9 T
Periods	20
Width	77 mm
Operating gaps	14 mm, 18.16mm

The tune effects of this wiggler are shown in Figure 12. As the gap was closed from 200mm to 14mm beta beating increased to 5% horizontally, and 10% vertically. LOCO was used to determine the horizontal and vertical field strength of the wiggler.
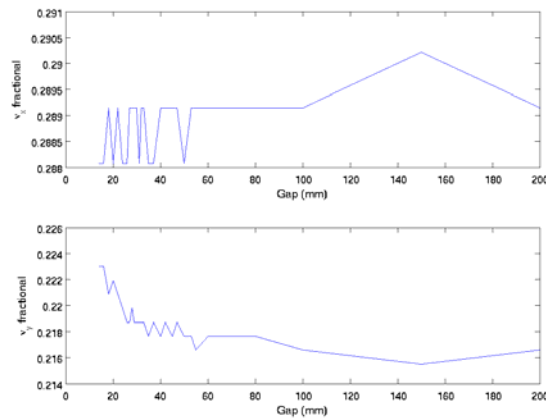
Figure 12: Tunes as a function of wiggler gap.

To measure the k_x and k_y of the wiggler [7], a calibrated model was created with the wiggler open at 200 mm. This model was then used as the starting point for a new calibrated model with the wiggler at the operating point. A simple 4×4 matrix was used to model the wiggler and the focusing elements of this matrix were used as the fit parameters for the LOCO calculation. Table 5 shows the values found.

Table 5: k_x and k_y of the wiggler at the working points.

Wiggler gap	k_x, and k_y (m^{-1})
18.16 mm	5.7×10^{-4} and -2.4×10^{-2}
14 mm	1.1×10^{-3} and -2.9×10^{-2}

These values can then be included in an ideal model. A fitting algorithm was then developed to calculate adjustments to the neighbouring QF and QD magnets to restore the symmetry of the ring, and global corrections to restore the tunes. This compensation returned the tunes to normal and removed the beta beating.

3.5.7 Singular Value Selection

Some time has been spent on the method to select singular values. Initial applications of the calibrated model solutions did not converge. It was found that this

was due to too many singular values. Plots were created for Chi and parameter family standard deviation as a function of singular value selection (see Figure 13).
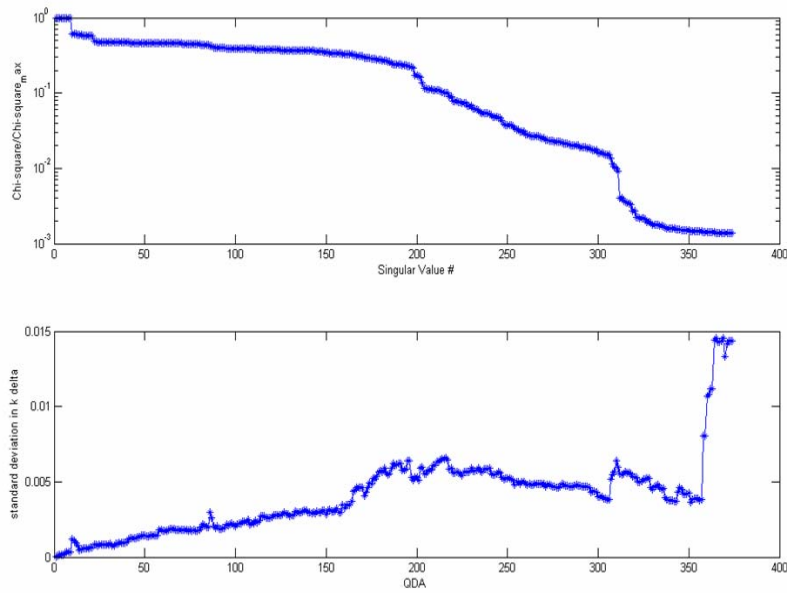
Figure 13: Chi and QFA family standard deviation as a function of singular values selection.

The top plot in Figure 13 shows that the Chi value does not reduce significantly after 350 singular values, therefore any singular value above this point may be chosen and an equally 'good' solution will be found. However, the second graph shows that the standard deviation of the QDA family dramatically increases after 358 singular values. Since we know that this will lead to a worse ring symmetry, the number of singular values used should be somewhere between 350 and 358. Graphs of the mean of a particular parameter family as a function of singular value selection show that there is often also an optimum singular value associated with the mean value.

3.5.8   Conclusions and Future work

LOCO has been a powerful tool during the commissioning of the Australian Synchrotron. It has been used to:

- Correct the beta functions.
- Control the dispersion.
- Calculate optics compensation for insertion devices.
- Correct the coupling.
- Analyse the coupling present in the BPMs.
- Accurately model the tune.

In the future it is intended to:

- Attempt to gang the central QF magnets to prevent divergence in their strengths.

- Model all magnet rotations and translations including the dipole magnet (which includes its quadrupole component).
- Completely calibrate a model with all possible fit parameters to be used as a base model for future LOCO runs.
- Investigate possible methods of singular value selection and how it relates to divergence in the fit parameter families.
- Investigate an improvement of the coupling correction in order to minimise the coupling.
- Attempt to measure the x and y translations of the sextupole magnets by measuring their quadrupole contribution.

3.5.9 References

1. G. LeBlanc, "Status of the Australian Synchrotron Project", proceedings of the 2007 Asia Particle Accelerator Conference, Indore, India, (2007).
2. A. Jackson, "The Australian Synchrotron Project", proceedings of the 2007 Particle Accelerator Conference, Albuquerque, New Mexico (2007).
3. J.W. Boldeman, D. Einfeld, "The physics design of the Australian synchrotron storage ring", Nuclear Instruments and Methods, 521 (2004), 306-307.
4. Y.E. Tan, "Storage Ring Turn-By-Turn BPMs At The Australian Synchrotron", proceedings of the 2007 Particle Accelerator Conference, Albuquerque, New Mexico (2007).
5. private communication, James Safranek (SLAC)
6. J. Kulesza, E. Johnson, D. Waterman, A. Deyhim, C. Glover, "Development of a 100 mm period hybrid wiggler for the Australian Synchrotron Project", proceedings of the 2007 Particle Accelerator Conference, Albuquerque, New Mexico (2007).
7. G. LeBlanc, E. Wallen, "Evaluation of the MAX-Wiggler", Nuclear Instruments and Methods, 521 (2004), 530-537.

3.6 Linear Lattice Calibration for Frequency Map Analysis and Low Emittance Tuning using Orbit Response Matrix Analysis at the ALS[*]

Christoph Steier
LBNL, 1 Cyclotron Road, MS80R0114, Berkeley, CA94720, USA
Mail to: CSteier@lbl.gov

3.6.1 Introduction

Orbit response matrix analysis is being used extensively at the Advanced Light Source [1] since more than 10 years. Over the years, many different version of LOCO were used as the analysis tool and several code improvements were developed at the ALS. The initial application was to troubleshoot linear lattice errors leading to the discovery of scaling errors of the current regulation shunts of the individual quadrupole power supplies at the ALS [2, 3]. The results of the analysis allowed restoring the lattice symmetry, resulting in significantly improved injection efficiency.

A faster algorithm to calculate (in linear approximation) coupled orbit response matrices was implemented in 2000, allowing for the first time to analyze a complete (i.e. including the information of all corrector magnets and all beam position monitors) coupled orbit response matrix for a machine of the size of the ALS within a reasonable time [4].

This article describes two applications of orbit response matrix analysis at the ALS: The first is to calibrate the linear, coupled machine model, which allows accurate prediction of the nonlinear dynamics properties of storage rings. Frequency map analysis [5] is used as a tool to evaluate the quality of the nonlinear machine model. The first experimental frequency maps were measured at the ALS [6] – a technique now widely used at high performance storage rings. The second is to use the result of the analysis of coupled orbit response matrices to allow highly precise correction of coupling and dispersion errors, resulting in ultrasmall vertical emittances [7], as well as excellent control of local coupling and tailored vertical dispersion [8, 9].

Nowadays, orbit response matrix analysis is used regularly every 2-4 weeks at the ALS to restore the lattice symmetry and keep the complex vertical dispersion bump for the femtosecond slicing experiment optimized [9]. If one waits more than 4 weeks between lattice corrections, a measurable decrease in performance is observed (smaller injection efficiency, slightly reduced dynamic momentum aperture and particularly a larger sensitivity of the vertical emittance to the variation of undulator gaps/fields), which is caused by small long term drifts of the orbit in sextupoles as well as small power supply drifts.

3.6.1.1 *The Advanced Light Source*

The Advanced Light Source (ALS) [2] located at Lawrence Berkeley National Laboratory is one of the first 3rd generation light sources and has been in operation since 1993. It has pioneered many techniques to optimize storage ring performance and the Matlab Middle Layer Software as well as the Matlab version of LOCO developed in an ALS/SPEAR collaboration is now widely used at many other light sources worldwide. The ALS currently has more than 40 simultaneously operating user beamlines and is serving more than 2200 user per year. It was originally optimized for the VUV and soft x-ray part of the spectrum, but by now it is serving users all the way from the IR part of the spectrum to hard x-rays (up to about 40 keV).

3.6.2 Calibrating the Linear Lattice Model for Nonlinear Dynamics Studies

To understand the dynamics in an accelerator it is essential to have a good model representing its realistic lattice. The main method used at the ALS to calibrate the linear (coupled) accelerator model is the analysis of orbit response matrices. One can combine this method with frequency map techniques, both in tracking and experiments at the accelerator. Comparing the results of simulated and measured frequency maps shows how accurately the accelerator model describes the nonlinear beam dynamics. In addition measured frequency maps can serve as a model independent tool to evaluate the quality of a lattice. The measurements at the ALS clearly show the network of coupling resonances and the agreement with the simulation using the calibrated model is very good whereas the disagreement is large when using an ideal accelerator model.

Orbit response matrix analysis at the ALS allows the determination of all gradients (quadrupoles and due offsets in sextupoles) with a relative accuracy of much better than

10^{-3}. In addition one gets relative gain factors of all correctors and all beam position monitors. The β-beating after a correction, based on the results of the model fitting, is small; about 0.5% rms. Since 2000 LOCO is also used to calculate a complete, fully coupled machine model within reasonable computation time. This allows the determination of localized coupling terms.

3.6.2.1   *Frequency Map Analysis*

Resonances can lead to irregular and chaotic behavior for the orbits of particles, which eventually will get lost by diffusion to high amplitudes. To calculate the strength of a resonance usually a tracking code is employed, which numerically simulates the evolution of beam particles. The dynamics of the resulting 4-dimensional symplectic return map can be analyzed using Frequency Map Analysis (FMA) [5]. The FMA numerically constructs a map from the space of initial conditions to the frequency space. For each selected initial condition the particle motion is tracked numerically, and the trajectory is recorded turn by turn. Then a numerical algorithm based on a refined Fourier technique (NAFF) is used to search for a quasiperiodic solution. If the trajectory is regular, the KAM theorem requires that the motion is quasiperiodic, with two fundamental frequencies ν_x, ν_y. In this case, the frequencies can be determined with very high accuracy since the algorithm converges like N^{-4}.

3.6.2.2   *Ideal Lattice versus Calibrated Machine Model*

Frequency maps provide a clear and intuitive view of the global dynamics of the complete phase space of the system. This can be seen in Fig. 1 (left) where a frequency map for a grid of initial conditions (equidistant in betatron amplitudes) with tracking over 1000 turns is shown. This is about 1/20th of the damping time due to synchrotron radiation which has been ignored in the computations. In the lattice model the chromaticity (like in the real machine) is adjusted to be slightly positive using the two families of sextupoles. Besides the sextupoles, the lattice used for the calculation was ideal with a perfect 12-fold periodicity and a working point of 14.25, and 8.18. Due to the detuning with amplitude the betatron tunes change for particles with non-zero amplitudes. Initial conditions with only horizontal or only vertical amplitude correspond respectively to the lower-right and upper-left envelope of the plot. The lines appearing in the figure are resonances which show up as distortion of the frequency map. In addition chaotic zones appear corresponding to non-regular behavior of the frequency map. The color code is indicating the diffusion rate as defined by the change in betatron tune per revolution on a logarithmic scale.
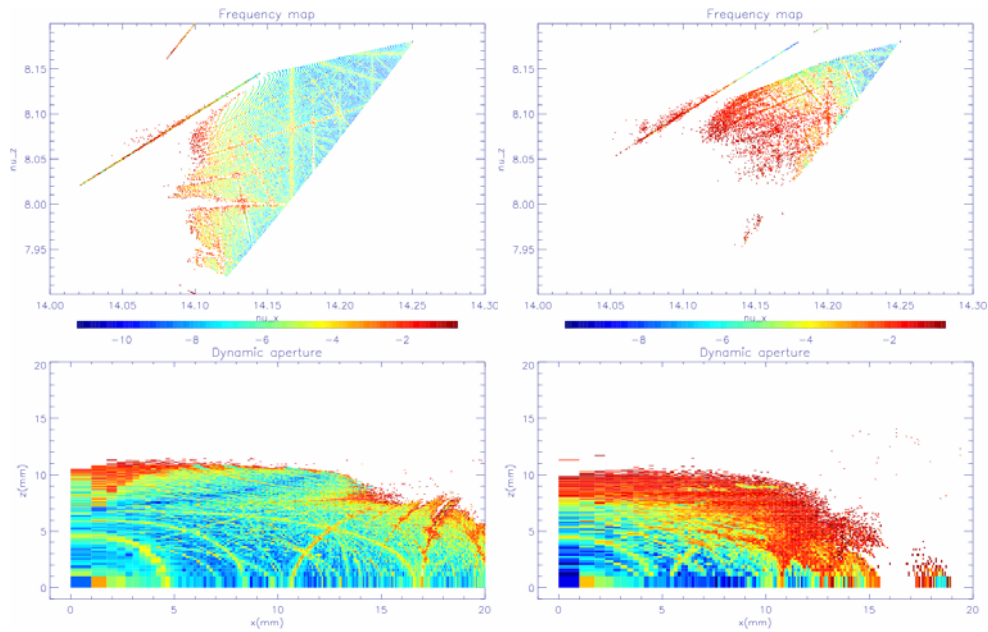
Figure 1: Frequency map of the ALS for an ideal lattice (left) and a realistic, measured lattice with small gradient and skew gradient errors (right).

The errors of the real machine reduce the size of the regular region by destroying the 12-fold periodicity and exciting additional resonances. Fig. 1 (right) shows a frequency map, where fitted linear (gradient and coupling) errors have been included in the model. The stable region in this case is significantly reduced in comparison with the ideal lattice. In addition the loss mechanisms are very different. In the ideal case particle loss is very fast (a few turns) and happens on high order, allowed resonances. For the calibrated model the loss is a slow diffusion (some thousand turns) on (intersections of) lower order resonances.

In order to determine, whether any of those two models represents the nonlinear dynamics of the ALS correctly, a measurement of a frequency map was carried out providing a picture of the global dynamics of the real beam [6].

3.6.2.3   *Measured Frequency Maps*

Two tools were used to perform the measurements at the ALS. First, there is a set of two single turn (600 ns) kickers (`pinger magnets'). Together, both pinger magnets are able to launch the beam simultaneously to variable horizontal and vertical amplitudes. The second tool is turn-by-turn beam position monitors (BPM). During an experiment, the ring is filled with a train of 40 consecutive electron bunches (to get better resolution of the BPMs). The total current is 10 mA ($4*10^{10}$ electrons). During each run, two sets of measurements are taken. First, an orbit response matrix is measured to calibrate the linear model. Then a set of turn-by-turn data is recorded for the frequency map. In order to obtain a regularly distributed image, the horizontal and vertical pinger strengths are set such that the squares of those strengths are evenly spaced.

For the first experiment we selected tunes and chromaticities close to the nominal conditions for user operation. The linear lattice was measured and adjusted to make it as

close to 12-fold periodic as possible (0.5% rms β-beating, <1% emittance ratio). The frequency analysis was performed with 25 by 25 initial conditions, compare Fig. 3 (a). One clearly sees two strongly excited coupling resonances of 5th order which are 'unallowed' for 12-fold periodicity and do not show up in a calculated frequency map for the ideal lattice. They are excited by small remaining gradient and coupling errors. This shows that the ideal lattice is not a good representation of the real machine. Moreover we found that a lattice model with random errors also did not agree well.

In order to check our calibrated lattice model, we calculated a frequency map based on the orbit response matrix data from the same day, see Fig. 2 (b). The agreement of the two frequency maps is excellent. We therefore conclude that in the case of the ALS, a model using nominal sextupole strengths and calibrated gradient and coupling errors is describing the nonlinear dynamics very accurately.
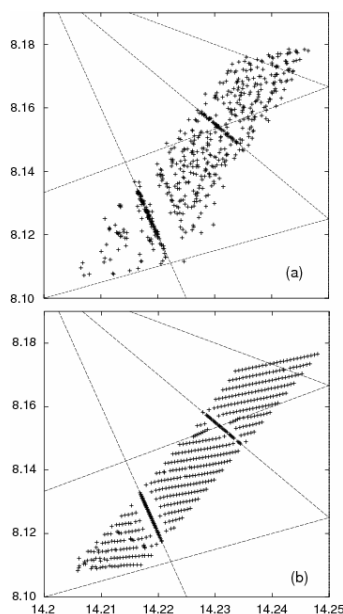
Figure 2: Experimental frequency map (a), and numerical simulation (b) for the ALS with its nominal settings. Resonances of order ≤5 are plotted with dashed lines.

Orbit response matrix analysis is now used as the standard tool at the ALS, to calibrate the linear, coupled machine model, whenever nonlinear dynamics calculations are carried out. The results are accurate enough, that the dynamic momentum aperture for every lattice point around the ring can be calculated quantitatively, allowing a prediction of the Touschek lifetime with an error of a few percent.

3.6.3   Low Emittance Tuning

For synchrotron light sources and for damping rings of linear colliders it is important to be able to minimze the vertical emittance and to correct the spurious vertical dispersion. This allows to maximize the brightness and/or the luminosity. A commonly used tool to measure the skew error distribution is the analysis of orbit response matrices using codes like LOCO. The following subsection describes results using the Matlab version of LOCO [10], which was developed in 2002 in a

SPEAR/ALS collaboration. To correct local and global coupling as well as spurious vertical dispersion, 18 individual skew quadrupoles were used which are distributed over the 12 arcs of the ALS.

3.6.3.1   *Simulation of Emittance Correction*

A number of simulations were performed to find the smallest number of individual skew quadrupoles which still allows an effective emittance correction, as well as good lattice locations for those skew quadrupoles and finally to find an optimum correction algorithm. The result was that 12 skew quadrupoles (one in each sector) would be sufficient, six of them located at high dispersion points and six of them at lower dispersion points with a larger product of horizontal and vertical beta-functions. In the simulations many different minimization algorithms were used, but it turned out, that orbit response matrix analysis to fit an effective skew quadrupole distribution gave already very good results and was much simpler than other optimization algorithms. It has the advantage of requiring very few iterations. It also is perfectly suited to be used with measurement data on the real machine. Further simulations were used to optimize the parameters of LOCO like the weight factor of the dispersion function, the outlier rejection tolerance, and the number of singular values. Fig. 3 (left) shows the results of one of those simulation runs for 100 random seeds of misaligned machines. In this particular case it was possible to correct the vertical emittance below 5 pm for 25% of the error seeds. Fig. 3 (right) shows how the average final emittance after correction depends on the weight factor of the dispersion in the response matrix analysis.
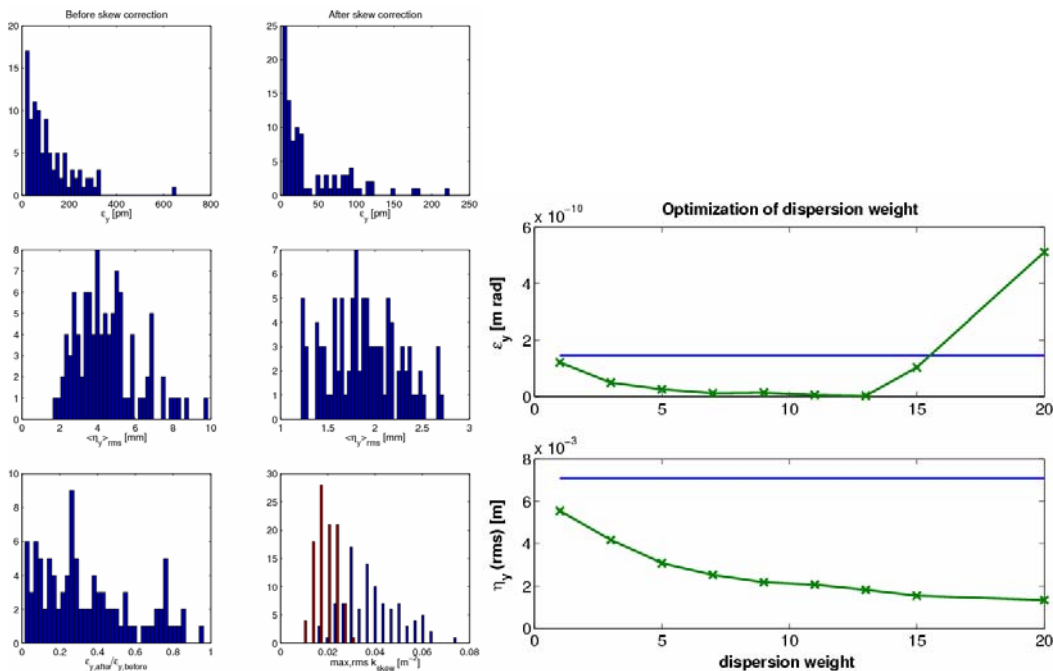
Figure 3: Histograms showing the results of simulated vertical emittance and dispersion correction for 100 randomly misaligned error seeds (left). Dependence of the final emittance and spurious vertical dispersion on the weight factor for the dispersion in the orbit response matrix analysis (right).

3.6.3.2 *Emittance Measurements*

Because of the resolution limit even of x-ray beamlines it is quite difficult to measure emittances in the few pm range accurately. The primary beamline to measure emittances at the ALS uses an imaging optics with a KB-mirror pair, carbon filters to select the x-ray wavelength (1.5 keV) and to attenuate, a BGO crystal to convert to visible light and a microscope with CCD. Even though the fundamental resolution limit would allow a direct measurement of emittances of a few pm, aberrations of the optics create a larger limit. Therefore we used three somewhat indirect but independent methods to measure the very small vertical emittances:

The first method was to determine the resolution of the beamline using Touschek lifetime measurements for various beamsizes (see Fig. 4). We then corrected the beamsize measurements for the beamline resolution to deduct the real vertical emittance. The second method was based on the analysis of an orbit response matrix, using a large number of skew gradient error fit parameters. With the calibrated machine model one can then calculate the vertical emittance using a lattice code. The final method used a scan of the RF-acceptance while measuring the Touschek lifetime. For low RF amplitudes, the Touschek lifetime is strictly proportional to the bunch volume. Therefore one can deduct a very small emittance from a beamsize measurement at moderate coupling.
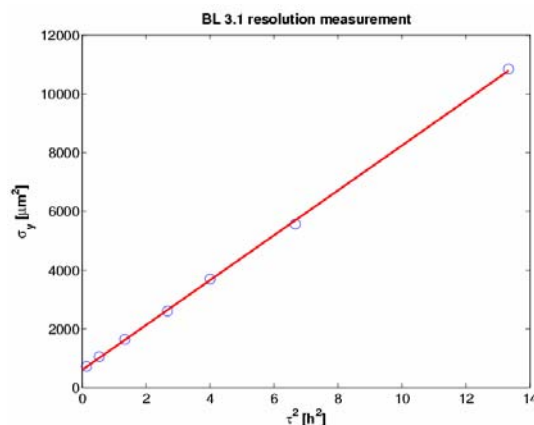
Figure 4: Resolution measurement of the ALS diagnostic beamline using Touschek lifetime measurements in a regime where the momentum aperture is fully determined by the RF bucket height.

All three methods gave consistent results. In the best case, the measured vertical emittance as determined by the three methods was 4-7 pm, corresponding to an emittance ratio of less than 0.1% at 1.9 GeV (natural emittance is 6.75 nm). Fig. 5 shows an example of the change in beamsize and local tilt angle in one iteration of the emittance correction. The mean value of the emittance measurements of about 5 pm at that time in 2002 was a world record for vertical emittances in electron/positron storage rings. Since than a slightly smaller vertical emittance of about 4 pm has been achieved at the ATF, however for a much smaller horizontal emittance and therefore significantly larger emittance ratio [11]. It is interesting to note that emittances this small are within one order of magnitude of the theoretical limit due to the finite opening angle of the synchrotron radiation emission.
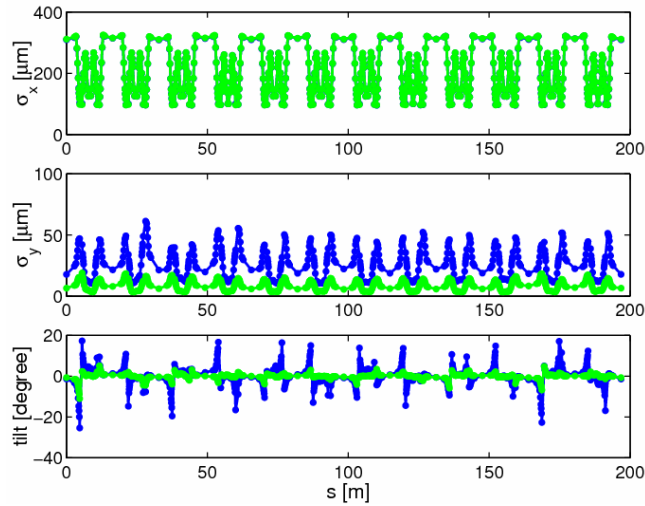
Figure 5: Horizontal/vertical beamsize and beam tilt as calculated from calibrated machine model using orbit response matrix analysis. The blue case is before coupling correction, the green one after one iteration.

3.6.3.3   Vertical Beamsize/Emittance Control

In light sources it is often necessary, to control (increase) the vertical emittance to achieve a better compromise between brightness and Touschek lifetime, or to actively stabilize the vertical bemsize/emittance. Historically at the ALS a controlled excitation of the nearby linear coupling resonance has been used to increase the vertical beamsize. After installing individual skew quadrupoles in 2002, we switched to a different scheme. The emittance and vertical dispersion is corrected and then 12-20 skew quadrupoles are used such as to introduce a global vertical dispersion wave, without introducing coupling. In that case, the vertical emittance is generated directly via quantum excitation. The local emittance ratio around the ring can be made fairly flat and all local tilt angles are small.

The main advantages of this method are a better beamsize stability (especially for scanning undulators/wigglers), better dynamic (momentum) aperture and less sensitivity of the momentum aperture to the vertical physical aperture. An example of the improvement in longtime beamsize stability can be seen in Fig. 6.
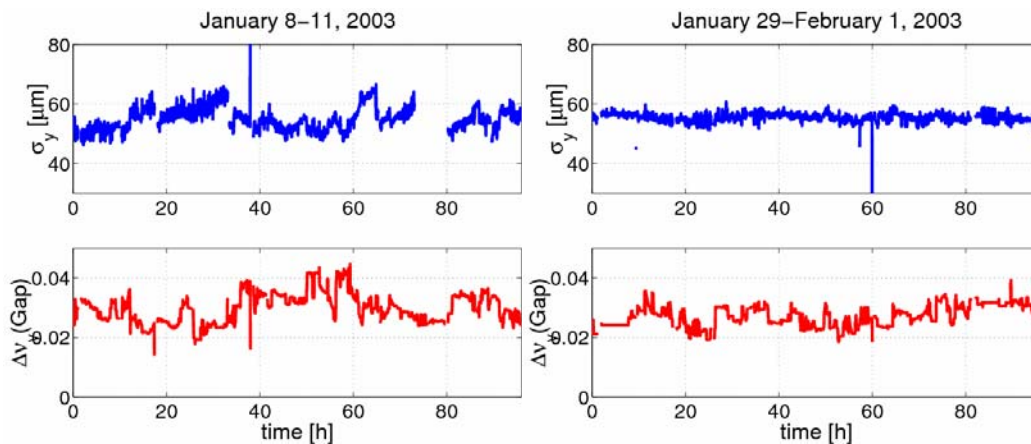
Figure 6: Vertical beamsize for two four day periods. Using a global vertical dispersion wave to increase the vertical emittance (right) leads to much better beamsize stability than excitation of the coupling resonance (left).

3.6.3.4   *Single Particle Beam Dynamics at Small Coupling*

Since the lifetime at all (low energy) third generation light sources is (strongly) Touschek limited, the momentum aperture of the ring is very important [12]. For top-off operation, injection efficiency becomes very important as well (i.e. on-energy dynamic aperture). For most light sources the dominant factor for the momentum aperture is the transverse single particle dynamics and in most cases the particles are lost on the narrowest vertical apertures. Therefore it is important to understand and optimize the dependence of the momentum aperture on the vertical physical aperture.

We found that for the current ALS lattice the dependence of the momentum aperture (lifetime) on the vertical physical aperture became much weaker both for the case with corrected vertical emittance and the case with vertical dispersion wave, compared to the case with artificially excited coupling resonance (compare Fig. 7). Based on this and some other lattice improvements it was possible to reduce insertion device gaps from 8-9 mm to now a little over 5 mm.
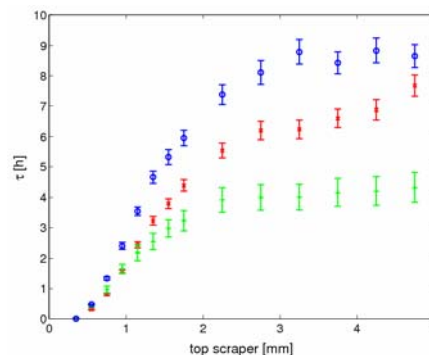
Figure 7: Measured lifetime of the ALS versus half aperture in one straight for three different cases: excited coupling resonance (red), corrected coupling and vertical dispersion (green), vertical dispersion wave (blue). The two cases with excited coupling resonance and dispersion wave were measured for identical vertical emittance.

Simulating the effects in tracking, we found good agreement between measurements and simulations. The simulations showed that a correction of the coupling reduces the sensistivity of the dynamic momentum aperture to the vertical physical aperture (see Fig. 8).
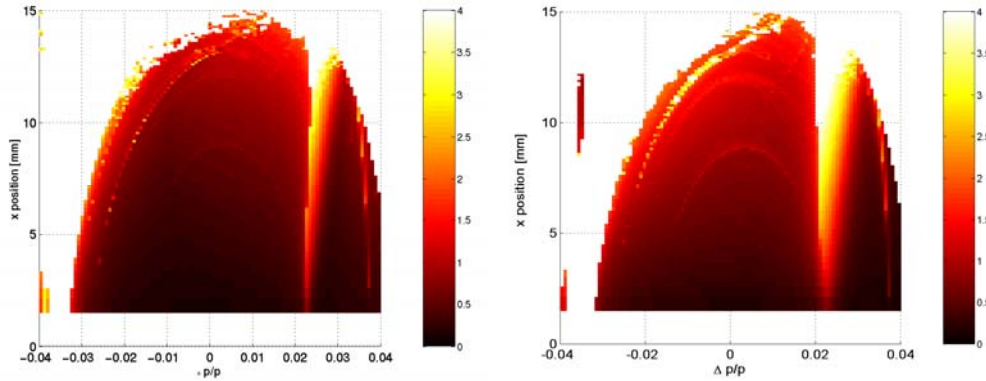
Figure 8: Maximum vertical oscillation amplitude reached by particles tracked for 10000 turns versus initial energy offset and horizontal oscillation amplitude (without synchrotron oscillations). The emittance ratio is about 2% in both cases. The left picture shows a case where the vertical emittance is dominated by dispersion (and betatron coupling is very small), whereas on the right the vertical emittance is dominated by coupling.

3.6.4   Conclusion

Orbit response matrix analysis has been used since over ten years at the ALS, allowing a predictive optimization of the storage ring performance, as well a precise calibration of the lattice model, which is essential to allow accurate prediction of nonlinear dynamics properties. Quantitative calculations of the dynamic (momentum) aperture based on the calibrated machine models agree extremely well with measurable quantities like Touschek lifetime and injection efficiency.

Response matrix analysis at the ALS has become an indispensable tool and is used every 2-4 weeks in routine machine setups. This enables the use of a very complex vertical dispersion and coupling bump for the femtosecond slicing experiment. Emittance correction and emittance control allow significant improvements in brightness, while at the same time improving the (beamsize) stability for experimenters.

3.6.5   Acknowledgements

3.6.6   References

1.   "1-2 GeV Synchrotron Radiation Source Conceptual Design Report", LBNL PUB-5172

Rev. (1986)

2. D. Robin, J. Safranek, and W. Decking, *Phys. Rev. STAB*, Vol. 2, 044001 (1999).

3. D. Robin, C. Steier, J. Safranek, W. Decking, "Enhanced Performance of the Advanced Light Source through Periodicity Restoration of the Linear Lattice", Proceedings of EPAC 2000, Vienna, Austria, p. 136 (2000)

4. C. Steier, D. Robin, "Fully Coupled Analysis of Orbit Response Matrizes at the ALS", Proceedings of EPAC 2000, Vienna, Austria, p. 1080 (2000)

5. Dumas, H. S., Laskar, J., "Global Dynamics and Long-Time Stability in Hamiltonian Systems via Numerical Frequency Analysis", Phys. Rev. Lett. 70, 2975-2979 (1993)

6. D. Robin, C. Steier, J. Laskar, L. Nadolski, "Global dynamics of the Advanced Light Source revealed through experimental frequency map analysis", Phys. Rev. Lett., 85, 3, 558 (2000)

7. C. Steier, et al., " Coupling Correction and Beam Dynamics at Ultralow Vertical Emittance in the ALS", Proceedings of PAC 2003, Portland, OR, p. 3213, (2003)

8. C Steier, et al., "Successful Completion of the Femtosecond Slicing Upgrade at the ALS", Proceedings of PAC 2007, Albuquerque, NM, p. 1194, (2007)

9. C. Steier, et al., "Accelerator Physics Challenges of the fs-slicing Upgrade at the ALS", Proceedings of PAC 2003, Portland, OR, p. 397, (2003)

10. J. Safranek, G. Portmann, C. Steier, "MATLAB-based LOCO", Proceedings of EPAC 2002, Paris, France, p. 1184, (2002)

11. Y. Honda, et al., "Achievement of Ultralow Emittance Beam in the Accelerator Test Facility Damping Ring", Phys. Rev. Lett. **92**, 054802 (2004)

12. C. Steier, et al., "Measuring and Optimizing the Momentum Aperture in a Particle Accelerator", Phys. Rev. E 65, 056506 (2002)

3.7 Transverse Impedance Distribution Measurements using the Response Matrix Fit Method at APS

V. Sajaev, Argonne National Laboratory, Argonne, IL 60439 USA
Mail to: sajaev@aps.anl.gov

3.7.1 Introduction

The Advanced Photon Source (APS) is a third-generation synchrotron light source based on a 7-GeV electron storage ring. In third-generation light sources the synchrotron radiation is mainly produced in undulators. In order to achieve high photon flux and tunability, the magnet gap in undulators has to be as small as possible. Therefore, the undulators are installed on dedicated small-gap insertion device (ID) vacuum chambers.

APS has thirty-five 5-m-long straight sections available for undulators. At the time of the measurements, there were 31 straight sections occupied with various insertion devices, and 4 straight sections were still empty. Most of the ID vacuum chambers have a 8-mm in-vacuum gap, and two chambers have a 5-mm gap. These narrow-gap vacuum chambers are believed to be the main source of the transverse impedance of the machine.

One can measure the combined impedance by measuring the transverse tune slope with single-bunch current. Comparing this slope before and after installation of the narrow-gap vacuum chamber, one can deduce the impedance of the chamber [1]. It is difficult to accurately measure the change in the tune slope after one or a few new ID

chambers are installed. If several identical ID vacuum chambers are installed over a period of time, then one can estimate the contribution of one ID chamber.

Over the last few years there have been a number of attempts to measure the impedance of separate components of accelerators. Phase-advance measurements from beam position monitor (BPM) turn-by-turn histories were used at LEP [2] to measure the impedance distribution around the ring. Researches at LEP were able to fit average impedance in the long sections of the LEP arc and determine the impedance of the rf sections. The method was tried at APS; however, the accuracy of the measurements was not enough to determine the small impedance of a single ID vacuum chamber. There is also a different approach that uses local orbit bumps to probe different parts of an accelerator. The orbit bump method was done at BINP [3], APS [4], and ESRF [5]. All these methods have one common feature: they employ the fact that the beam sees the impedance as an additional defocusing quadrupole whose strength depends on the beam current.

At APS we use an orbit response matrix fit to determine the distribution of focusing errors around the machine, and then use these errors to calculate beta functions [6]. Since the beam sees the impedance as a quadrupole whose strength depends on the beam current, the measurement of the beta functions with different currents could be used to determine the impedance distribution around the machine. This approach was first used at APS and reported in [7].

3.7.2 Response Matrix Analysis at APS

The APS storage ring has 40-fold symmetry. Figure 1 shows one sector of the ring and its beta functions. Each sector consists of two dipoles, ten quadrupoles, and seven sextupoles. There are also eight horizontal and eight vertical steering magnets and nine to eleven BPMs per sector. Possible focusing errors could come from quadrupole power supply miscalibrations (each quadrupole at APS has its own power supply) and from horizontal orbit errors in sextupoles, so that the total possible number of focusing errors per sector could be up to 17. Obviously, there are not enough BPMs to resolve all possible focusing errors[2], therefore we keep only quadrupoles in our model. Since the average betatron phase advance per quadrupole is only 0.18π in the horizontal plane and 0.1π in the vertical plane, we assume that the quadrupoles alone could accurately reproduce all possible focusing errors in the storage ring.

In order to limit the size of the derivative of the response matrix, we use only 40 horizontal and 40 vertical correctors and all available BPMs. In this case, the two-dimensional uncoupled response matrix contains about 32000 elements and depends on approximately 1400 variables. The overall size of the derivative in double precision is about 350 MB. The fully-coupled response matrix analysis is also performed at APS, but it is much slower due to the size of the problem, and it is not relevant for this work.

---

[2] Smaller storage rings like the NSLS X-ray ring or ALS at BNL can inject electron beam with sextupoles turned off. This allows them to separate focusing errors produced by quadrupoles and sextupoles. The APS storage ring has larger natural chromaticity and is not able to store beam without sextupoles.
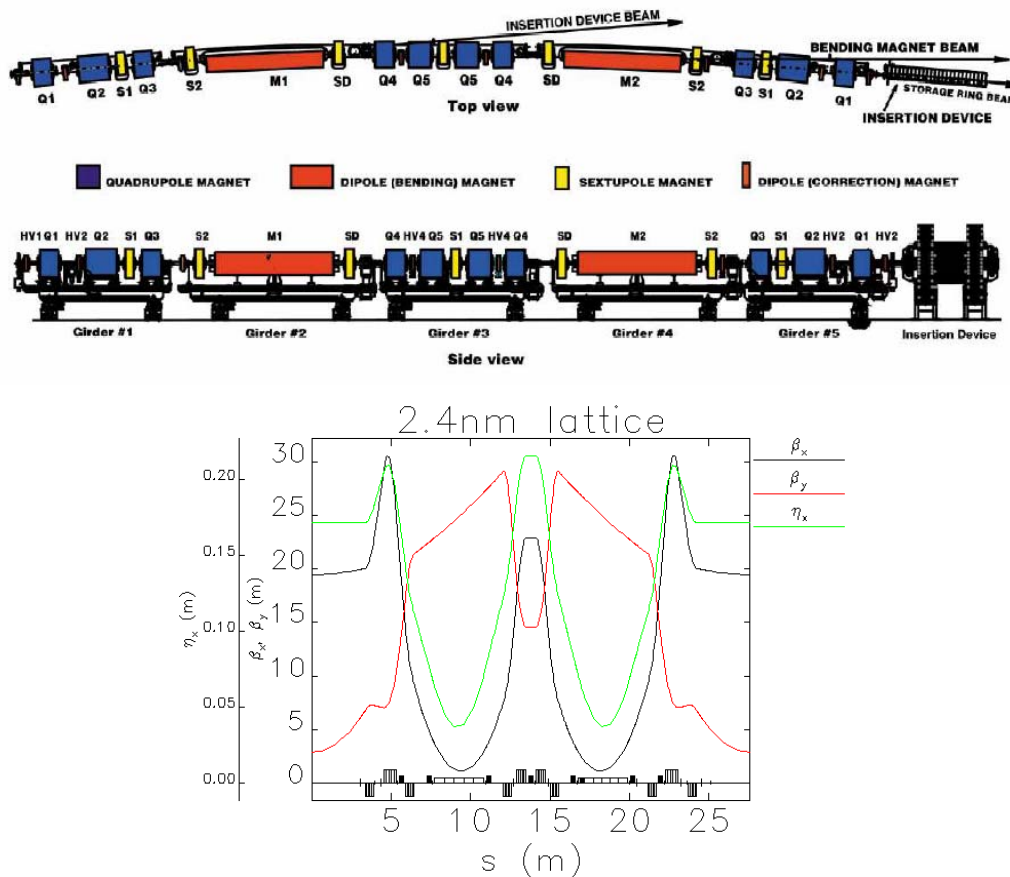
Figure 1: Top - one sector of the APS storage ring. The storage ring consists of 40 identical cells. The insertion device where the narrow-gap vacuum chambers are located is shown at the right side of the picture. Bottom – beta functions of one sector.

The response matrix fitting program is written in Tcl/Tk. It uses `elegant` [8] for all accelerator-related calculations and the SDDS Toolkit [8] for data processing. It has a convenient graphical user interface that allows the user to choose any element for fitting (quadrupoles, correctors, BPMs) and a lot of fitting parameters and files. The output of the program is a file of fitted variables in the format of the "parameter" file of `elegant`. This file is used to update the ideal `elegant` model of the storage ring. Before the fitting, a typical rms difference between the ideal model and the measured orbit distortions is about 30 μm. After the fit is done, the rms difference is decreased to the noise level of the BPMs, which is about 1 μm. In order to achieve such accuracy, we had to include BPM nonlinearities into the fitting process. This was done by introducing an additional cubic term fitting of the BPM residual errors.

The updated model can be used for all kinds of calculations in `elegant`, including calculation of the β-function around the ring. Although the accuracy of beta function determination is difficult to determine due to the method's complexity, it can be estimated by taking several measurements and comparing the results. The rms

difference between beta functions derived from different response matrix measurements was found to be about 0.3%.

3.7.3   Measurements

Vacuum chambers of the APS storage ring are made of aluminum, which minimizes the impedance, and have an elliptic 85x42 mm size. When an undulator is installed, the vacuum chamber at that location is replaced with a small-gap chamber. Most of the APS insertion devices have 8-mm-gap vacuum chambers, and two IDs in sectors 3 and 4 had 5-mm-gap vacuum chambers at the time of the measurements (one 5-mm vacuum chamber was recently replaced with an 8-mm one). Normal and ID vacuum chambers are connected with 20-cm-long tapered transition pieces. Figure 2 represents locations of the small-gap vacuum chambers installed at the APS storage ring at the time the measurements were done. We expect the vertical impedance to be dominated by these small-gap ID vacuum chambers.
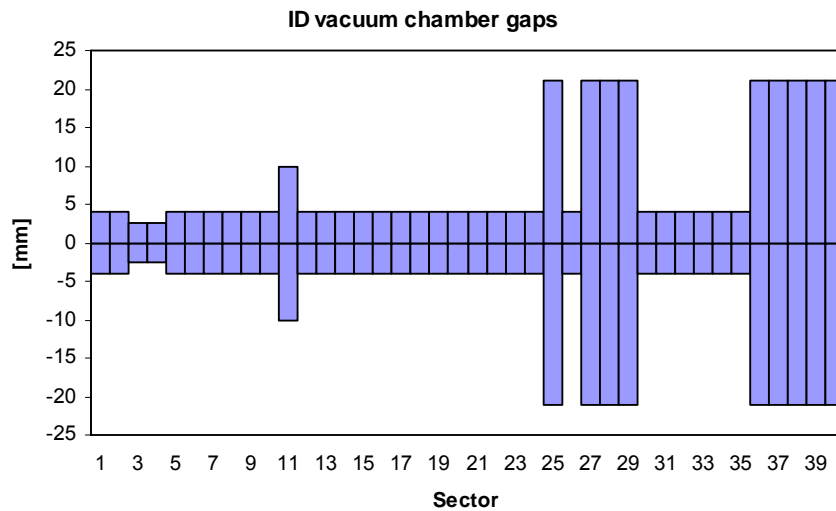
Figure 2: ID vacuum chamber gaps at the time of the measurements. Note – ID vacuum chamber in sector 11 (ID11) is made of stainless steel, while all other chambers are made of aluminum.
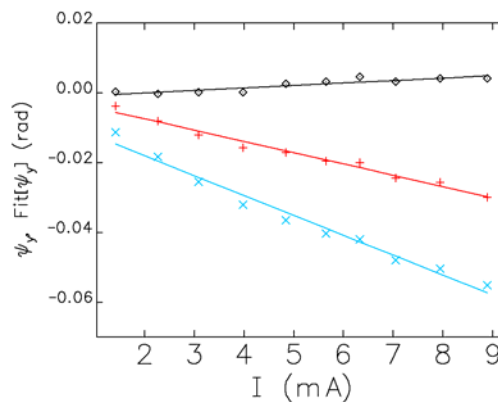
Figure 3: Example of linear fit of phase advance slope shown for several different BPMs. Constant phase offsets are removed.

In order to obtain the change of focusing around the ring with the beam intensity, we measured response matrices for different single-bunch currents and analyzed them to get beta functions and betatron phases. To achieve good measurement accuracy, the single bunch current was scanned from 10 mA down to 1 mA. After the phase advances were calculated using the response matrix fit, the linear fit was performed to get phase slope with beam current at each BPM location. Figure 3 shows examples of local vertical phase slopes and linear fits for several BPMs. Individual phase slopes were then combined into a plot of phase advance distribution along the ring, which is shown in Figure 4. One can see a sharp change in phase caused by the 5-mm chambers in sectors 3 and 4 and flat regions corresponding to no ID chamber in sectors 25 to 29 and 36 to 40. Fast oscillation of the phase-advance difference is the result of beta function mismatch, caused by changes in focusing. Figure 4 confirms our expectations that the main contribution to impedance comes from the ID vacuum chambers, since it follows the distribution of vacuum chamber gaps from Figure 2.
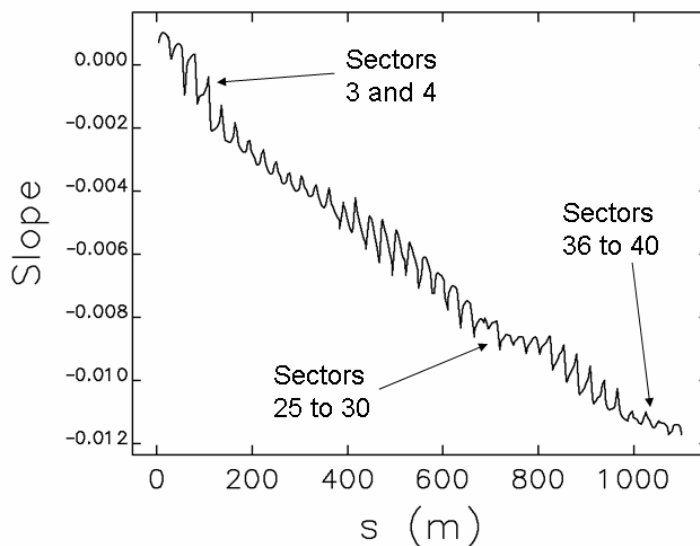
Figure 4: Betatron phase advance slope as a function of longitudinal position along the machine.

To obtain the local impedance distribution, we analyzed the phase-advance plot in Figure 4. One might ask why not use additional quadrupoles simulating impedance during response matrix fit, and then use those quadrupoles directly to calculate impedance. This was not done because in the response matrix fit we use all available quadrupoles to get as good a fit as possible. In the vertical plane this means that there are 18 quadrupoles per one betatron oscillation. Such a large number of quadrupoles provides very accurate fit of the response matrix but leads to some ambiguity in the resulting strength of quadrupoles. The ambiguity in quadrupole strength does not affect the accuracy of the betatron function and betatron phase determination, but it does not allow using individual quadrupole strengths to represent impedance effects directly during response matrix fit.

Instead of using additional quadrupoles during response matrix fit, we use additional quadrupoles to fit the phase slope curve from Figure 5 and try to minimize the number of quadrupoles used for the fit. The most obvious minimal set of quadrupoles is the set of quadrupoles located in the middle of each straight section where most of the

impedance is located (40 quadrupoles total). We had to add artificial quadrupoles in the middle of the ID straight sections and called them Q0. However, this set does not fit the measured phase slope curve satisfactorily – it can be used to reproduce the average slope but it does not fit the fast oscillations of the phase. The next guess would be to add one more quadrupole in the middle of each sector to represent the impedance of the sector outside of the ID straight section. We used existing quadrupoles that were called Q5. This quadrupole set (80 quadrupoles total) fits the phase-slope distribution nicely; the result of the fit is shown in Figure 5. The resulting quadrupole strengths are shown in Figure 6. The top plot in Figure 6 shows all quadrupoles. Points with low K1 values (every other point) correspond to quadrupoles in the middle of the sector, or Q5s, while points with higher K1 values correspond to quadrupoles in the ID straight section, or Q0s. The bottom plot in Figure 6 shows K1 values of only these stronger quadrupoles corresponding to ID vacuum chamber impedance. ID vacuum chambers from Figure 2 are also shown in this plot.
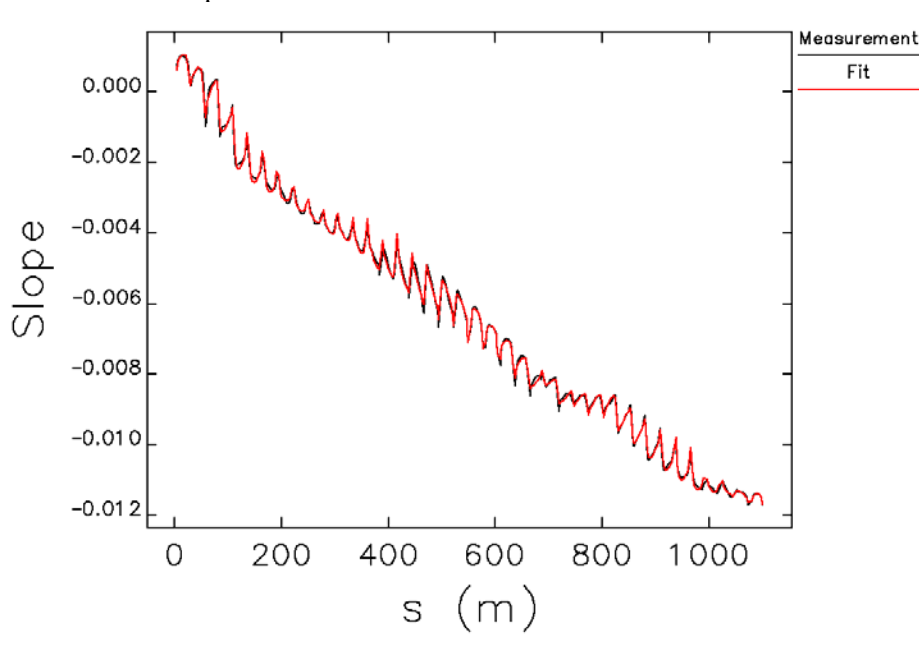
Figure 5: Betatron phase slope and its fit using two quadrupoles per sector.

3.7.4   Impedance Calculation

The effective transverse impedance is the integral over the machine impedance multiplied by the bunch spectrum squared. For a particular impedance component, it can be found from the measured slopes of the phase shift with current $d\mu/dI$ [2] that

$$Z_{eff}^i = \frac{E\sigma_s}{R\beta_i}\frac{d\mu}{dI},$$

where E is the electron energy, σ_s is the bunch length, and β_i is the beta function at the impedance location. This formula can be rewritten to substitute fitted quadrupole strengths K_1L instead of the measured phase slopes

$$Z_{eff}^{i} = \frac{1}{2} \frac{E\sigma_s}{R} \frac{\beta_q}{\beta_i} \frac{d(K_1 L)}{dI},$$

where β_q and β_i are the beta functions at the location of the artificial quadrupole and impedance, respectively.
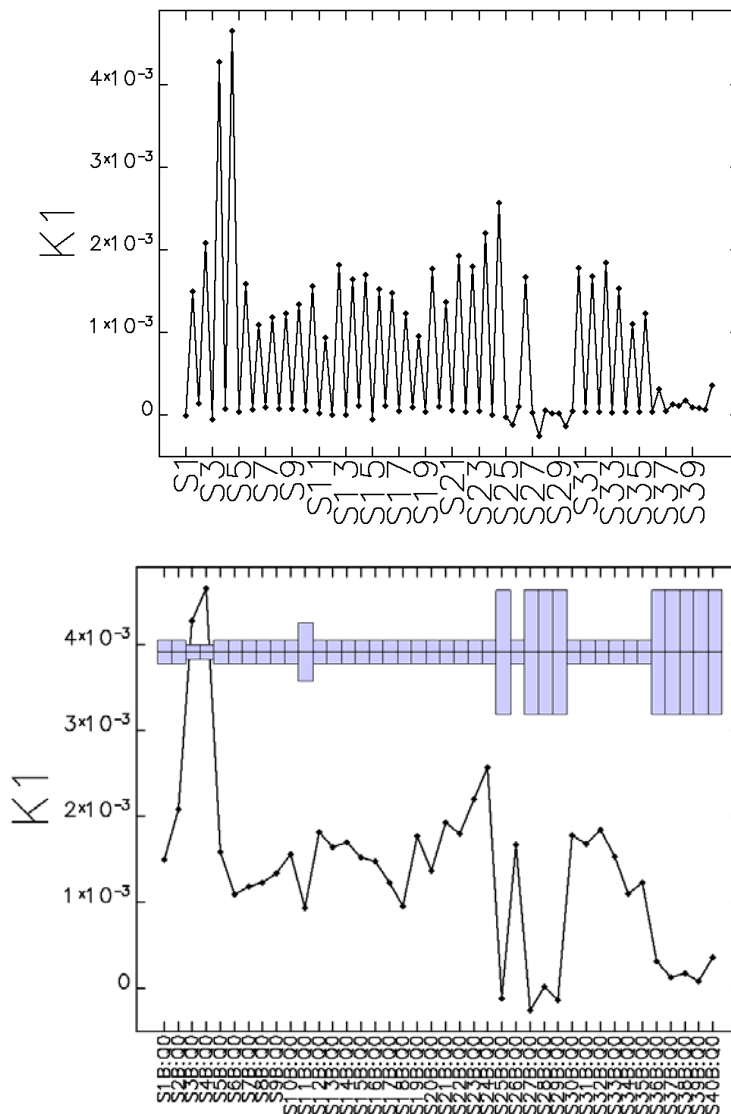
Figure 6: Top – strength of all quadrupoles obtained in the fit. Bottom – strength of Q0 quadrupoles representing ID vacuum chamber impedance together with ID vacuum chamber gaps.

The impedance beta functions have to be taken at the location of the impedance elements, which are ID straight sections for Q0 quadrupoles, and averaged over a sector for Q5 quadrupoles. The bunch length was maintained at approximately at 40 ps during measurements by varying the rf voltage. The resulting values for the various sectors as well as the total effective vertical impedances are shown in Table 1. Quadrupole strengths and impedances shown in the table are averaged over all similar sectors, i.e.,

over all Q5 quadrupoles for the impedance of a sector, all Q0 quadrupoles located at 8-mm ID vacuum chambers, etc. The accuracy of the impedance measurements is hard to evaluate, but we can look at the spread of the impedance results for 28 8-mm-gap vacuum chambers. The relative rms spread of that impedance is 23%. The impedance values of ID vacuum chambers presented in Table 1 compare well with the APS impedance database: Z_{8mm}^{eff} =28 kΩ/m, Z_{5mm}^{eff} =110 kΩ/m, and Z_{total}^{eff} =1.2 MΩ/m [10].

Table 1: Quadrupole strength slopes for different impedance elements obtained using fit of measured phase-advance slopes and corresponding impedance values.

β_y at Q0	*m*	*2.9*
β_y at Q5	m	15.0
$\langle \beta_y \rangle_{sector}$	m	16.1
$\langle \beta_y \rangle_{ID}$	m	3.6
$\langle dK_1 L/dI \rangle_{Q5}$	1/A	0.025
$\langle dK_1 L/dI \rangle_{RF}$	1/A	0.021
$\langle dK_1 L/dI \rangle_{ID11}$	1/A	0.094
$\langle dK_1 L/dI \rangle_{8mm}$	1/A	0.16
$\langle dK_1 L/dI \rangle_{5mm}$	1/A	0.45
Z_{sector}^{eff}	kΩ/m	5.7
Z_{RF}^{eff}	kΩ/m	4.0
Z_{ID11}^{eff}	kΩ/m	18
Z_{8mm}^{eff}	kΩ/m	31
Z_{5mm}^{eff}	kΩ/m	86
Z_{total}^{eff}	MΩ/m	1.3

3.7.5   Conclusion

Analysis of the measured orbit response matrix provides detailed information concerning storage ring optics. The achieved optics measurement accuracy at APS is so precise that one can see the phase advance difference due to different beam current in the vertical plane. This was used to derive the distribution of the vertical impedance around the APS storage ring. It was found that the small-gap ID vacuum chambers contribute the most to the storage ring impedance. The actual values of the impedance of the chambers with different gaps were measured.

Horizontal impedances were not measured because total horizontal effective impedance (derived from tune slope with current) was six times smaller than the vertical one, making it very difficult to achieve good accuracy of measurement in the horizontal plane.

3.7.6   Acknowledgements

The author would like to thank Steve Milton for his encouragement and support of this work and Louis Emery for tremendous help with operational and physics issues. Also, the author would like to thank Kathy Harkay and Y.-C. Chae for numerous useful discussions and H. Shang, B. Soliday, and M. Borland for help with programming.

3.7.7   References

1. K. Harkay and N. Sereno, "A Potpourri of Impedance Measurements at the Advanced Photon Source Storage Ring," Proceedings of the 1997 Particle Accelerator Conference, Vancouver, Canada, p. 1700 (1998).
2. D. Brandt et al., "Measurements of Impedance Distributions and Instability Threshold in LEP," Proceedings of the 1995 Particle Accelerator Conference, Dallas, p. 570 (1996).
3. V. Kiselev, V. Smaluk, "Measurement of Local Impedance by an orbit bump method," Nucl. Instrum. Methods A **525**, 433 (2004).
4. L. Emery, G. Decker and J. Galayda, "Local Bump Method for Measurement of Transverse Impedance of Narrow-Gap ID Chambers in Storage Rings," Proceedings of the 2001 Particle Accelerator Conference, Chicago, p.1823 (2001).
5. L. Farvacque, E. Plouviez, "Probing the Transverse Impedance of the ESRF Storage Ring," Proceedings of the 2002 European Particle Accelerator Conference, Paris, p. 1550 (2002).
6. V. Sajaev, L. Emery, "Determination and Correction of the Linear Lattice of the APS Storage Ring," Proceedings of the 2002 Particle Accelerator Conference, Paris, p. 742 (2002).
7. V. Sajaev, Transverse Impedance Distribution Measurement Using the Response Matrix Fit at APS," Proceedings of the 2003 Particle Accelerator Conference, Portland, p. 417 (2003).
8. M. Borland, "elegant: A Flexible SDDS-Compliant Code for Accelerator Simulation," APS LS-287, 2000.
9. R. Soliday, M. Borland, L. Emery, H. Shang, "New features in the SDDS Toolkit," Proceedings of the 2003 Particle Accelerator Conference, Portland, p. 3473 (2003).
10. Y.-C. Chae, "The Impedance Database and its Application to the APS Storage Ring," Proceedings of the 2003 Particle Accelerator Conference, Portland, p. 3017 (2003).

4   Activity Reports

4.1   Commissioning of the Australian Synchrotron

Greg LeBlanc, Mark Boland, Rohan Dowd, Martin Spencer, Eugene Tan
Australian Synchrotron, 800 Blackburn Road, Clayton Victoria 3168, Australia
Mail to: greg.leblanc@synchrotron.vic.gov.au

4.1.1   Introduction

The Australian Synchrotron is a 3 GeV light source that was recently commissioned at a site in the Metropolitan District of Melbourne. On July 14, 2006 less than three years after earth moving machines started to prepare the site, beam was captured,

accumulated and stored in the storage ring. Storage ring commissioning continued through March 2007, after which the facility became operational. At present, there are five operational beamlines with another four under construction.

In order to realise the relatively short project schedule with a small team, most of the systems were delivered by turn-key contracts. Contracts for the following systems included all design, engineering, project management, installation and commissioning:

- Injection system
- Storage ring RF system
- Storage ring vacuum vessels
- Beamline photon delivery systems
- Storage ring girders
- Front ends

The original schedule milestones can be seen in below.

- Design announced.   January 2003
- Building contract placed   July 2003
- Building complete   February 2005
- Staff move into building   March 2005
- Installation begins   April 2005
- Injection system commissioning begins   October 2005
- Storage ring installation complete   May 2006
- Storage ring commissioning begins   June 2006
- First turns in the storage ring   June 2006
- Beamline installation begins   September 2006
- Beamline commissioning begins   February 2007
- Transition to operations   April 2007

The major schedule milestones were all achieved within days of the target dates, including the start of accelerator installation in April 2005, the completion of installation in May 2006 and first turns in the storage ring in June 2006. This article describes the accelerator systems and presents the performance along with commissioning experiences.

4.1.2   Injection System: Linac

The Australian Synchrotron linear accelerator is very similar to the Swiss Light Source and Diamond Light Source linacs.

4.1.2.1   Layout

The 100 MeV injector linac layout is shown in Figure 1 It consists of an electron gun, a 500 MHZ sub-harmonic pre-buncher, two 3 GHz bunchers, and two 3GHz travelling wave linear accelerator sections. Diagnostics equipment is included at various locations along linac. The various components are described below.
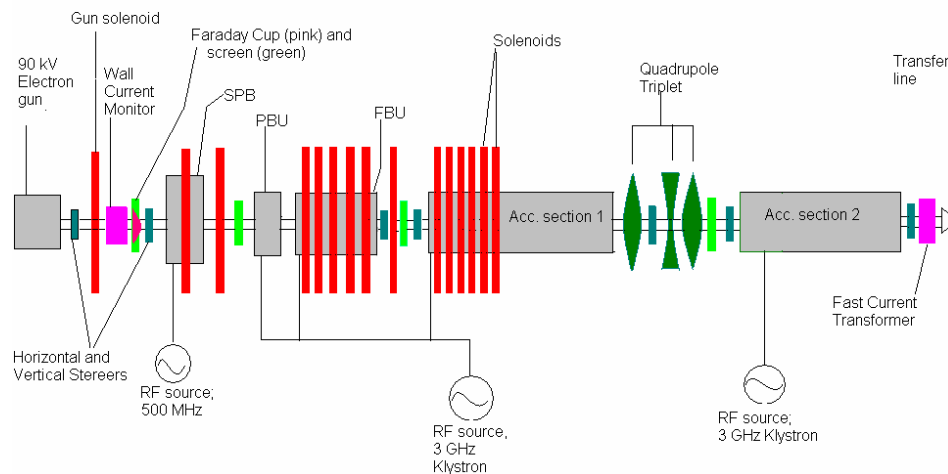
Figure 1: Linac Schematic.

4.1.2.2   Electron Gun

The electron gun is a 90 keV thermionic cathode. It can operate in Single, or Multi bunch mode, with the output charge controlled via bias voltages. In single bunch mode, a single 2 ns charge pulse is produced, designed to fit into the 500 MHz RF buckets of the booster synchrotron. In multi-bunch mode the gun bias is modulated by a 500MHz signal, which generates a train of 2ns pulses. The gun can produce pulse trains between 50 ns and 1 μs long, although due to the rise and fall times of the booster kickers, the upper limit for pulse trains is 150 ns.

4.1.2.3   Sub-harmonic Pre-buncher

The sub-harmonic pre-buncher compresses the bunches into a 500 MHz bucket to increase acceptance into the booster. It consists of a single 500 MHz standing wave cavity fed by a 500W pulsed RF source and imparts a ± 30% longitudinal energy spread along the bunch. It is followed by a bunching drift section.

4.1.2.4   Primary Bunching Unit (PBU)

The 3 GHz primary bunching unit consists of four 20 mm cells and increases the mean energy of the beam from 90 keV to approximately 300 keV. It is a travelling wave structure which operates in a $2\pi/3$ mode. As its name implies, the main bunching of the beam into 3GHz

4.1.2.5   Final Bunching Unit (FBU)

The Final Bunching Unit has sixteen 42.22mm cells and operates in the $8\pi/9$ mode at 3 GHz. While it is mainly used for β-matching, with the beam energy increased from 300 keV to 3 MeV, final bunching also takes place here.

4.1.2.6   Accelerating Structures 1 and 2

The main beam acceleration is done in two 5.2m long, 3GHz accelerating structures which take the beam energy up to 100 MeV. They operate in the 2 π/3 mode with an accelerating gradient of 11 MV/m.

4.1.2.7   MEBT

The Medium Energy Beam Transport (MEBT) is the section between the two main accelerating structures. It contains a focusing triplet, two corrector magnets and a diagnostic screen.

4.1.2.8   Diagnostics

The linac has several different types of diagnostic equipment. There are 4 fluorescent (YAG) screens positioned between each cavity section, which provide information on beam position and shape throughout the acceleration process.

Just after the electron gun there is a Faraday cup and wall current monitor. The faraday cup provides a measure of the total charge emitted from the gun. The wall current monitor (WCM) is a non-destructive measurement of the charge emitted from the gun. The Faraday cup and WCM signals can be viewed at the same time and the Faraday cup signal is used to calibrate the WCM.

A fast current transformer (FCT) is located at the end of the linac and provides another non-destructive charge measurement. Combined with the earlier WCM measurement, this allows a linac transmission measurement to be taken.

For energy spread measurements and emittance measurements, optical transmission radiation (OTR) screens are used in the Linac to Booster (LTB) transfer line. The energy spread measurements were done in a region of high dispersion, and the emittance measurements in a region where it is possible to have no dispersion.

4.1.2.9   Klystrons and Modulators

The Linac RF power is supplied by two 37 MW, pulsed, 3GHz Klystrons for the main accelerating and bunching sections. Two 500 W, pulsed, 500 MHz amplifiers supply the gun modulation and pre-buncher. The Klystron pulse lasts for 4.5 μs and is capable of a repetition rate of 50Hz, although only 1 Hz is required. The 3 GHz frequency is supplied by applying a 6 times multiplication to the master RF signal.

One klystron feeds power to the bunching sections and first accelerator section, the other feeds the second accelerating section. A series of waveguide power splitters and phase shifters allows for independent power and phase adjustments in each cavity structure.

4.1.2.10   Performance

The linac specifications and measured performance is shown in Table 1. The transmission was optimised with a parameter scan of the solenoid magnet and MEBT quadrupole strengths [1].

Table 1: Linac beam parameters

Parameter	Specification	Measured
Single Bunch Charge	>0.5 nC	> 1.5nC
Multi-bunch Charge	>5 nC	> 12nC
Transmission	40%	84%
Single Bunch Energy Spread	<0.5% rms	<0.2% rms
Multi Bunch Energy Spread	<0.5% rms	<0.5% rms
Normalised Emittance	<50 π mm mrad (both planes)	<50 π mm mrad
Energy	$\geq$100 MeV	100 MeV

4.1.3   Injection System: Booster

The booster synchrotron ring is designed to ramp the beam from the injection energy of 100 MeV up to the extraction energy of 3 GeV, providing full energy injection into the storage ring. RF power is provided by a 5 cell 500 MHz cavity with a voltage of 1.1 MV and 65 kW peak power at the top of the ramp. The main parameters for the booster are showing in Table 2. During a continuous 8 hour acceptance test the injection system delivered 3 GeV beam into the BTS at 1 Hz with 95.8% availability.

Table 2: Latest machine parameters for the booster ring.

Parameter	Unit	Value	
Energy	GeV	3	
Circumference	m	130.2	
Current (max. to date)	mA	0.6 (single)	6 (multi)
Periodicity		4	
RF Frequency	MHz	499.6715	
Harmonic Number		217	
Peak RF Voltage	MV	1.1	
Tunes (changes during ramp)		9.26 (H)	3.21 (V)
Natural Chromaticity		-8.8 (H)	-11.5 (V)
Momentum Compaction		0.0098	
Natural Energy Spread	%	0.1	
Horizontal Emittance	nm rad	30	

4.1.3.1   Lattice

The booster lattice is a FODO type ring where the main focusing and defocusing gradients are built into the combined function dipoles. For fine adjustments of the tune and chromaticity there are a small number trim quadrupoles and sextupoles. The lattice functions for one of the four super-periods are shown in Figure 2. The combined function magnets make for a compact magnetic lattice, leaving ample space in the straight sections between the super-periods for injection elements, extraction elements,

114

RF cavities and diagnostics. However, the lattice is sensitive to relative settings of the focusing bend (BF) and defocusing bend (BD) magnets and 1% changes result in tune shifts of up to 0.4 in the vertical plane and .1 in the horizontal plane. The tune walk up the ramp was measured with a triggered spectrum analyser connected to a stripline pick-up and the data is show in Figure 3. A small change in the ratio of the BF and BD at low energy pushes the tunes over the quarter integer resonance line in the horizontal and might be the cause of an instability and beam loss just prior to the start of the ramp (see Figure 5 in section 4.1.3.2). Future studies will be conducted to improve the booster, but for now it is performing satisfactorily for three injections per day.
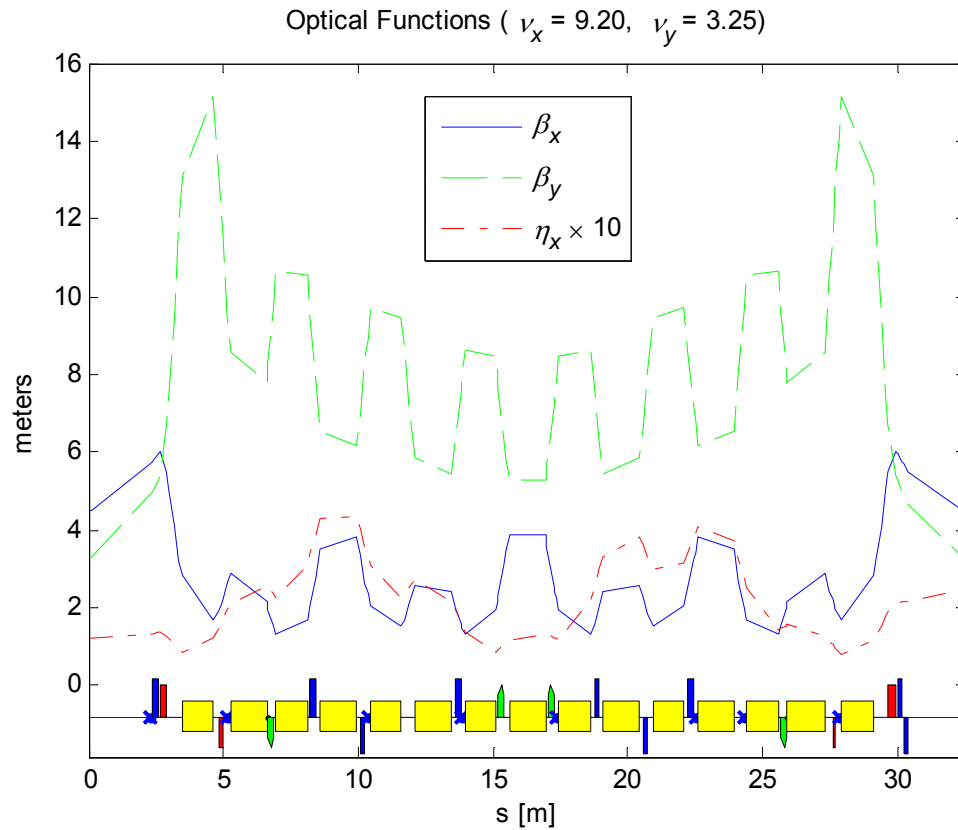
Figure 2: Booster lattice function for one of the four super-periods
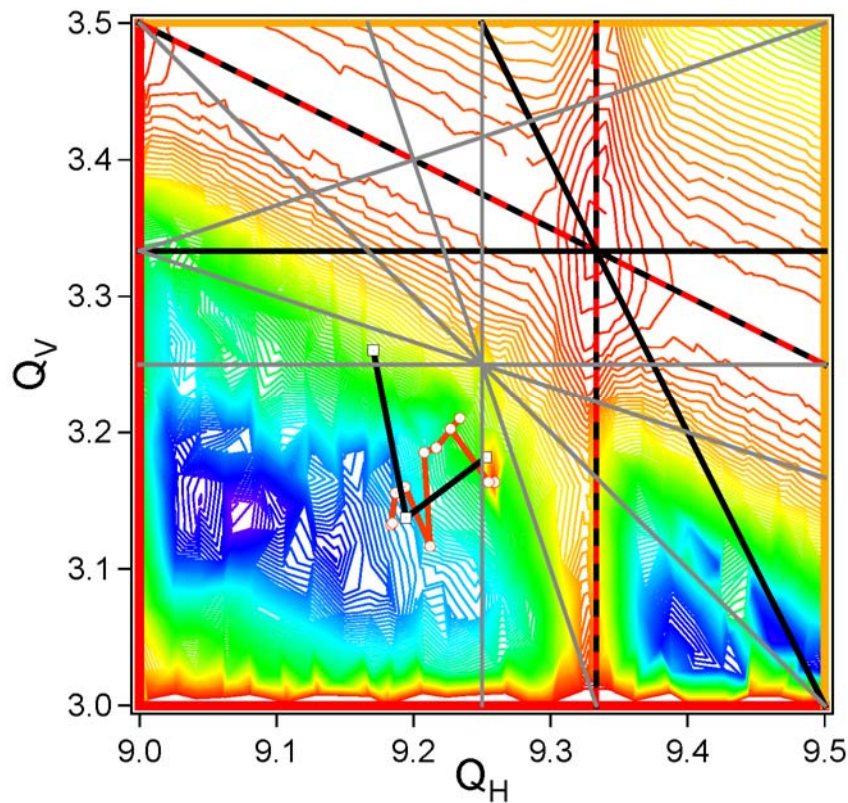
Figure 3: Booster tune walk measured during the ramp. The right most point is injection, the left most extraction. Red points – May 2006 measurement, black points – August 2006. The contours show the beam stability, red – unstable and blue – stable.

4.1.3.2   *Injection*

Bunch trains of up to 150 ns (75 bunches) are injected into the booster ring. A single turn fast injection technique is used with all elements in the same horizontal plane. A 100 MeV beam is guided into the booster with a pulsed septum and an in-vacuum kicker. The booster injection kicker pulse has a flat-top of 400 ns (see Figure 4) and a decay time of <200 ns so the field is zero when the head of the bunch train completes the first turn of the booster in 434 ns.
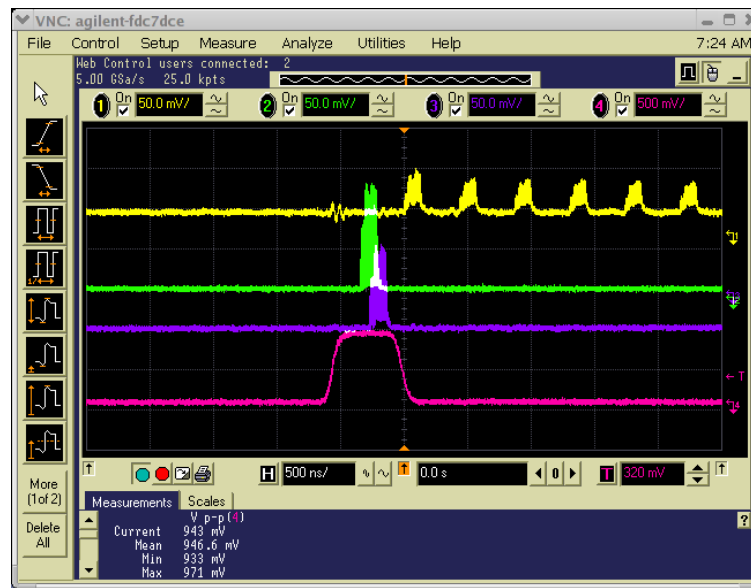
Figure 4: Booster injection kicker pulse (pink) with the current transformer pulses in multi-bunch mode: LTB FCT1 (green), LTB FCT2 (purple) and booster FCT (yellow).

4.1.3.3   Ramp

Ramping occurs at a 1 Hz repetition rate and the ramp shape is controlled by an arbitrary function generator ramp curve with flat plateaus at the injection and extraction parts of the ramp. A typical injection cycle produces 3 mA (1.3 nC) of beam extracted from the booster in multi-bunch mode (see Figure 5). When the booster is carefully tuned it can achieve 6 mA per shot in multi-bunch mode and 0.6 mA in a single shot in single bunch mode.

Figure 5: Booster ramp (red) and booster DCCT (blue) during a 1 second injection cycle.

4.1.3.4   Extraction

The extraction from the booster is via a slow-bump fast-kick technique. Three bumper magnets are slowly ramped over 23 ms to get the beam orbit close to the pulsed extraction septum. The final kick pulse has a rise time of ~250 ns (see Figure 6) which is what limits bunch train length in the booster to ~150 ns (booster orbit period 434 ns).
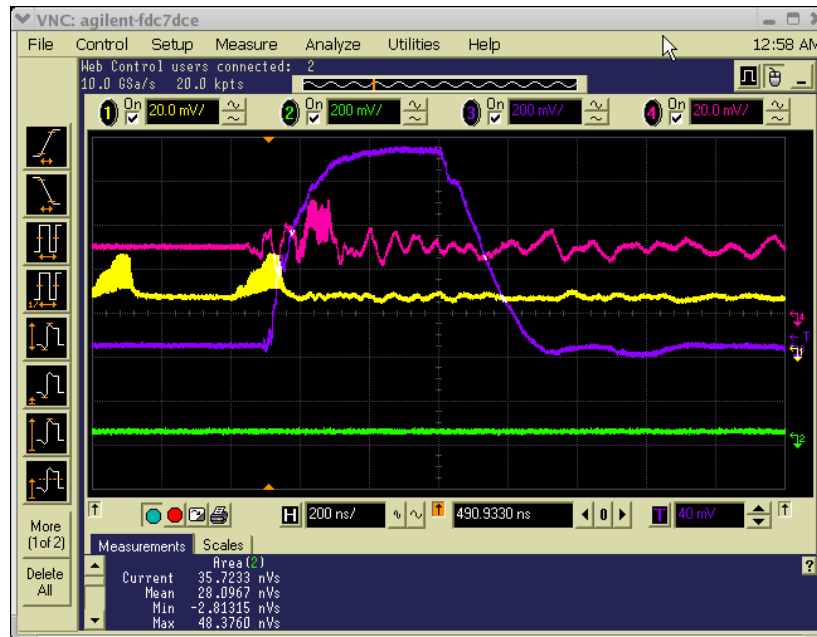
Figure 6: Booster extraction kicker pulse (purple) with the fast current transformer traces in multi-bunch mode: Booster FCT (yellow) and BTS FCT (pink).

4.1.4   Storage Ring Injection

Injection into the storage ring is achieved with a thin wall septum at the end of the booster to storage ring transfer line (BTS), and four fast in-vacuum kicker magnets in the storage ring. The kickers are deflecting magnets made to the DELTA design [2]. These were chosen for the simplicity of design and low impedance profile. They are positioned about the injection point in straight 1 (see Figure 7).

118
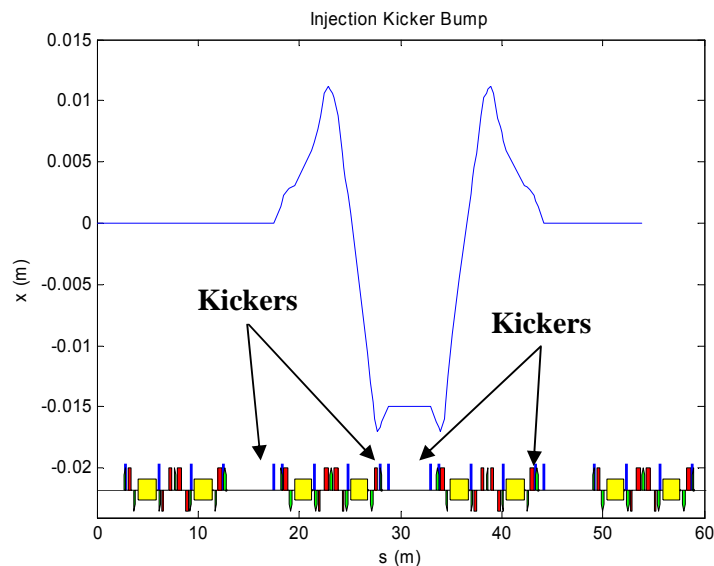
Figure 7: Injection kicker positions in the storage ring lattice.

With four kickers the position and angle of the bump can be controlled to produce a parallel orbit shift at the point of injection. Figure 7 shows the stored beam orbit at the peak of the kicker pulses. The kicker pulse is a 4.3 μs half sine wave, and is applied over five turns (storage ring orbit period is ~720.5 ns). The horizontal fractional tune is ~0.3, so by the third turn after injection the beam has to have moved back far enough to avoid colliding with the septum.

4.1.5 Storage Ring

4.1.5.1 Lattice

The Australian Synchrotron (AS) storage ring [3, 4] is a Chasman-Green type lattice with two bending magnets that are 1.726 m long gradient dipoles with a focusing strength of –0.329 m^{-2}. There are 3 families of quadrupoles (two QFs and one QD) and 4 families of sextupoles (2 sets of SDs and 2 sets of SFs). To save space the 42 horizontal and 56 vertical correctors and 28 skew quadrupoles are generated using extra coils on the sextupole magnets. All quadrupoles, sextupoles and correctors have individual power supplies. The lattice parameters are shown in Table 3 and the lattice functions in Figure 8.

The betatron tunes and dispersion can easily be controlled using the 3 families of quadrupoles. In general the middle pair of QFs has a more significant effect on the dispersion leaked into the straight sections while the outer pair of QD and QF magnets control the betatron tunes.

Chromaticity correction is generally achieved by using the pair of SF and SD magnets between the dipoles where the dispersion is the highest. For larger chromaticities the SF and SD sextupoles generate geometric aberrations that can be compensated for (albeit not perfectly) by using the outer SF and SD "harmonic" sextupoles. Some studies on the optimal settings for the "harmonic" sextupoles were

done prior to commissioning and are reviewed in the next section on frequency map analysis. The reason for the relatively large vertical chromaticity will be discussed in later sections on beam instabilities.

Table 3: Latest machine parameters for the storage ring

Parameter	Unit	Value		
Energy	GeV	3		
Circumference	m	215.9925		
Current	mA	200		
Periodicity		14		
RF Frequency	MHz	499.6715		
Harmonic Number		360		
Peak RF Voltage	MV	3		
Radiation Loss	keV	932		
Tunes		13.29 (H)	5.216 (V)	0.011 (S)
Nominal Chromaticity		2 (H)	6 (V)	
Natural Chromaticity		–28 (H)	–27 (V)	
Momentum Compaction		2×10^{-3}		
Natural Energy Spread	%	0.1		
Horizontal Emittance	nm rad	16		
Critical Photon Energy	keV	7.8		
Bunch Length	ps	23		
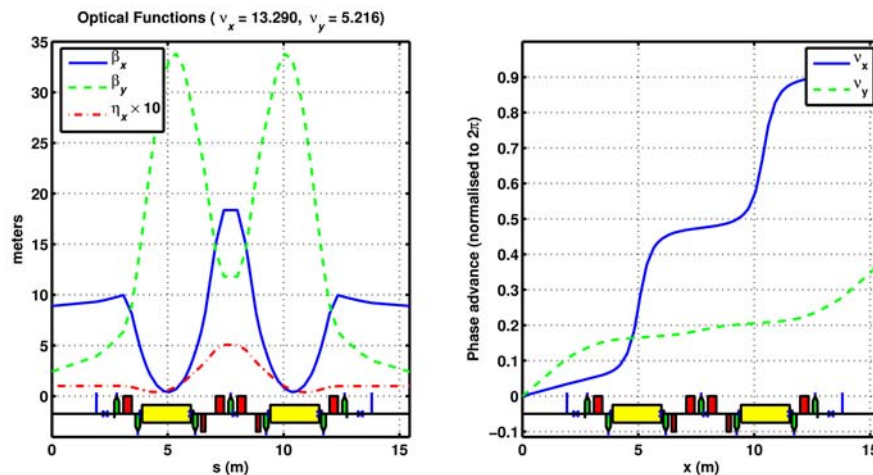
Figure 8: Lattice functions (left) and phase advance (right) per cell. The magnet arrangement is schematically shown at the bottom of the plots; dipoles (yellow rectangle), quadrupoles (red rectangles), sextupoles (green pentagram), correctors/kickers (vertical lines), BPMs (crosses).

The above emittance value is for the standard achromatic lattice, i.e. zero dispersion in the straight sections. By introducing distributed dispersion (dispersion in the straight sections) the emittance can be reduced to as low as 7 nmrad. In general the smaller the emittance the smaller the beam size and hence a higher photon flux. However due to the

increased dispersion coupled with the natural energy spread, the reduction of the emittance past ~10 nmrad does not result in further reductions in the beam size. Figure 9 below shows the minimum effective emittance and beam size to be around 0.14 m. For this reason the nominal user lattice was tuned to 0.1 m distributed dispersion. For commissioning the zero dispersion lattice was used.

Our large periodicity means that many of the lower order resonances are effectively suppressed and therefore we are relatively insensitive to tune changes. To preserve the symmetry and create a calibrated model we use LOCO (Linear Optics Closed Orbits). LOCO was also used in a number of other areas during commissioning [5].
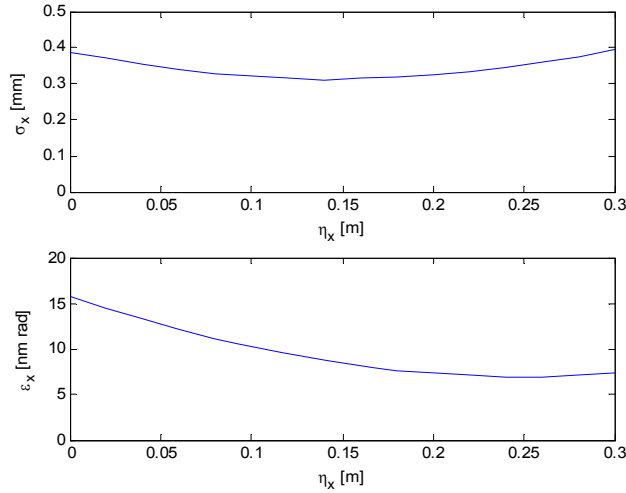
Figure 9: Variation of the electron beam size and emittance with dispersion in the straight sections.

4.1.5.2   *Frequency Map Analysis*

When designing storage rings for light sources, beam stability and a long lifetime is important. To achieve these requires a large acceptance. To ensure the acceptance is optimised, the dynamic aperture of the lattice should be studied. The dynamic aperture is simply the physical limits, horizontal and vertical, within which the particles have stable orbits. One method of analysing the dynamic aperture is through the use of Frequency Map Analysis (FMA). This technique was applied to understand the resonances that affect the aperture and how the "harmonic" sextupoles can be used to enlarge the dynamic aperture [6].

The theoretical basis of frequency maps comes from the Kolmogorov-Arnold-Moser (KAM) theorem which states that small nonlinear perturbations to integrable Hamiltonian systems (stable particle orbits with well defined periodic motions) will deform the solution and generate particle motions that are quasi-periodic. In some special cases, e.g. at resonances, the trajectories will become chaotic or wander off into infinity. For a given initial condition of a particle, it will travel around the ring and sample fields that will be different to another particle that had different initial conditions. If such particles were to encounter perturbations that cause it to be unstable then it can be detected by analysing small changes in the tune of the particle over short

timescales (less than the damping time). By tracking particle trajectories with different initial conditions we can discern which are stable and which are unstable and thereby generate maps indicating locations of unstable beam motion. A description of the technique and its application to other light sources can be found in [6, 7].

The technique is relatively simple where a matrix of particles with various amplitudes is tracked in simulation over 2000 turns. The first and second lot of 1000 turn oscillations at a given point are analysed using an FFT algorithm to extract two sets of tunes. The particle's initial position, and tune can then be plotted and colour coded depending on the difference between the two sets.
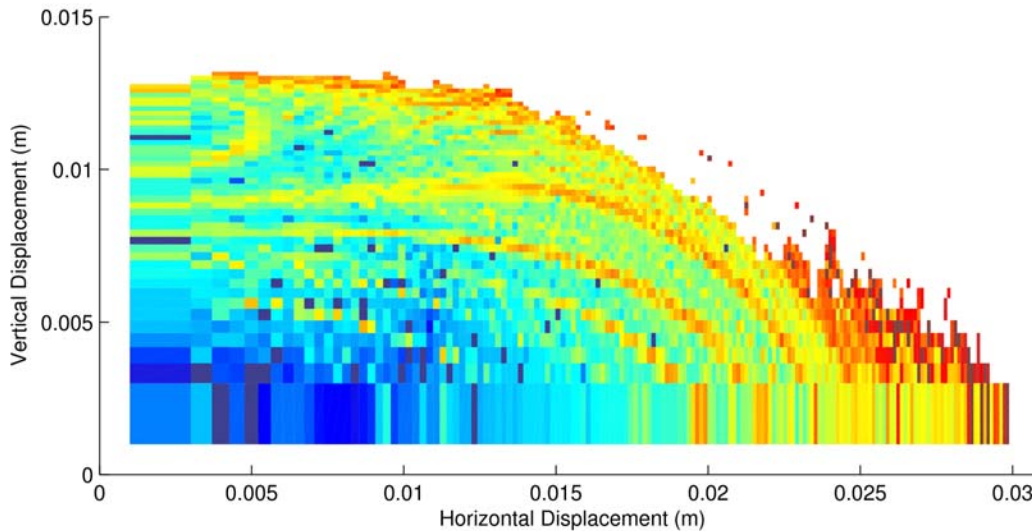
Figure 10: Dynamic aperture of an early lattice with the two families of harmonic sextupoles set to $\pm20\mathrm{m}^{-2}$, zero chromaticity and zero dispersion.

The first frequency map showing the dynamic aperture was done using the ideal lattice with zero chromaticity and zero dispersion. The results showed a large aperture that seemed instability free to 18 mm horizontally and 8 mm vertically as seen in Figure 10. The corresponding plot in tune space is shown in Figure 11. This shows "folds" at larger amplitudes where the sign of the tune shift with amplitude ($\partial v/\partial J$) is changing. This is an indicator that nonlinear terms are dominant at these large amplitudes.

The plots in tune space also show what resonances are being excited and are limiting the aperture. In general, if the symmetry of the lattice is preserved and there is a high periodicity, much of the lower order resonances (that are also stronger) are significantly suppressed enlarging the stable areas in tune space. When this symmetry is broken (field errors, misalignments or IDs that result in beta beatings) these regions are "sliced" up by the lower order resonances reducing the stable areas and usually reducing the dynamic aperture at the same time. For this reason restoring the symmetry is very important and is highlighted in later sections on LOCO.
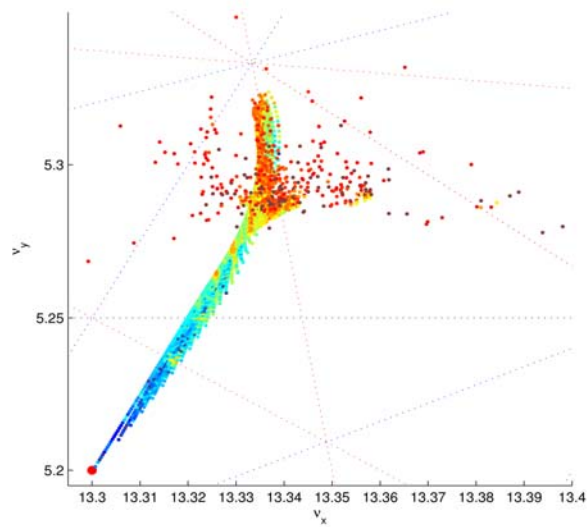
Figure 11: Frequency map in tune space showing folds. The lines in background show the resonance lines assuming a periodicity of 14 for the ideal lattice.

This seemed reasonable to begin with however when the chromaticity was increased to unity in both planes and the dispersion set to 0.1 m, there was a significant reduction in the aperture with very large amplitude dependent tune shifts as shown in Figure 12 and Figure 13.
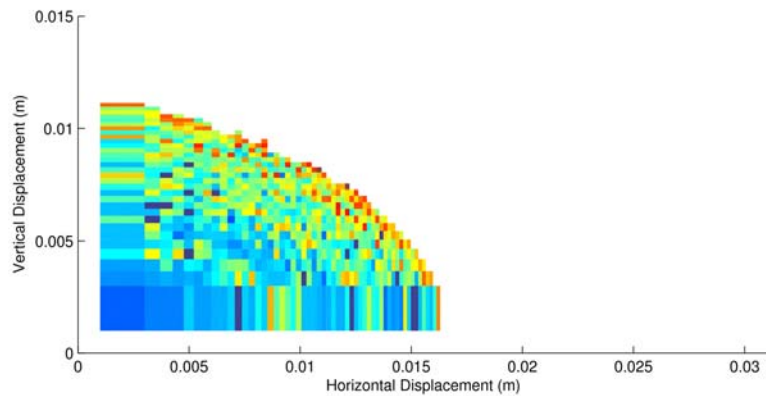
Figure 12: Large reduction in aperture when increasing the chromaticity and dispersion. The harmonic sextupoles were not changed.
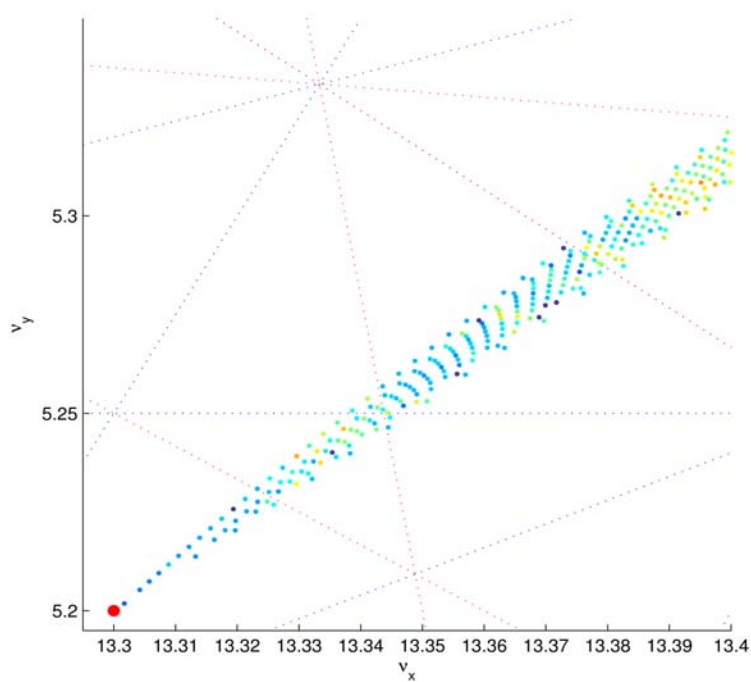
Figure 13: Frequency map shown large tune shifts with amplitude when increasing the chromaticity and dispersion.

After doing some scans of the harmonic sextupoles it was found that setting them to 24 m–2 and -26 m–2 recovered much of the lost aperture (Figure 14).
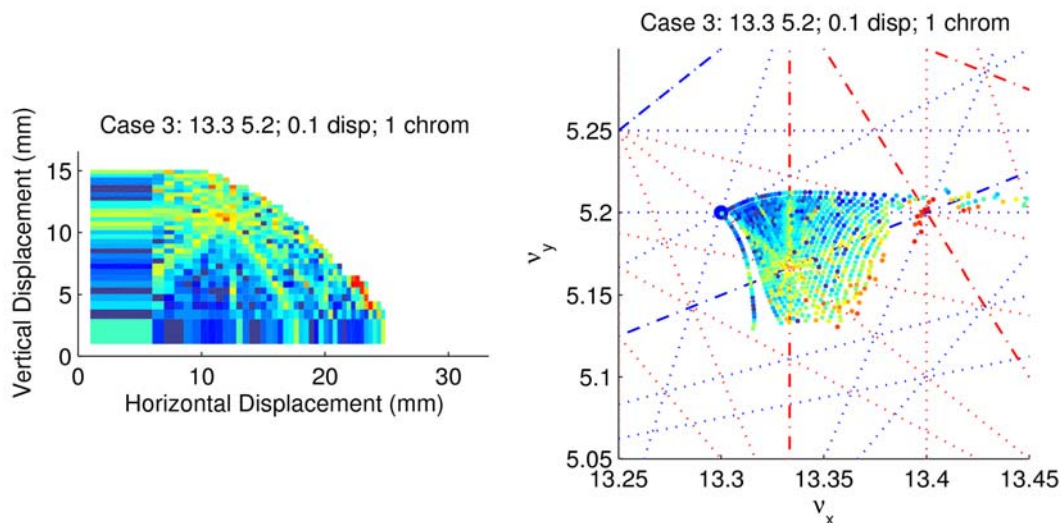
Figure 14: Dynamic aperture re-enlarged with new harmonic sextupole settings. Map in tune space also shows a better tune shift with amplitude.

This technique can also be used to do resonance analysis where the tune maps are analysed to discover what order resonances are being excited and what is causing these perturbations. Another avenue of analysis is measuring and optimising the momentum aperture [8].

The conclusions from the various studies showed:

1. Though non destructive the initial design tunes of 13.3 and 5.2 sat directly on a resonance line. Empirically during commissioning we moved the tune to 13.29 and 5.216 and got a better lifetime.
2. Settings of the harmonic sextupoles needed to be $> 20 \text{ m}^{-2}$. With our large chromaticities they are now 31.2 m^{-2} and -33.2 m^{-2}. As seen above, the SD still needs to be slightly stronger than the SF to maximise the dynamic aperture.

Experimental verification of the model will be available in the future when pinger magnets (single turn kickers) are installed in the ring.

4.1.5.3   *Modelling the Electron Path through Gradient Dipoles*

The path of an electron through a gradient dipole can be modelled as a hyperbolic sin function, however this is not exactly true and numerical integration of the equation of motion through measured fields is necessary. In [9], analysis of the gradient dipole in SPEAR3 showed that the hyperbolic sin function overestimated the total distance that the electron takes though the gradient dipole. Though only fractions of a millimetre per dipole, overall this resulted in a shortening of the actual circumference of the ring by a few millimetres. A numerical analysis using a 2D field scan of one of our gradient dipoles was performed.
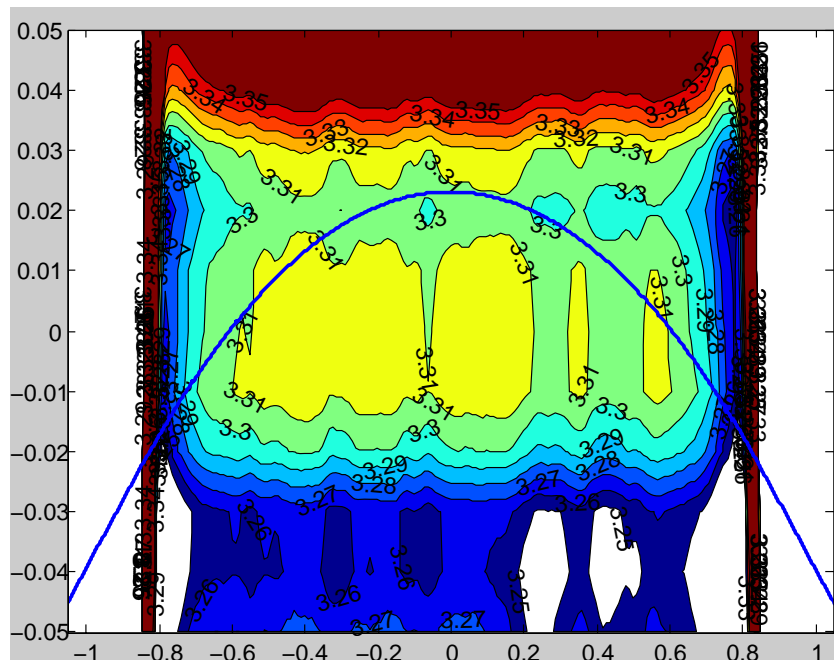
Figure 15: Electron trajectory through 2D field map of the gradient dipole.

The results of the analysis showed that there was a total path length reduction of -5.36 mm corresponding to an increase in the RF frequency of 12.4 kHz. During commissioning the actual RF frequency change was 17.4 kHz taking the real frequency from the theoretical 466.6541 MHz to 499.6715 MHz.

4.1.5.4   Edge Angle/Focusing on Gradient Dipoles

For normal rectangular flat dipoles, the dipole model with edge focusing that is dependent on the incoming angle (half the bending angle) is well defined and understood. When the particle enters the dipole field at an angle it effectively sees a field gradient and thus contributes to the focusing of the beam (edge focusing). In the case of gradient dipoles the edge focusing can change as the extent of the fringe fields modifies the field gradient that the beam sees as it enters the dipole. It was found that the effective edge angle of the gradient dipoles was increased by as much as 20-30%. The source of this increase in the edge angle and focusing is the chamfering of the pole edges (see Figure 16 below). Normally with no chamfers, L_{eff} (larger gap) $> L_{eff}$ (smaller gap) when applying the canonical rule that the magnet fringe field effective length is proportional to the half gap. The gradient dipoles have chamfers designed in them that should make it such that L_{eff} (larger gap) $= L_{eff}$ (smaller gap).
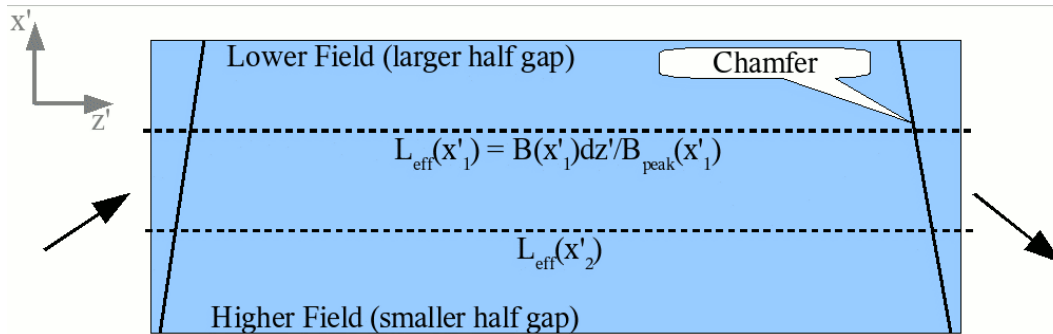
Figure 16: Chamfers on the gradient dipoles designed to ensure that $L_{eff}(x'_1) = L_{eff}(x'_2)$.

The 2D magnetic measurement data showed this was not the case, in fact it appears as if the chamfers on the dipoles had over compensated and now L_{eff} (larger gap) $< L_{eff}$ (smaller gap) increasing the "pole face angle" by 23 mrad (nominal edge angle is 0.1122 rad). Another method of inference (based on tracking the electron trajectory as discussed in the previous section) put this angle closer to 36 mrad. In the model this possible discrepancy has been taken into account however it still remains to be verified conclusively.

4.1.5.5   Amplification Factors

The effects of mechanical alignment and vibrations need to be determined. Studies were conducted to determine the amplification factors for entire girder and dipole movements. Vibrations were measured to be in the tens of nm range and element to element alignments are better than the girder alignments. Thus we decided to analyse the amplification factors based on the dipole and girder alignment tolerances. The following tolerances were deemed realistic and were used in the following study.

Table 4: Alignment tolerances for dipoles and girders

Element	X trans (μm)	Y trans (μm)	X rot (μrad)	Y rot (μrad)
Dipole	87	62	48	70
Short girder	62	62	61	82
Centre Girder	62	62	62	62

In this study 100 seeds were used and for each seed the girder or dipoles around the ring were set with random (equal distribution) misalignments and the maximum closed orbit distortions recorded. The amplification factors are calculated simply as the maximum orbit distortion in each plane divided by the misalignment. The results of the study are shown in the table below.

Table 5: List of amplification factors calculated for dipole and girder movements

Element	Horizontal Plane				Vertical Plane			
	X trans	Y trans	X rot	Y rot	X trans	Y trans	X rot	Y rot
Dipole	4.10	0.00	0.73	20.57	0.00	51.11	44.52	0.00
Short girder	15.05	0.00	0.16	5.55	0.00	27.32	16.45	0.00
Centre Girder	18.25	0.00	0.05	4.14	0.00	22.14	9.03	0.00

The rotation error of the dipole about the z-axis is known to have a large amplification factor so a simulation was done. Over a 1000 seeds and a maximum rotation tolerance of 50 μrad the calculated amplification factor for dipole rotation was 0.38 in the horizontal plane and 31.84 in the vertical.

4.1.5.6   Accelerator Control

At the Australian Synchrotron the chosen control system is EPICS which is widely used in the accelerator community. For accelerator physics studies, control of the various elements is done through the Matlab Middle Layer toolbox that has been developed at the ALS and SSRL. The Middle Layer toolbox is a collection of scripts that act as middle-ware, interfacing the user transparently to any control system for accelerator control with the added ability to seamlessly switch to a model for simulated machine studies.
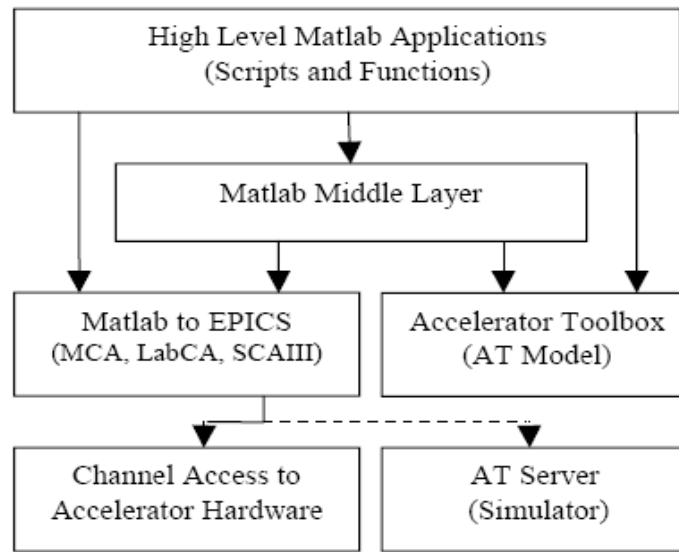
Figure 17: Software flow diagram with Middle Layer interfacing though EPICS. With appropriate drivers written the interface can be to any control system [10].

In this fashion someone running a script to make some measurements using Middle Layer in Australia (EPICS) can easily send the script to someone at Soleil (TANGO) and repeat exactly the same measurement with little or no change to the code. The programming environment within Matlab is also very user friendly with an aim to rapid prototyping. It is this sort of environment that makes it very easy to write a simple program to carry out measurement and analysis, saving lots of time. The toolbox also contains a collection of standard applications/scripts that are used as part of operations, such as beam based alignment (BBA), response matrix measurements, orbit control and Linear Optics from Closed Orbits (LOCO).

4.1.5.7 *Beam Based Alignment*

Misalignment of magnets around the storage ring will significantly affect the performance of the ring. With recent advances in laser tracking technology, mechanical alignment of magnets is accurate to 20 μm, relative to nearby elements. However in practice, with mechanical tolerances in manufacturing magnets, girders, and pedestals, the absolute magnetic centres cannot be mechanically aligned to one another to better than 50 μm. Beam based alignment references the ideal orbit around the ring to the centre of the quadrupoles. The current resolution/repeatability of the BBA is ~5-10 μm, which is better than what is possible with mechanical alignment.

The entire process is completely automated and only required changes to some configuration files to get it to work for the storage ring. This was done long before commissioning by using Middle Layer in simulator mode. A complete run will take roughly 3 hours (8 measurements per BPM per plane, a total of 1568 measurements)

Beam based alignment was able to identify an interference we had with a wiggler ID. For some time we were having difficulty in correcting the orbit around the straight section. It was not until we decided to measure the offsets with the wiggler open and closed that we realised that the offsets were changing by 20 and 40 μm in the upstream

128

and downstream BPMs. These offsets correlated exactly with the residual orbit in those BPMs that could not be corrected. When we inspected the device we realised that as the gap closed the vertical I-beam would flex under the magnetic forces (~189 μm) and cause the corrector coils that were bolted to the frame to push against the vacuum chamber.

4.1.5.8 Orbit Control and Slow Orbit Feedback

For orbit control there are many techniques available and two were used during commissioning; the most effective corrector method (MICADO) and response matrix method. Early in commissioning we had limited success with using a model response matrix to correct the orbit and found it best to couple it with the MICADO method. We would begin with correcting the large deviations using the MICADO method before using a model response matrix to correct the closed orbit. As the tunes were close to the model the difference in the phase advances would not have been very different between the model and the machine and therefore using a response matrix derived from the ideal model worked quite well. The tools for orbit control are readily available through the Middle Layer toolbox.

The orbit response method is a straight forward technique and has been well developed over the years. It can be expressed simply in the following way

$$\Delta x = R \Delta \theta \quad \rightarrow \quad R_{ij} = \left[\frac{\partial x_i}{\partial \theta_j} \right],$$

where R is the measured response matrix analogous to a Jacobian, θ the corrector kick, and x the change in the orbit. By inverting the matrix R using the singular value decomposition (SVD) method, it is possible to create a pseudo-inverse matrix R^{-1} that can then be used to generate a list of $\Delta\theta$ from a list of desired Δx. It is also possible to calculate the RF frequency component in the closed orbit (shows up as a dispersion component in the closed orbit) and correct the RF frequency (the same can be applied to the corrector pattern). In our case we have 98 BPMs but only 42 horizontal correctors and 56 vertical correctors. Therefore in both planes we are over constrained and cannot generate perfect corrections at all 98 BPMs. At present the closed orbit RMS across all BPMs is ~19 μm in both planes and the corrector RMS < 10% of their total capacity. This was a good indicator what we had good mechanical alignment.

A slow orbit feedback program in Matlab is also available through the Middle Layer toolbox and is used in regular operations to correct the closed orbit at rates between 0.25 to 1 Hz. This is generally used to correct for slow the thermal drifts that occur in the system. These thermal drifts have been documented and shown to be as large as 500 μm over a 48 hour period after a shutdown period (for regular maintenance).

4.1.6 Instabilities

Thus far, we have only observed one coupled bunch instability. At high stored beam current we observe a blow-up of the vertical beam size. Looking at the frequency spectrum of the vertical betatron tunes we see a maximum at the first harmonic above the RF harmonic and then a sharp fall off with increasing harmonic number. This is suggestive of the $\omega^{-1/2}$ pattern for a resistive wall effect.
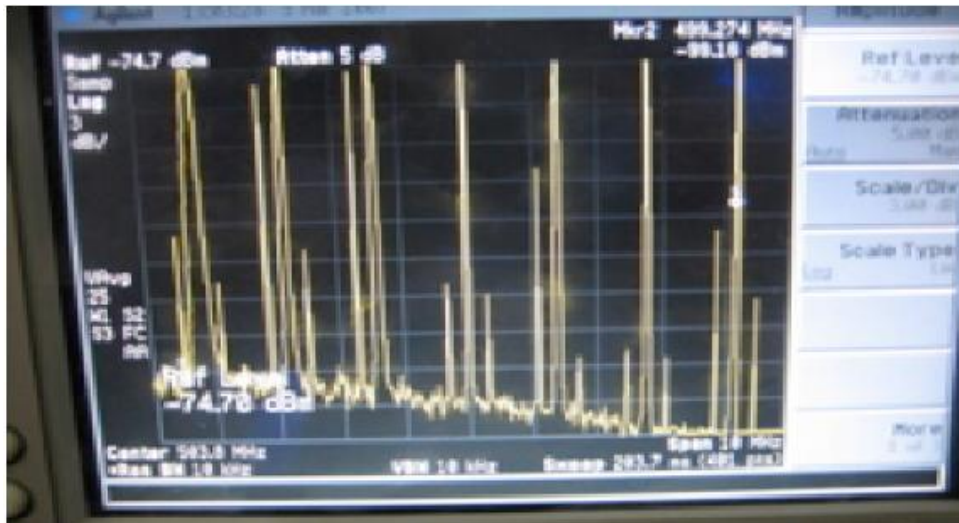
Figure 18: Spectrum analyser image of the vertical tune lines for the RF harmonic (leftmost) and first 6 harmonics.

4.1.6.1   *Resistive Wall Threshold*

If we consider the transverse impedance of our vacuum chamber using [12], we obtain a vertical transverse impedance $Z_y/n = 0.94$ MΩm^{-1}. Using this value and an average 15 m vertical beta function we then obtain a resistive wall growth rate of 1.5 ms for a beam current of 200 mA. The storage ring vertical radiation damping rate is only 4.8 ms, clearly indicating the need for extra damping to stabilise this mode. We currently achieve this damping through the use of positive vertical chromaticity. The above calculation is for a uniform vacuum chamber, with no insertion devices. There are currently plans for the addition of one 2 m and two 3 m long in-vacuum undulators (IVU), with gap heights of 6mm and 6.6 mm respectively.

A study into the effects of adding the IVUs found that due to the very small gap heights there was a considerable increase in resistive wall impedance, with each IVU adding around 25% on top of the current total ring impedance. We expect to be able to control this extra impedance effect with a transverse feedback system which is expected to be commissioned soon.

4.1.6.2   *Chromaticity Damping*

By increasing the global vertical chromaticity to large positive values we can use the tune spread to combat resistive wall instabilities (Landau damping). We currently do not have any models or diagnostics to determine the actual damping rates to tell us what to set our chromaticities to. With our nominal fill pattern we currently require a vertical chromaticity of 6 to be able to reach 200 mA without instabilities. We have made some observations that show that the appropriate choice of fill pattern also helps reduce the impact of the instability. These investigations are still ongoing.

With such high chromaticities there is a significant reduction in the dynamic aperture and this results in significant decrease in the injection efficiency. To recover our dynamic aperture we have to tune our "harmonic" sextupoles (the emphasis on

harmonic is because with distributed dispersion this term is not strictly true). Such a study was conducted using frequency map analysis, FMA (see earlier sections), and showed settings that recovered our aperture for chromaticities of 1. FMA is quite a time consuming analysis and in the end an empirical approach was taken instead and showed that we set the harmonic sextupoles to 31 and -33 m-2 to regain our injection efficiency. This result is in line with the earlier studies that also showed that slightly stronger SDs were required. Follow up dynamic aperture studies have yet to be completed at the time of writing.

4.1.7   Storage Ring RF

4.1.7.1   Layout

The Australian Synchrotron storage ring RF system consists of 4 normal conducting copper cavities, fed by 4 independent 150 kW klystrons. This design approach was chosen to allow for the failure and repair of 1 klystron, while still allowing the other 3 klystron systems to operate and store a reduced current beam. As it happened, due to a hardware failure in one of the systems, much of the early commissioning of the storage ring was done with only 3 klystrons operating.

4.1.7.2   RF Generation and Distribution

The 4 klystrons have a maximum power output of 145 kW. Full beam loading with 200mA current at nominal cavity voltage draws a power of 125 kW from each system. In the case of a klystron failure, the 3 remaining klystrons could support a beam current of around 130mA, although with reduced beam quality.

The RF power is fed to the cavities through a conventional waveguide system into the accelerator tunnels. A 200 kW circulator connected to a 180kW water cooled load is included in the waveguide system to protect against reflected power. The circulators are water cooled and temperature regulated to maintain a good coupling with the waveguide and minimise power reflected back into the klystron.

The waveguide system connects to a coaxial coupler at the top of the RF cavities, where the air to vacuum interface is a ceramic window.
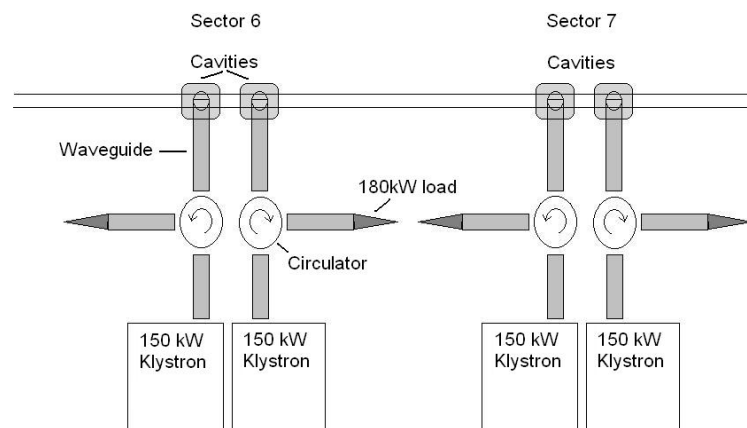
Figure 19: Storage Ring RF System Layout.

4.1.7.3 Cavity Design

The storage ring cavities were based on the cavities currently in use at the Photon Factory [13] and are normal conducting copper cavities operating in the $\pi/2$ mode. The input coupler transfers the RF power into the cavity magnetically via coaxial input with a loop connection. The input couplers have been set to $\beta = 1.6$ to give optimal coupling between the generator and cavity at nominal beam loading (200mA).

The shunt impedance of the cavities has been measured as 3.6 MΩ and is achieved with a nose-cone geometry. The beam pipe in the cavities is 125mm and was chosen as a compromise between shunt impedance and trapping higher order modes (HOMs) in the cavity. Taper sections connect the nominal rectangular (32 mm by 70 mm) vacuum chamber to the circular 125 mm cavity beam pipe.

The 125mm beam pipe diameter means HOMs with frequency larger than 1.8 GHz will not be trapped in the cavity. SiC ducts are installed on either side of the cavities to absorb the HOMs that escape the cavity. The modes which remain trapped in the cavities are absorbed using HOM damper antennas. There are 4 longitudinal HOM modes identified using cavity simulations, at frequencies of 792 MHz, 1314 MHz, 1356 MHz and 1725 MHz. To appropriately damp the HOM modes with an antenna, care was taken to not couple significantly to the 500 MHz accelerating mode through the positioning of the antennas at the walls of the cavity where the accelerating mode fields are weak. The electric fields of the HOMs concentrate in two different regions and therefore require two antennas in each cavity, one on-centre and one off-centre damper. The on-centre damper is inserted along the centre line of the cavity (perpendicular to the beam axis) such that it is close to the high field areas of the TM011 and TM021 modes. The off-centre damper is placed with a 10 cm offset from the cavity centre line, in order to absorb the TM012 and TM022 HOMs.
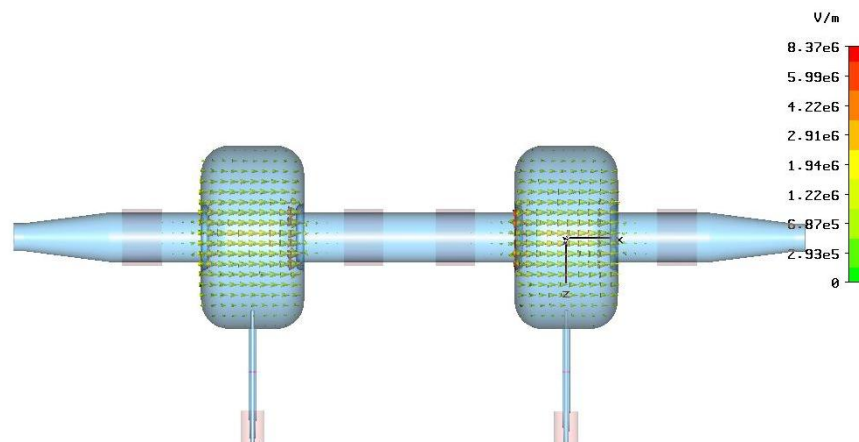
Figure 20: 2 Cavity pair cross-section showing Electric field vectors of the TM010 accelerating mode. HOM damping on-centre antenna is shown, and SiC absorbers are shown in pink.

The dampers also do a good job of damping most of the transverse modes observed, although the horizontal and vertical TM110 modes remain above threshold. These modes are detuned from the beam spectrum using a fixed HOM detuning plug and thus far have not had any observable effect on beam performance.

On-site low power tests found that most of the HOMs were successfully damped below instability threshold, with only 0.25% of the accelerating mode coupling into the HOM dampers. The entire power absorption corresponds to ~600W at full beam current of 200mA and is within the 2 kW heat absorption capacity of the antenna. Results of the tests with no damping are shown in table 6 and with damping in table 7. More details of the damper design can be found in [13, 14]

Table 6: HOM measurements with no damping

Mode	Freq. (MHz)	R/Q	Measured Q	R_{shunt} (Ω)	Threshold R_{shunt} (Ω)
TM011	790	56	5011	280,616	31,645
TM012	1313	10	1331	13,310	19,040
TM021	1355	14.6	9854	143,868	18,450
TM022	1725	10	1681	16,810	14,492
TE111(H)	704	3.7	19567	72,006	100,000
TE111(V)	710	3.7	12697	46,725	100,000
TM110(V)	797	402	2431	976,290	100,000
TM110(H)	802	402	23844	9,575,750	100,000
TM111(H)	1005	676	10957	7,403,645	100,000
TM111(V)	1011	676	6899	4,667,654	100,000

Table 7: HOM measurements with damping

Mode	Freq. (MHz)	R/Q	Measured Q	R_{shunt}	Threshold R_{shunt}
TM011	790	56	447	25,032	31,645
TM012	1313	10	914	13,310	19,040
TM021	1355	14.6	Not measured	-	18,450
TM022	1725	10	Not measured	-	14,492
TE111(H)	692	3.7	482	1,774	100,000
TE111(V)	707	3.7	853	3,139	100,000
TM110(V)	797	402	2190	879,504	100,000
TM110(H)	802	402	21243	8,531,188	100,000
TM111(H)	993	676	71	47,974	100,000
TM111(V)	1005	676	75	50,677	100,000

Cavity tuning is controlled by a single movable plunger in each cavity. The plunger is positioned by a stepper-motor and controlled by a frequency tuning feedback loop. The frequency feedback loop can be adjusted to allow for the deliberate detuning of the cavities necessary to overcome the Robinson instability.

The frequency loop works by picking up the RF signal from the main pickup antenna in the cavity and comparing it to the signal of the forward power, monitored from a directional coupler just before the cavity. The plungers work to keep the cavity at resonance during thermal expansion and contraction of the cavities. An offset can be introduced into the loop to deliberately de-tune the cavities to overcome the Robinson instability.
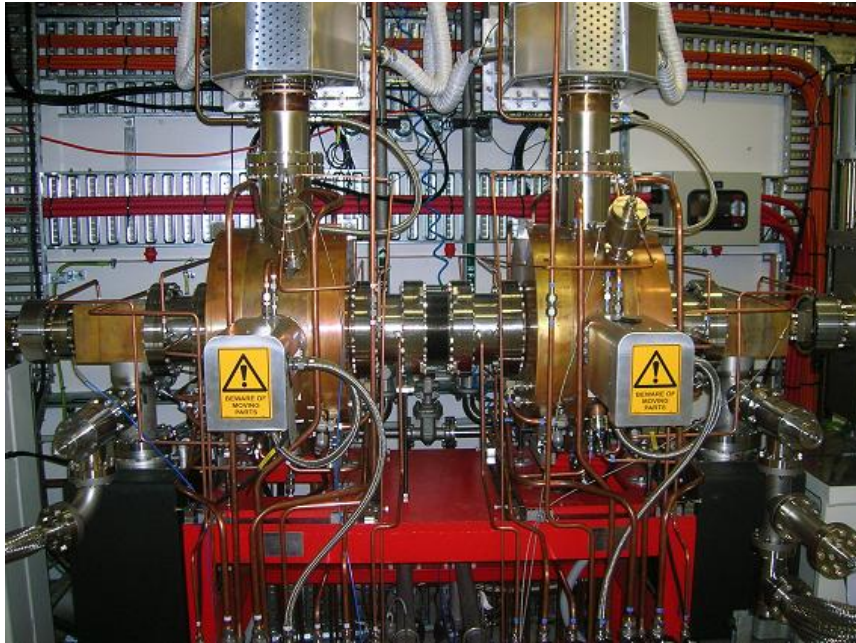
Figure 21: 2 Cavity pair, as installed in the Storage Ring.

4.1.7.4 Low Level Electronics

Each Cavity system is controlled by a separate low level electronics (LLE) unit which monitors RF signals from the waveguide and cavities and feeds back on the amplitude and phase of the 20W pre-amplifier and cavity tuning plungers through various control loops. The RF signal from the master oscillator is split into 4 channels which are then fed to the 4 independent LLE modules. A master phase shifter allows for an adjustment of the phase of all subsystems simultaneously, while 4 other phase shifters allow for independent phase adjustments.
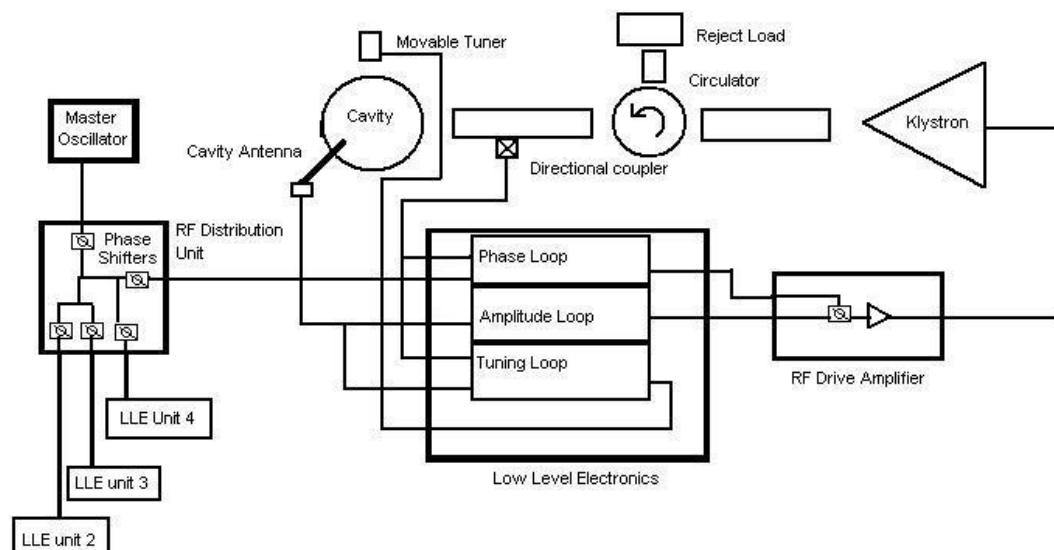
Figure 22: Overview Schematic of the LLE system

Each Low Level Electronics module contains 3 different control loops; a phase loop, an amplitude loop and a tuning loop. The Phase loops compare the phase of the incoming master RF against the phase of the RF wave in the waveguide just before the cavity. Any phase difference caused by the RF distribution system, including the klystrons, is then corrected for using a phase shifter just before the drive amplifier.

The Amplitude loop monitors the cavity voltage and compares it against the set point. If there is a difference (due to beam loading for example) it modifies the drive power level to compensate.

The tuning loop compares the phase of the RF wave in the waveguide to the phase of the resonant RF in the cavity. A frequency difference between these signals shows up as a phase difference. The tuning plungers are then moved to eliminate this phase difference. A user defined offset can be introduced in order to deliberately detune the cavities for Robinson stability.

The initial system had 2 nested phase control loops, one that controlled just the klystron, phase, and another for the whole distribution system. Two loops were used due to concern that one loop may not have a large enough dynamic range to control the whole system. During commissioning it was found that these phase loops could interfere with each other and cause spontaneous phase jumps (sometimes 180 degrees) between cavity operation periods. The klystron phase loop was therefore removed from the system and these phase jumps have since disappeared.

The phase loop stability was measured by observing the cavity phase over several hours of high power operation. The system stability was found to be ±0.5 degrees. Similarly the amplitude loop stability was measure by observing the cavity voltage over a long period and found to be stable within 0.5%.

There are a number of monitors attached to the RF system that form part of the Equipment Protection System (EPS). The EPS monitors things like, RF power levels, arc detectors, water flow rates, temperatures, etc. In the event of a fault, the EPS will shut down the RF system for the cavity experiencing the fault.

Due to the large number of safety interlocks present, during a system trip multiple faults may be recorded. In order to properly diagnose the cause of the fault, it is important to determine the sequence of faults. Sequential fault logging is achieved through a Fast Fault Memory (FFM) system. When a fault occurs, the FFM system is triggered, and records interlock signals as they occur, with a time resolution of microseconds, for a period of 20 milliseconds. Each RF system has a separate FFM module, and these are synchronised to each other through a shared trigger. This means in the case of multiple cavity trips, it is possible to determine which cavity trip was first, and why.

Figure 23: An example of the FFM display after a fault on both cavities in sector 6. The trigger appears as the first fault on both systems, but the timing of the other faults in relation to the trigger indicated that it was cavity 1 (labelled SR06RF01) in sector 6 which faulted first. The Input coupler Arc fault, seen last on both sequences is indicative of a radiation burst from the beam being lost.

4.1.7.5 *Performance and Commissioning Experience*

During commissioning, the fault logging allowed us to keep track of any recurring problems with the cavities. The majority of trips could be attributed to cavity arcing during the initial ageing period. During attempts to store first beam a number of 'input coupler arc' faults were recorded. These faults are triggered by a photo-sensor connected to an optical fibre which points at the input couplers, and is designed to protect the system against any arcing which could damage the coupler ceramic. It was found that these faults were not real arcs, but were being somehow induced by high radiation levels in the tunnel, as they were always associated with beam loss and would occur even when the cavities were not operating.

One of the first tasks on the RF system, after achieving stored beam, is to check the phase balance of the cavities. In order to ensure that the beam sees the same phase in each cavity, the relative phase of each RF station must be adjusted to compensate for the cable delays and electron flight time differences between each cavity. The required phase difference between cavities is simply the electron path length between the cavities divided by the RF wavelength, with appropriate offsets due to cable delays factored in.

During initial testing, the cavities phase differences were measured and set according to this requirement. When commissioning however, this phase adjustment did not capture beam and was instead adjusted to maximise the number of turns achieved by the injected beam. Once stored beam was present, phase balancing was achieved empirically by balancing the beam loading between cavities. Phase balance was also confirmed by observing a significant reduction in the beam spectrum synchrotron sidebands, to the point where they became difficult to detect.

The initial failure of the phase settings to store the beam has since been explained. It was found that due to the interference between the original nested phase control loops in the LLE, the actual cavity phase had altered significantly between the initial calibration and the first beam capture efforts. Once this interference was understood and corrected it was found that the empirically discovered phase settings were only a few degrees different from the originally calculated settings. The phasing was also checked by measuring the synchrotron tune. This measurement agreed with the value predicted by the total cavity voltage and indicated that the effective voltage was indeed maximised.

Initial commissioning of the storage ring took place with the cavities tuned completely on-resonance. In this condition only around 20 mA of current could be stored before synchrotron oscillations grew so large that beam was lost. The presence of synchrotron oscillations was confirmed by observing horizontal oscillations on BPMs in the dispersive regions of the storage ring and large synchrotron sidebands on the beam spectrum. Using the tuneable plunger phase offset control the cavities were manually detuned to overcome the Robinson instability and no more oscillations were seen.
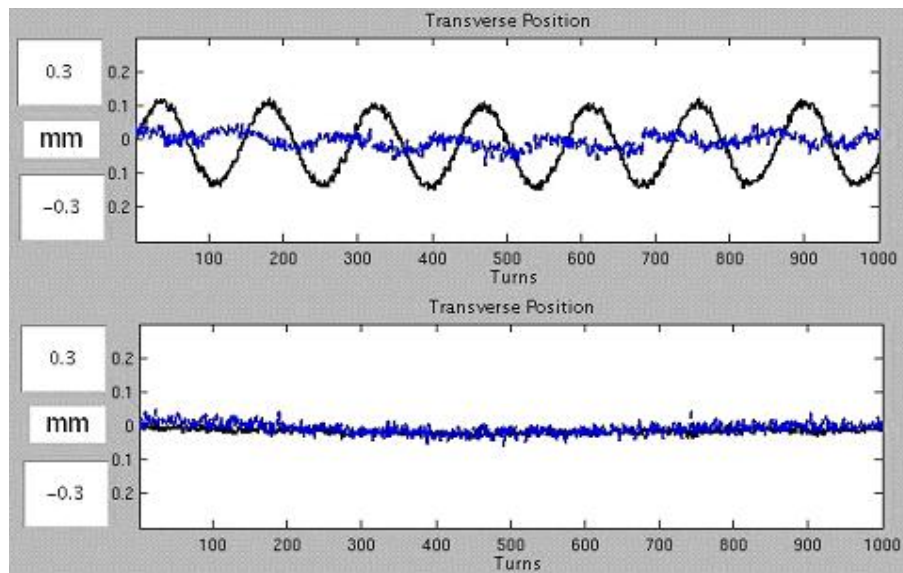
Figure 24: Transverse BPM position (black = horizontal, Blue = vertical) versus turn number in a dispersive area of the lattice. The top image shows the synchrotron oscillations before Robinson detuning, the bottom graph is after detuning of the cavities.

At present, there exists no method of measuring the beam loading on the cavities except by observing the increase in forward power required to maintain the cavity voltage due to beam loading. While this method does appear to work well, it does not give any information about the amount of detuning required to maintain Robinson stability. In the future we plan to install a cavity phase and amplitude monitoring system that will allow us to plot each cavities current state on a Smith chart, so that we can fine tune the cavity detuning and phase balancing. The proposed method for doing this will involve a digital IQ demodulator circuit that monitors the RF wave entering the cavity against the signal from the cavity antenna. This system is currently under development and we expect to begin testing and integration shortly.

Bunch length measurements have measured a bunch sigma of 25 ps for 0.6 mA single bunches. This result is quite consistent with theoretically expected bunch lengths for our machine parameters and indicates that the RF system is working as intended.

4.1.8 Diagnostics

The Storage ring has a straight section which is largely devoted to diagnostic equipment [16]. This straight section includes horizontal and vertical stripline kickers, a Direct Current Current Transformer (DCCT), 4 stripline pickups, and 4 scrapers. (See Figure 25). Elsewhere around the ring there are a total of 98 BPMs that monitor the orbit position at the revolution frequency.
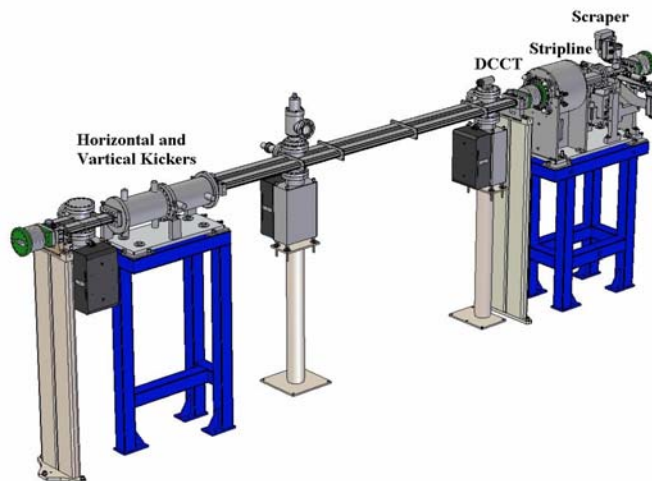
Figure 25: Diagnostics straight.

4.1.8.1 Scopes

The two main scopes used during commissioning were a 3 GHz Agilent and a 600 MHz LeCroy. In general, these scopes were connected to an Ethernet network and remotely controlled from the control room.

During the early commissioning of the storage ring the main use of the scopes was to allow the direct measurement of the beam injection. Once stored beam was achieved, this scope's role shifted to monitoring the fill pattern (Figure 26).

The other more minor role of these scopes has been to monitor timing signals and their relationship to each other. In particular, the jitter of certain signals has been an important quantity. Figure 26 shows the 3 GHz scope being used to make a measurement of the jitter between channels on a DG535.
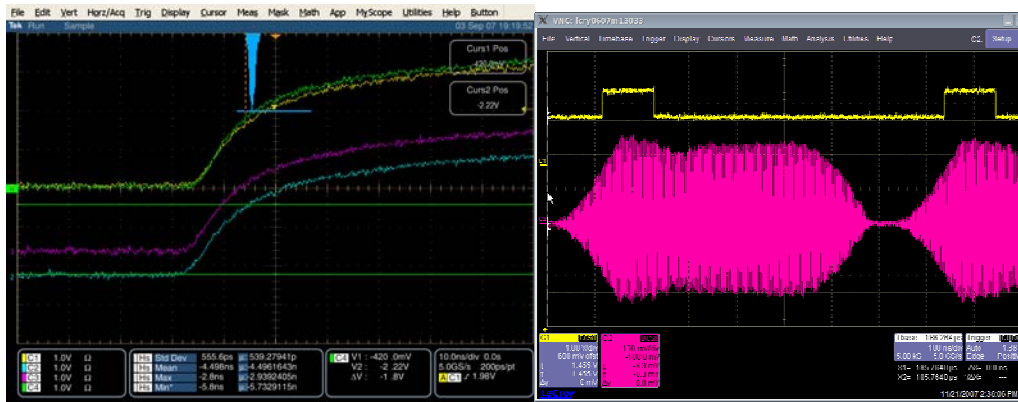
Figure 26: Left: Jitter measurement using the 3 GHz Tektronix scope. Right: Fill pattern measurement made using the 600 MHz LeCroy scope.

4.1.8.2   Tune Measurement

4.1.8.2.1 Swept Spectrum Analyser

Our nominal tune measurement is provided by a swept spectrum analyser. A simple software driver was written for this device which passes the peak positions to an EPICS process variable.

The output signal from the spectrum analyser is used to oscillate the beam. This signal is amplified to around 100 mW before being fed to the horizontal and then the vertical stripline kickers.

Initially, the input to the spectrum analyser was provided directly from a stripline pickup. This required a large oscillation of the beam to resolve the tunes. The input signal to the spectrum analyser is now provided by amplifying the difference between the signals from two diagonally opposed stripline pickups. The accuracy of this tune measurement system is around $\pm 1.5 \times 10^{-3}$.

Figure 27: Typical spectrum analyser tune measurement.

4.1.8.2.2 Real Time Spectrum Analyser

A real time spectrum analyser provides a better frequency resolution than the swept spectrum analyser. In the most common configuration, the input signal is provided by a direct connection to a stripline pickup. The beam is excited with an FM signal which covers the region of interest around a particular orbit harmonic. This FM signal is provided by a function generator and then amplified and fed to the horizontal and then the vertical stripline kickers.

The accuracy of this tune measurement is as good as $\pm 5 \times 10^{-5}$ and is restricted by the tune peak width and tune movement.
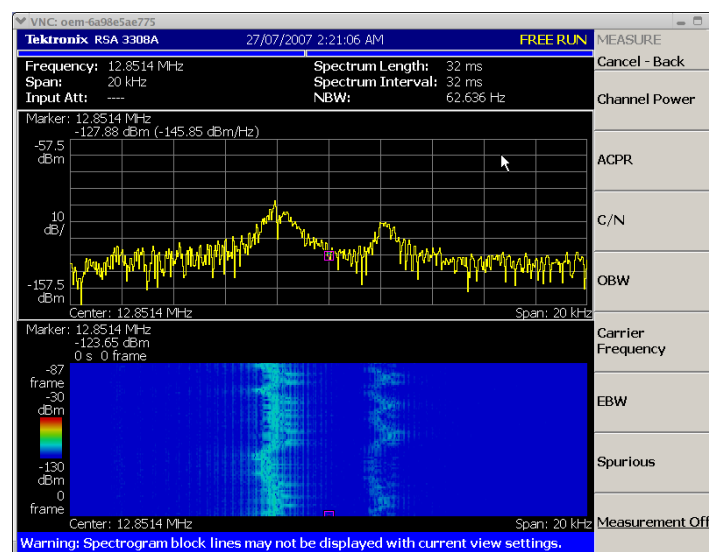
Figure 28: Real time spectrum analyser being used to perform a 'tune-split' measurement

4.1.8.2.3 Injection Kickers with Turn by Turn Data analysis

If a single injection kicker is turned on and set to small amplitude, then a spectrum analysis of the triggered turn-by-turn data from the BPMs can reveal the tunes (Figure 29). This method is not possible during user beam time because the kickers disturb the stored beam. The resolution of this method depends on the number of turns used in the analysis. Under typical ring chromaticity the damping time means that the beam ceases to oscillate after about 2000 turns giving a tune resolution of around $\pm 5 \times 10^{-4}$.
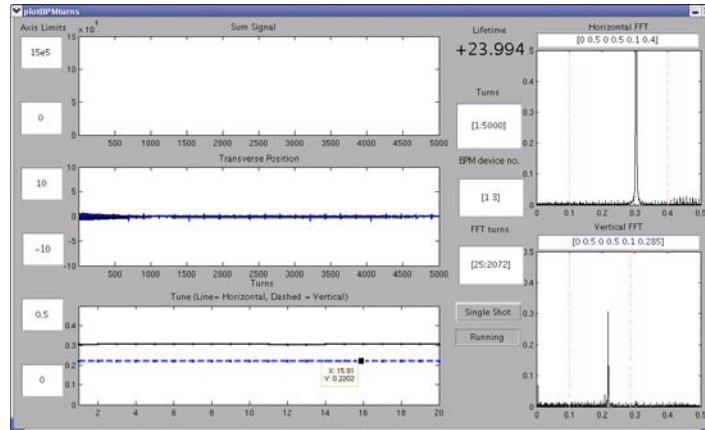
Figure 29: GUI which shows the analysis of the turn by turn BPM data. The right hand plots show the horizontal and vertical tunes.

4.1.8.3   Beam Current and Lifetime measurements

The DCCT is a Bergoz model which outputs an analogue 0 V to 10 V proportional to 0 to 200 mA. This signal is monitored using an ADC input on an IOC. The ADC is set up to read the DCCT output at 1 kilo-samples per second. An averaging calculation is performed so that an EPICS PV is updated at 1 Hz. The nominal lifetime calculation is based on the most recent 150 seconds of data and consists of a simple least squares exponential fit to the raw 1 Hz current data

4.1.8.3.1 Mechanical improvements to the DCCT head.

It was discovered that the DCCT head had been secured to the vacuum chamber rigidly. According to Bergoz [17] this method will increase the effect of any temperature changes on the current measurement. Decoupling the head from the chamber resulted in a better measurement. It was also decided to remove water flow through the DCCT mounting. This water was only designed to run during bake-out to protect the measurement head. It was found that the temperature stability of the head was better without water flow.

4.1.8.3.2 Methods to improve the lifetime measurement

A number of different lifetime measurement methods have been trialled in an attempt to improve the variation in lifetime measurement at low beam current:
- Smoothing of the raw DCCT beam current data using an '$\alpha\beta$'- Kalman filter.
- Utilising BPM sum data as an alternative to the DCCT current measurement.

- A weighted average between a 'short' and 'long' lifetime measurement based on the difference between them.

Unfortunately, none of these methods showed a significant advantage over a simple least squares fit.

4.1.8.4 Scrapers

The diagnostics straight contains 4 scrapers, two horizontal and two vertical. Each scraper is water cooled, but the outer scraper in particular will absorb some synchrotron light when it is inserted. The scrapers have mainly been for reducing beam current and to study the vertical aperture of the ring (Figure 30) to study the effects of in vacuum undulator installation.
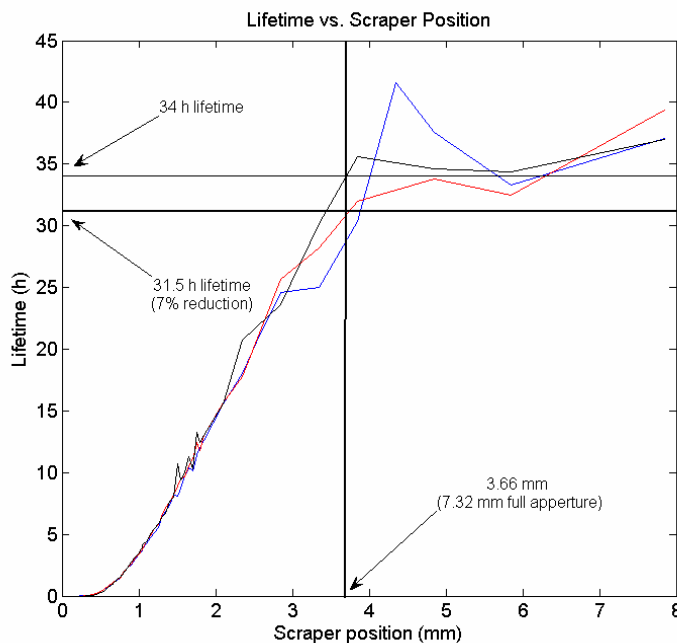
Figure 30: Lifetime as a function of vertical aperture.

4.1.8.5 Beam Position Monitors

Each of the 14 cells in the lattice has been fitted with 7 beam position monitors, totalling 98 BPMs, all of which are connected to Libera Electron Beam Position Processors (EBPPs) from Instrumentation-Technologies [19]. These are the most prolific of diagnostics and enables control over the closed orbit. The choice of location of the BPMs (and correctors) should in the first instance be guided by the phase advance of the lattice functions. Spreading the BPMs will ensure that lattice functions are properly sampled and maximises the ability to correct any closed orbit distortions due to magnet errors/misalignments. The usual rule of thumb is to have 4 BPMs to every 2π phase advance. For the AS lattice we have 7 BPMs and these should be considered optimal for the following reasons; 4 BPMs around the two gradient dipoles where the largest phase advance is located, one BPM also has to be located at the centre

to capture the beta and dispersion peak and two around the straight sections to monitor the beam in the straights (or insertion devices).
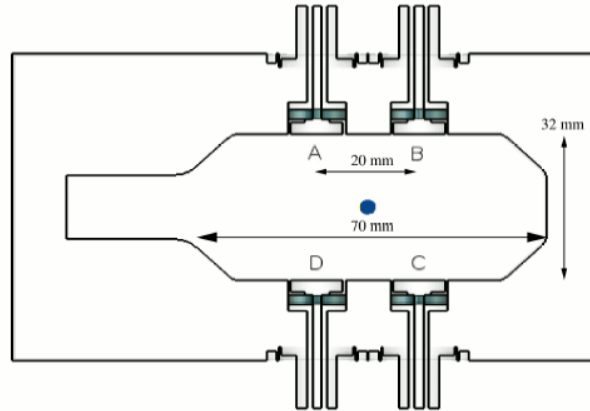
Figure 31: BPM cross-section showing button location and dimensions of a typical chamber. The buttons are 12 mm in diameter. The electron beam is going into the page.

The sensitivity of the BPMs at these locations to the motion of the electron beam is determined by the geometry of the BPM buttons (Figure 31). The inverse of the sensitivity value is also known as the BPM gain as shown in the following equation,

$$ x_{meas} = k_x \frac{V_C + V_B - V_A - V_D}{\sum V} \quad y_{meas} = k_y \frac{V_A + V_B - V_C - V_D}{\sum V} $$

where kx,y are the bpm gains, and VA,B,C,D are the induced voltages on the buttons. Solving the electrostatic problem numerically using POISSON it was possible calculate the gain factors. Simulating it as a static problem is valid if the bunch length (15.41 mm, FWHM) >= button diameter. The simulation results gave gain factors of around 14.6 mm in both planes while later measurements on the storage ring, using LOCO, gave values closer to 15.3 mm ±1%.

In the vicinity around the electrical centre of the BPM buttons the relationship between the measured position (x_{meas} and y_{meas}) and the actual position (x_{act} and y_{act}) is linear and starts to diverge as the position of the beam starts to move further away. This is known as the pincushion effect and it has been characterised in this simulation. Figure 32 shows the percentage error in position that one can expect due to this effect. As shown, within a region of $x = \pm3$ mm and $y = \pm2$ mm the apparent position is accurate to < 5%. Given that most studies will not involve orbits > 1 mm, real time inversion of the pincushion effect is not seen as necessary. Only in instances where large orbit deviations are required for beam dynamics studies will we need to invert this effect.
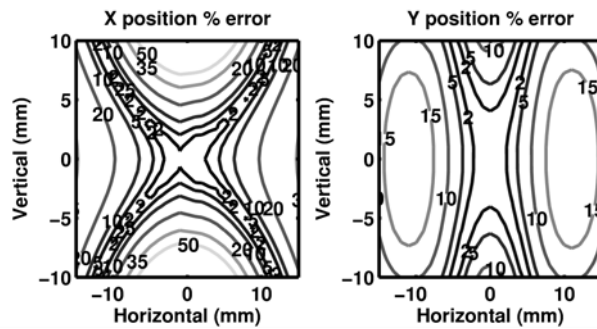
Figure 32: Error in the measured beam position due to the pincushion effect.

The detector electronics used to calculate the beam positions are called Libera Electron Beam Position Processors from Instrumentation Technologies [20] (Liberas). The package has an analogue front end to treat the 4 RF signals before going into 4 individual channels that digitises the signal using 12 bit ADCs. The digital waveform is then fed into an FPGA that does all the calculations to extract turn by turn (TBT) data (revolution frequency of 1.389 MHz). This data is then down-sampled to generate other data streams at 10 kHz (mainly for Fast Global Orbit Feedback systems) and at 10 Hz slow acquisition data (SA). The FPGA is also attached to a single board computer that is used to manage the system and distribute the data through our control system (EPICS).

The unit is pretty much self-contained and worked straight out of the box. Its requirements, aside from integrating it into the control system, were to provide timing and synchronisation signals to the Libera. There are two main signals that it requires; a clock at the revolution frequency to synchronise the units internal sampling clock and a general data acquisition trigger signal. These were generated from our timing system and fed into a custom built TTL fan-out unit that distributed the signal around the ring in a star formation.

The initial design of the system did not sufficiently take into account the issue of synchronisation. As a result of a combination of the time of flight of the electron around the ring, RF and timing signal cable lengths, each unit samples the bunch train at different periods (see Figure 33). This means that there is 1.5 turn ambiguity between the BPMs making it difficult to accurately quantify the specific motion of an electron bunch for a given turn. To get first turns, the TBT data was post processed based on the expected delays calculated using measured cable lengths.
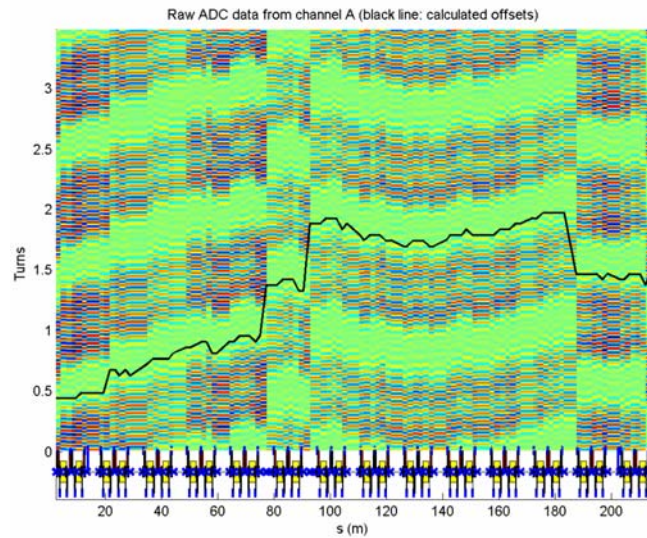
Figure 33: This is a surface plot of the raw ADC data for all the BPMs around the ring showing the electron bunch train as it circulates the storage ring. The line drawn on the plot shows the calculated offsets based on measured cable lengths. The measured and calculated offsets agree well.

The solution to the synchronisation problem has been made available in software by I-Tech by allowing the ability to set offsets to the sampling clock relative to the timing signal. This in effect gives us a variable delay on the sampling with a resolution of 32 ns and should resolve the 1.5 turn ambiguity. It has yet to be implemented here.
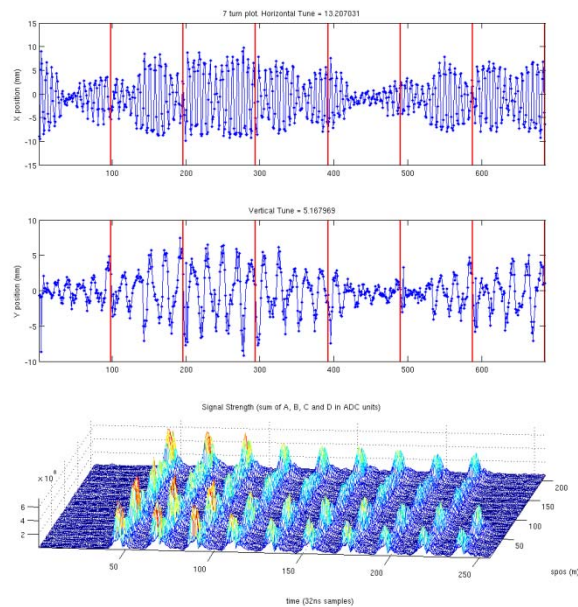
Figure 34: The beam position around the ring was plotted to show the oscillation for 10 turns (top and middle). The vertical lines represent one revolution. The sum signal was also shown to give an indication of how fast the beam was decaying.

Aside from timing and synchronisation there were also some software and hardware issues early on, however they did not impact significantly on our ability to use it for first turn measurements on the first day of storage ring commissioning. These issues were eventually resolved.

Having first turn data on hand during the first day of commissioning was very helpful and enabled us to quickly identify problems. Figure 34 shows a snapshot after achieving > 10 turns around the storage ring with a 75 bucket bunch train, ~21% of the total ring. From the position data it was possible to get an estimate of the tune so we could be confident we were near our nominal working point.

Under normal operating conditions these detectors were initially thought to be capable of measuring the beam position with an RMS of 0.2 μm for narrowband measurements, SA data and 6 μm for wideband, TBT measurements. Measurements of the resolution of the BPMs have been made and are shown in Figure 35. The results show that on average for our standard 80% fill the RMS on our SA data is ~150 nm while TBT data is ~8 μm. These values are quite good and in line with the current published specifications of the Libera Electron devices. It should be mentioned that given this is measured with beam it is possible that the beam itself is unstable. At present only resistive wall instabilities have been found and are identified by vertical oscillations that show up as the vertical tune in an FFT analysis. During the acquisition of the data for Figure 35 this was not observed.
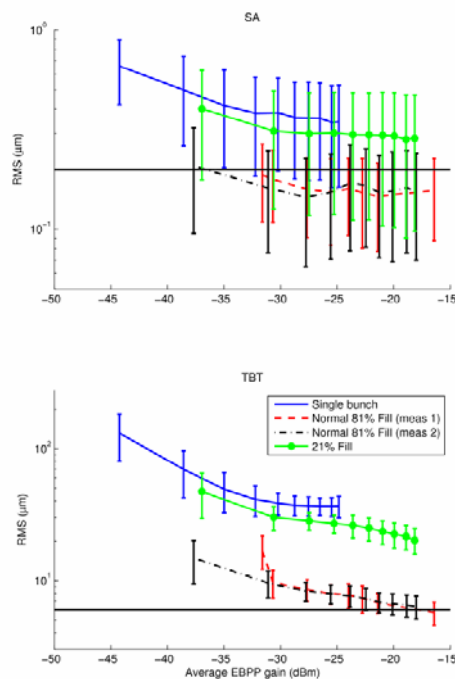
Figure 35: The plots show the average RMS resolution of the BPMs for various input powers and different fills. The error bars shows the deviation of the average RMS resolution between the BPMs. The horizontal line represents 0.2 μm (top) and 6 μm (bottom). Single bunch measurements were taken in 1 mA steps from 1–10 mA. 21% fill measurements were taken in 3 mA steps from 3–30 mA. 81% fill measurements were taken in 10 mA steps from 10–100/125 mA.

We have also observed some significant beam current dependence on the BPMs. At 30 mA we have signals that range between –22 and –37 dBm that increases to between –12 and –25 dBm at 100 mA. Between 30 and 100 mA, we have observed changes in the beam position by as much as 100 μm when the specifications are 12 μm (max). The changes have been shown not to be beam motion related and could possibly be related to a phase mismatch in the RF cables. Investigations carried out by Diamond [6] have shown that a mismatch of $> 30^{o}$ can result in significant increases in beam current dependence in the Libera units. This is still an ongoing investigation.

Mismatch in the RF cable attenuation can also result in artificial cross talk between the planes of the BPMs. Using the LOCO technique it was possible to fit the BPMs using the following formula and parameters:

$$\begin{bmatrix} x \\ y \end{bmatrix} = \begin{bmatrix} \cos(\theta) & \sin(\theta) \\ -\sin(\theta) & \cos(\theta) \end{bmatrix} \begin{bmatrix} 1 & C \\ C & 1 \end{bmatrix} \begin{bmatrix} k_x & 1 \\ 1 & k_y \end{bmatrix} \begin{bmatrix} x_{raw} \\ y_{raw} \end{bmatrix}$$

where θ is the BPM roll, $k_{x,y}$ are the BPM gains and C is the "crunch" value. It is the crunch that is a measure of the cross talk between planes. Simulations on an equivalent circular chamber (valid within a small region about the geometric centre of the buttons) have shown that a 0.2 dB difference in a single channel can result in a cross-talk of ~1%. In Figure 36 we see a plot of the cross-talk values fitted using LOCO and the simulated values using the measured attenuations of the BPM cables post-installation. The results show a good correlation after the measured values are offsets by 2%. This 2% offset is, unfortunately, inherent in the Libera analogue front-end and has been confirmed by I-Tech.
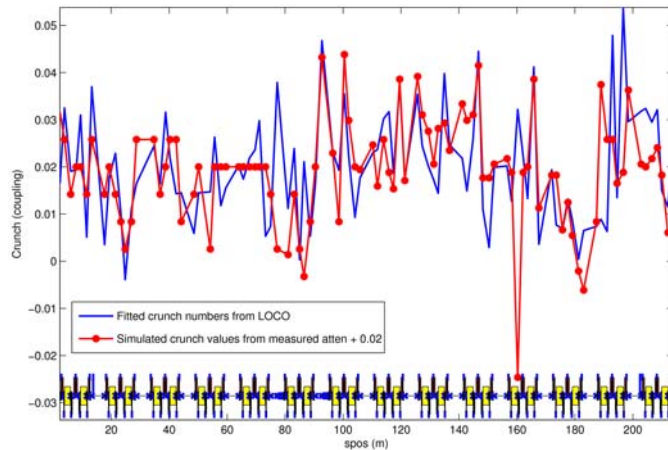
Figure 36: A good correlation between simulated cross-talk values based on measured attenuations and calculated values using LOCO. The 2% offset in the simulated data reflects the inherent properties of the analogue front-end of the Liberas.

The Liberas also have orbit interlock functionality and issues an interlock through an open collector at the back of the unit. The Libera uses the 10 kHz data stream to check for interlocking conditions and can issue an interlock in < 1 ms. The interlock is connected to the Equipment Protection System (EPS) which is made up of a series of

PLCs and has a latency of ~70 ms between the Libera issuing an interlocking signal and the beam being dumped. The AS requirement for orbit interlock is to dump the beam within 200 ms and this is currently implemented for all ID straight sections. Plans have been made to also include the IR beam line as the mirror is also sensitive to miss-steer.

4.1.8.6   Beam Loss Monitors

14 Bergoz PIN diode beam loss monitors were purchased and distributed around the ring using a Cosy-lab control system. The control system allows easy relocation of BLMs using a daisy-chain architecture. This means that we might choose to locate a single BPM in each sector, or locate 4 in one small area around an in-vacuum undulator for example.

This system has not been used significantly during commissioning. PIN diodes are not appropriate for transfer lines because of the short time that beam is present. Also, problems with calibration and measurement sensitivities have taken a long time to rectify. It is not confirmed weather these problems are associated with the Cosy-lab control system or the Bergoz beam loss monitors.

4.1.8.7   Optical Diagnostic Beamline

The Optical Diagnostic Beamline (ODB) was commissioned with a range of optical instrumentation to measure the longitudinal and transverse structure of the beam.   A list of the instruments and the initial data taken with them follows.

4.1.8.7.1 Streak Camera

The most useful optical instrument for use in detecting the visible part of the synchrotron radiation is the streak camera. It is a dual sweep 250 MHz type tube and provides the only direct measurement of the bunch length in the storage ring. Figure 37 shows a dual sweep trace of individual bunches in the bunch train taken during first light into the ODB.
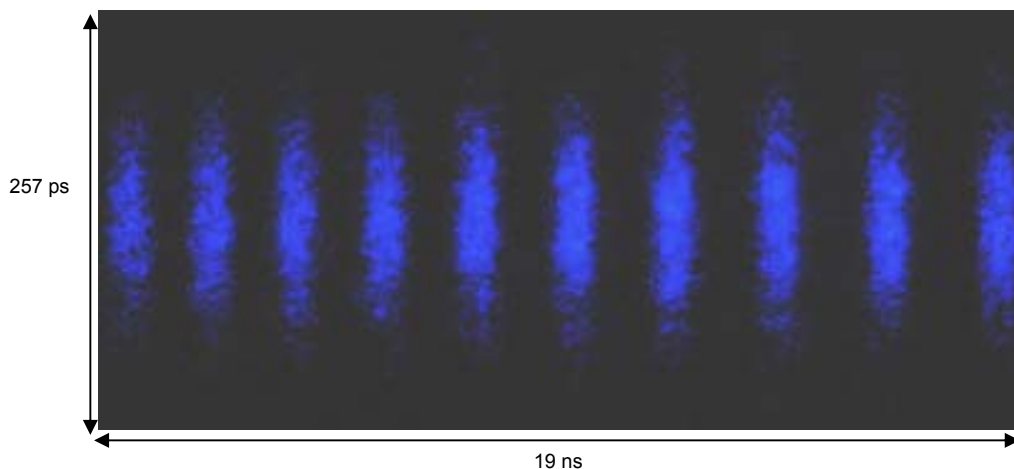
Figure 37: Streak Camera image of individual bunches in the storage ring.

4.1.8.7.2 Fill Pattern Monitor

To monitor the fill pattern in real-time and make it available in EPICS as a PV, a fast photodiode and a high speed digitiser were used to measure the light intensity of the bunch train with time. Figure 38 shows a comparison between the traditional method of monitoring the fill using a fast scope on a stripline pickup and the fill pattern monitor (FPM). The scope data only provides information that can be checked visually by an operator, while the FPM can be used for shot-to-shot targeting of individual buckets on a feedback loop controlling the injection timing.
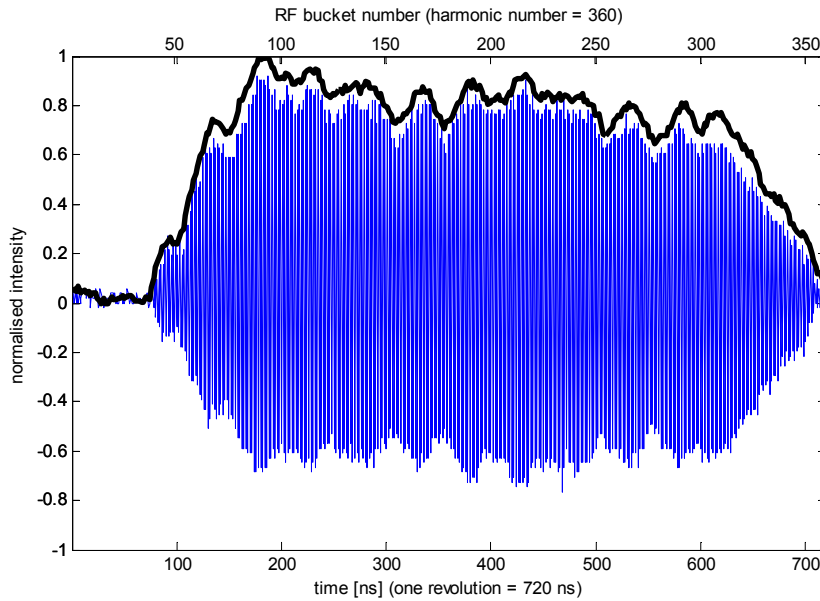
Figure 38: Comparison of the fill pattern measured on the optical monitor (thick black) and the stripline response on an oscilloscope (blue).

4.1.8.7.3 Position Sensitive detector

A position sensitive detector (PSD) with 1 μm resolution and a 1.4 MHz digitisation rate monitors the optical beam spot position. The data can give both transverse and frequency components to characterise the beam stability. During commissioning of the cavities there were several instabilities which were captured and are shown in Figure 39.
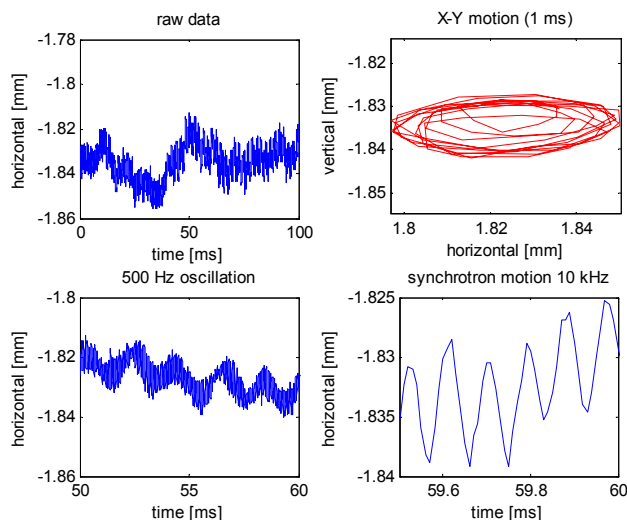
Figure 39: Beam stability measurements during RF cavity commissioning with a 2D position sensitive detector. At the maximum digitisation rate the synchrotron tune can be observed at approximately 10 kHz.

4.1.8.8   X-ray Diagnostic Beamline

The X-Ray Diagnostic Beamline (XDB) is an x-ray pinhole camera system and is contained entirely within the storage ring tunnel. It does not have a photon shutter and is therefore in continuous operation when the machine is running. The source point for the XDB is close to the centre of the second bend in sector 10. The XDB provides a simple but powerful diagnostic tool which will deliver data to the machine group as well as information to the machine status display for the users.

4.1.8.8.1 General Layout

Figure 40 shows the schematic layout of the XDB with a sketch of the beam profile measurement.
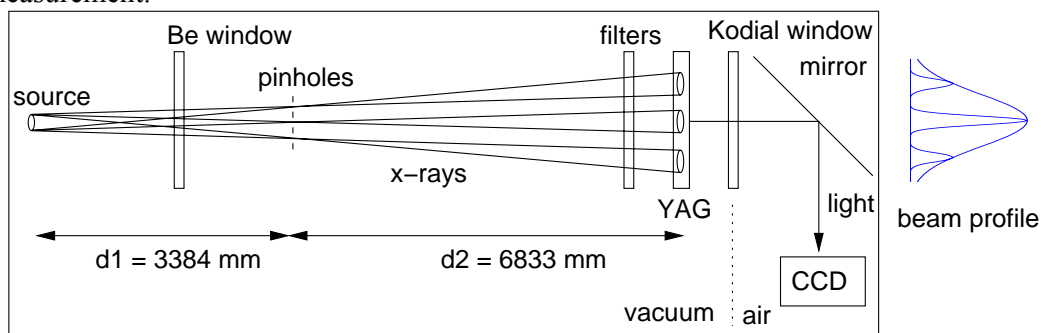
Figure 40: Schematic layout of the X-Ray Diagnostic Beamline viewed from side on.

The electron beam parameters for the source points are shown in Table 8 for the storage ring with the nominal lattice of zero dispersion in the straights and assuming 1% coupling.

Table 8: Electron beam parameters at the XDB source point from the design lattice model.

Parameter	XDB (bend 2)
β x (m)	0.386
β y (m)	32.464
σx (μm)	98
σx′ (μrad)	241
σy (μm)	72
σy′ (μrad)	7

The horizontal and vertical beam profile measurement will allow the beam size, divergence, emittance and position to be calculated and displayed in the control system. The nominal emittance is calculated to be 15.8 nm rad.

4.1.8.8.2 Pinhole Array

A pinhole array was chosen so both the beam size and divergence can be measured simultaneously. The array spacing is 1 mm along the horizontal direction and 0.5 mm along the vertical direction in order to capture more than five fully resolved images on the YAG screen. The intensity variation in the beam images on either side of the central beam provides a measure of the divergence of the beam (see beam profile in Figure 41). The circular pinholes are 20 μm in diameter, which is calculated to be the optimum size for minimising diffraction blurring and maximise resolution by following the calculations in [18]. The geometry of the XDB generates multiple images of the beam with a magnification of

$$M = d2/d1 = 6833/3384 = 2.02.$$

A typical image produced at the CCD camera is shown in Figure 41.
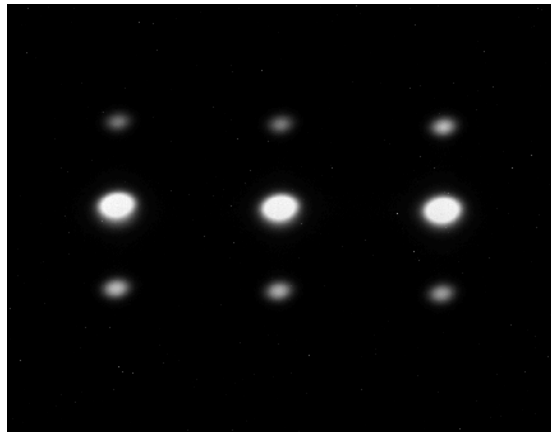
Figure 41: X-ray diagnostic beamline image array of the dipole source through the pinhole array.

The overall resolution of the XDB is expected to be approximately 10 μm. The electron beam size is estimated as follows:

Source-to-pinhole distance d_1 = 3384 mm,
Pinhole-to-YAG screen distance d_2 = 6833 mm,
Pinhole separation in horizontal p = 1 mm,
Beam spot separation on YAG screen:

$$a = p\frac{d_1 + d_2}{d_1} = 3.02\,\text{mm}.$$

Beam spot on the YAG screen σ_{YAG} = 229.3 μm,
Electron beam spot is:

$$\sigma_x = \frac{\sigma_{YAG}}{M} = \frac{229.3}{2.02} = 113.5\,\mu\text{m}.$$

Using the same technique the vertical beam size is determined to be:

$$\sigma_y = 46.6\,\mu\text{m}.$$

4.1.8.8.3 Filter Array

A filter array holds up to four foils that can be inserted into the beam by remote control to filter the photon beam. Adding filters reduces the intensity of the x-ray beam at high electron beam currents and improves the resolution of the measurements.

4.1.8.8.4 Imaging Cross

The x-ray images made by the pinhole array are projected onto a 100 m thick YAG crystal positioned perpendicular to the beam. The visible light that fluoresces from the YAG screen is deflected down out of the beam plane and digitised by a Firewire camera (Flea Hi-Res IEEE-1394 camera from Point Grey Research [19]). The camera has a fixed focal length lens and is triggered by the timing system. The control system is capable of providing a continuous stream of size, position and emittance data from the XDB as well as an image for the beam status screen. The Be window at the start of the beamline (see Figure 40) prevents any unwanted visible light from reaching the imaging cross.

4.1.9 Timing System

4.1.9.1 Timing for LINAC Commissioning

The timing system evolved over the course of the commissioning. To begin with the e-gun and the linac were triggered using stand alone programmable delay generators (PDG) by Stanford Research Instruments (model DG535). These were sufficiently stable to trigger the gun board and the PFNs to the klystrons at 5 Hz for conditioning of the RF structures in the linac (normal operation is 1 Hz). TTL triggers were generated

to pre-trigger the PFNs, followed by the klystrons, and then the e-gun was triggered along with the RF measurement modules for the diagnostic system. The length of the e-gun trigger pulse was varied with the PDG in order to control the emission of a single bunch or a bunch train of up to 75 bunches (150 ns). Since the e-gun rack is at −90 kV relative to the ground in the timing cabinet, an optical-fibre link was installed to convert the TTL signal to a light pulse and then back to an electrical pulse for the gun board.

During the early stages, while commissioning the linac independently of other components, the PDG internal 10 MHz reference signal was used as a time base. This internal clock was used up until instabilities were later observed in the booster extraction and storage ring injection process that appeared to be trigger related. This will be discussed in more detail later. Figure 42 shows the timing setup for the standalone commissioning of the linac during RF condition of the structures, prior to synchronizing with other subsystems of the injection system.
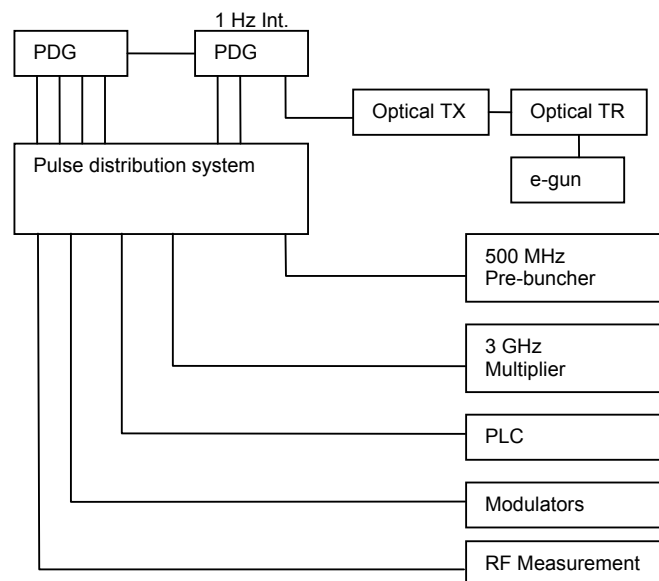
Figure 42: Timing system configuration for standalone commissioning of the linac systems.

When commissioning the linac in stand-alone mode the timing requirements were not stringent, accuracy of around 1 μs was sufficient to time the RF pulse with the gun pulse and to trigger the cameras observing the YAG screens. In multi-bunch mode, the 500 MHz modulation on the e-gun determined the timing of the bunches with respect to the RF buckets, so the <100 ps jitter on the PDG for short delays was more than sufficient.

4.1.9.2   *Mains frequency and Master Oscillator Synchronization*

Once RF conditioning was completed, additional synchronization was required for commissioning with beam. In order to stabilise the gun current and remove fluctuations caused by amplitude variations in the 50 Hz mains supply, our trigger generator unit (Micro-Research Finland EVG-200 [23]) was designed to provide an injection trigger at a nominal 1 Hz that is synchronised to the Master Oscillator (MO) and the 50 Hz. This

trigger is then sent to a collection of PDGs to set delays for the pulsed and ramped magnets in the injection system. Synchronising the trigger to the mains frequency also helps to ensure the stable operation for our pulsed magnets.

4.1.9.3   *Jitter reduction for DG535s*

At this point the stability of the internal reference clock in the PDGs became an issue, since the delay from injection to extraction in the booster is >600 ms. In order to reduce the drifts from one PDG to another, one PDG was chosen to be the master and its 10 MHz reference clock was distributed in a daisy chain to the others. During the booster commissioning this configuration proved sufficiently stable to deliver beam to the start of the booster-to-storage ring transfer line, where an FCT was used to detect the extracted beam. The FCT was used to diagnose if the beam was successfully extracted from the booster and also gave a measure of the extraction kicker timing jitter. The expanded timing system that was used to commission the whole injection system is shown schematically in Figure 43.
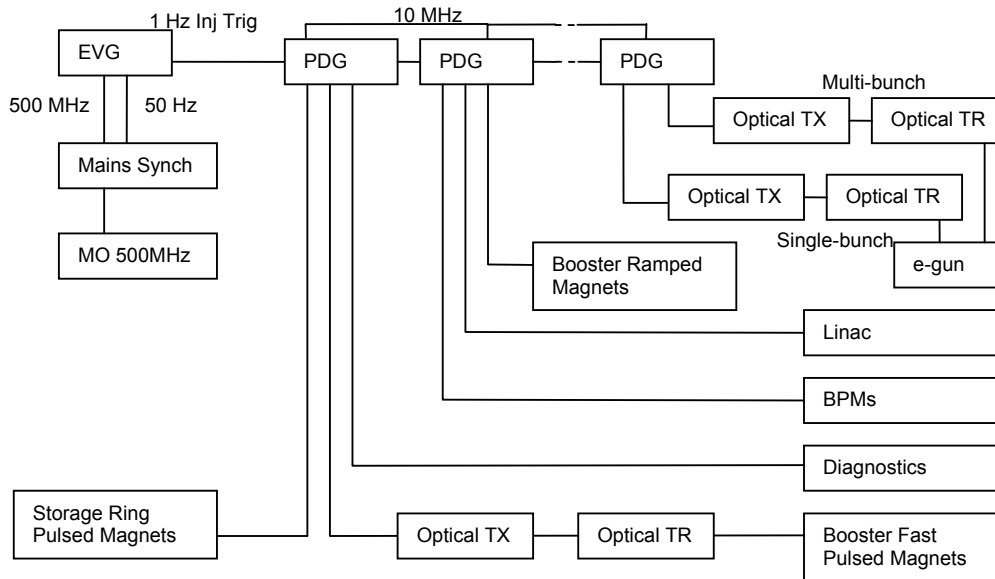
Figure 43: Timing System for commissioning of the whole injection system.

A continuous 8 hour stability demonstration test was performed on the injection system using the above timing system and the result was a >95% extraction efficiency of bunches from the e-gun to the FCT in the BTS. To some extent this demonstrated the timing stability, however the more critical test was the injection efficiency and stability into the storage ring, since the matching of the injected beam to the stored beam is a more sensitive procedure than extracting through the FCT in the BTS. At this point in the commissioning it became critical to improve the stability of the timing system. The first sign of instability with the commissioning timings system was the jitter in single bunch mode. Since there is no 500 MHz modulation on the gun when in single-bunch mode, the trigger from the timing system determines the emission of the bunch, so this trigger needs to be stable relative to the RF buckets in the booster. Figure 44 shows the RF jitter when the scope is triggered on the single-bunch pulse to the gun. The $3\sigma \sim$ 300 ps jitter can be unfolded into approximately 200 ps apparent jitter quoted by the

PDG manufacturer [22] that can be expected when observing on a scope, plus a similar jitter from the optical link pulse converter to the gun rack.
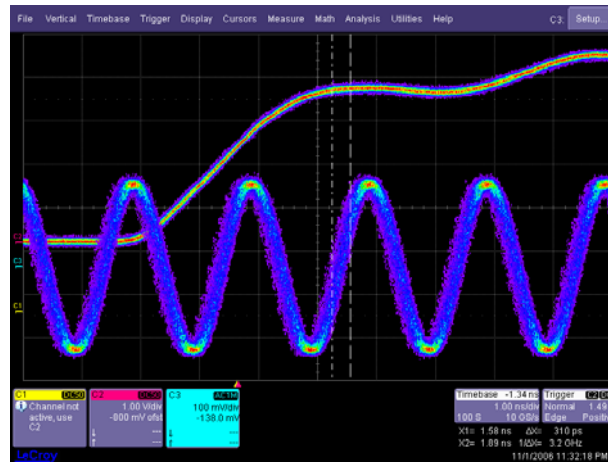
Figure 44: Single-bunch trigger jitter relative to the Master Oscillator 500 MHz signal on a 600 MHz scope.

In addition this timing jitter translated into an energy jitter in the linac where the 3 GHz RF pulses are even more sensitive to the phase at which the bunch arrives due to the shorter wavelength. Adjusting the phase in the booster RF relative to the linac removed some of the timing jitter effect, but the bunch purity was quite poor for single bunch mode during the commissioning phase. Figure 45 shows there is a small pigmy bunch following the main bunch as measured on the FCT in the BTS with a 3 GHz scope. The 2 ns spacing corresponds to the 500 MHz RF bucket structure in the booster and the amplitude of the second bunch indicates a significant bucket spillage at some point in the acceleration process. This level of impurity of a few percent is unacceptable for accurate time resolved experiments with a single bunch in the storage ring.
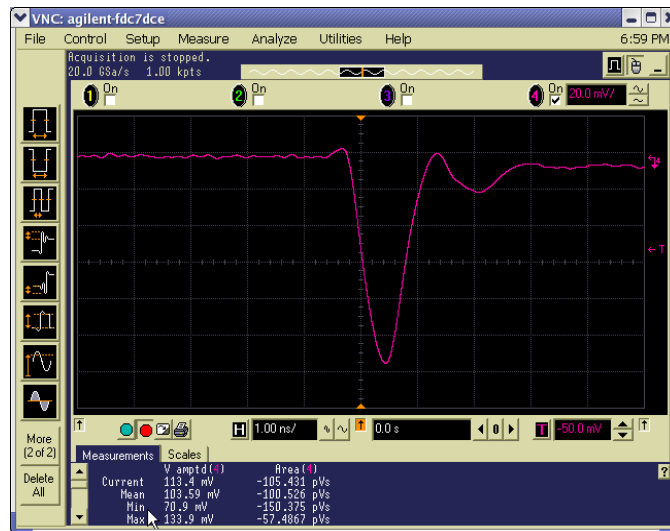
Figure 45: FCT pulse measured in the BTS with a 3 GHz scope showing a pigmy bunch following the main single bunch.

In addition to the single bunch jitter, there was a non-linear increase in the jitter from the PDGs with increasing output delay. This jitter was both in the time from the input trigger to the output trigger and jitter between the different output channels. The former affects the extraction magnets in the booster and the storage ring injection magnets. All these elements are triggered around 600 ms after the gun trigger which introduces a significant jitter. The magnitude of the two types of jitter from the PDG output triggers are shown in Figure 46 and Figure 47 which are provided by the manufacturers. From Figure 46 the jitter using an internal time base and a 600 ms delay results in a jitter of ~7 ns. In the case of the storage ring kickers, an additional jitter between each of the PDG outputs is also present.

Figure 47 show that even for 10 ns delay between channels there is a ~800 ps jitter, and adding that in quadrature results in an additional 1.6 ns jitter in theory. The relative jitter was measured to be up to 3.5 ns as seen in Figure 48. Another problem with the commissioning configuration was the poor quality and long lengths of some of the timing cables, which is also demonstrated in the very slow rise times (>20 ns) in the trigger pulses in Figure 48.

Some of these issues were addressed in the operations timing system described in the following section. The main lesson learned from the commissioning timing system was to synchronise the time base of the PDGs due to the long delay times involved with a 1 Hz injection system repetition rate.
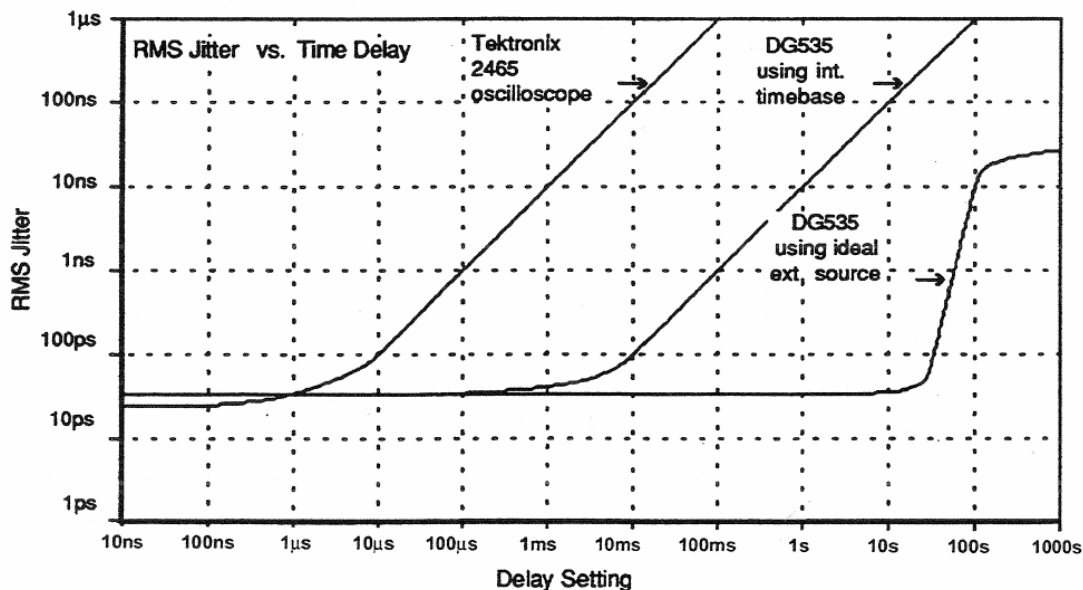
Figure 46: Plot of increasing jitter with output trigger delay in PDG. (Source: Stanford Research Systems Ref [22] p. 8.)
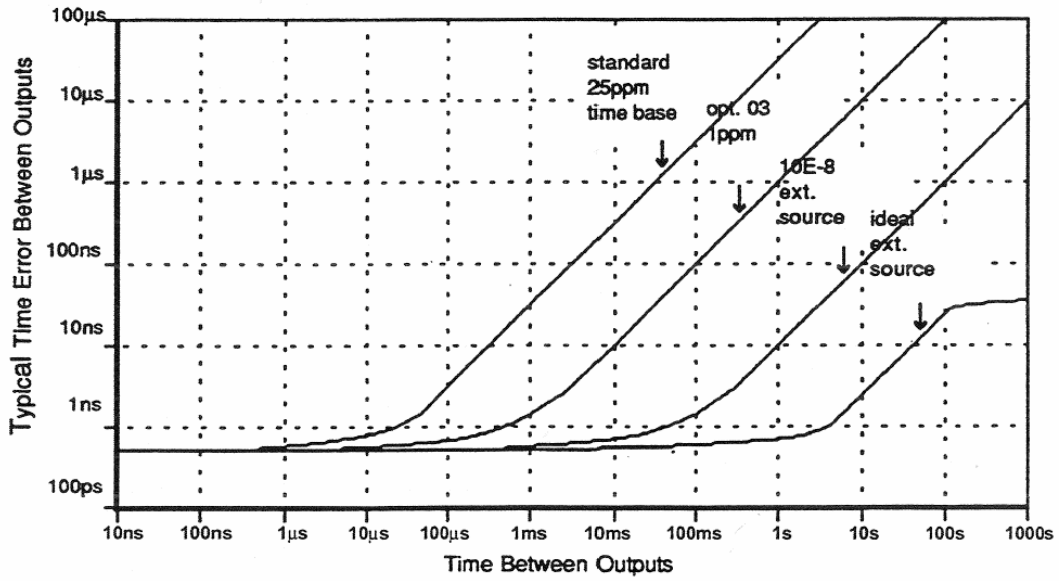
Figure 47: Plot of increasing trigger jitter between channels on PDG. (Source: Stanford Research Systems Ref [22], p. 6.)

Figure 48: Relative jitter in the four PDG out puts to the storage ring kickers with a ~600 ms delay.

4.1.9.4 Improved Timing System for Operations

The main issues that needed improving in the timing system for a stable operations system were:

1. reduced jitter on the e-gun trigger,
2. synchronization of the time base on all PDGs to the MO,
3. reduced jitter in the long delay triggers, and
4. improved rise time in the long cable length runs.

It was decided that the most cost effective and best available off the shelf solution to address the issues above was to expand the event system from Micro-Research Finland. During commissioning the event generator was only used to produce an injection trigger and an orbit clock trigger synchronized with the 500 MHz MO and the 50 Hz mains. However, if used in conjunction with event receivers a far more powerful and flexible timing system can be built. During commissioning of the linac, a control system error in setting the e-gun pulse length resulted in burning up the gun and blowing-up the gun pulser board. Based on this experience it was also decided that the new gun pulse transmitter and receiver modules from Micro-Research were also worthwhile installing in the timing system. A schematic of the operations timing system now is use can be seen in Figure 49.

At present the event system is limited to providing only the following triggers:

1. single-bunch trigger,
2. multi-bunch trigger,
3. 1 Hz clock,
4. 1 Hz injection trigger (mains synchronized),
5. storage ring orbit clock (500 MHz / 360), and
6. 500 MHz RF reference.

In this configuration the gun trigger jitter has been reduced to only a few ps, improving the linac stability. It has also provided a very low jitter (<10 ps) and a fast rise time (<0.5 ns) trigger for the streak camera on the optical diagnostic beamline used to measure single bunch phenomena including the storage ring bunch length. Many of the PDGs have remained in place from the commissioning system. In the operations system they are now provided with a 10 MHz reference signal from the MO which reduces the jitter for long trigger delays (see Figure 46). The EPICS control interface to the gun transmitter and receiver system provides a 2 ns delay (with 10 ps resolution fine control) to hit any RF bucket in the storage ring, including a pre-programmed pattern fill algorithm for arbitrary fill sequences. The sequencer controlling the injection would sometimes drive the single-bunch trigger high during tests. To prevent pulses of >1 μs from passing through to the gun, a pulse clipper was installed just before the gun trigger board. This protection prevents the gun and trigger board from being destroyed as happened during commissioning.
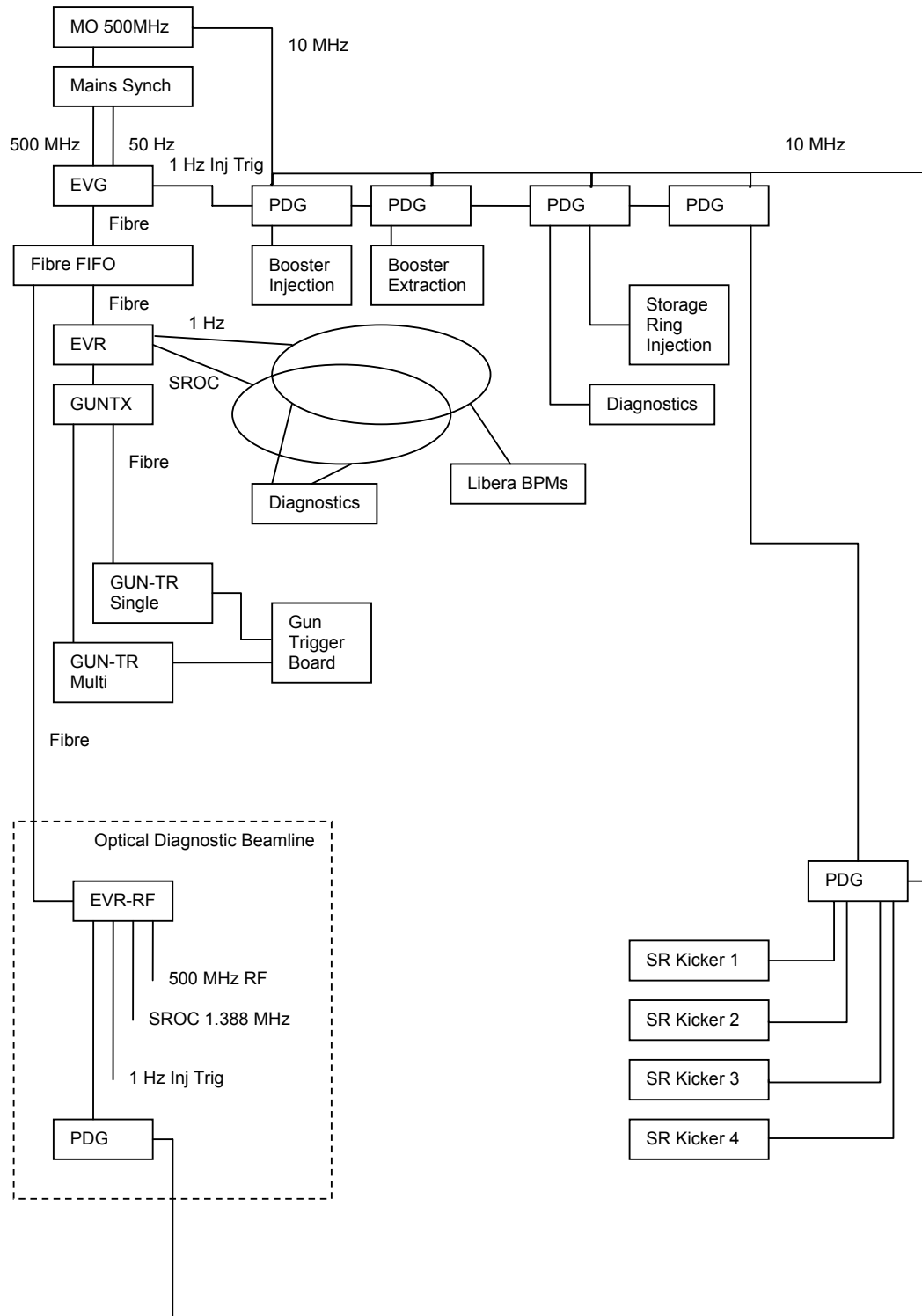
Figure 49: Operations timing system based on an event system.

The event system currently consists of the following VME modules:

1. EVG-230
2. EVR-230
3. GUN-TX
4. GUN-TR (single and multi bunch, non-VME separate power supply)
5. EVR-230RF (500 MHz RF recovery for streak camera synchroscan)
6. FOUT Fibre 12 slot expansion board

As shown in Figure 49, the 1 Hz is distributed to all the Libera BPM electronics in the storage ring which is used to trigger the turn-by-turn data acquisition. The 1 Hz and SROC timing signals are currently distributed along coax-cables in a star pattern to each equipment rack, with local fan-out PCBs that were developed in-house. Diagnostic devices such as scopes and spectrum analysers are also triggered off these signals.

4.1.9.5   *Future Developments*

In the future the timing requirements will become more demanding as the facility prepares for top-up operations. The first stage in this process will be to further reduce the jitter in the triggers by installing a fibre distribution network with more event receivers. This will reduce the attenuation and the slow rise times on signals currently sent by long length coax-cables. It will also allow for more flexible programming of the pulsed elements that will need to be kept on and inhibited, but ready to be triggered once every two to three minutes. For most applications it will eliminate the need for PDGs, except were ps resolution is required. Certain diagnostic equipment also requires a synchronized trigger in the kHz range, which lies in between the current trigger frequencies of 1 Hz and 1.388 MHz. This can easily be achieved by dividing the event clock by up to 65536 [24] (e.g. 125 MHz/65536 = 1.9 kHz).

4.1.10 References

1. E. Meier et al., submitted to NIMA.
2. G. Blokesch et al, NIMA 338, 151-155 (1994).
3. J.W. Boldeman, D. Einfeld, "The physics design of the Australian synchrotron storage ring", Nuclear Instruments and Methods, 521 (2004), 306-307.
4. G.S. LeBlanc, et. al., "The Australian Synchrotron Project Storage Ring and Injection System Overview", in proceedings of EPAC, 2004, p. 2263.
5. M. Spencer, "LOCO at the Australian Synchrotron", this ICFA edition.
6. Y.-R.E. Tan, et. al., "Applying Frequency Map Analysis To The Australian Synchrotron Storage Ring", in proceedings PAC, 2005, p 407.
7. J. Laskar, "Frequency Map Analysis And Quasiperiodic Decompositions", in proceedings of the School Hamiltonian Systems and Fourier Analysis, 2001.
8. L. Nadolski, J. Laskar, "Review of Single Particle Dynamcis for Third Generation Light Sources Through Frequency Map Analysis", Phys. Rev. ST AB, 6:114801, 2003.
9. C. Steier, et. al., "Measuring and Optimizing the Momentum Aperture in a Particle Accelerator", Phys. Rev. E, 65(056506), 2002.
10. M. Yoon, et. al., "Analysis of a Storage Ring Combined-Function Magnet: Trajectory Calculation and Alignment Procedure", NIM A, 523, pp 9-18, 2004.
11. G. Portmann, et. Al., "An Accelerator Control Middle Layer Using Matlab", in Proceedings PAC, 2005.

12. R. Gluckstern, J. Zeijts, "Coupling impedance of beam pipes of general cross section " B. Zotter, Phys. Rev. E, 47 (1993) 1
13. T. Koseki, M. Izawa, and Y. Kamiya, Rev. Sci. Instrum. 66(2), Feb. 1995, p1926
14. J. Wantabe et. al., Design and Cold Model Test of 500MHz Damped Cavity for ASP Storage Ring RF System, PAC 2005 proceedings, Knoxville
15. J. Wantabe et. al., Higher Order Mode (HOM) Damper of 500MHz Damped Cavity for ASP Storage Ring, EPAC 2006 Proceedings, Edinburgh
16. M. Spencer, et. al,. "Diagnostics and Timing at the Australian Synchrotron", EPAC, 2006.
17. Julien Bergoz, private communication.
18. W. B. Peatman and K. Halldack, J. Synchrotron Rad. 5, 639-641 (1998).
19. Point Grey Research, <http://www.ptgrey.com>.
20. A. Kosicek, "Libera Electron Beam Position Processor", in Parcitle Accelerator Conference, 2005, p. 4284
21. G. Rehm, et. al,. "Digital EBPMs At DIAMOND: Operational Experience And Integration Into A Fast Global   Orbit   Feedback", DIPAC, 2007.
22. Stanford Research Systems, MODEL DG535 Digital Dealy/Pulse Generator Operation and Service Manual, Revision 2.8, 04/2005, page 7, Figure 4.
23. Micro-Research Finland Oy, Valitalontie 83 C, FI-00660 Helsinki, Finland.
24. Micro-Research Finland Oy, EVR-230TREF-001, 11 May 2007, p. 7.

4.2 Commissioning of the Storage Ring of SOLEIL, the French 3rd Generation Synchrotron Radiation Facility

JM Filhol, C Herbeaux, A Nadji, N. Bechu, JC Besson, F Bouvet, P Brunelle, L Cassinari, ME Couprie, JC Denard, JF Lamarre, P Lebasque, MP Level, A Loulergue, P Marchand, L Nadolski, R Nagaoka, MA Tordeux
Synchrotron SOLEIL, BP 48, F-91192 Gif-sur-Yvette, France
Mail to: jean-marc.filhol@synchrotron-soleil.fr

4.2.1 Introduction

SOLEIL is a third generation Synchrotron radiation Source, located in France near Paris. The Storage Ring consists in a 354 m circumference ring, with 16 cells and 24 straight sections, out of which up to 21 can house Insertion Devices (ID). The optics features a low 3.7 nm.rad emittance at the 2.75 GeV operating energy, so as to provide high brilliance, from the VUV up to the hard X ray domain. In order to reach a long beam lifetime, and beam position stabilities in the micron range, significant attention was paid at each design stage (optics, magnets, beam position monitors, vacuum and RF systems,..), including during the design of the building. This resulted in some unprecedented approaches such as the intensive use of NEG coating vessels, or the development of a dedicated SC RF cavity and of 200 kW solid state RF amplifiers. The injector system (110 MeV Linac) and the 3 Hz full energy Booster synchrotron have reached nominal operating conditions by fall 2005 [1,2], while the ring commissioning started in May 2006. Innovative ID's were designed and built so as to provide the best possible performances in a wide energy range (5 eV to 50 keV) [3]. This paper will mainly focus on the commissioning results and on the performance of the vacuum system.

4.2.2   Storage Ring description

4.2.2.1   Lattice

The SOLEIL storage ring consists of 16 Double Bend cells and 4 super periods. The 2 central cells of these later are modified to create 2 additional straight sections (3.6 m) by drifting apart the two quadrupole doublets located in-between the two bending magnets of the cell [4]. The machine provides 24 straight sections (4x12 m, 12x7 m, 8x3.6 m) with a circumference of 354.097 m. The injection occupies one long straight and the RF cavities occupy two medium straights. The magnet structure is composed of 32 bending magnets, 160 quadrupoles with independent power supplies grouped into 10 families and 120 sextupoles powered in 10 families. The orbit correction is performed using 120 BPMs and 56 correctors in each plane. The lattice, with distributed dispersion in the straight sections, is designed to achieve an emittance of 3.73 nm.rad at 2.75 GeV. Figure 1 shows the optical functions of one of the four super periods.
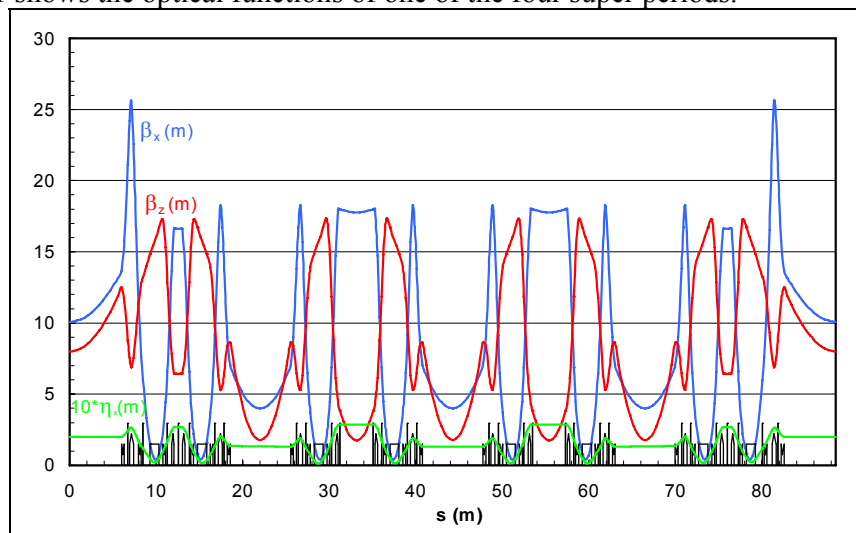
Figure 1: SOLEIL storage ring optics.

4.2.2.2   Specific Equipment

4.2.2.2.1   Supporting structure

The synchrotron building was designed so as to minimize the transmission and amplification of vibrations: The very thick storage ring and experimental hall slabs (95 cm and 75 cm respectively) are lying on 600 piles, 15m deep, whilst the other parts of the building (metallic frame supporting the roof and the cranes, technical rooms, labs, circulation path) are resting directly on the ground. This provides an excellent decoupling between the "noble" areas and the place where vibrations could be generated: the resulting vibration at the SR slab level was measured well below 1 μm, and at frequencies below 20Hz. The girders supporting the magnets were optimised so as to push the first eigen modes of vibration towards high frequencies. They are made of very massive supporting beams strongly clamped onto the SR slab. The dipole magnets

are sitting on 2 adjacent girders. As a result, the first eigen mode of the girder appears at 45 Hz, i.e. quite far away from the frequency domain that can be amplified by the slab.

4.2.2.2.2 Superconducting RF cavities

Special care was devoted to the longitudinal stability of the electron beam, so superconducting technology was adopted for the RF cavities. Two cryomodules, each containing a pair of superconducting cavities are required to provide the maximum power of 600 kW needed at 500 mA. The first cryomodule, was specifically designed by the CEA and CERN, was tested on the ESRF Storage Ring in 2002, was then refurbished and finally tested at CERN : Its performances exceed the requirements for the SOLEIL normal operation: 150 kW per coupler and 1.5 MV per cavity. It was installed on the ring in November 2005, cooled down and RF conditioned in May 2006 and will, alone, enable operation up to 300 mA [5]. A second cryomodule, being built by ACCEL will allow reaching 500 mA in 2008.

4.2.2.2.3 Solid state RF amplifiers

Each of the four cavities is powered by a 190 kW solid state amplifier consisting in a combination of four "towers" producing about 50 kW each. The solid state amplifiers, technology specifically developed at SOLEIL, combine the RF power amplified by a large number of 315 W elementary modules (150 for the booster amplifier and four sets of 180 ones for each 190 kW storage ring amplifier). A first step was reached in 2004 with the operation in CW of the 35 kW-352 MHz solid state amplifier of the booster. In April 2006, the two amplifiers of the storage ring were able to deliver each 180 kW to a dummy load which is a world record with this technology. Since then, they have been running very smoothly powering the 2 cavities during the SR commissioning.

4.2.2.2.4 Insertion Devices

SOLEIL, thanks to the high straight section length over total length ratio, can accommodate up to 24 insertion devices for 21 beamlines. The energy range covered by the SOLEIL Insertion devices (ID) extends from the UV to VUV, soft and hard X ray range, following a shortening of the period length. The first four undulators, HU640, HU256, H80, U20[3] were already installed before the start of the commissioning and did not lead to specific difficulties. Magnetic design was carried out and optimised using RADIA and SRW. The predicted effects of the ID's on the stored electron beam were computed with the codes BETA and TRACY2, leading to tolerances regarding field integral, trajectory and high orders harmonics of magnetic fields for each specific device. After magnetic shimming, significant beam time was dedicated to define the feedforward correction tables that enable to reduce within a few μm the stability of the closed orbit when changing the field of these ID's [3].

4.2.2.3 Vacuum system description

4.2.2.3.1 Vacuum vessels

The design of the vacuum vessel of a storage ring must fit with three requirements:
- Achievement of the required quality for vacuum (pressure and gas composition)

---

[3] The number refers to the magnetic period in mm

- Dissipation of the radiated power deposited on the vacuum vessels
- Reduction of the impedance effects.

At SOLEIL, a mixed solution for the material of the vessels has been chosen:

- 6060 T6 extruded aluminium for all the straight vacuum vessels in association with NEG coating (quadrupole type and insertion device vacuum vessels). Water cooling channels were extruded at the same time than the beam tube.

- 316LN and 316L stainless steel for the dipole vacuum vessels, the BPM's, the bellows and the taper of the straight sections and any other vacuum components like valve, pumps, gauges,…

Bimetallic Conflat type flanges made of explosion bonded aluminium stainless steel material, provided by ATLAS Technology are used to connect aluminium to stainless steel vacuum vessels.

The power radiated in the bending is dissipated by copper or Glidcop water cooled photon absorbers located in dipole and taper vessels. The so called crotch absorber placed just downstream the dipole magnet has been design to evacuate 8.8 kW @ 500 mA.

4.2.2.3.2 Pumping system

The vacuum system of the SOLEIL storage ring had been initially designed using standard pumps like Sputter Ion Pumps (SIP) and Titanium Sublimation Pumps (TSP). Following the results observed at ESRF and other synchrotron facilities, it was decided to use Non Evaporable Getter (NEG) coating in addition to the foreseen traditional pumps.

Conventional pumping: The SIP's have been distributed around the storage depending on the local outgassing. 150 $l.s^{-1}$ SIP have been place at pumping ports of the quadrupole vacuum vessels and close to the absorbers of the taper. 400 $l.s^{-1}$ SIP have been placed close to the crotch absorbers where the outgassing induced by the PSD, was expected to be the higher.

In addition to the SIP's Titanium Sublimation Pumps, 250 l.s-1, have been placed at pumping ports of the quadrupole vacuum vessels and at the upstream pumping port of the dipole vessel.

In total the conventional pumps provide a 60.000 $l.s^{-1}$ nominal pumping speed distributed along the circumference of the ring.

NEG coating: The NEG coating technology, developed at CERN [6], consist on a deposition by magnetron sputtering of a layer of ternary alloy of titanium, zirconium and vanadium (30%, 30% and 40% respectively). It has been shown that after activation, the NEG coating can reduce drastically the Photon Stimulated Desorption effect [7], hence the conditioning time.

At SOLEIL, in addition to the standard pumps, the use of NEG coating has been implemented in an extensive way to all the aluminium straight vacuum vessels of the storage ring that means quadrupole type and insertion device (ID) vacuum vessels which represent a total length of 200 m that is about 56% of the circumference (see figure 2).

In the case of the quadrupole vessels, it was not possible to coat the pumping ports so the NEG layer is present only on the electron beam tube. To assess and compare the

beneficial vacuum properties of the NEG coating, one cell of the ring has been equipped with special quadrupole vacuum vessels without pumping ports that is to say without traditional pumping means.

NEG coated extruded aluminium vessels in the straight sections: The 10 medium straight sections have been equipped with 5.3 m long 10 mm vertical aperture vessels. 7 of the 8 short straight sections (dedicated for the installation of the in-vacuum undulators) have been initially equipped with 2.5 m long quadrupole type vessels (2 of them have now been replaced by in-vacuum undulators). A 10.5 m long NEG coated vacuum vessel with a vertical aperture of 14mm has been installed on one of the long straight section without any additional pumping. As no NEG coating facility for a so long vessel was available, it has been fabricated from two 5.3 m long vessels, NEG coated and then welded together. Care was taken to prevent any destruction of the NEG layer in the vicinity of the welding.
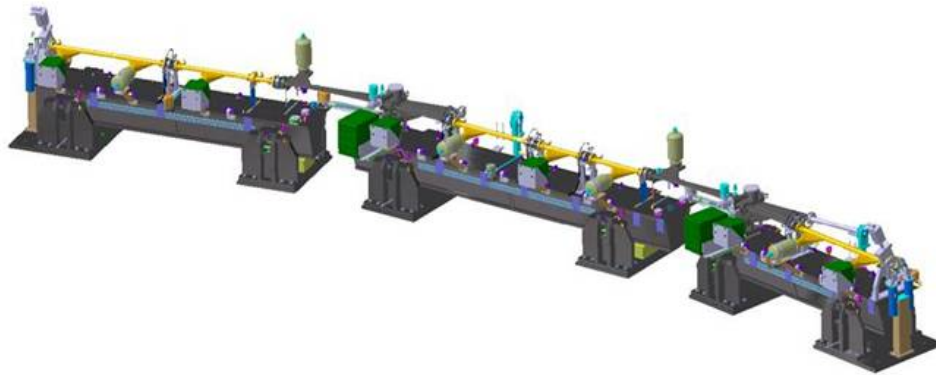
Figure 2 : Vacuum system of a typical cell. In yellow the aluminium coated quadrupole vessels. In grey the stainless steel vessels.

The effect of the NEG coating on the resistive wall impedance has been evaluated [8]. It has been shown that a large roughness of the deposited layer may increase the ring impedance. A roughness of Ra = 0.3 µm of the substrate surface was measured. This value was not increased by the NEG coating. In addition, the roughness is lower in the extrusion direction, the same than the electron beam direction. The layer thickness must be kept as small as possible in the area where the image current density is larger. A sputtering with two cathodes allowed us to deposit a non uniform layer with a thickness of 0.5 µm on the horizontal surfaces of the beam channel, where the current density is large, and 1.5 µm on the vertical sides where the primary photons flux is the highest.

4.2.2.3.3 Bake out process

The NEG coating was activated at 180°C during the bake out of the vacuum system. As the vacuum system is composed of a mixture of coated Aluminium vessels and non coated stainless steel vessels, a particular bake out procedure has been applied. First the stainless steel parts were heated at 180°C during at least 24 hours while keeping the

coated vacuum vessels at 100°C. Then the stainless steel parts were cooled down to 100 °C and the NEG coated parts were heated at 180°C for activation. When an activation rate of 90% was reached, the stainless steel was cooled down to room temperature. Finally the NEG coated parts were cooled down to room temperature. (see Figure 3).
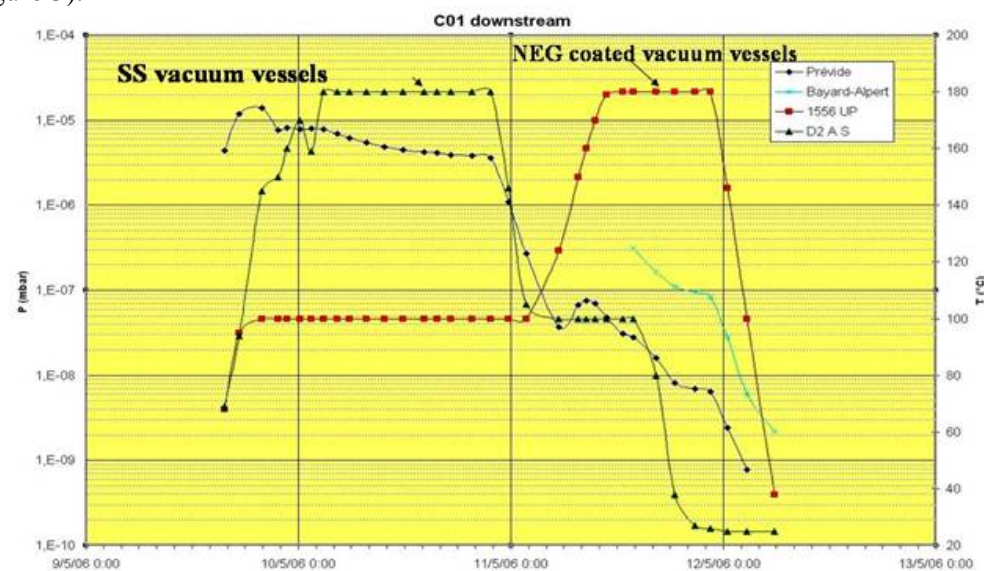
Figure 3 : Bake out sequence of one cell showing the temperatures applied to the Stainless steel parts and to the NEG coated aluminium parts.

4.2.3   Commissioning

4.2.3.1   Challenges

Before injecting the first electrons, the storage ring was incorporating equipment integrating new technologies and challenging issues which potentially, could have jeopardized the commissioning schedule:

Limited vertical aperture: All the ID vacuum chambers were installed on the 10 medium straight sections (10 mm vertical aperture 5 m long) and on the 3 long straight sections (14 mm vertical aperture 10 m long). Moreover 4 insertion devices (1 Apple II type, 1 in-vacuum and 2 electro-magnetic undulators) were already in place.

Beam loss restriction: After the first days, during which the tunnel radiation shielding was validated, radiation monitors were installed all around the ring (ionization chambers for gamma rays detection on the tunnel roof, and neutron detectors along the inner wall), with interlocking levels set to 2 micro-Sievert over 4 hours period, so as to guarantee during the whole commissioning period, that the radiation levels were always kept below the values authorized for public access. This was quite constraining but resulted in a very "clean" commissioning, without generation of high activation in any part of the ring.

New digital BPM electronics: For the first time, the LIBERA BPM electronic modules [9] were used on a large ring to monitor the positions of the injected beam (single turn acquisition mode) and of the stored beam.

New control system: For the first time, the TANGO control system [10] was used to control and supervise a full facility from the accelerators to the beamlines.

4.2.3.2   First Turns

The first electron beam was injected into the storage ring on May 14th 2006 [11]. With the quadrupoles and sextupoles powered on at their theoretical values and no RF power, the beam performed up to 100 revolutions in the ring, as shown on the Fast Current Transformer situated in the last quarter of the ring (Figure 4).
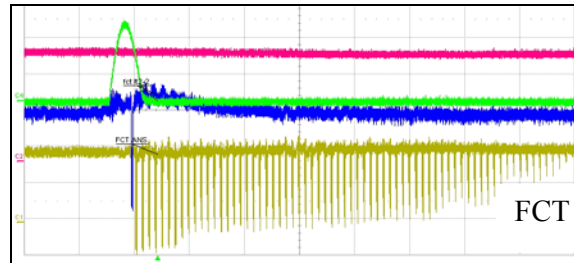
Figure 4: The beam performed many turns with no RF power

When the RF cavities were powered on and after optimisation of the RF-phase (between the Booster and the Storage Ring), centering of the horizontal orbit by varying the RF frequency, and decreasing slightly the horizontal focusing, the beam was stored and then accumulated at the very first trial. The optics was measured close to the model value.

4.2.3.3   Fast Progression

Despite few problems such as some RF fingers badly mounted which were creating severe aperture limitations (they were rapidly localized and replaced during the summer shutdown), the progress was then very fast and, after only 8 effective weeks of commissioning, 300 mA were stored in ¾ filling pattern end of September 2006, after having integrated a cumulated dose of only 30 A.h. The main milestones achieved during the commissioning period from May till December 2006 are summarized hereafter:

May 14	**First turn**
June 02	**First stored beam**
June 04	**First beam accumulation : 8.35mA**
July 04	**100mA achieved**
July 10	**5 A.h beam dose**
	Shutdown July-August
Sep. 13	**First photons to a beamline (DIFFABS)**
Sep. 16	**200mA achieved**
Sep. 21	**First photons to a beamline (TEMPO)**
Sep. 25	**300mA achieved ; 30A.h beam dose**
Sep. 29	**First in-vacuum undulator closed at 5.5mm gap**
Oct. 13	**First photons to a beamline (ODE)**
Oct. 10	**Beam lifetime =8h @100mA in 312 bunches**
	Shutdown November
Dec. 12	**First photons to a beamline (SAMBA)**
Dec. 13	**First photons to a beamline (DESIRS)**
Dec. 21	**Beam lifetime =10h @100mA in 312 bunches; 70 A.h beam dose**

The first photons were delivered to a beamline after only 6 effective weeks of commissioning.

4.2.3.4   Main Beam Dynamics Results

Table 1 summarizes the comparison between designed and achieved values of the main machine parameters.

Table 1: Achieved results as of October 2007.

Parameter	Unit	Design	Achieved as of October 2007
Energy	GeV	2.75	2.74
RF frequency	MHz	352.2	352.197
Betatron tunes (H/V)		18.2 / 10.3	18.1995 / 10.2990
Natural chromaticities (H/V)		-53 / -23	-53 / -19
Momentum compaction	$\alpha 1$ $\alpha 2$	$4.5\ 10^{-4}$ $4.6\ 10^{-3}$	$4.55\ 10^{-4}$ $4.30\ 10^{-3}$
Emittance H	nm.rad	3.73	3.70 ± 0.2
Energy spread		$1.016\ 10^{-3}$	$1.0\ 10^{-3}$
Coupling, $\varepsilon v / \varepsilon h$		<1%	0.3% without correction 0.08% after correction
Current in multibunch mode	mA	500	300
Average pressure at max current	mbar	10^{-9}	$2.3\ 10^{-9}$
Beam lifetime	h	16	10 @ 300mA / 15 @ 200mA
Current in single bunch mode	mA	12	20
Beam position stability, (H)	µm	20 (rms)	2 ptp
Beam position stability, (V)	µm	0.8 (rms)	1 ptp

4.2.3.5   Closed Orbit

Significant efforts were devoted to achieve high quality quadrupole magnets and to determine as precisely as possible the magnetic axis of each quadrupole, using a dedicated high precision rotating coil bench: After magnetic measurements, the magnetic centers of the quadrupoles were known within rms values of 8.4 µm and 7.5 µm respectively in H and V planes, and with a rms tilt error of 40 µrad [12]. Then a very thorough alignment methodology enabled to align the magnets within 60 µm rms in both planes (quadrupole + girder assembly). As a result, the natural beam orbit featured rms values as low as 3.1 mm and 0.41 mm respectively in horizontal and vertical planes. Moreover, this natural uncorrected orbit didn't change significantly after 18 months which demonstrates the outstanding long term stability of the ring (thanks to the 95 cm thick slab of the storage ring tunnel, supported by 140 piles, 15m deep).

Beam Based Alignment (BBA) measurements have been performed in both planes, to calibrate the BPMs offsets with respect to the magnetic centers of adjacent quadrupoles. Offsets less than 100 µm rms in both planes have been included in the SVD based global orbit correction using 120 BPMs and 56 correctors in each plane. In the horizontal correction, path-length effects are corrected with the RF frequency. The rms residual orbits after correction are around 42 µm horizontally and 58 µm vertically.

This is achieved using all the eigenvalues in both planes. The required strengths of the correctors (typically $\sim$ 0.753 A rms H and ~1.583 A rms V), are well below their maximum capability.

4.2.3.6 *Beam Position Stability*

A Slow Orbit FeedBack operating at 0.1 Hz, reading the high resolution LIBERA BPM electronics and using the same algorithm as for closed orbit correction is routinely used to stabilize the beam position during Beamline operation. Figure 5 shows the beam position stability (H & V) at some source points during a Beamline shift of 8 hours. Routinely, we achieved position stability of 1μm (resp. 2 μm) peak to peak in the vertical (horizontal) plane and angle stabilization of 0.6 μrad (1 μrad) peak to peak in the vertical (horizontal) plane.
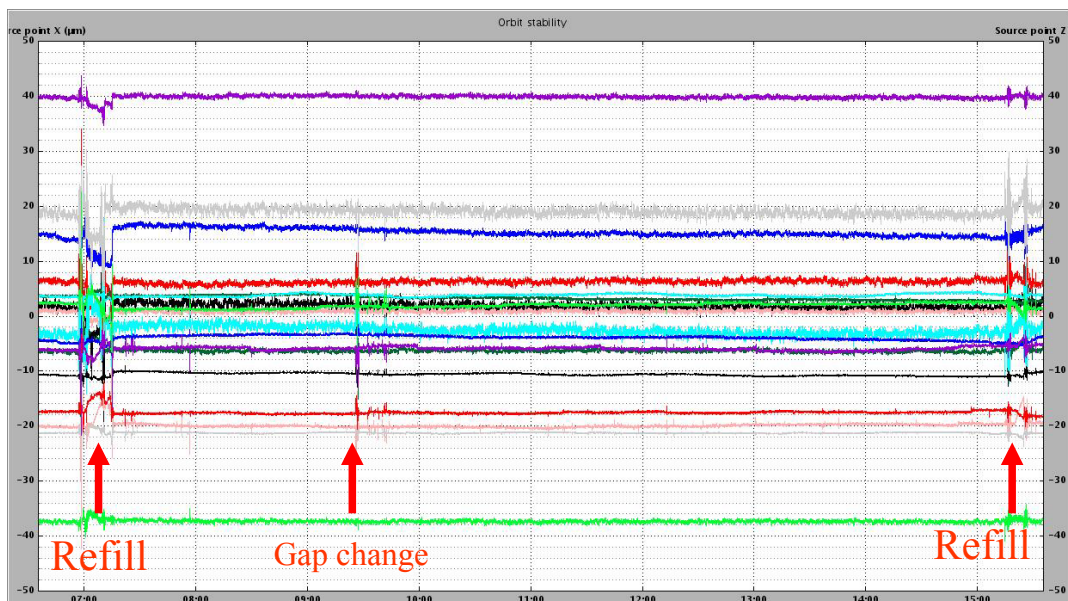
Figure 5: Beam positions (H &V) recorded on several source points during a 8 hours shift

Work is still undergoing in order to minimise or to suppress the identified noise sources, such as the effect of the crane movement, the 3 Hz Booster power supplies, the drifts with temperature (SR-tunnel temperature regulation) and the perturbations induced by Insertion Devices changes.

The first resonance mode of the magnet supporting girder predicted at 43 Hz, was determined to be 47 Hz through experimental modal analysis and confirmed by the actual beam noise spectrum [13]. The beam noise integrated in a spectral frequency span of 0-500 Hz is below 2 μm rms in both planes. A Fast Orbit FeedBack [9] is under test and will be installed early in 2008 in order to further reduce this noise.

The closing of the four-kicker injection bump was worked out and presently the induced horizontal betatron oscillation amplitude is around 100 μm at maximum kick amplitude. It will be further reduced so as to make as transparent as possible the injection process during top-up operation.

4.2.3.7   Linear Optics

The four-fold symmetry of the lattice has been restored by using the LOCO code [14]. After two successive steps to restore the optic symmetry, the betatron and dispersion function beatings are below 0.5 % rms at the BPM positions. Figures 6 and 7 display respectively the residual beta beating and the horizontal dispersion error in the BPMs.
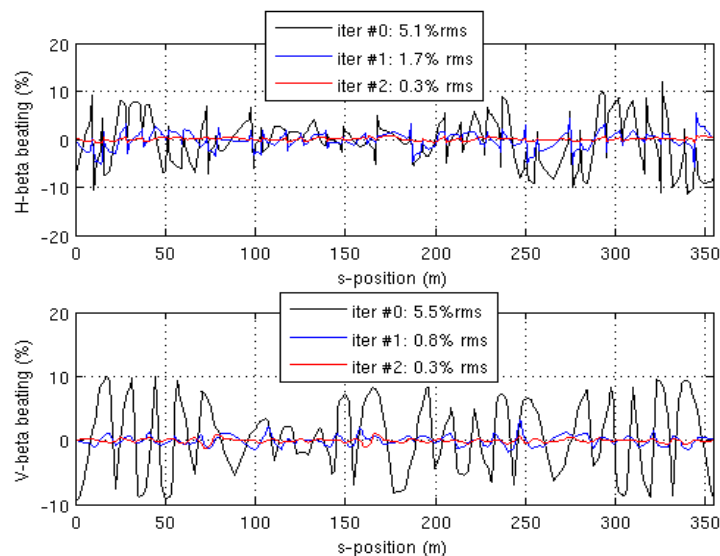
Figure 6: Beta-beating reduction from the bare lattice (black) after two successive iteration steps using LOCO.
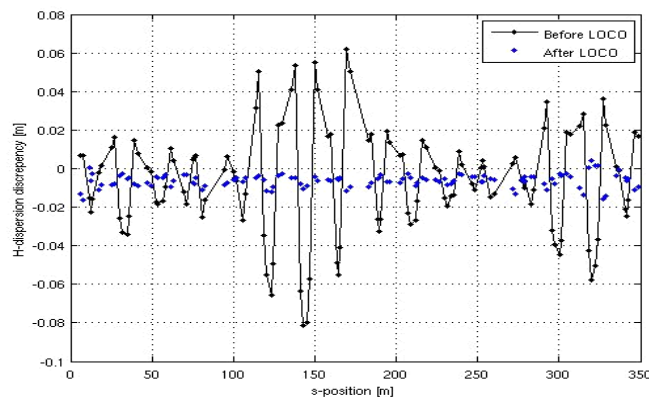
Figure 7: Horizontal dispersion function error before and after correction with LOCO.

The amplitude of gradient variations of the 160 individually powered quadrupoles is within a few ‰ as shown in Figure 8. There is one exception around the center of the storage ring where variations can reach up to 1.2%. This feature is not fully understood yet but appears clearly in the natural orbit (closed orbit with all correctors turned off) and in the dispersion function.

170

As a result of this symmetrization, improvements of a few percents are observed on the injection efficiency, and the effects of some insertion devices on the injection efficiency have been reduced.
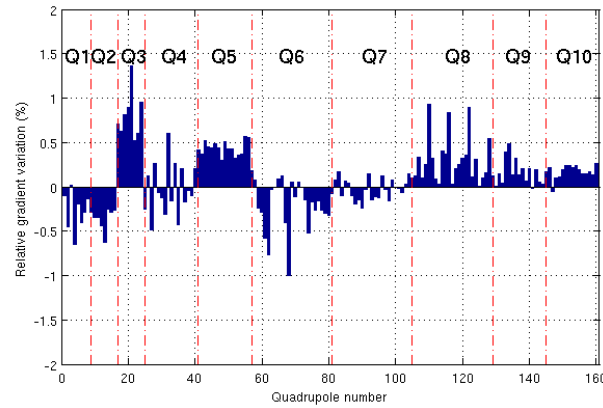
Figure 8: Total relative gradient variations after two iterations of the LOCO code. The values are sorted by quadrupole families.

The operational working point is the one targeted at the design. It provides high injection efficiency (above 95% without insertion devices and after symmetrization) and a good lifetime. The tuning range is large (0.01 to 0.49) in both planes and the beam can be set on the non systematic 3rd order resonance ($3\nu_x = 55$) without loss though with lower a lifetime. The variation of tunes with momentum deviation is in excellent agreement with the model as shown in Figure 9.
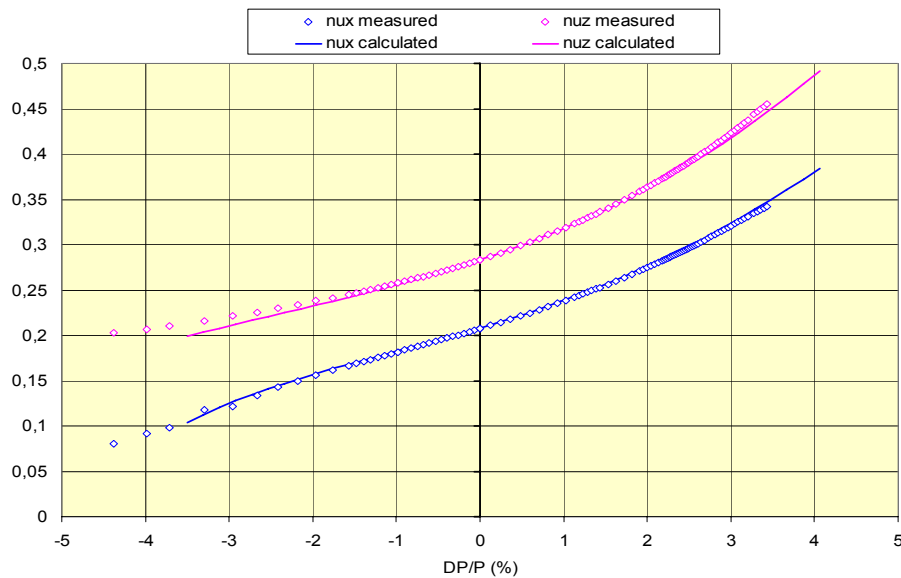
Figure 9: Tune shifts with energy: Comparison between measurement and modelling for the nominal lattice.

The measured natural total chromaticities (-52 and -19) are close to theory (-53 and -23). The main difference in the vertical plane is due to the fact that the energy

dependence of the dipole fringing field effect was not taken into consideration in our numerical model.

4.2.3.8   Emittance and Coupling

The horizontal and vertical beam emittances have been measured by observing the X-part of the synchrotron radiation by means of a pinhole camera [15], (see Figure 10). The horizontal value of the emittance confirmed the design value of 3.73 nm.rad within ± 0.2 nm.rad. The use of the 5th harmonic photon spectrum of the PROXIMA1 beamline in-vacuum undulator U20 indicates also that the horizontal emittance and the energy spread are very close to the design values.
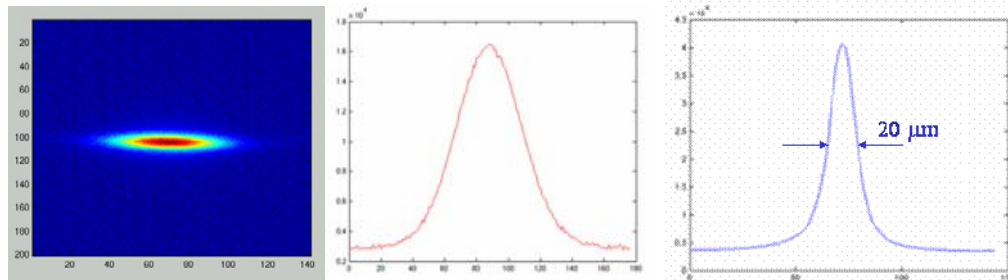
Figure 10: Image of the photon beam and its projections: horizontal (red) and vertical (blue).

Without correction, the integrated betatron coupling was measured at 0.08%, using the closest tune approach. Thus, the 11 pm.rad measured vertical emittance corresponds to a very low 0.3% natural coupling. Using 32 skew quadrupoles, the machine could be tuned down to a very low coupling (~1‰) with a vertical emittance below 5 pm.rad, as deduced from the measured image, using SRW software [16]. In view of improving the lifetime in the few bunch mode of operation, the vertical emittance can also be enlarged by increasing the vertical dispersion using the skew quadrupoles, without modifying the betatron coupling, thereby providing a coupling above 6% all around the ring.

4.2.3.9   Beam Current and Lifetime

After few problems related to overheating of some equipment (some badly mounted RF fingers had to be changed) have been resolved and with an RF-feedback, stable conditions up to 300 mA could be achieved with both a ¾ filling pattern and rather large normalised chromaticities ($\xi_H = 0.2$, $\xi_V = 0.5$). The maximum current is presently limited by the maximum power that can be delivered to the 2 RF cavities installed in a single cryomodule. The installation of a second RF cryomodule, in 2008, will enable to raise the current up to 500 mA.

No coupled-bunch instability was observed in the longitudinal plane as expected with superconducting RF cavities.

Transversally, a mixture of resistive-wall and ion induced instabilities are observed in both H- and V- planes. The behaviour of the ions induced instability depends much on the beam filling pattern. The detail of these instabilities, their thresholds and the comparison with expectation are reported in [17]. Since spring 2007, a bunch by bunch transverse feedback combats very efficiently the transverse instabilities [18] and the high chromaticities are no more needed. The beam is kept stable up to the maximum

current of 300 mA at zero chromaticities in both planes, which keeps the injection efficiency > 90%. The feedback is routinely used during user operation.

In the **multibunch mode**, with 300 mA in 312 bunches (out of 416 buckets); the beam lifetime reaches 10 hours. It is mainly limited by the average pressure in the ring (2.3×10^{-9} mbar at 300 mA). Since beginning of 2007, during user operation, a 200 mA beam is stored with the natural low coupling and 15 hours of beam lifetime (2 MV RF-voltage and 1.2×10^{-9} mbar average pressure).

In the **single bunch mode**, the current could be raised easily up to 20 mA without being limited by instability. Using a streak camera, the zero current bunch length was measured at 20 ps rms with 2 MV RF accelerating voltage, a value close to the expected theoretical one at very low current. The bunch length increases by roughly a factor of 2.5 from 0 to 20 mA, but no energy widening was observed [17].

It is foreseen to deliver the beam to the users in **8 bunch mode** by the end of 2007. With a global coupling of 6.7% and 2.8MV RF voltage, a beam lifetime of 12 hours is achieved at 50mA in 8 bunches. The good performances of the Linac gun enable to reach, without any cleaning action, a ratio of 1 to 10^{-5} between the main bunches and the parasitic bunches, which fits the SOLEIL users requirement.

4.2.3.10   Control and Software Tools

The system architecture is based around the TANGO framework. SOLEIL is the first accelerator using it as a full control system. TANGO is an evolution of TACO the in house developed control system of the ESRF. It is a software bus that permits to communicate between distributed applications thanks to a software interface called "Binding". This is the link between TANGO and the software applications that get all the tools permitting data processing, sequencing, etc. The SOLEIL supervision layer is Global Screen (from Ordinal Technologies). It brings high level functionalities necessary to make synoptic. Those are representing the essential machine control graphic interface for the operator. Besides Matlab is the expert application for machine configuration.

The Matlab Middle Layer toolkit [19] was adapted and used to adjust, save and restore optics and power supplies settings, to measure, display, and correct, the closed orbit, the dispersion and the optical functions. Other functions concerns BPM configuration and measuring, first turn measurements, local orbit bump generation, BPM offset measurement using Beam Based Alignment, energy calibration, lattice symmetry restoration (using LOCO), coupling correction, dynamics aperture measurement, frequency maps, tune, chromaticity, dispersion tuning, emittance and lifetime measurement. The slow orbit feedback and the synchronization system are also presently operated via dedicated Matlab applications.

4.2.3.11   Vacuum Conditioning

The average static pressure in the storage ring before injecting the first beam was 4×10^{-10} mbar after having baked the whole ring (except the injection straight section), and after having activated all Titanium Sublimation pumps (TSP), using local controllers.

With the first stored beam (I=0.8 mA), the maximum pressure rise was 2×10^{-8} mbar. The conditioning effect progressed smoothly and by the end of October 2007, after having accumulated an integrated dose of 400 A.h, the average dynamic pressure is now

1.3 10^{-9} mbar with 200 mA in multibunch mode. The corresponding 15 h beam lifetime is still essentially limited by the residual pressure.

Figure 11 presents, for a typical cell, the average pressure normalized to beam current versus the integrated current dose. This Log-Log plot illustrates the conditioning with beam of the vacuum vessel walls. Initially, this variation conforms to the usual measurements made in other synchrotron facilities with a negative slope of about 0.6. From January 2007 onwards, remote control of the TSP was made available and all TSP are re-activated every 3 weeks. As a result, the conditioning slope was increased from 0.6 to 0.96.

Average pressure of Cell C07 normalised to current Vs. the beam dose

$y = 3E{-}10x^{-0,6558}$
$R^2 = 0,9718$

Before sublimations

After sublimations

$y = 9E{-}10x^{-0,9197}$
$R^2 = 0,9597$

Pav / I (mbar/mA)

Integrated Beam Dose (A.h)
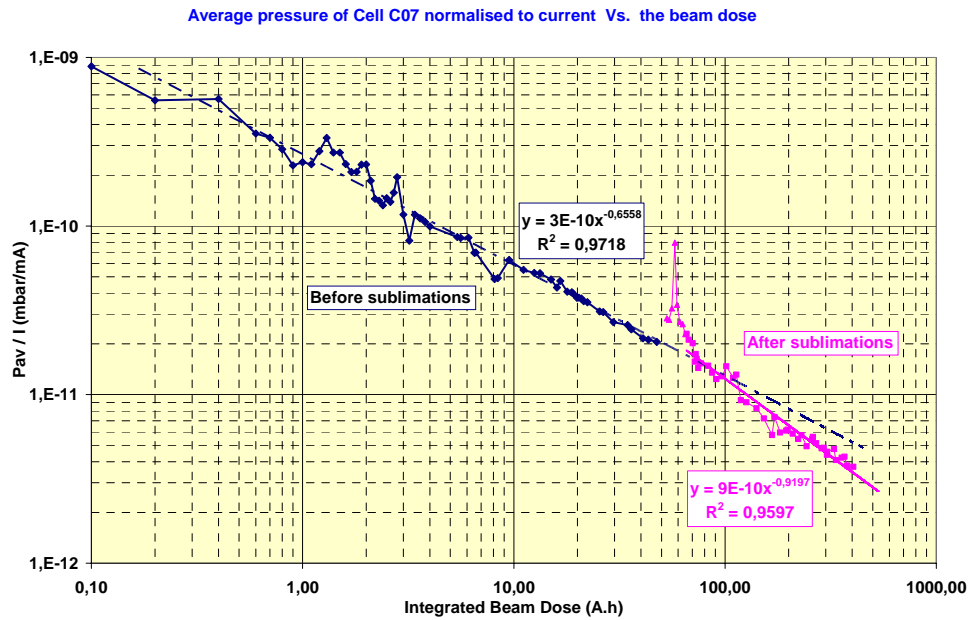
Figure 11: Vacuum conditioning of a typical cell

Figure 12 presents for the same cell, the relative behaviours of the pressures measured in the NEG coated Aluminium vessel and in the Stainless Steel vessels. One can observe that pressure is lower in the coated vessels and that the conditioning slopes are similar.

Average pressure of Cell C07 normalised to current   Vs. the beam dose
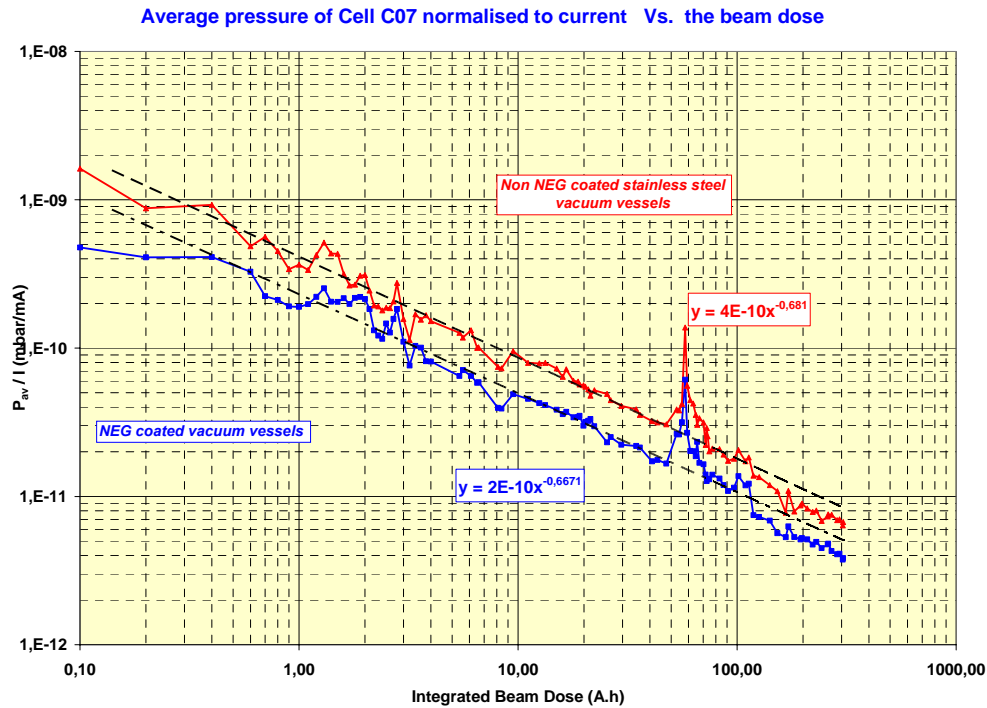
Figure 12 : Comparison of the vacuum conditioning of NEG coated and stainless steel vessels

Figure 13 presents the pressure distribution along one typical cell with a 300 mA current. It shows that the pressure profile is quite flat, despite the high photon power deposited downstream the bending magnets, where the crotch absorber and the longitudinal absorber stop about 60% of the photons radiation generated in the bending magnet. It also show the pressures measured along the cell without pumping ports (pumping provided only by the NEG coating). One can observe that the pressures are not significantly different. This result would mean that there is no additional flux coming from the neighbouring quadrupole vessels. **It clearly demonstrates that the NEG coating alone enables to keep the pressure at low level.**
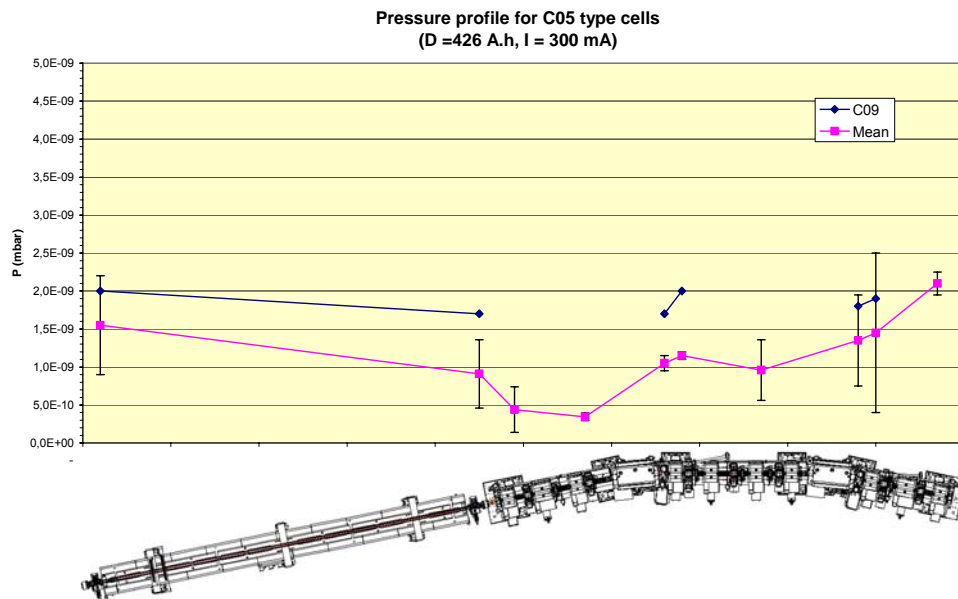
Figure 13: Pressure profile along one typical cell (in pink). The pressure in the test cell 9, which doesn't have additional pumping in the quadrupole vessels is shown in black

4.2.4   Operation for beamlines

By the end of October 2007, 13 beam-lines from infrared to X-rays are using the photon beams. Beam is routinely delivered to the beamlines in the following conditions: 200 mA stored beam current in multi-bunch filling pattern (312 filled RF-buckets out of 416), with natural small vertical emittance (0.4% of coupling) featuring a 15 hours beam lifetime (with 2 MV RF-voltage and a $1.2\ 10^{-9}$ mbar average pressure). The machine availability reached 94.5% over the 2500 hours running time scheduled for the beamlines from January till October 2007.

4.2.5   Conclusion

Despite numerous technological challenges, the SOLEIL storage ring commissioning went very smoothly and the machine features excellent performances in term of beam position stability, reliability and evolution potentialities. The RF system worked remarkably inducing only 3 beam trips over the whole commissioning period! The conditioning of the vacuum system with the NEG coated aluminium vessels is under good progress and will enable to reach the targeted 10^{-9} mbar average pressure at 500 mA. We also benefited from a very realistic modeling of the machine, which together with the Matlab Middle Layer package, enabled to prepare any optical settings in a very reliable and efficient manner.

The SOLEIL accelerator complex is now fully operational and running to deliver beam to the beamines. The transition from the commissioning phase to the operation phase was very fast, thanks to an excellent team work relying on one side, on a strong implication and participation of the operation group during the commissioning of the

machine, and on the other side on the significant efforts made by the machine physics groups and the different groups in charge of equipment to transfer their knowledge to the operation crew.

4.2.6 References

1. A. Setty et al, "Commissioning of the 100 MeV Preinjector HELIOS for the SOLEIL Synchrotron", EPAC 2006, Edimburg
2. A. Loulergue, "Commissioning of the SOLEIL Booster", EPAC 2006, Edimburg
3. C. Benabderrahmane et al, "Commissioning of the first Insertion devices at SOLEIL", PAC 2007, Albuquerque
4. M.P. Level et al, "Status of the SOLEIL Project", EPAC 2002, Paris
5. P. Marchand et al, "Operation of the SOLEIL RF systems", PAC 2007, Albuquerque
6. C. Benvenuti, et al, Vacuum 60, 2001, 57-65
7. P. Chiggiato, R. Kersevan, Vacuum 60, 2001, 67-72
8. R. Nagaoka, "Study of Resistive-wall Effects on SOLEIL", EPAC 2004, Lucern
9. N. Hubert et al, "The SOLEIL BPM and Orbit Feedback Systems", DIPAC 2007, Venezia, May 2007
10. A. Buteau, P. Betinelli, "Status of SOLEIL Control Systems", EPAC 2006, Edimburg
11. A. Nadji et al, "First Results of the Commissioning of SOLEIL Storage Ring" EPAC 2006, Edimburg
12. P. Brunelle et al, "Magnetic Measurements Results of the Dipoles, Quadrupoles and Sextupoles of the SOLEIL Storage Ring", EPAC 2006, Edimburg
13. J.M. Filhol et al, "Overview of the status of the SOLEIL Project", EPAC 2006, Edimburg
14. J. Safranek, G. Portmann, A. Terebilo, C. Steier, "Matlab based LOCO", EPAC 2002, Paris.
15. M-A. Tordeux et al, "Ultimate Resolution of SOLEIL X-Ray Pinhole Camera", DIPAC 2007, Venezia, May 2007
16. O. Chubar, P. Elleaume, "Accurate and Efficient Computation of Synchrotron Radiation in the Near Field Region", EPAC98 Conference Proceedings, Stockholm 1998, 1177-1179
17. R. Nagaoka, M.P. Level, L. Cassinari, M.E. Couprie, M. Labat, C. Mariette, A. Rodriguez, R. Sreedharan, "Beam Instability Observations and Analysis at SOLEIL", PAC 2007, Albuquerque
18. R. Nagaoka, L. Cassinari, J.C. Denard, J.M. Filhol, N. Hubert, M.P. Level, P. Marchand, C. Mariette, F. Ribeiro, R. Sreedharan, T. Nakamura, K. Kobayashi, "Transverse Feedback Development at SOLEIL", PAC 2007, Albuquerque
19. J. Corbett, G. Portmann, and A. Terebilo, "Accelerator control middle layer", PAC 2003, Portland.

4.3 Dynamic Aperture, Impedances and Instabilities in CANDLE Light Source

G. Amatuni, R. Balayan, R. Dallakyan, B. Grigoryan, M. Ivanyan, S. Hakobyan, D. Kalantaryan, V. Khachatryan, E. Laziev, K. Manukyan, K. Sargsyan, A. Tarloyan, A. Tsakanian, V. Tsakanov, A. Vardanyan
Center for the Advancement of Natural Discoveries using Light Emission, Acharyan 31, 375040 Yerevan, Armenia
Mail to: tsakanov@asls.candle.am

4.3.1 Introduction

The new synchrotron light source project named CANDLE - Center for the Advancement of Natural Discoveries using Light Emission - is a 3 GeV nominal energy electron facility [1,2], the spectrum of synchrotron radiation from bends, wigglers and undulators of which covers the most essential region of photons energy 0.001- 50 keV suitable for investigations at the cell, virus, protein, molecule and atomic levels.

The beam physics issues are of most important parts of the synchrotron light sources design study that define the quality and stability of electron and photon beams. In this article after a short overview of the CANDLE facility design we present the main results of the study related to machine dynamic aperture, broadband impedances, coupled bunch instabilities and ion trapping.

4.3.2 The Project Overview

The CANDLE design is based on a 3 GeV electron energy storage ring, full energy booster synchrotron and 100 MeV S-Band injector linac (Fig.1). The full energy booster synchrotron has the repetition rate of 2 Hz and the nominal pulse current of 10 mA
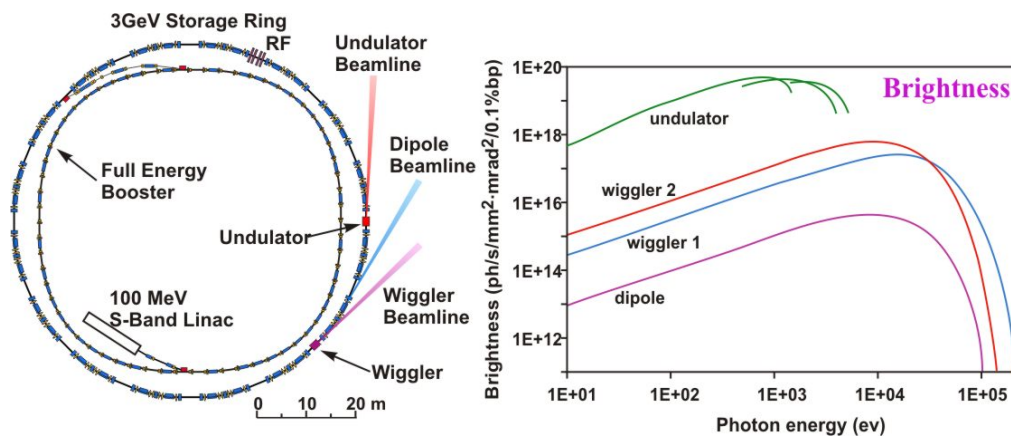
Figure 1: The general layout of CANDLE facility (left) and the spectral brightness from bends, wigglers and undulators (right).

The storage ring of 216m in circumference has 16 Double-Bend-Achromat (DBA) type periods. The main parameters of the facility are given in Table 1.

Table 1: The facility main parameters

Energy, E (GeV)	3
Circumference, L (m)	216
Current, I (mA)	45
Number of DBA lattice periods, N	16
Betatron tunes (ν_x / ν_y)	13.2 / 5.6
Chromaticities (ξ_x / ξ_y)	
Horizontal emittance, ε_x (nm·rad)	8.4
Total beam lifetime (hours)	18.4

The design of the machine is based on conventional technology operating at normal conducting conditions. The cavities total gap RF voltage is 3.3 MV ensuring the Touschek lifetime of about 40 hours. With 1 nTorr vacuum pressure the total beam lifetime is at the level of 18.4 hours. The vacuum chamber of the ring is based on the stainless steel antechamber geometry design. In total 13 straight sections of 4.8 m in length are available for insertion devices. Fig. 1 (right) presents the CANDLE spectral brightness for the dipole (1.35 T), undulator (0.3 T) and wiggler (1.3 T, 2 T) sources. The facility design implies the operation in the single, multi-bunch and top-up modes thus providing the broadband application of the experimental techniques.

4.3.3 Optics and Dynamic Aperture.

One of the main features of CANDLE project design study was the optimization of the facility performance based on the achievement of a high brightness photon beams from insertion devices and the stable stored electron beam by means of the large dynamical aperture of the ring [3].
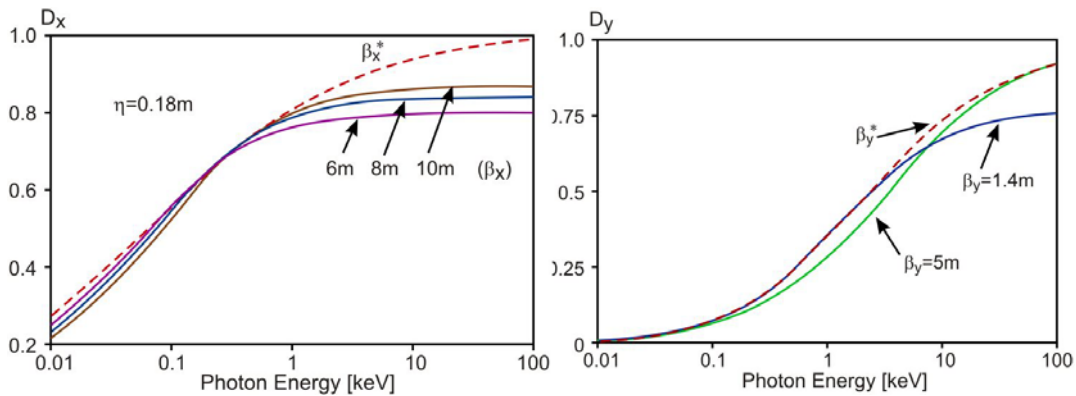
Figure 2: The normalized CANDLE brigthess versus photon energy for various horizontal (left) and vertical (right) beta function in the middle of strahgt section.

The DBA focusing lattice of the storage ring has non-zero horizontal dispersion $\eta_x = 0.18\text{m}$ in the middle of the straight section that provides 8.4 nm-rad horizontal emittance of the beam. Fig.2 shows the dependence of the normalized brightness on the emitted photon energy for different horizontal and vertical beta values at the source point. Dashed line corresponds to the optimal beta values associated with each photon energy. The improvement of the brightness with small horizontal beta is visible only for the photon energies below 0.1 keV. Starting from 0.5 keV the brightness increases with larger horizontal betatron function. In vertical plane, the small emittance of the beam shifts the characteristic regions of the brightness behaviour to harder X-ray region.

To keep the dynamical aperture of the storage ring large, the horizontal and vertical betatron functions in the middle of the straigth sections are optimized to $\beta_x = 8.1\text{m}$, $\beta_y = 4.85\text{m}$. Fig.3 shows the horizontal and vertical dynamic apertures of the ring with 3% energy spread in the beam which is sufficient for facility stable operation.
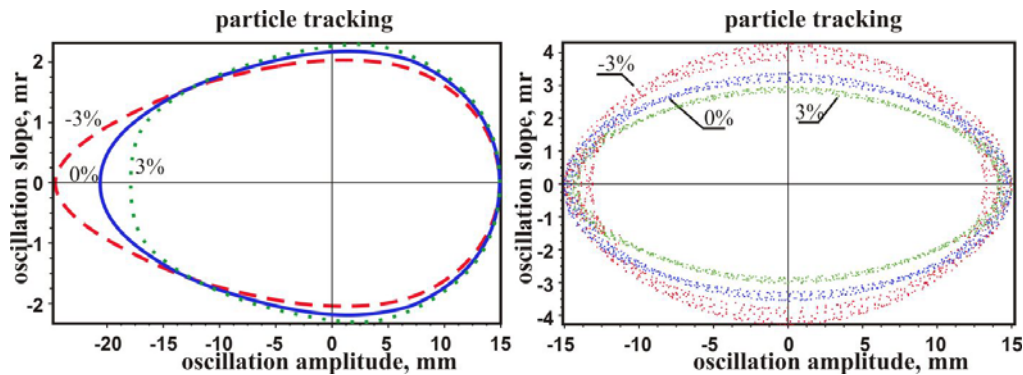
Figure 3: Horizontal (left) and vertical (right) dynamic apertures of the storage ring.

4.3.4   The Storage Ring Broadband Impedance

The stable operation of advance accelerator facilities requires careful examination of vacuum chamber longitudinal and transverse impedances that can drive various types of beam instabilities [4,5]. More advanced study is required for the technical solutions of vacuum chamber design to obtain high vacuum or reduction of the ring impedance. Very often these technical solutions imply the use of laminated vacuum chamber: stainless steel covered by cupper, cupper chamber covered by the NEG (Non-Evaporated Getter).

Fig. 4 presents the longitudinal and transverse impedances of the CANDLE storage ring for various distributed impedance ordinary sources: vacuum chamber resistive walls and surface roughness, BPM's and transitions. The normalized longitudinal broadband impedance for the CANDLE storage ring without insertion devices is at the level of 0.35 Ω. The corresponding single bunch threshold current is 8.9 mA.

The transverse impedance of the ring without insertion devices is 12.6 kΩ/m that defines the threshold current of 113 mA for the transverse single bunch instability. The CANDLE nominal operation current of 350mA implies the single bunch current of 1.24 mA that is far below of the threshold currents.
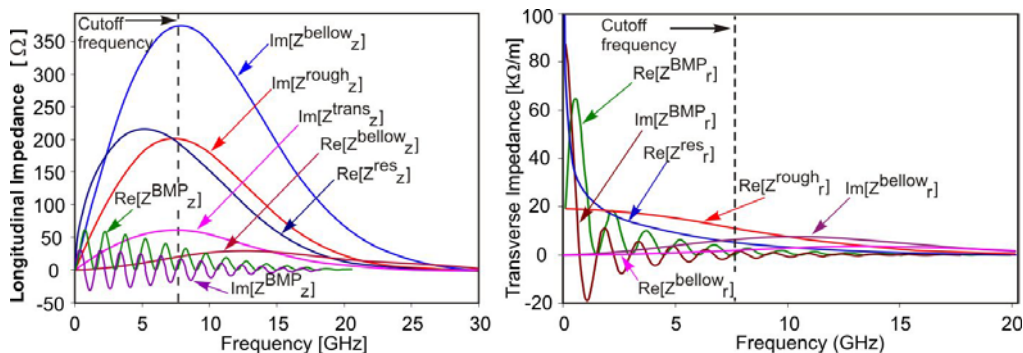
Figure 4: Longitudinal (left) and transverse (right) impedances of the ring caused by the walls resistivity, roughness, BPM's and transitions.

More rigorous study has been performed to evaluate the expected contribution from the small gap undulators to general impedance. The copper vacuum chamber of the

undulator is expected to be covered by NEG to obtain high vacuum pressure, that refer us to impedance of two layer tube. Therefore the study of the resistive impedance for two-layer tube is an important issue to evaluate the complete longitudinal and transverse impedances of the storage. The results of our study are summarized in Ref [6-9]. In particular, for the metallic type layers, a good approximation for the longitudinal resistive impedance is obtained [7]:

$$Z(k) = -\frac{jZ_0}{\pi k}\left[a^2 + 2\frac{a\varepsilon_1}{\varepsilon_0\chi_1} \times \frac{1 + \alpha th(\chi_1 d_1)th(\chi_2 d_2)}{th(\chi_1 d_1) + \alpha th(\chi_2 d_2)}\right]^{-1}$$

where $\alpha \approx (\sigma_1/\sigma_2)^{1/2}, d_i, \sigma_i, \chi_i$ are the layers' thickness, conductivities and radial propagation constants, a is the vacuum chamber inner radius, ε_1 is the inner layer dielectric permeability, ε_0 is the vacuum dielectric constant and $Z_0 = 377\Omega$ is the free space impedance. Fig. 5 presents the real parts of longitudinal (left) and transverse (right) impedances for the cooper-NEG circular vacuum chamber of 5 mm inner radius.
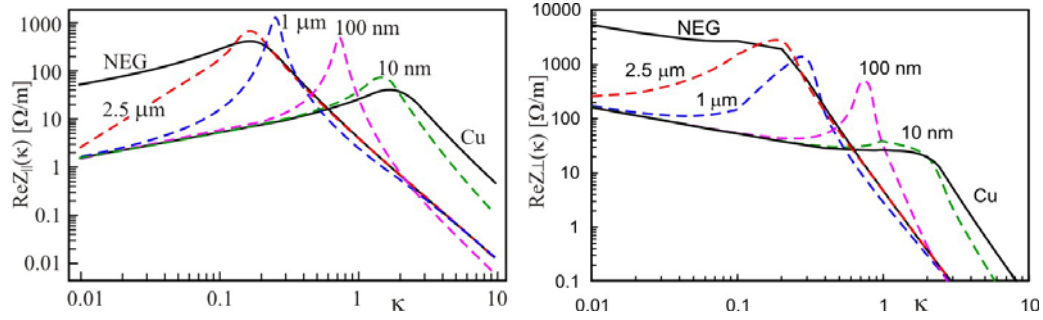
Figure 5: Real part of copper-NEG tube longitudinal (left) and transverse (right) impedances for various cover thickness; κ is a dimensionless wave number, related to copper material [4].

The impedances in Fig.5 are calculated for various cover thickness thus indicating the transition between the copper and NEG dominated impedances. The results of this section will be used to evaluate the real broadband impedance of the ring equipped with small gap undulators.

4.3.5 Coupled Bunch Instability

The narrow band impedance of the storage ring, basically the longitudinal and transverse High Order Modes (HOM) excited by beam in the RF cavities, determine the longitudinal and transverse multi-bunch instabilities [4].

The longitudinal and transverse coupled bunch instabilities for the CANDLE storage ring have been studied for the original ELETTRA cavity option [10]. Fig. 6 presents the growing rate of longitudinal and transverse coupled bunch instabilities versus the relative mode index n for the 282 beam oscillation modes.
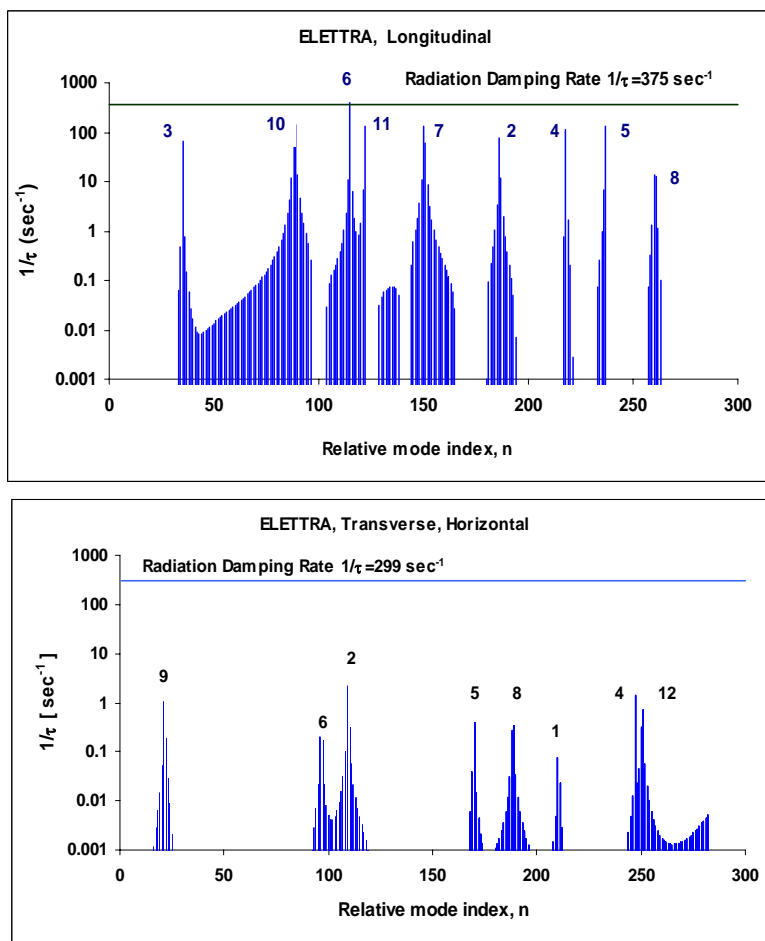
Figure 6: The longitudinal and transverse coupled bunch instabilities growing rate versus beam oscillation modes.

The growing rates of instabilities are mostly below the synchrotron radiation damping coefficients, except for L6 longitudinal mode that excites the instability at relative oscillation mode of n=115. After the cavities RF measurements, the instability cures will be developed to ensure the stable operation of the facility.

4.3.6   Ion Trapping and Fast Ion Instability

To prevent the reduction of the beam lifetime due to ion trapping, the stability of the transverse motion of the ions has been checked along the regular lattice of the storage ring [11]. The results are presented in Fig. 7.
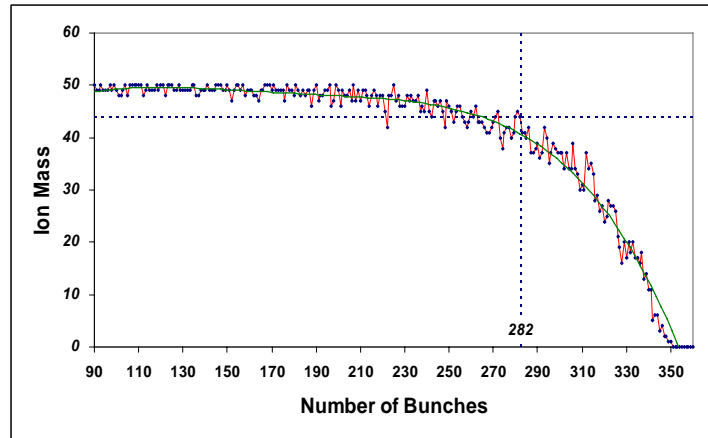
Figure 7: Number of unstable ions versus number of bunches in the ring.

The effect of the ion trapping is observed when the number of bunches in the ring exceeds 90. The optimal value of the number of bunches for the CANDLE storage ring has been defined $h = 282$ which provides an ion-cleaning gap of 78 RF buckets not filled with the electrons. With such a cleaning gap, only 6 ions number are trapped. An additional criterion for the optimisation of the number of bunches in multi-bunch operation mode is an analysis and comparison of the list of trapped ions with the mass numbers of real residual gas species. Fig. 8 presents the trapped ion masses versus filled RF buckets.
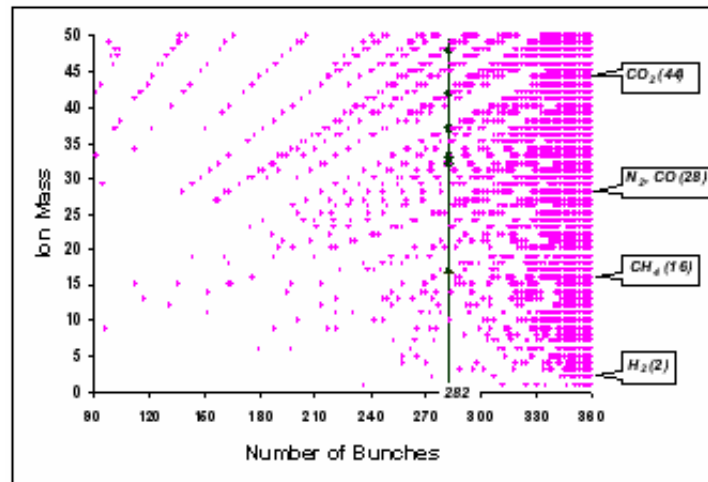
Figure 8: The trapped ion masses versus number of the filled RF buckets.

The trapped ion mass numbers in CANDLE storage ring are given in Table 2; the number of bunches is 282. The comparison with species of the ions in the residual gas that can occur in the chamber shows that for the given number of bunches 282 no components of residual gas will lead to trapped ions in the ring. The chosen number of bunches in the storage ring, 282 bunches from available 360 RF buckets, provides practically trapped ions-free operation of the machine at almost 80% filling.

Table 2: Trapped ion masses and residual gas species.

Trapped ion masses	Residual gas species
-	2, H_2
-	16, CH_4
17	-
-	28, N_2,CO
32	-
33	-
37	-
42	-
-	44, CO_2
48	-

4.3.7 References

1. A. Abashian et al, CANDLE Design Report, ASLS-CANDLE R-001-2002, July 2002.
2. V. Tsakanov et al, "CANDLE – A New Synchrotron Light Source Project in Armenia", Rev. Sci. Instrum. **73:**1411-1413, 2002.
3. M.Ivanyan, Yu. Martirosyan, V.Tsakanov, "On the brightness of diluted photon source in synchrotron light facilities", Nucl. Instrum. Meth. A **531**: 651-656, 2004
4. A.W. Chao,"Physics of Collective Beam Instabilities in High Energy Accelerators," New York, John Willey & Sons, Inc., 1993.
5. B.W. Zotter and S.A. Kheifets, "Impedances and Wakes in High-Energy Particle Accelerators," Singapore, World Scientific, 1997.
6. M. Ivanyan, V.Tsakanov "Analytical Treatment of Resistive Wakes in Round Pipe", Nucl. Instrum. Meth, A **522**: 223-229, 2004.
7. M. Ivanyan, V. Tsakanov, "Longitudinal impedance of two-layer tube", Phys. Rev. ST-AB, **vol. 7**, 114402, 5 p., 2004.
8. M. Ivanyan, A. Tsakanian "Analytical Presentation of Resistive Impedance for the Laminated Vacuum Chamber" , Phys. Rev. ST –AB, **vol. 9**, 034404, 2006.
9. M.Ivanyan, E.Laziev, A.Tsakanov, A.Vardanyan, A. Tsakanian and S. Heifets, Multi-Layer Tube Impedance and External Radiation, Phys. Rev. ST-AB, 2007 (to be published).
10. Yu. Martirosyan, M. Ivanian, V. Tsakanov, "Beam Current Limitations in CANDLE Light Source", Proc. of EPAC2002, Paris, France, 2002, pp. 718-720.
11. M. Ivanyan, Yu. Martirosyan, V. Tsakanov **"**Beam Physics Issues in CANDLE Synchrotron Light Source Project", Proceedings of 37th ICFA Advanced Beam Dynamics Workshop on Future Light Sources, Hamburg, 2006, WG101.

4.4 Lattice and Beam Dynamics of the ALBA Storage Ring

Marc Muñoz, Dieter Einfeld
ALBA-CELLS, Edifici Cn, UAB, Bellaterra, Spain
Mail to: marc.munoz@cells.es

4.4.1 Introduction

ALBA is a synchrotron light source under construction near Barcelona, Spain. The storage ring with an energy of 3 GeV has a circumference according to budget reasons

of roughly 270 m. The lattice design was determined by the condition 1.) to have small beam cross section, 2.) to have a lot of straight sections, 3.) to have a four fold symmetry with at least 4 long straight sections, and 4.) to have in a lot of straights a so called mini beta sections. As lattice was chosen an extended DBA structure with combined function bending magnets in order to get a compact magnetic structure. The lattice has a distributed dispersion function to get in all magnets a so called TME - structure which leads to a minimized emittance. The emittance is 4.3 nmrad and the lattice provides overall 24 straight sections: 4 long (8 m long), 12 medium (4.3 m long), and 8 short (2.3 m long). Overall 38 % of the circumference is devoted to straight sections. The medium straights have so called "mini beta section" to reduce the size of the stored beam and lead to a high photon flux density. The radio frequency system (using normal conducting cavities), the vacuum system and the rest of the components is designed to store an electron beam up to 400 mA.

4.4.2   The Lattice of ALBA

4.4.2.1   *Conditions for the Redesign of the ALBA Light Source*

The original conceptual design for the ALBA project (called LLS at the times, [1]) was based in a 12 fold TBA lattice operating at energy of 2.5 GeV and a circumference of 250 m. This project was worked out during the period from 1993 to 1998. In 2003 the central Spanish Government and the State Government of Catalan approved the Spanish Light Source ALBA, which has to be build near Barcelona. After reconsidering the scientific case with a survey of the Spanish user community (including several workshops) the following conclusion where reached in order to fulfill the needs of the community and reach the requirements of a modern 3rd generation light source:

- The energy should be 3 GeV in order to reach with "in-vacuum" undulators photon energies of 15 to 20 keV.
- According to the available budget the circumference has to be smaller as 270m
- The symmetry of the machine should be 4 fold with 4 long straight sections (at least 8 m long) and 12 straights (at least 4 m long). One long straight is required for the installation of all injection elements.
- The lattice should be optimized for a high photon flux density, which means to introduce in some straight section the so called "mini beta sections".
- The natural emittance has to be in the range of smaller as 5 nmrad.
- The "topping up" injection mode must be possible in order to have a constant head load on the optical components of the beam lines.
- The lifetime should be large enough (› 15 hours) to reduce the radiation level in the experimental hall.
- For reaching the required lifetime the energy acceptance should be et least 3%
- Feedback systems have to be introduced to get sub-micron-stability of the stored electron beam.
- The option to use in a later stage the single bunch should be kept open.

4.4.3 Selection of the ALBA Lattice

4.4.3.1 Design Philosophy

The performance of a synchrotron light source is given by: 1) the emitted photon spectrum required by the users, 2) the brilliance of the emitted radiation, 3) the overall length of the straight sections, and 4) the stability of the beam. These performance factors are determined by the following parameters of the machine:

The emitted spectrum is proportional to the square of the energy of the electrons ($E_{ph} \approx E_{electr}^2$).

The brilliance of an undulator is proportional to the stored current (I), to the length of the undulator (L_{ID}), and inversely proportional to the horizontal emittance (ε_x) of the stored electron beam ($Br \approx I\, L_{ID} / \varepsilon_x^{1.5}$).

The overall length of the straight sections depends upon the design of the lattice and is proportional to the circumference (C) of the machine.

The stability of the beam is given by the rf-, vacuum-, feedback- systems, etc.

By fixing the energy, according to the required photon spectrum and assuming a stable beam, the overall brilliance of the machine is determined by the length of the straight sections, the emittance of the beam and therefore by the design of the lattice. For a fixed circumference the emittance is given by the lattice (magnetic structure within the unit cell). In general the emittance is given by the following formula:

$$\varepsilon_x = C_q \gamma_0^2 \frac{1}{J_x} \frac{1}{3*4\sqrt{15}} \varphi_0^3$$

$$\varepsilon_x = 31.66\,\text{nmrad} * K * \frac{1}{J_x} * (E/\text{GeV})^2 * (\varphi/\text{rad})^3$$

$$(1)$$

where E is the energy of the beam and φ is the deflection angle of the bending magnet. K is a constant of the lattice and is given by the distribution of the beta- ($\beta(s)$) and dispersion ($\eta(s)$) functions within the bending magnets. A minimum of both functions within the bending magnet results in a small K-value. From the theoretical point of view K is equal 1 for the TME -, equal 3 for the DBA- and equal 7/3 for the TBA –structure [2]. For real lattices the K –values are roughly a factor of 3 higher as the minimum theoretical ones, in order to obtain a sufficient dynamic aperture and energy acceptance. For getting a small emittance one should try to get the TME structure in most of the magnets. This is possible by using a so called "distributed dispersion lattice". J_x in formula (1) is the partition number in the horizontal direction. For combined bending magnets this value of J_x is roughly 1.3. Hence by using combined bending magnets with vertical focussing one reduces the emittance by roughly 30 %. Furthermore with the vertical focussing bending magnets one can skip the corresponding vertical focussing quadrupoles and the lattice is the most compact one.
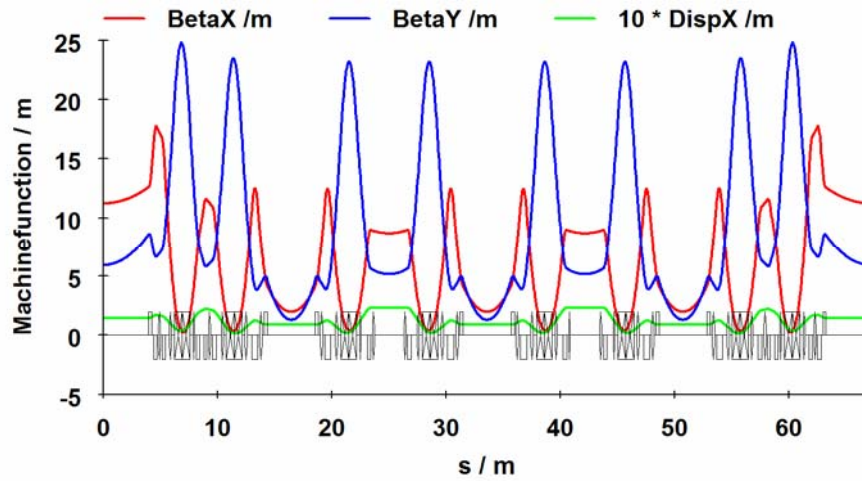
Figure 1: Machine function within one quadrant of the ALBA storage ring, existing of two unit cells (in the middle) and the matching sections at the beginning and end

By using the above numbers and taking a required emittance of 5 nm rad, the deflection angle per bending is 0.1967 rad or 11.26 degrees, which means one should have 32 bending magnets within the lattice. The lattice of ALBA (see Figure 1) exists of two unit cells (in the middle of the arc) and the matching sections on both ends. On both side of the unit cell, there are the mini beta sections to reduce the beam size (these are the medium straights of ALBA) and the short straights in the middle of the lattice.

With the requirement of having 4 long straight sections the lattice of one quadrant is build up with two unit cells and two matching sections as shown in Figure 1. The main parameters for this lattice are given in Table 1.

The lattice of ALBA has 24 straights: 4 long (7.97 m), 12 medium (4.19 m) and 8 short (2.6 m). Overall 38.6 % of the circumference is devoted to straight sections. Most interested for the users are the medium ones with the smallest cross section resulting in the highest photon flux density. At ALBA is has been decided that all the elements needed for the operation of the machine (diagnostics, feedback systems, cavities, etc) have to be located in the short straight sections, 6 of these straights are needed.

Table 1: The main parameters of the ALBA lattice

Parameter	Unit	
Energy	GeV	3
Tunes (Q_x / Q_y)		18.179 / 8.372
Natural Chromaticities (ξ_x / ξ_y)		-40.0 / -25.6
Momentum Compaction Factor (α_1)		8.8×10^{-4}
Second Order (α_2)		2×10^{-3}
Energy Spread ($\delta E/E$)		1.05×10^{-3}
Revolution frequency (f_0)	MHz	1.1161
Damping Times (τ_x / τ_y / τ_s)	ms	4.05 / 5.29 / 3.12
Partition Numbers (J_x / J_y / J_s)		1.3 / 1.0 / 1.7
Energy Loss per turn (U_0)	MeV	1.017
Harmonic Number (h)		448

Table 2: The machine functions and beam sizes in the middle of the straight sections

Parameter	Unit	
Long Straight Section		
Length	m	7.97
Beta (β_x / β_y)	m/rad	11.2 / 5.93
Dispersion (η_x)	m	0.146
Beam Size (σ_x / σ_y)	μm	271 / 16.2
Medium Straight Section		
Length	m	4.19
Beta(β_x / β_y)	m/rad	2.00 / 1.31
Dispersion (η_x)	m	0.087
Beam size (σ_x / σ_y)	μm	131 / 7.6
Short Straight Section		
Length	m	2.6
Beta (β_x / β_y)	m/rad	8.65 / 5.15
Dispersion (η_x)	m	0.234
Beam Size (σ_x / σ_y)	μm	315 / 15.1

4.4.3.2   Performance of Synchrotron Light Sources

To make a comparison between different Synchrotron Light Sources three parameters have been calculated: 1) the percentage of the circumference that is devoted to straight sections, 2) the *K*-value according to Eq. (1) (remember: a small *K*-value means a good lattice design), and 3) the total brilliance, which is equal to the total length of all straight sections divided by the emittance to the power of 1.5. A synchrotron light source has a good performance if 1) and 3) are high and 2) is small. In a presentation for a NATO workshop [3] the performances of the different Light Sources have been calculated and it is shown that ALBA can compete with other new build machines.

4.4.3.3   Optimization of the Working Point

The working point that fulfills the target of the design will lay in the region between 16 and 20 units in the horizontal, and between 6 and 10 in the vertical. The most promising regions in that area have been investigated, optimizing the lattice in each one of the points and obtaining the best setting of the sextupoles in each case. After this investigation, the region between 18 and 18.5 in the horizontal, 8 and 8.5 in the vertical has been selected as the one that provides the best compromise between linear performance (beam size, emittance) and non-linear parameters (lifetime, energy acceptance, dynamic aperture). Figure 2 shows the resonance diagram for this region. The working point selected for the operation is (18.18, 8.37), and the gradient of the bending magnet has been selected to provide the right focusing for it. However the lattice has enough flexibility, with a fixed gradient in the bending magnets, to move the working point ±0.5 units in both planes using only the individually powered quadrupoles. For greater flexibility the combination of individually powered extra coils and radial displacement of the bending magnets is also consider:
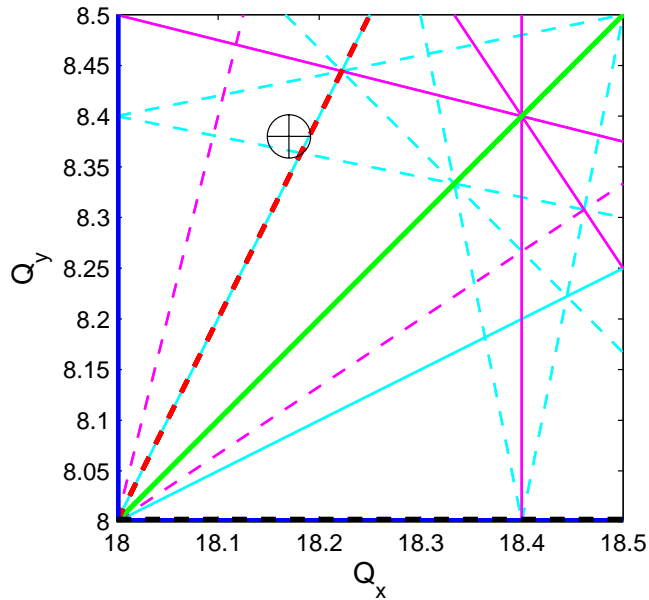
Figure 2: Resonance Diagram, showing the allowed resonances up to order 6, for the 4-fold symmetric lattice. The selected working point is the one show by the cross. The color of the line correspond to the order of the resonance (1st order is black, 2nd order is blue, 3rd order is red, 4th order is green, 5th order is magenta, and 6th order is cyan). Continuous lines correspond to normal resonances, and dashed line to skew ones.

4.4.4 Beam Dynamics

4.4.4.1   Dynamic Aperture

Figure 3 shows the dynamic aperture at the middle of the long straight section, for 10 sets of realistic misalignment and error correction, and high order multipoles in the magnets, for the on energy particle and for ±3% momentum deviation. . The aperture is limited mainly by the physical one**.** Figure 4 shows the frequency map of the lattice, including a 1 % coupling and one set of multipoles errors, and the resonances that affect most the dynamic aperture are identified.

The procedure to optimize the dynamic aperture is the one described in reference [4]. The OPA [5] and BETA [6] codes have been employed to optimized the settings of the 9 families of sextupoles, in order to obtain the desired dynamic aperture and energy acceptance. The approach is based in the minimization of the first order driving terms of the resonances (in the OPA case), and in the tune shift with the amplitude (BETA).
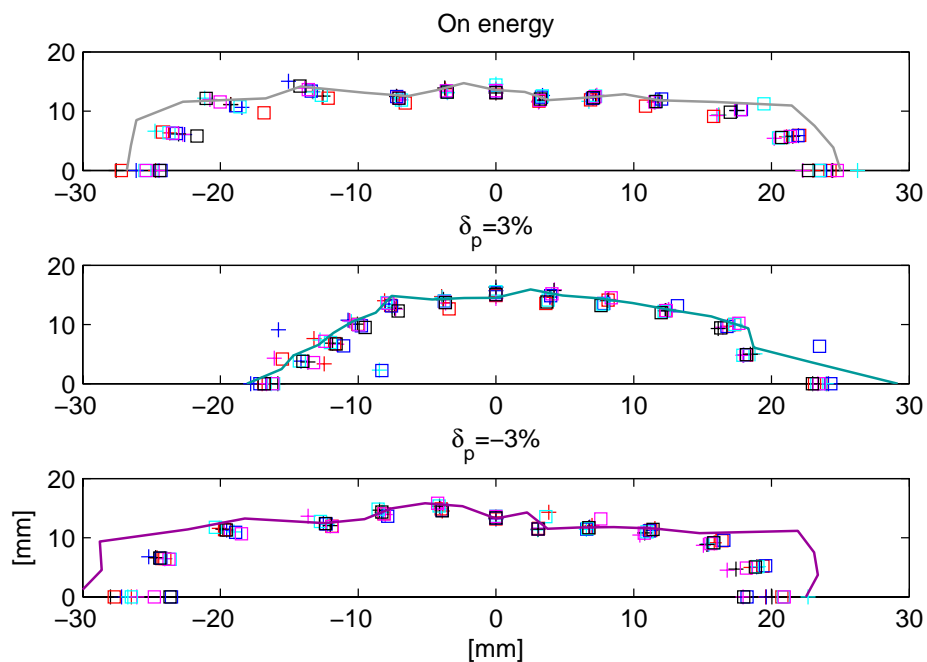
Figure 3: Dynamic aperture at the centre of the long straight section (β_x=11.2, β_y=5.9), for the on energy particle, and for ±3 % energy deviation, for both the ideal lattice (solid lines) and for 10 sets of orbit and multipole errors (after correction). The projection of the physical aperture in this point corresponds to ±16 mm in the horizontal (limited by the septum sheet) and 6.5 mm in the vertical (given by in-vacuum insertion devices and the bending vacuum chamber)

4.4.4.2 Coupling

The selected working point (18.18, 8.37) is far away of any systematic coupling resonance. Due to that, the coupling generated by the position errors is small, in the range of 0.2 % to 0.5 % for all the sample machines simulated. If an increase in the coupling is required either by the users or to increase the lifetime, the working point can be move close to a coupling resonance, or the vertical beam size can be increase by creating vertical dispersion

190
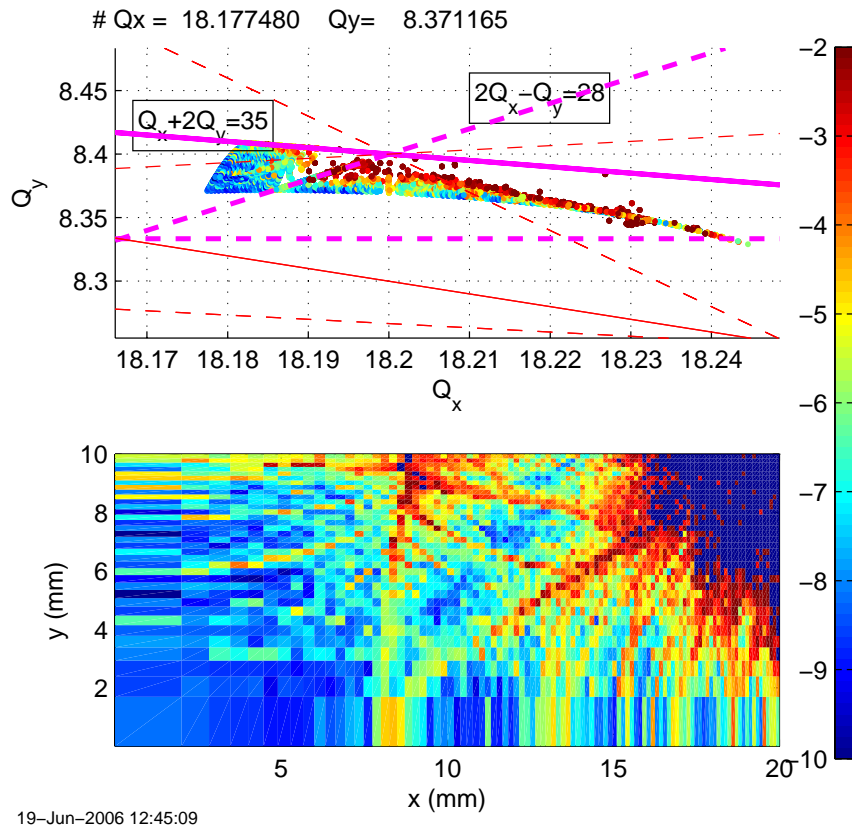
Figure 4: Frequency map for the ideal lattice, including 1% coupling and multipole errors.

4.4.4.3 Tune Shifts

Figures 5 shows the tune shift with amplitude, and Figure 6 shows the tune shift with the momentum deviation for chromaticity (1,1). The selected working point is far away from any coupling resonance, and the tune shifts are too small to couple the tunes.
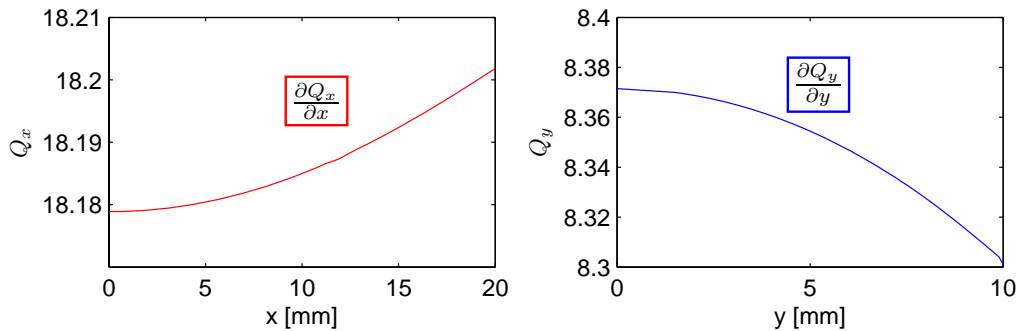
Figure 5: Tunes shift with the amplitude, calculate in the middle of the long straight section (β_x=11.2, β_y=5.9).
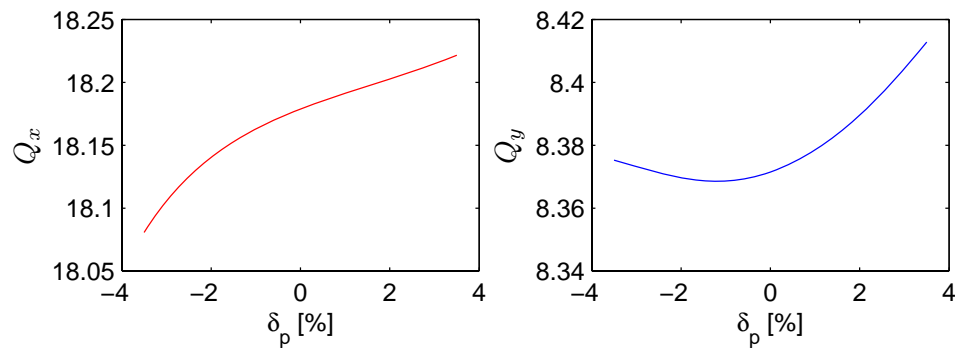
Figure 6: Tunes shift with the amplitude, calculate for the (1,1) chromaticity.

4.4.5 Effect of Errors and Closed Orbit Correction

One of the main requirements of a modern light source is to provide a stable beam at the source points. The usual requirement of a stability of 10 % of the beam at source points means a sub-micron vertical stability, both for slow displacements (due thermal drifts, ground settlement, seasonal changes, etc) as for fast displacements (due to ground vibrations or changes on the gaps or phase of the insertion devices) of the beam. In order to minimize the effect of vibrations et al. the magnets are mounted on girders with a high eigenfrequency. To measure the position of the electron beam, up to 120 beam position monitors (BPMs) can be employ, and to correct the orbit 88 horizontal and vertical correction coils have been added to the sextupole magnets to correct the orbit.

4.4.5.1   Orbit Correction

Two sources of errors have been considered:
- Error in the position of the girders: A realistic Gaussian error of misalignment of the girders of 150 μm rms in the vertical and horizontal position and a rotation error of 0.25 mrad.
- Error on the aligment of the magnetic axis of the elements in the girder: A realistic Gaussian error of misalignment of the magnetic center of the magnets of 50 μm rms in the vertical and horizontal position, and a rotation error of 0.1 mrad.

The strength required in the corrector magnets is of 300 μrad, well in the margin of the 1 mrad provided by the corrector magnets. Figure 7 shows the rms strength required in each one of the correctors for one quarter of the ring. Under the assumption of the closed orbit can be corrected to the desired sub-microm meter level at the BPMs and insertion devices, and under 50 μm elsewhere.
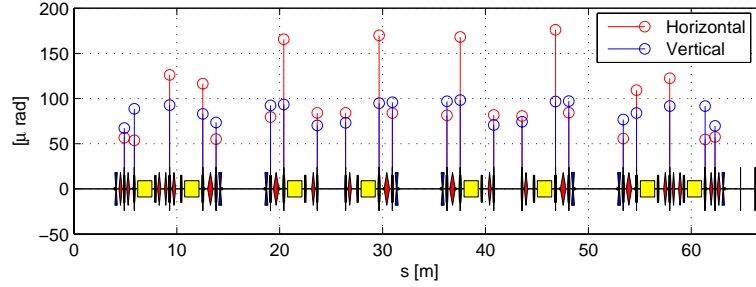
Figure 7: Distribution of the required corrector strength for realistic settings of the errors. The bars show the required rms strength for each family of correctors. The residual orbit at the BPMs and at the medium and long straight sections is under the μm, and under 50 μm elsewhere.

4.4.6 Beam Life Time

For the operating conditions of ALBA (400 mA of current in 400 bunches, 1 nTorr of resisudal N_2 pressure, 1% coupling, orbit errors plus orbit correction), the lifetime for the different contributions are:

- Elastic scattering: $\tau_E = 78$ h
- Bremsstrahlung: $\tau_B = 60$ h
- Touschek: $\tau_T = 28$ h
- Total Lifetime = 15 h

The Touschek lifetime depends strongly in the local energy acceptance of the machine, given by the minimum between the RF energy acceptance (3% in the ALBA case) and the local acceptance of the lattice. This last one depends on the optics and sextupole arrangement, the coupling and the physical limitation (vacuum chamber, in-vacuum devices, septum). For the ALBA case and for most of the realistic situations studies (errors, multipoles, insertion devices, etc) the energy acceptance of the lattice has been found to be larger than the one of the RF.

This lifetime (even assuming a reduction by a factor two due to other contributions) is still large enough for a reliable operation in the planned top-up mode, with an injection cycle every few minutes.

A detailed description of the lattice and the non linear behaviour can be found in the proceedings if the PAC and EPAC conferences [7], [8] and [9].

4.4.7 Effect of insertion devices

The portfolio of beam lines for the fist phase of ALBA includes the use of 2 in vacuum planar undulators with a gap of 5.5 mm, 2 Apple-II type undulators and 2 wigglers (see Table 2) The effect of the in-vacuum is mainly due to the reduction of the vertical physical acceptance of the machine, and a small reduction of the energy acceptance for high chromaticities has been observed. The effect of the Apple-II and wigglers is more complicated, including a tune shift, and in the case of the Apple-II, coupling. However, as they will be placed in the medium straight section, the effects are moderate.

4.4.8 Conclusions

The lattice selected for ALBA fulfills the requirements given by the scientific needs of ALBA. The use of combined function magnets reduces the space required by the magnets, allowing a larger number of cells for a given circumference, with the corresponding reduction in the emittance, while keeping relatively small chromaticities that simplifies the design of the sextupole system. The lattice has similar performance (lifetime, injection efficiency, beam stability) that other modern light sources, with a small circumference. With the scaling of the lattice to dimensions of the NSLS-II one could come up to an emittance of 0.7 nmrad without any damping wigglers.

4.4.9 Acknowledges

The authors want to acknowledge the help and contributions of Les Dalin (CLS), E. Levichev and P.Piminov (BINP) for the beam dynamics calculations as well as the members of the ALBA design and construction team.

4.4.10 References:

1. LLS Design Team, "Design of the LLS" in ICFA Beam Dynamics Newsletter, number 28, pag 19, September 2002.
2. L.C. Teng, "Minimum emittance lattices for synchrotron radiation storage rings", ANL/FNAL LS-17, May 1985.
3. D. Einfeld, "Synchrotron light sources, status and new projects", in "Brillian light in life and material sciences", Springer, NATO Security throught Science Series-B: Physics and Biophysicis, 2007.
4. J. Bengtsson, "The sextupole scheme for the Swiss Light Source: An analytic approach", SLS-Note 9/97, PSI, 1997.
5. OPA, A. Streun, reference page: http://slsbd.psi.ch/~streun/opa/opa.html
6. L. Farvacque et al. "The BETA users guide", ESRF, Grenoble.
7. M. Muñoz, D. Einfeld, "Optics for the alba lattice" in Proceedings of 2005 Particle Accelerator Conference, Knoxville, Tennessee.
8. M. Muñoz, D. Einfeld, T. F. Günzel, "Closed orbit correction and beam dynamics issues at alba", in Proceedings of EPAC 2006, Edinburgh, Scotland.
9. D. Einfeld, M. Belgroune, G. Benedetti, M. De Lima, J. Marcos, M. Muñoz,M. Pont, "Modelling of gradient bending magnets for the beam dynamics studies at ALBA", in Proceedings of PAC07, Albuquerque, New Mexico, USA.

4.5 Beam Based Alignment in Synchrotron Light Sources[*]

Christoph Steier, Greg Portmann
LBNL, 1 Cyclotron Road, MS80R0114, Berkeley, CA94720, USA
Mail to: CSteier@lbl.gov

4.5.1 Introduction

Beam Based Alignment has been used successfully for many years to improve the performance of storage rings. This article will deal specifically with the case of (3rd generation) synchrotron light sources, where beam based alignment is now used routinely and frequently for initial commissioning [1], after realignment of storage ring components as well as to routinely optimize everyday operation. It has also been used at linear accelerators and is proposed for future linac driven X-ray FELs as well as the ILC, but this will not be discussed here.

The reason why beam based alignment is necessary is the fact that even with best engineering efforts, beam position monitor (BPM) installations usually have rms offsets in the range of several 100s of microns relative to the magnetic centers of neighboring magnets. There are many individual error sources contributing to this and it is impractical to reduce all of them to the level achievable with beam based alignment, which can easily reach precisions of 10s of microns in light sources. The ultimate error of beam based alignment is often dominated by systematic effects – some of it will be briefly discussed later in this article – and not by measurement noise.

Knowledge of the relative position of the BPM centers relative to the magnetic centers of quadrupoles on the scale of 10s of microns is important to minimize spurious effects, namely dipole kicks in quadrupoles, as well as quadrupole and skew quadrupole feed-downs in sextupoles. These could otherwise cause spurious vertical dispersion, emittance coupling, and beta beating and therefore a reduction in brightness as well as deterioration of the dynamic aperture and dynamic momentum aperture. Beam based alignment nearly always gets supplemented by further beam based optimization. In most cases orbit response matrix analysis is used to experimentally determine the quadrupole and skew quadrupole error distribution and correct it. The fact that these methods achieve a very high precision relaxes the requirements on beam based alignment significantly, however to achieve ultimate performance it is necessary to combine both techniques.

On a more practical level, the use of BPM offsets determined by beam based alignment in many cases makes it possible to use all singular values in the SVD based orbit correction, while correcting to the ideal orbit. If one would not use those offsets and try to correct all BPM readings back to zero while retaining all singular values, corrector magnets which typically have maximum strengths of less than 1 mrad would often not have sufficient strength.

Finally, beam based alignment allows an easier and predictive alignment of the user photon beamlines at light sources, since it establishes the beam position relative to the magnets, which can be easily surveyed. This optimizes the performance of the photon beamlines and therefore the overall light source facilities.

The resolution requirement for beam based alignment has evolved over time with all 3rd generation light sources (including the older ones) progressively reducing the natural emittance over time by using increasingly aggressive lattices. It started in the range of nearly 100 microns but nowadays is in the range of 10-30 microns for the newest machines. There is also a more practical resolution requirement, which demands to always strive for the best resolution possible: since the so-called golden orbit, which is used during user operation of light sources, is usually based on the beam based alignment offsets, it is extremely important to not introduce sudden changes of the source points coordinates for users. From this standpoint a resolution in the range of 1 micron would be desirable, however this is usually not achievable so far. Therefore, many light sources reduce the frequency at which the golden orbit is updated (at the

ALS we usually do not update the golden orbit more often than once a year, unless work on the BPM system causes significant offset changes).

4.5.1.1   *Example: Advanced Light Source (ALS)*

The Advanced Light Source (ALS) [2] located at Lawrence Berkeley National Laboratory is one of the first 3rd generation light sources and has been in operation since 1993. It has pioneered many techniques to optimize storage ring performance and the software for beam based alignment developed at the ALS is now widely used at many other light sources worldwide. The ALS currently has more than 40 simultaneously operating user beamlines and is serving more than 2200 user per year. It was originally optimized for the VUV and soft x-ray part of the spectrum, but by now it is serving users all the way from the IR part of the spectrum to hard x-rays (up to about 40 keV). Figure 1 shows a list of the current ALS beamlines.
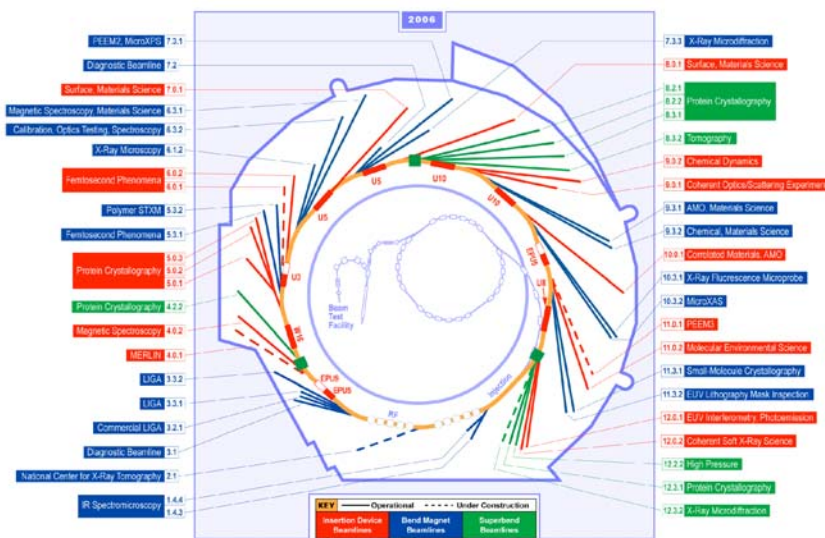
Figure 1: Beamlines at the ALS in 2006.

The ALS like nearly all other 3rd generation light sources has a highly periodic lattice, in this case a triple bend achromat lattice with a strong gradient in the bending magnets. There are 12 achromats with three of them modified by the addition of 6 T superconducting bend magnets. Figure 2 shows a sketch of one of the ALS arcs including beam position monitor and magnet locations. Most quadrupoles in the ALS are powered by individual power supplies. The one family of quadrupoles on a chained power supply has additional shunt resistors installed, that allow beam based alignment. In combination, at least 6 of the 8 BPMs in every arc can be used for quadrupole beam based alignment (all 8 of 8 in the Superbend sectors). The remaining BPMs could be used for sextupole beam based alignment, however, this is not done routinely.
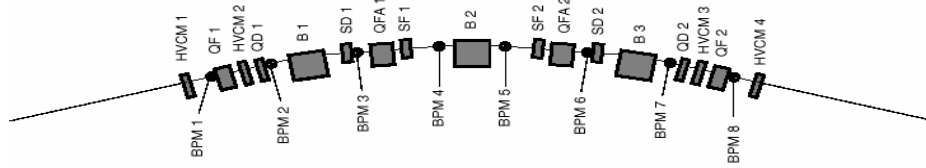
Figure 2: Sketch of one arc of the ALS, showing magnet and beam position monitor locations.

Beam based alignment at the ALS is carried out multiple times every year. Most of the times, the results are just documented and examined to identify BPM problems. After every major shutdown (once a year), the results are used to establish a new golden orbit (which is a smooth approximation through all beam based alignment centers). The beam based alignment software is fully automated and a complete measurement for the whole ring (78 quadrupoles) takes about 8 hours. The results of the beam based alignment measurements at the ALS tend to be fairly stable over time (on the 10s of microns level), unless BPM electronics are exchanged, RF cables reconnected, or magnets/vacuum chambers realigned.

4.5.2   Measurement Method

The beam based alignment algorithm used at the ALS is straightforward [3, 4]. The procedure starts with an orbit correction to the old offset orbit. Then the orbit is swept through the BPM/quadrupole combination to be centered and at each step the quadrupole is changed. After the new centers are established for every quadrupole, the process is usually iterated, to minimize systematic errors if the initial offset orbit was too far away from the correct one.

For the details of the algorithm there are many choices and they can be easily configured in the software being used at the ALS. To sweep the orbit, it is possible to use one magnet (with proper phase advance) or use a local bump. To avoid systematic errors due to effects in other magnets and due to a large orbit angle if the BPM is longitudinally offset from the quadrupole center it is usually more desirable to use a local bump. Another parameter is the number of steps and the size of the orbit sweep.

In terms of the change in quadrupole current it has proven to be essential to stay on one hysteresis branch (directional sweep). This is especially true if C-shaped quadrupoles are used. It also helps to precondition the hysteresis state, so that the quadrupole response to a current change is linear. Again, the number and size of quadrupole strength steps can be configured and needs to be optimized to minimize errors due to nonlinearities.

The ALS software uses the change in orbit at all BPMs in response to a quadrupole strength change to determine the quadrupole center. In this process, automatic cuts are applied to eliminate BPMs with poor sensitivity (due to phase advance) or noisy data. However, currently no orbit fit is used, since the results at the ALS are sufficiently good. An orbit fit in general could help to reduce systematic errors further and has been used successfully at the ATF and PEP-II [5]. It does require a reasonable machine model (which is available at all light sources, since orbit response matrix analysis is used).

4.5.3 Challenges

Several effects can create systematic errors of the beam based alignment. The random error due to BPM noise is usually negligible compared to those. Possible systematic errors start with the effects of real orbit jitter [6]. At most light sources, the orbit jitter even without fast orbit feedback (which has to be off during beam based alignment) is relatively small (few microns). If this is the dominating effect, it can be reduced by using an orbit fit for the kick created by the quadrupole whose strength was changed.

One problem that initially created a very larger problem at the ALS is the fact that the different multipole fields of a single magnet do not necessarily have the same magnetic center. This is especially true for the C-shaped quadrupole magnets (without flux bypass) used at the ALS [4]. The symmetry break introduced by the C-shape of the quadrupoles for example changes the magnetic center by 100s of microns when the hysteresis branch is changed. The solution for this problem was to use a directional sweep of the quadrupoles and to always stay on the same hysteresis branch – this approach also improves systematic errors for other magnet types.

If shunt resistors are used to change the strength of individual magnets, which are otherwise powered by one chained power supply, the transient current variation when the shunt is closed, can leave to hysteresis effects in all other magnets on the string. This is caused by the fact that powersupply regulators usually are not fast enough to react to the change in overall resistance caused by the shunt, resulting in a small, temporary current glitch. The error due to this effect can again be minimized by using an orbit fit, or by using a small, regulated and floating power supply to actively shunt some current, thereby avoiding any current glitch.

A large orbit angle at the location of the quadrupole/BPM location can cause fake offsets in the result of the beam based alignment, if there is some longitudinal separation in the position of the quadrupole and the BPM, which is often the case, since BPMs are usually located next, but not inside, quadrupole. This effect can be minimized by using proper local bumps with zero angle at the position of the quadrupole/BPM and/or by carrying out the beam based alignment iteratively with the global offset orbit of the first alignment used as the starting point for the subsequent one.

Finally there are other possible systematic errors of not using a local bump to sweep the orbit across the quadrupole to be aligned. If it is impractical to use a local bump, those can be reduced again by iteration, orbit fit, choice of proper individual corrector magnets and amplitude of the orbit sweep.

4.5.4 Some Examples of Results

Figure 3 shows the results of the beam based alignment of one individual magnet at the ALS. The topmost plot shows the raw results of all BPMs for a quadrupole strength change for 5 different orbit locations. The middle 2 plots show fits to the raw data with some BPMs based on their noise or small slope (insensitive due to phase advance) automatically excluded. The lowest plot shows the results for the quad center as calculated by the orbit change at each of the other BPMs. BPMs that were rejected are shown in red, the ones that were kept are shown in blue. The statistical error of the final result is well below 10 microns.
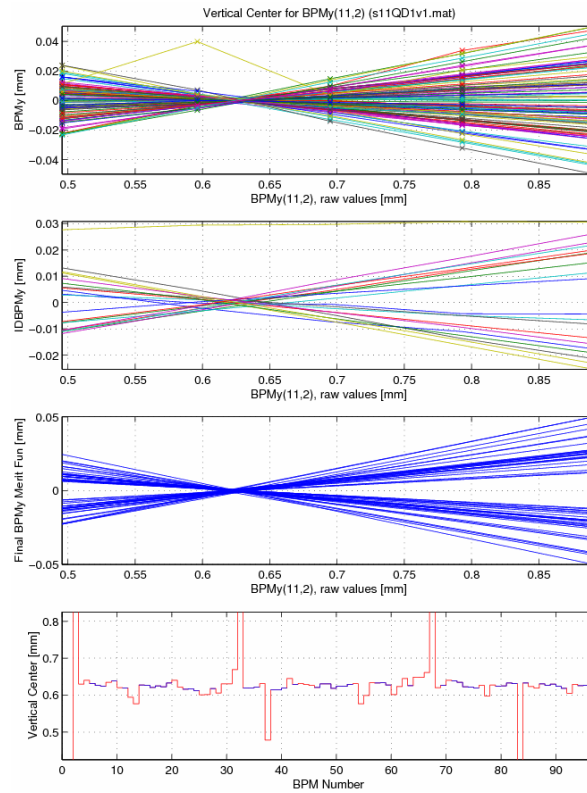
Figure 3: Example of a beam based alignment measurement for one BPM/quadrupole combination at the ALS.

The BPM offsets we measure at the ALS are fairly significant, with the rms value being several 100s of microns (see Figure 4). This is fairly similar of all other newer light sources as well, with the rms always being in the 100s of microns. However, the offsets stay constant over time and beam based alignment at the ALS is only necessary after hardware changes or a realignment of the storage ring.
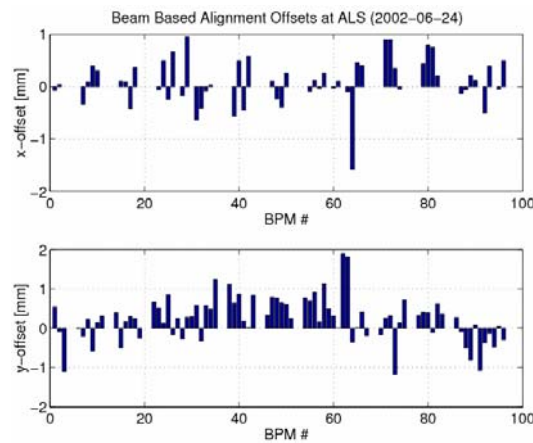
Figure 4: Beam based alignment offsets for 78 (of the 96) BPMs at the ALS. The offsets are very sizeable (many 100s of microns), however, they stay very stable (10s of microns) over time

To confirm the accuracy of the beam based alignment at the ALS, a measurement of the spurious vertical dispersion was carried out with the sextupoles being switched off (i.e. at natural chromaticities of about -30, -24). Since the spurious vertical dispersion for a given set of dipole kicks scales like the absolute value of the chromaticity, this is a very sensitive measurement of how well centered the orbit is in the quadrupoles. Based on the scaling of the vertical dispersion with larger orbit errors it was possible to conclude that the beam based alignment had been accurate to at least 30 microns in the vertical plane.

In nominal conditions, i.e. with the sextupoles back on, the remaining symmetry breaking and coupling from offsets in sextupoles and the resulting quadrupole and skew quadrupole feed-downs can be relatively easily corrected with beam based lattice diagnostics (response matrix analysis; phase advance measurements; MIA). In the example of the ALS, the rms beta beating is routinely corrected to below 0.5%, the spurious vertical dispersion to about 2 mm rms, and the smallest vertical emittance achieved has been 5 pm, for a horizontal emittance of 6.75 nm [7].

We have also experimented with using orbit response matrix analysis to carry out beam based alignment of the sextupoles at the ALS. In this case we measure response matrices with different sextupole strengths (including sextupoles off). The results for the sextupole centers are reasonable, however, not quite as accurate for quadrupoles. At the moment, those sextupole offsets are not used in the offset orbit, instead quadrupoles are used to restore symmetry including the errors coming from the sextupole feed-downs.

The beam based alignment software at the ALS is part of a bigger software package, the Matlab Middle Layer, which was originally developed in an ALS/SPEAR collaboration and is now widely used at Light Sources worldwide. It is described in more detail in the following subsection.

4.5.5 Matlab Middle Layer

The ability to build more and more complexity accelerators is in part due to better computers and software tools. Unfortunately, history has shown that one of the most likely deliverables to go over cost and schedule even with scope reduction is software. And the day it is delivered starts a feature creep effort that only ends when the accelerator is turned off. This increased demand for software has outpaced most software budgets. One possible solution is collaboration. At all levels of software effort laboratories around the world are making large efforts to share resources and burden. EPICS and Tango are two examples of large accelerator control systems at running at multiple facilities and were written by a group effort. Accelerator tracking codes are another example. High level control of particle accelerators has probably seen less sharing of software but that is rapidly changing. SDDS from APS and XAL from Oak Ridge are examples of sharable high level software for doing accelerator physics. In a joint effort between ALS and Spear3 (SLAC), a Matlab based high level control software system has been gain popularity in the world [8].

Matlab has been used in particle physics at many institutions for a long time. Matlab was first used at the ALS in the early 1990s shortly after commissioning. In the beginning it was primarily used as a scripting language for machine physics shifts but has now grown into a larger and more general high level control tool. The name Matlab Middle Layer is no longer appropriate since it is much more than a middlelayer, but the

MML acronym has stuck. Matlab is a matrix manipulation language originally developed to be a convenient language for using and developing algorithms. Matlab does cost money but it comes with a huge and ever expanding function library. The ever expanding part also comes from an active world-wide developer base. The advantage of using a commercial product is that some of the desirable feature creep is done by a company and not the laboratory. Actually, many more features are added ever year then needed but the cost is very small and having room to grow is almost required in an R&D environment.

The software collaboration started with ALS and SPEAR3 then expanded to the Canadian Light Source, Pohang Light Source, NSLS VUV and X-ray rings at Brookhaven, and Duke FEL. The MML project substantially expanded in the past years with the three new light sources in the world – Soleil, Diamond, and the Australian Synchrotron Project – making extensive use of the MML software for commissioning and operations. The next two light sources in the world at Shanghai (SSRF) and Barcelona (ALBA) are planning to join the collaboration has well. Lastly, the light source in Thailand (SPS) is presently commissioning the MML software. The MML is very applicable for resource limited countries (both in funds and experience in particle physics) because they can quickly come up to speed and try the same algorithms used all around the world. Since the MML software uses the AT (accelerator toolbox) simulator, one can also test algorithms on any of the above accelerators. In total, eleven accelerators are presently using the MML software and at least 2 more will be using it in the next year.

Although the MML software was designed to be a scripting tool for designing and testing complex algorithms predominately during physics shifts, the MML software has also migrated into machine operations. This is a departure from the more standard programming languages used in the control room and had to overcome perception problems among software engineers. However, the reliability and speed of Matlab has proven to be more than adequate for machine operations. Typical storage ring operations uses include lattice configuration save/restore, energy ramp, global orbit correction, slow orbit feedback, and insertion device compensation. The core functionality of the MML software is focused on accelerator setup. This includes orbit control, beam-based alignment, tune correction, chromaticity correction, response matrix measurement, LOCO, insertion device compensation, photon beam steering, and as a general scripting language for machine physics studies. As the complexity of accelerators and need for precision increases, the need for more advanced and flexible programming environments that can support a collaborative effort increases. What makes Matlab so appealing for accelerator physics is the combination of a matrix oriented programming language, an active workspace for system variables, powerful graphics capability, built-in math libraries, and platform independence.

This collaboration has produced three Matlab toolboxes written for accelerator physics – MML, AT, and LOCO. All three are well integrated and have proven to be quite useful for machine studies and control at several operating machines. The relatively user-friendly software and almost machine-independent programming language have fostered a number of collaborations. Most scientists find the syntax quite intuitive making it possible for visitors to participate in machine development studies with minimal training. Having multiple laboratories use the same high level software has proven to be quite useful.

Not every laboratory has to spend the resources to write the same algorithms. For new laboratories it's a very inexpensive and fast way to acquire high level control and simulation software that has also been thoroughly tested on other machines. Software development is not only expensive from a labor point of view, it is very expensive to test and commission new software from a beam time perspective. Having the same software package debugged at many laboratories has improves reliability. Thousands of dedicated accelerator hours have been spent testing, improving, debugging, and exercising the MML, AT, and the LOCO software packages. As with the EPICS collaboration, software expansion, suggestions, and new ideas come from a bigger pool of people.

The number of physicists and engineers trained on the Middle Layer is growing rapidly. That way visiting scientists can work immediately on the new accelerator with very little training. This is particularly usefully during commissioning phase of an accelerator. Running the same code on different accelerators makes it easier to find similarities and differences between accelerators. This is very helpful when trying to reach the design performance of an accelerator.

Being able to switch between so many different accelerators in a simulated mode is very informative when developing new algorithms and test designs for future accelerators. Writing software in a machine independent way is more time consuming but the final product tends to be better written and more robust.

Fig. 5 shows the same beam-based alignment algorithm run at CLS (Canada) and Spear3 (USA) – different accelerators, same software. It is also very helpful to know ahead to time what the experimental results should look like. A good guess comes from running the algorithm on the machine simulator and comparing experimental data with a similar type accelerator. Often the first time an online measurement is attempted the results are not very clean so having this information greatly speeds up trouble shooting. The ultimate goal the MML collaboration is to speed up the implementation of known ideas to that there is more time left to experiment with new ones.
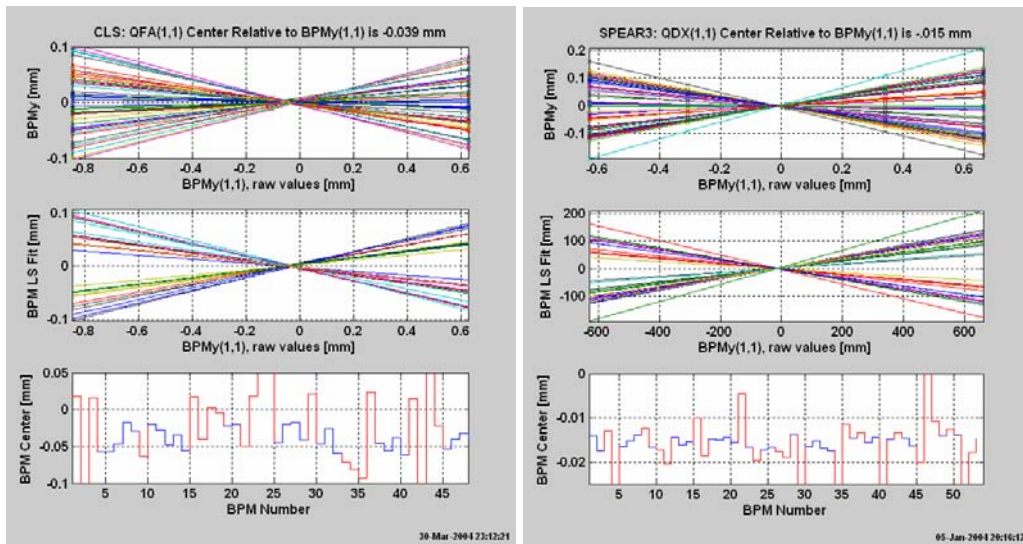
Figure 5: Beam Based Alignment of a Quadrupole at CLS and Spear-3 using the MML.

4.5.6 Summary

Beam based alignment is routinely used at all 3rd generation light sources. The algorithms used are automated and allow a complete measurement of the rings on the order of less than one day. Beam based alignment is essential to optimize the performance of the light sources and are also very useful to align photon beamlines in a predictive way. The achieved systematic errors of the offsets are below 30 microns, with the statistical errors contributing only insignificantly. This resolution is good enough. Combining this with other beam based correction techniques like response matrix analysis one can nearly perfectly compensate gradient and skew gradient errors. Achieved beta beating is well below 1% and emittance ratios of less than 0.1% have been achieved.

The long term stability of measured beam based alignment offsets is good (for well designed vacuum chamber - magnet supports), offsets typically change by much less than the average annual ground settlement. To achieve good accuracy of the beam based alignment, it is very important to analyze all relevant systematic errors. Some of them (like hysteresis in C-shaped magnets) can have huge influence on the results.

The Matlab middle layer provides many standard tools for storage rings (including beam based alignment). It is now widely used at light sources worldwide.

4.5.7 References

1. J. Safranek, et al., "Spear3 Commissioning", Proceedings of APAC 2004, Gyeongju, Korea, p. 39-43 (2004)
2. "1-2 GeV Synchrotron Radiation Source Conceptual Design Report", LBNL PUB-5172 Rev. (1986)
3. G. Portmann, et al., "Initial Beam Based Alignment of the ALS Quadrupoles", Proceedings of PAC 1995, p. 2693 (1996)
4. G. Portmann, et al., "Beam-based alignment of C-shaped Quadrupole Magnets", EPAC 1998
5. M. Woodley, et al., "Beam-Based Alignment at the KEK-ATF Damping Ring", Proceedings of EPAC 2004 and LBNL-55728.
6. K. Kopp, "Comparison of Beam Based Alignment Algorithms in the Presence of Beam Jitter", (2005)
7. C. Steier, et al., "Coupling Correction and Beam Dynamics at Ultralow Vertical Emittance in the ALS", Proceedings of PAC 2003, Portland, Oregon, p. 3213 (2003)
8. G. Portmann, et al., "An Accelerator Control Middle Layer using Matlab", Procceddings of PAC 2005, Knoxville, Tennessee, p. 4009 (2005)

4.6 Beam Physics Activities at Northern Illinois University

B. Erdelyi, J. Lewellen, P. Piot, Dyshkant, D. Mihalcea, I. Pogorelov, B. Terzic, N. Vinogradov, L. Bandura, J. Maloney, T. Maxwell, E. Nissen, M. Rihaoui, B. Sprague, S. Zownorega
Northern Illinois University, Northern Illinois Center for Accelerator and Detector Development & Department of Physics, DeKalb, IL, 60115
http://www.nicadd.niu.edu/research/beams/
Mail to: erdelyi@nicadd.niu.edu

4.6.1 Introduction

The Beam and Astrophysics Group (BPAG) at Northern Illinois University was founded in August 2002 by the late Professor Courtland Bohn. Currently the group consists of two faculty members (having joint appointments with Fermi National Accelerator Laboratory and Argonne National Laboratory), an adjunct faculty, six graduate students, and four postdoctoral scientists associated with the group. The group is housed in the Department of Physics and part of the Northern Illinois Center for Accelerator and Detector Development (NICADD).

The context of BPAG research encompasses theory, simulations and experiments, and spans both electron and hadron beams. Concerning electron beams, our group's focus is diverse. Of special interest are high-brightness electron sources that will feed 4th-generation light sources and/or a linear electron-positron collider, high-average-current sources that will feed accelerator drivers for high-average-power free-electron lasers, and space charge dominated electron dynamics in rings. Concerning hadron beams, our focus is on high-average-current accelerators such as is required for copious production of spallation neutrons, on exotic beam facilities, and on heavy-ion cancer therapy machines.

Our work includes laboratory experiments involving novel beam diagnostics that have been done at the Fermilab/NICADD Photoinjector Laboratory. We are involved in experiments on space-charge-dominated beams and novel phase space manipulation concepts in collaboration with the Argonne Wakefield Accelerator at Argonne National Laboratory. We are also collaborating with the University of Maryland in planning experiments on the fundamental dynamics of space charge in beams that will be done at the University of Maryland Electron Ring. We have an in-house Beam Diagnostic Laboratory that includes a novel low energy electron source, a femtosecond-class laser and generic instruments.

On the theory front, we study Hamiltonian systems in general, which historically led to the development of seemingly two different branches of mathematics: the theory of dynamical systems and symplectic geometry. Both fields have undergone dramatic recent development and it is becoming clear that there is a common core that leads to a new field called "symplectic dynamics". We are active in this field since one of the best test beds of this new field is the accelerator (or particle beams in general).

In summary, we are developing new theories and methods to describe, simulate, measure and gain further insight into the behavior of particle beams. The methods range from abstract mathematics from symplectic geometry and topology, through advanced numerical methods such as differential algebra and symplectic integration, to experiments. Our goal is to have a complete program whereby we clear and pave new ground in theory, simulations, and experiments toward reaching our overarching objective of enhancing substantially the understanding of the fundamental dynamics of nonequilibrium high-brightness beams. With that, our ultimate goal is to be able to do end-to-end simulations of accelerators of high-brightness beams, in which space charge, wakefields, coherent synchrotron radiation, i.e., collective effects in general, are accurately included, whereby the accuracy will have been established via detailed code verification and validation.

An important activity of our group is education in accelerator physics and mentoring postdoctoral scientists. To this end, we developed a graduate curriculum in beam

physics, we offer summer undergraduate internships, and mentor summer students at Argonne National Laboratory.

In the following sections we describe the main current research topics of interest in our group.

4.6.2   Electron Beams

4.6.2.1   *Modelling of Electron Beams (Pogorelov, Sprague, Terzić)*

4.6.2.1.1 Improvement of Wavelet-Based Algorithm

Our group has constructed a wavelet-based Poisson solver for use in particle accelerator simulations [1]. The ultimate goal of this project is to develop a space-charge potential solver which is able to show more small scale detail of the beam simulation while keeping the simulation time comparable to the current FFT-based solver. This improvement is accomplished by taking advantage of the relative sparseness of the wavelet basis expansion of the density and potential of a particle beam as compared to a Fourier basis expansion.

The first version of this solver was combined with the accelerator code Impact-T and shown to be a competitive alternative to a FFT-based solver. It uses an iterative conjugate gradient algorithm to solve the Poisson equation in wavelet space, allowing the use of the previous time step's solution to accelerate the convergence of the current solution. Boundary conditions were applied in a prior stage using a Green's function approximation for a grounded rectangular pipe. Exclusively orthogonal wavelet bases were used, and a diagonal preconditioner was used to reduce the condition number of the Laplacian operator to the order of the number of grid points.

We are currently working on improving the power and efficiency of the wavelet-based approach. In order to reduce the computational and memory overhead of applying the Laplacian operator matrix in wavelet space, we are planning to utilize the "non-standard" form of the operator, in which the operator is applied to each scale in the wavelet analysis separately. In this form, the natural sparsity of the operator in wavelet space is more readily exploited.

The new solver will also be generalized for the bi-orthogonal basis of interpolating wavelets. Due to the special properties of these wavelets, this will allow us to create an adaptive grid structure, in order to apply "open" boundary conditions without requiring an extra stage for the Green's function approximation, as well as ensuring the accuracy of the boundary conditions. This renders the new approach more easily parallelizable.

4.6.2.1.2 Progress toward a Grid-Free Vlasov-Poisson Equation Solver

We explored three main approaches to solving the Vlasov-Poisson equation (VPE) directly: (1) decomposing the VPE in the orthonormal basis of functions and directly solving for time-dependent coefficients; (2) directly solving for time-dependent coefficients of the VPE by using a splitting scheme in which advection and acceleration steps are done separately; and (3) using a gridless *N*-body method based on approximation of particle distribution function (DF) sampled by a finite number of macroparticles in an orthonormal basis of functions.

A considerable energy and time were expended on improving the work done by our former group leader Courtlandt Bohn [2,3] on direct solution of Fokker-Planck and

Vlasov-Poisson equations by decomposing fully the DF, writing it as a superposition of orthogonal functions that satisfy open boundary conditions. To obtain a practical solution, one has to truncate the sequence of coupled differential equations for the time-dependent coefficients. The truncation leads to a numerical instability when integrating the system of equations for the expansion coefficients (via standard Runge-Kutta) as power gradually trickles down to finer scales and "piles up" at the higher order coefficients. Previous work did not propose a remedy for this instability, but rather settled for relatively short-time simulations in which no numerical instability ensued. We therefore attempted to devise and implement a remedy which involves: (i) choosing highly compatible orthogonal functions (the basis) and (ii) truncating in a manner that still conserves total particle number (or normalization of the DF), total momentum, total energy, and low order Casimir invariants (particularly $C[f^2]$, i.e., the integral of f^2 over the phase space). Enforcing Casimir constraints rendered the mathematical problem ill-posed in all the bases in which we attempted this direct formulation, thus proving unable to remedy the numerical instability in computation of time-dependent expansion coefficients.

The second attempt to directly solve for time-dependent coefficients of VPE in an orthonormal basis, was to generalize the approach of Schummer & Holloway [4] and use the "splitting scheme" to solve for the time-dependent coefficients of the VPE. The difference here is that we use (symmetrically and asymmetrically weighted) Gauss-Hermite basis functions in both coordinates and velocities (as appropriate for the Maxwellian-Boltzmann distribution of the charged-particle beam), whereas they use Gauss-Hermite basis in velocities and Fourier basis in coordinates (as appropriate for plasma). Within the splitting scheme, the advection and acceleration terms of the VPE are solved separately using $O(\Delta t^4)$-accurate Runge-Kutta method. The splitting method conserves to varying orders some of the properties conserved in realistic systems: total particle count, total energy, total momentum, Casimir $n=2$ integral (L_2-norm of the DF), but its inability to adequately conserve the L_2-norm of the DF again leads to numerical instability, equivalent to the one we saw in the first attempt. The conclusion from these two attempts to directly solve for the time-dependent coefficients of the DF as they evolve under VPE is that the conserved quantity cannot be directly enforced to the satisfactory order, which leaves room for intermittent numerical instabilities (particularly in the L_2-norm of the DF), eventually leading to unreliable results for long integration times. We have, however, acquired a valuable knowledge and expertise in Gauss-Hermite functions, which we used in the third approach to solving the VPE described below.

The third approach is based on devising a gridless N-body method for solving the VPE based on an analytic approximation (in an orthonormal basis of functions) to the particle DF. In this iterative method the DF is sampled by N macroparticles at a time t_0, after which: (1) the DF is analytically approximated using the scaled and translated Gauss-Hermite (STGH) basis; (2) the Poisson equation is solved in the same basis to obtain corresponding potential and self-forces acting on each macroparticle; (3) the system (each individual macroparticle) is advanced forward in time by a small time-step Δt to $t=t_0+\Delta t$ using Newton's equation; (4) the steps (1)-(3) are repeated until the final simulation time is reached. The preliminary results are encouraging, as we have demonstrated that the STGH approximation is more efficient and at least as accurate as a cosine approximation used in a gridless N-body code of Bassi et al. [5]. Furthermore, the STGH approximation is immune to unphysical (and negative) fluctuations in the

tails of the distribution which plague the cosine approximation [6]. We are currently working on implementing the two- and three-dimensional algorithms, after which we will verify and benchmark this gridless code against the traditional grid codes.

4.6.2.1.3 Improvement of CSR Algorithm in Impact-T

Our current work on 1D coherent synchrotron radiation (CSR) modeling is focused on the design of adaptive and more robust algorithms that maintain accuracy in the presence of sharp, narrowly localized peaks in the charge density distribution. The approach is based on the use of adaptive parametric (e.g., piecewise-polynomial) models to fit the charge density distribution. Depending on one's definition of what constitutes "the best fit" of such a parametric model to the original density data, the optimal algorithmic approach to finding the model parameters (e.g., the coefficients of the approximating polynomials) may differ significantly from one definition to the next. For example, we have implemented an SVD-based procedure for computing the coefficients of the approximating polynomials that provide a least-squares best fit to the charge density deposited on a grid. Once the coefficients of the approximating polynomials are known, the 1D CSR wake can be computed analytically (which is how it is actually done in our adaptive parametric-model approach). At present, we are testing the new algorithms to determine the extent to which the computational cost and result itself are sensitive to the order of the approximating polynomials, the degree of smoothness at the interface points, and a particular choice of the criteria that define "the best fit".

Future work includes the inclusion of a fully 3D CSR algorithm that will take advantage of the compact storage afforded by our use of wavelets to facilitate integration over history (i.e., the computation of the retarded 4-potential). In essence the bunch distribution can be described with few (30-50) wavelet eigenfunctions, so its history can be compactly stored compared to the aforementioned codes. We have experience with such a wavelet approach as it was already implemented in the aforementioned space charge algorithm. The end result would be a fully three-dimensional model of CSR, something that has been notoriously difficult to achieve to-date, within a well supported program with extensive beamline elements (Impact-T). Having an accurate model of CSR effect in a PIC code such as Impact-T would pave the road to more accurate end-to-end simulations within one code thereby bringing to reach beamline optimization.

4.6.2.2   *Electron Sources & Injectors (Lewellen, Mihalcea, Piot, Rihaoui, Vinogradov, Zownorega)*

4.6.2.2.1 Low Energy Electron Source for Time-Resolved Electron Microscopy and Compact Terahertz Light Source

Our group in collaboration with Argonne National Laboratory has built a low energy (20 keV) electron source. An overview of the practical implementation of the proposed THz source is presented in Figure 1 (right). The electron bunches are produced via photoemission using a commercially available ultraviolet laser pulse impinging a copper photocathode (Note: In the future we may be able to use a gated field-emission cathode and thereby circumvent the need for the laser). The source was built and is presently under commissioning; see Figure 1 (left). The design and commissioning activities involved a graduate [7] and undergraduate student [8]. The

initial purpose of this electron source was to demonstrate the production of nanoseconds duration pencil (sub-micrometer radius) electron bunches for possible application to time-resolved scanning electron microscopy. If successful, such a source augmented with a GaAs photocathode could produce spin-polarized electron bunches which have applications to study ultrafast nanoscale magnetodynamics and electrodynamics. The emitted bunch exits the anode with a kinetic energy of approximately 15-20 keV. In parallel to this program we aim at using the source to produce Terahertz radiation via Smith-Purcell free-electron laser [9]. A longitudinal magnetic field (few hundred Gauss) is applied by a pair of Helmholtz coils, thereby imparting angular momentum to the beam. Three skew quadrupoles downstream of the source apply a torque on the beam and remove the angular momentum; the net result is an exchange of phase-space coordinates between the two transverse degrees of freedom resulting in a flat beam. The flat beam is then passed above the grating located in the "Smith-Purcell chamber" which incorporates radiation extraction ports and a support for the grating that can be translated and rotated (a total of six degrees of freedom for the grating). . The electron-beam source, transport beamline, and Smith-Purcell chamber are under moderate vacuum (already achieved). For this proof-of-principle experiment, the anticipated length of the apparatus is approximately 1 meter. It will incorporate key diagnostics for characterizing both the electron beam and the THz radiation, in order to correlate the properties of the generated THz radiation with incoming electron-beam properties. We plan to perform parametric studies and optimization of the efficiency of the SPFEL.
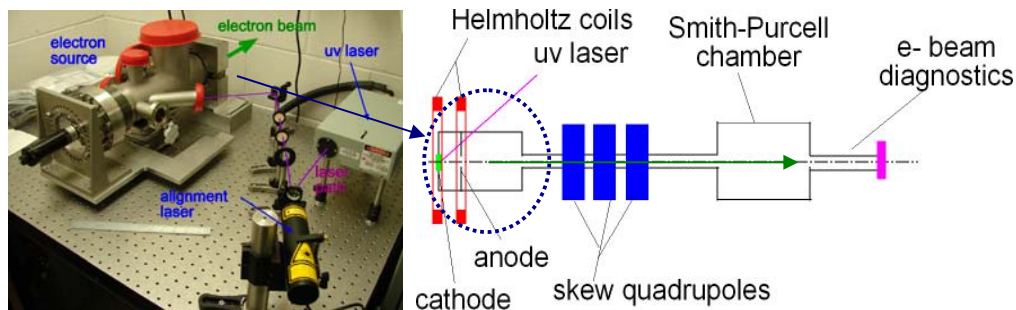
Figure 1: Left: electron source commissioning setup as of August 2007. Right: overview of the Smith-Purcell free-electron laser.

4.6.2.2.2 Modeling of High Average Current Electron Source

The next generation magawatt-class JLab Free Electron Laser (FEL) will require improved quality of the electron beam compared with the existing 10kW FEL [10]. In particular the average beam current must be increased to ampere level and the normalized transverse emittance should be lowered to a few microns. An upgraded Photoinjector, based on a dc photoemission source, was designed at Advanced Energy Systems (AES) [11], and is under construction at Jefferson Lab. This new photoinjector couples a normal-conducting DC gun with a section of three 750 MHz superconducting RF single cells and third harmonic 2250 MHz cavities. Electron bunches of up to 2nC charge and about 20 ps (rms) long are extracted from a photocathode illuminated with an infrared mode-locked Nd:YLF laser. The maximum accelerating gradient in the DC gun is 6 MV/m and the electron energy at the exit from the gun is about 1 MeV. The

three 750MHz superconducting RF single cell cavities increase the beam energy up to 6 MeV. A third harmonic cavity is used to linearize the longitudinal phase space and thereby minimize the longitudinal emittance.

Our group has been involved in the optimization of this photoinjector design with particular emphasis to halo formation. The simulations were performed with Parmela [12] and Impact-T [13]. Specifically, we simulated the beam dynamics in a photoinjector, known as the 'AES/JLab Photoinjector', that is presently under construction at Jefferson Lab. We found that, in generating 1-nC bunch charges, if the cathode spot is smaller than about 2.8 mm in radius, then copious halo is formed. This machine is short; there is simply not enough time for the constituent electrons to execute more than a single 'betatron' oscillation, and this time frame is too short for orbits to mix appreciably. Instead, as a consequence of space charge alone, a fraction of the beam is launched to large amplitudes by a phenomenon akin to 'tidal shocking'. This mechanism is illustrated in Figure 2.
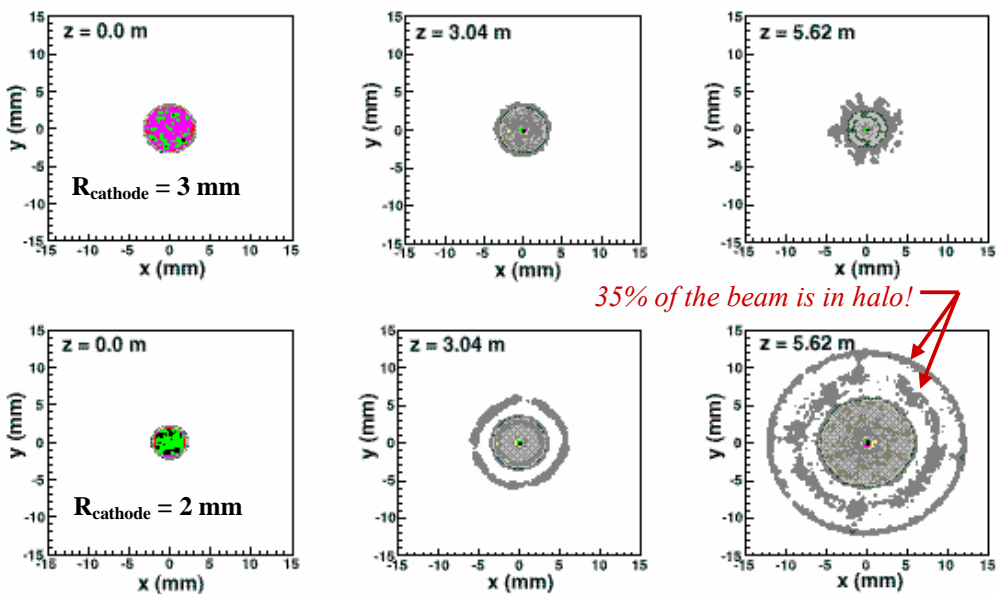
Figure 2: Transverse halo in 1-nC bunches generated with the AES/JLab Photoinjector and given a cathode spot of radius 3 mm (top) and 2 mm (bottom). The rightmost panels correspond to the output beam.

4.6.2.2.3 Modeling of High Brightness Electron Source for the ILC Test Accelerator and Advanced Accelerator R&D Applications

Fermilab is constructing an ILC test accelerator (ILCTA) to study critical components of the ILC accelerator and do reliability tests of sub-systems. The accelerator will eventually incorporate three ILC accelerating module thereby producing electron beam with maximum energy of approximately 700 MeV [14]. In parallel to ILC-related activities, we are exploring possible advanced accelerator R&D activities [15]. Such activities require the production of high-brightness electron bunches (small emittance, and high peak current). BPAG has designed, in collaboration with Fermilab, a 40-50 MeV photoinjector capable of producing tunable beam

parameters. The photoinjector, shown in Figure 3, incorporates a 1+1/2 rf gun, two TESLA type cavities, a 3rd harmonic accelerating cavity and a magnetic chicane for bunch compression. The injector is also capable of producing flat beam (i.e. beams with high transverse emittance ratio). Detailed simulations of the injector are being finalized, but we foresee the injector to enable the production of beams with parameters of interest for several advanced accelerator R&D activities such as laser acceleration in open iris loaded structures [16,17], acceleration of flat beams in slab dielectric structures [18], and demonstration of the image charge undulator principle [19].
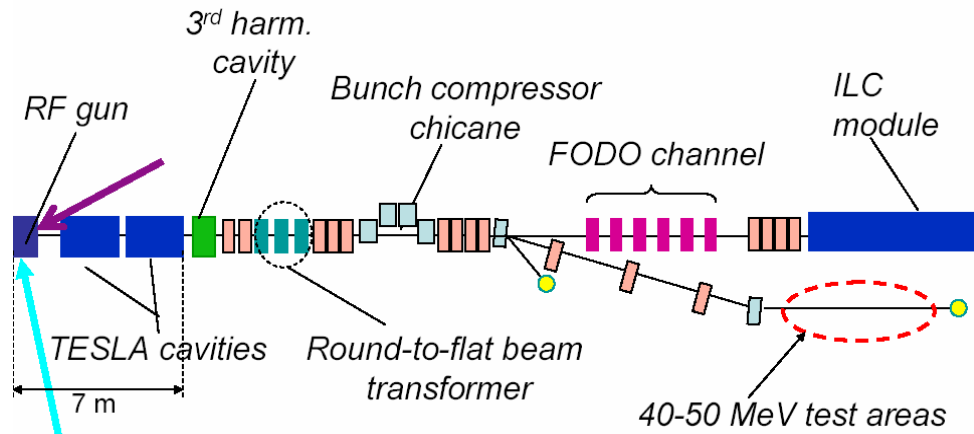
Figure 3: Overview of the injector for the ILC test accelerator at Fermilab

4.6.2.2.4 Precise Benchmarking of Space Charge Simulation

In collaboration with the Argonne Wakefield Accelerator (AWA) group in Argonne, we have designed and performed an experiment to perform precise benchmarking of space charge algorithms. The experiment consists in launching a quincunx patterned beam in the AWA and studying its distortion for different accelerator settings. An example of simulated and measured patterns is shown in Fig. 4.
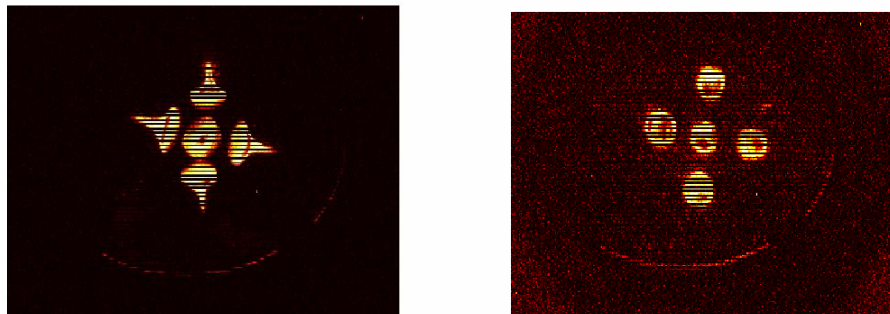
Figure 4: Evolution of quincunx pattern in the Argonne Wakefield Accelerator when space charge is at work (left image) and for low charge (right image). The images represent the transverse density of the beam in the (x,y) plane.

4.6.2.3   Electron Beam Manipulation (Piot, Rihaoui)

The possibility of exchanging transverse and longitudinal phase spaces was first noted by Robinson [20]. Few years ago M. Cornacchia and P. Emma proposed a scheme for exchanging the emittances associated to the longitudinal and one of the transverse phase spaces [21]. The purpose of this "emittance swapping" was to increase the slice energy spread so as to mitigate potential microbunching instabilities due to longitudinal space charge and/or coherent synchrotron radiation in FELs-driver linacs. A typical exchanger is composed of a deflecting cavity flanked by two dispersive sections. In collaboration with the Argonne Wakefield Accelerator team we are presently designing a proof-of-principle experiment to demonstrate and perform parametric study of this emittance exchange process (see Figure 5). The experiment incorporates a round-to-flat beam transformer to vary the incoming transverse emittance ratio and a transverse-to-longitudinal exchanger based on [22]. The experimental setup includes an extensive suite of diagnostics to fully characterize the beam parameters and measure the transfer matrix of the exchanger [23]. This research forms the basis for the Ph.D. project of one of our graduate students.
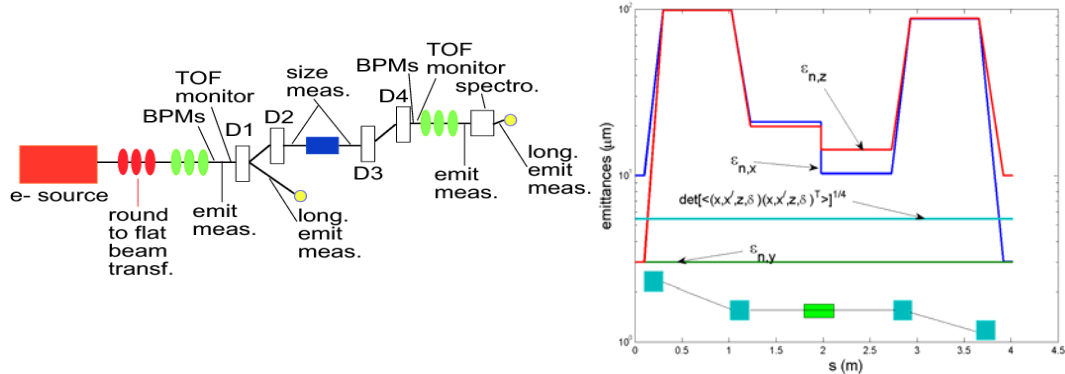
Figure 5: Proof-of-principle of the transverse-to-longitudinal emittance exchange planned at the Argonne Wakefield Accelerator. Overview of the planned experimental setup (left) and single-particle simulation of the emittance exchange (right).

4.6.2.4   Electron Beam Diagnostics R&D (Dyshkant, Maxwell, Piot, Vinogradov)

4.6.2.4.1 Single-Shot Halo Diagnostics

Development of an electron accelerator that delivers high-average-current beam requires precise control of the beam halo, i.e. a very-low-density population of electrons that extends far from the beam core. Since the intensity in the beam core and halo tail can differ by a factor of 10^8 or even higher, a halo detector with sensitivity over a wide dynamic range is required, and its development is challenging. People have expended significant effort toward developing reliable halo-measurement techniques; however, their efforts have been almost exclusively within the context of ion beams. We are currently developing an ultra-sensitive halo detector for electron beams. In fact, we contemplate *two* detectors, one for a 0.5 MeV DC gun, and the other for a multi-MeV

photoinjector. Our plan is to use these detectors to study single-bunch halo formation in the Jefferson Laboratory's AES/JLab DC gun test facility.

Our design of an Ultra-Sensitive Halo Detector (USHD) is unlike that of any previous halo diagnostic. This innovative device is a scintillator-based detector designed to reduce background noise while amplifying the actual signal from the halo, thereby providing sensitivity at the level of a few single electrons. The conceptual design of the USHD appears in Fig. 6. A collimator with a narrow slit mounted on a linear-motion actuator cuts a small fraction of the primary beam that is being analyzed. This fraction also includes unwanted low-energy secondary electrons, such as can be produced by interaction of the primary beam with the slit edges, vacuum chamber walls, etc. A dipole magnet installed after the collimator is tuned to bend the primary beam 90° toward the detector. This eliminates most of the secondary electrons because their energies will differ significantly from that of the primary beam. The detector head is also mounted on a linear-motion actuator so its location can be adjusted to obtain the maximum signal. Preliminary numerical studies of the beam dynamics in the USHD support the viability of the concept. The simulations have been performed with SHOWER to analyze the secondary electrons production, and ELEGANT to simulate the transport of the beamlet from the collimating slit to the detector head location.

The key to ultra-high sensitivity lies in the design of the detector head in combination with special methods to amplify the signal. The idea is to use highly sensitive scintillating material so as to detect even extremely weak signals from diffuse halo. An additional isolated wire (not shown in Fig. 6) installed on the first actuator is used to measure the primary beam-core profile. Therefore, wire-scan measurement of the core profile with typical dynamic range of 10^3, combined with scintillating-based measurement of the halo tail with expected range of at least 10^3, will provide an integrated dynamic range of at least 10^6. A small Faraday cup (also not shown) attached to the second actuator will facilitate tuning the field of the bending magnet. A schematic of the detector head appears in Fig. 6 along with a simulated signal. We plan on performing preliminary measurements of the sensitivity of the scintillating fibers to radiation background at the Argonne Wakefield Accelerator Facility at Argonne National Laboratory. With these measurements we will mature the design of the detector-head.

To summarize, the envisioned Ultra-Sensitive Halo Detector will be capable of measuring the beam-halo profile with unprecedented sensitivity, down to a few single electrons, and with a dynamic range of at least 10^6. The USHD can contribute greatly toward the overall understanding of nonlinear beam dynamics, emittance growth and, basically, the fundamental physics of space-charge-dominated beams. The experimental test of three suggested configurations of the scintillating detector may result in further development of a non-destructive on-line halo monitor that is essentially desired at various accelerating facilities worldwide.
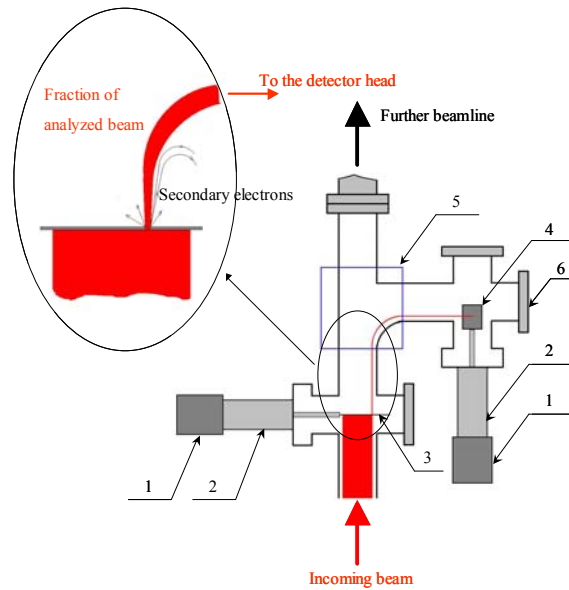
Figure 6: Conceptual design of the USHD: 1) stepper motor; 2) linear actuator; 3) collimating slit; 4) detector head; 5) bending magnet; 6) beam dump with secondary electron suppressor.

4.6.2.4.2 Sub-Picosecond Electron Bunch Length Diagnotics

A popular diagnostics relies on the detection and analysis of radiation emitted by the bunch in the coherent regime, i.e. at wavelength comparable or greater than the bunch length. In this regime the spectral angular power density associated to the radiation emitted by a bunch provides indirect information on the bunch temporal distribution. Such coherent radiation based diagnostics have become popular in the recent years because of their compactness and relatively low cost. Radiation mechanism popularly used includes transition, diffraction, Smith-Purcell and synchrotron radiations. Modern linear accelerators are capable of generating sub-millimeter or shorter length bunches. Even for state-of-art short-wavelength free-electron laser driver accelerator where bunch length approach few microns, the bunch is compressed in stages, usually via two bunch compressors installed at different energies, and the first stage typically produces bunches with sub-millimeter lengths. For sub-millimeter bunches the wavelength of interest for diagnostics based on coherent radiations is typically in the Terahertz (THz) regime ($0.1 < \lambda < 5$ mm) and two deleterious effects come into plays. First the size of the optics and apertures used in the instrument to collect and analyze the radiation (typically with characteristic sizes of a few cm diameters) are small enough to introduce diffraction effects. Second the far-field approximation used to design these instruments is not fulfilled in practice and a more detailed treatment should be applied. These two optical issues add up to other limitations due to detector performance in the Terahertz regime. Our group developed a numerical method based on vector diffraction to explore the limitations associated to bunch length diagnostics based on coherent radiations; see Figure 7 [24]. This software is being applied to analyze and refine the design of these frequency domain bunch length measurement techniques.
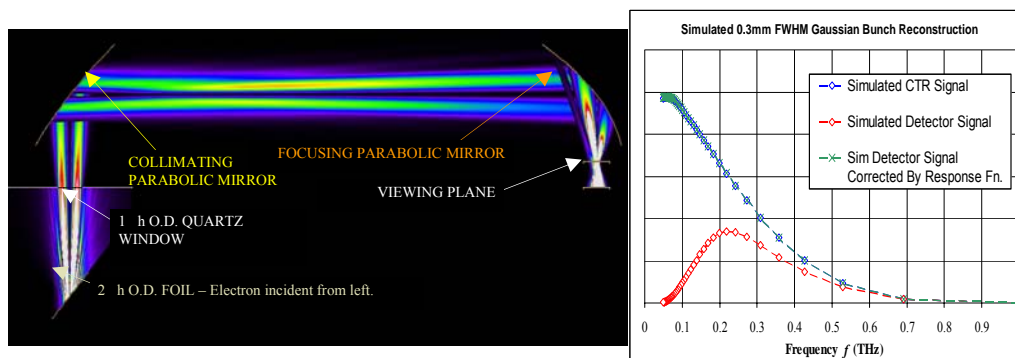
Figure 7: Example of application of vectorial diffraction simulation of Michelson interferometry of coherent transition radiation (in support to experiment performed at the Fermilab/NICADD photoinjector laboratory). Simulation of wavefront propagation through a simplified model of the interferometer (left), simulated measured spectrum and its correction (right).

In parallel to this work, we are also developing a non interceptive bunch length diagnostics based on electro-optical imaging. A mock-up experiment based on optical rectification to produce THz radiation to mimic the electron bunch field is in progress at NIU. In Parallel a ANL-FNAL-NIU collaboration is setting up a full scale experiment at the Argonne Wakefield Accelerator in Argonne [25].

4.6.2.5   UMER (B. Erdelyi, E. Nissen)

The University of Maryland Electron Ring (UMER) was designed specifically to study space charge dominated beams and currently is in operation at the Institute for Research in Electronics and Applied Physics. The understanding of the often complex nonlinear dynamics of intense beam transport is a very challenging problem that requires the combined efforts of theory, simulations, and experiments.

We initiated collaboration with local staff on some of the topics related to UMER. For details on the concepts involved and commissioning of the ring we refer to [26]. One aspect we are currently studying is the fundamental single particle nonlinear dynamics in the ring. We are building up a comprehensive model of the machine in the code COSY Infinity. The ideal layout description of the ring needs to be augmented by detailed field errors of the printed circuit magnets, the misalignment errors due to assembly and positioning in the ring, the Earth's magnetic field measured locally over the circumference of the ring (which cannot be neglected in the case of the low energy electron beam relevant in this application), and the additional fields of the installed Helmholtz coils used to cancel the Earth field on average. Special attention is given to the injection region, where careful optimization studies are envisioned. The purpose of these studies is to ascertain that there is no fundamental limitation in the operation of the ring due to single-particle effects and indeed the experiments may concentrate on understanding the space charge dominated regime. To this end, we will employ map-based analysis methods such as normal form methods and estimate the dynamic aperture.

The next step will be to gradually increase the space charge intensity and simulate the beam behavior with two alternate space charge codes. Code verification is an

important aspect of these studies as well as understanding of the interplay between single-particle nonlinear dynamics and space charge physics. Examples of such interplay are important to the dynamics of halo formation, various couplings between degrees of freedom, and the beam's long term evolution in phase space.

We are planning experiments in order to verify some of the predictions experimentally. Code validation is one of our goals. The details are being worked out, but our goal is to contribute to the optimization of the operation of the ring and experiments that hopefully will lead to better understanding of space charge dominated beams.

In summary, we intend to perform experiments, simulations, and theory in order to gain a better understanding of the interplay between single-particle, collective, and stochastic effects in beams in the context of UMER, and perhaps more generically. This research forms the basis for the Ph.D. project of one of our graduate students.

4.6.3 Heavy-Ion Beams

Our research involving beams of heavy-ions has two main thrusts: exotic beam facilities and cancer therapy. Also, some effort goes into preliminary work on heavy-ion diagnostics. In the following we present each area in more detail.

4.6.3.1 *Exotic Beam Facilities (B. Erdelyi, L. Bandura, J. Maloney)*

The next generation of research in nuclear physics requires advanced exotic beam facilities based on heavy-ion drivers. Over the last few years several projects around the world evolved, and today are in various phases from pre-conceptual design to commissioning. Among the prominent examples, we mention the RIBF at RIKEN, Japan, the FAIR at GSI, Germany, the SPIRAL2 upgrade at GANIL, France, and plans for an exotic beam facility in the US. Although the parameters of the latter facility are not yet firmly settled, it is considered to be the highest priority for a new research facility for nuclear physics in the US in the near future.

The main components of a heavy-ion based exotic beam facility are the primary beam production area, driver accelerator, fragment separator, in-flight area, gas cell, post-accelerator, and various experimental areas. We are focused on optical design concepts for the fragment separator area. The function of the fragment separator is to separate the isotope of interest from the primary beam and other by-products, and deliver the same with high efficiency to the experimental areas, while containing the large beam power of the unwanted products and primary beam. Although the requirements vary somewhat depending on the specific project, the main features of fragment separators are the same for all heavy-ion based exotic beam facilities. The production of rare isotopes via projectile fragmentation and fission of fast beams is one of the most important methods. The reaction kinematics, especially of the fission case, produces these rare isotopes over a large phase space volume. The small production cross-section of many isotopes of interest requires large primary beam powers and high energy. Often, the particles of interest are only a tiny fraction of all particles produced. The fragment separator should collect and transmit these, and only these, particles to the experimental areas while minimizing losses. Altogether, the next generation high-intensity fragment separators require large acceptance, high resolution, and large aperture superconducting magnets.
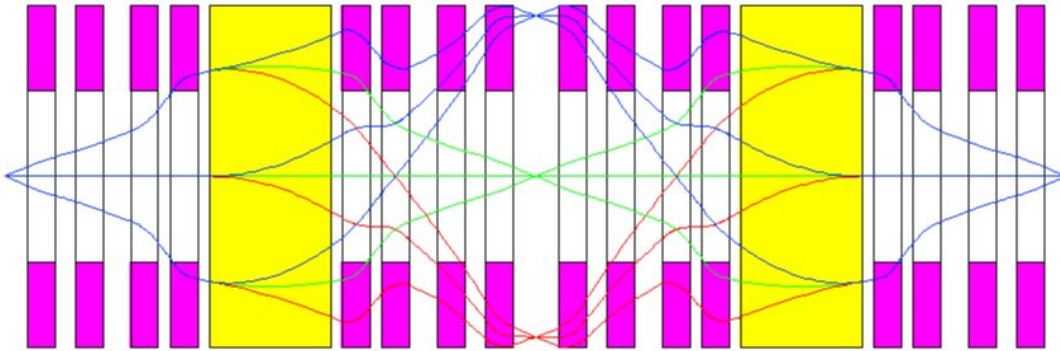
Figure 8: First order layout of the (first stage of the) proposed ion optics of the fragment separator.
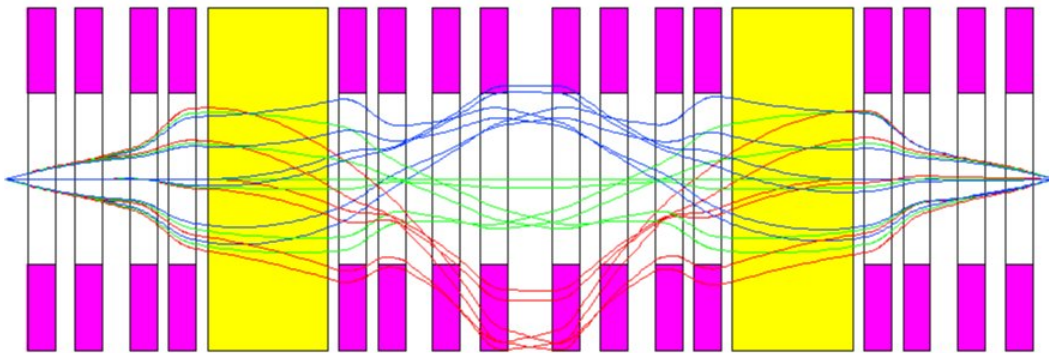
Figure 9: Third order layout of the (first stage of the) proposed ion optics of the fragment separator.

It is well known that electromagnetic fields are not enough for separating isotopes, since each isotope is characterized by a given mass and charge, while the equations of motion of a charged particle in electromagnetic fields depend only on the mass to charge ratio. To this end, a piece of absorbing material, i.e. energy degrader or wedge, is inserted in the system, resulting in Z-dependent energy loss. When combined, magnetic fields and energy degraders make possible the separation of isotopes (the so-called rigidity-energy loss-rigidity separation method). The achievement of large acceptance and high resolution is a challenge in the presence of large aperture superconducting magnets. It requires high precision treatment of the beam dynamics and correction of high order aberrations.

Depending on the specific task, the layout of the fragment separator could be different: for the in-flight method there is a two-stage separation where the two stages transmit isotopes along two intersecting lines in the mass-charge plane, and the isotope selected is the one on the intersection point; if the isotopes are to be stopped in a gas cell after the first stage of separation, a second stage is also needed, but in this case it is used to slow down and monochromatize the isotope beam.

It is interesting that all functions of the system can be obtained by repetition of the same basic cell. For the in-flight method the cell is repeated four times and for the gas-cell method three times. This fact highlights the usefulness of applying symmetries to the design of fragment separators. We developed our design of a fragment separator

based on several symmetries. Our approach is based on the fact that the basic cell mentioned in the previous paragraph should be a dispersive stage, which produces a high order achromat if repeated. Also, the achromat should be realized by a minimum number of magnets. See Figures 8 and 9 for the first order and third order horizontal envelope of a proposed solution [27]. In this example the separator is tuned to select a ^{132}Sn isotope from the fission of a 400 Mev/u ^{238}U primary beam. The emittance of the ^{132}Sn beam is huge: ±50 mrad both horizontally and vertically, and ±10% momentum dispersion.

The optical effects of the energy degraders spoil some of the properties of an otherwise perfect lattice. Currently, we are working on a high order aberration-free solution that includes the absorbers. A comprehensive and systematic study of separation purity and background distribution will follow in order to optimize the system settings and maximize the separation purity. This forms the Ph.D. project of one of our students.

There is also synergy with similar projects around the world. Specifically, we have active collaborations with Michigan State University, GANIL, RIKEN, and GSI. One specific project we are pursuing is the extraction of accurate field maps from measurements or superconducting current dominated magnet models (but which include the effects of the iron) and transforming them into transfer maps for optics design and optimization.

4.6.3.2   *Heavy-Ion Cancer Therapy (B. Erdelyi)*

Radiobiological research using radiation therapy has increased drastically over the last few years. The primary interest is due to application of beams in tumor therapy. Heavy charged particles are the most advanced tool of radiotherapy of deep seated tumors. In contrast to electromagnetic radiation the heavy-ion beams have small angular scattering and a finite range. Moreover, the energy deposition increases with depth penetration, culminating in the so-called Bragg peak close to the end of the range, sparing healthy tissue closer to the surface. High biological efficiency in the tumor is the prerequisite for successful treatment of tumors, and heavier ions exhibit an increased efficiency in the Bragg peak. This affects the oxygen effect, repair capacity, and the cellular radio-resistance. Although the physical and radiobiological properties of heavy-ion beams are very favorable for therapy, the necessity to produce these particles in an accelerator that are sufficient in energy and intensity has restricted a general application until now. The only facilities that are in operation or construction are located in Japan and Europe.

In the USA there are proton and neutron therapy facilities, but no heavy-ion therapy facility, although the very first experiments in this area were performed at the BEVELAC, Berkeley. Proton therapy is well established while heavy ions like carbon are considered more experimental, but might offer some benefits in the case of certain types of cancer. Northern Illinois University is also actively engaged in proton radiation therapy. The plans call for breaking ground in 2008 for a state-of-the-art four-room proton radiation treatment and research facility, with the first patient treatments in 2011. We hope that some of our tools described below and experience gained will be beneficial to the operation of the NIU proton facility.

Some of the difficulties surrounding heavy-ion facilities are size and cost. Most hospitals do not have the real estate to house such a facility, or the costs seem prohibitive. The medical advantages, combined with an innovative compact design

based on a superconducting synchrotrons with creative but simple magnet designs (such as the double helix concept) might lower the cost, both financial and real estate, enough to make it attractive to hospitals, or regional treatment facilities. Therefore, we are investigating if a heavy-ion facility at roughly the size and cost of a proton facility would be feasible from the beam dynamics point of view. More specifically, we intend to study the beam dynamics of a compact superconducting synchrotron for the purpose of a heavy-ion therapy facility. The beam dynamics is interesting because the ring should have a small circumference, which implies the use of superconducting combined-function magnets. Some innovative magnet designs, such as curved dipoles formed by two strands of "tilted solenoids" are envisioned. In such a ring none of the usual approximations used in high-energy large rings are valid. Therefore, an accurate treatment of the dynamics, without "small-angle" approximations, and realistic field calculations including fringe fields are necessary. Moreover, the dynamics of potentially any heavy ion needs to be studied. Moreover, there is the possibility of using short-lived radioactive ions that allow a precise tracking of the radiation dose delivered.

Using Differential Algebra-based computations, the fields generated by current dominated magnets can be computed very accurately. This data can be used for accurate computation of transfer maps, including in the fringe field region, possibly even with overlapping fringe fields (in synergy with the fragment separator research). The extracted Taylor map, for example by the code COSY Infinity, can be used for the analysis of the system, and, after symplectification, for studies of long-term behavior and dynamic aperture estimations. For this purpose we can use the synchrotron as a test bed for the advanced symplectification methods developed over the last few years by our group. Therefore, a compact superconducting synchrotron is not only an exciting application with important medical therapy potential, but also is an object that is useful for testing the tools developed for fundamental beam physics that have as their purpose the accurate and fast modeling and analysis of the dynamics and studies of basic nonlinear phenomena.

For accurate dose delivery calculations, the accurate treatment of the range of the primary beam and fragments produced by the collisions of the beam with tissue is needed. To this end, the sophisticated code that our group developed for fragment separator design and optimization of exotic beam facilities will be of great advantage. We can employ an integrated design and optimization approach of not only the synchrotron, but also the beamline, absorbers, etc. of the beam delivery systems, up to the actual tumor. For accurate scanning of the tumor site the beam position and sizes are very important, so again the knowledge of the nonlinear effects, aberrations, and accurate modeling of the atomic and nuclear processes are vital.

Finally, another area where our group is becoming active is a project aimed at a computed tomography system based on protons (pCT). In collaboration with Loma Linda University we plan to build a prototype in the next couple of years and in parallel to optimize image reconstruction algorithms.

4.6.4 Theory (B. Erdelyi)

Geometric methods have changed the face of modern physics. We are pursuing a program in beam physics to take advantage of the insight that these methods provide [28-30]. Specifically, by utilizing the beam dynamics infrastructure of map-based methods and an array of groundbreaking new results from symplectic geometry, we are

developing theories and methods in Hamiltonian dynamics and apply them to particle accelerators and other beam transport systems. The advanced algorithms for long-term simulation and the real symplectic invariants that we investigate will lead to enhanced insight into the behavior of particle beams and will improve our understanding of the accelerators, including their design and analysis. Hence, we are studying topics in beam dynamics from the point of view of symplectic geometry, and apply them to problems of practical interest in existing and planned particle accelerators.

Even if the dynamics is not purely Hamiltonian (as for example in high energy electron accelerators), symplectic dynamics still plays an important role, and non-Hamiltonian effects can be elegantly incorporated in the results. We are developing factorization methods for these cases that exhibit the interplay of the Hamiltonian effects with other deterministic and stochastic perturbations.

There are many exciting possibilities in this field. Our work can be categorized into two broad topics:

- **Advanced algorithms** for long-term simulation of particle beam dynamics
- **Symplectic invariants** as the study of quantities that constrain the transport of particle beams under general nonlinear Hamiltonian forces

Symplectic geometry provides a unique way of addressing these issues. The research delivers both quantitative and qualitative results. It advances both symplectic geometry and beam physics, and provides results of practical importance in the design, description, and understanding of particle beams. More specifically, the benefits are:

- **Advanced algorithms:** fast, accurate, efficient long-term tracking of particle trajectories and distributions
- **Symplectic invariants:** feasibility and quality checks in design of systems with specific requirements, and ideas for beam diagnostics

It is interesting to note that about 30 years ago there was no symplectic topology. It is exciting to be able to apply state of the art mathematics as it is being created to a discipline with so many practical applications and influences. We hope that this new geometrical perspective will give better insight into the behavior of particle beams. The underlying principle that guides this research program can be summarized by the following creed found in the preface of the book "The Geometry of the Group of Symplectic Diffeomorphisms" by Leonid Polterovich:

*"The trajectories of the flow [of a Hamiltonian system] form a complicated system of curves on the manifold. Usually, in order to understand the dynamics, one should travel along the manifold and thoroughly study the behavior of the trajectories in different regions. Let us change the point of view and note that our flow can be interpreted as a simple geometric object – a single curve t -> f_t - on the group of all diffeomorphisms of the manifold. **One may hope that geometric properties of this curve reflect the dynamics, and thus complicated dynamical phenomena can be studied by purely geometric tools**."*

4.6.5 Acknowledgements

Education, the Directed Energy Professional Society, the Department of Energy and the Department of Defense Office of Naval Research.

4.6.6 References

1. B. Terzić, I.V, Pogorelov and C. L. Bohn, Phys. Rev. ST Accel. Beams, **10**, 034201 (2007)
2. C. L. Bohn, Phys. Rev. Lett., **70**, 932 (1993)
3. C. L. Bohn, J. Delayen, Phys. Rev. **E. 50**, 1516 (1994)
4. J. Schumer, and J.P. Holloway, J. Comp. Phys. **144**, 626 (1998)
5. G. Bassi, J.A. Ellison, K. Heinemann, Proceedings of PAC'07, 3414 (2007)
6. B. Terzić, in preparation (2008)
7. S. Moten, *Construction and Initial Characterization of a Low Energy Electron Source for Electron Microscopy,* Masters Thesis, Northern Illinois University (2007) available at http://nicadd.niu.edu/research/beams/main.html#theses
8. N. Vinogradov, C. L. Bohn, P. Piot, J. W. Lewellen, J. R. Noonan, Proceedings Proceedings of PAC'07, 3011 (2007)
9. L. Schachter, A. Ron, Phys. Rev. A 40, 876 (1989); H. L. Andrews, C. A. Brau, Phys. Rev. ST Accel. Beams **7**, 070701 (2004); V. Kumar, K.-J. Kim, Phys. Rev. E 73, 026501 (2006)
10. D. Douglas, et al., Proceedings of PAC'01, 249, (2001).
11. A. Todd, et al., Proceedings of PAC'03, 977 (2003).
12. L.Young, *Parmela User Manual*, Los Alamos National Laboratory report LA-UR-96-1835 (1996).
13. J. Qiang, *et al*., Proceedings of PAC'05, 3316 (2005).
14. M. Church, S. Nagaitsev and P. Piot, Proceedings of PAC'07, 2942 (2007).
15. P. Piot, S Nagaitsev, and V. Shilstev, (Editors) Proceedings of the mini-workshop on Possible Advanced Accelerator R&D Directions at the ILC Test Accelerator at Fermilab, FNAL report Beams-doc-2595-v2 (2006), available at http://beamdocs.fnal.gov/DocDB/0025/002595/002/All_V12282006.pdf
16. M. Xie, *Laser Acceleration in Vacuum with an Open Iris-Loaded Structure,* Lawrence Berkeley National Laboratory report LBNL-40558 (1997)
17. P. Piot, R. Tikhoplav and A. Melissinos, Proceedings of PAC'05, 2503 (2005).
18. Wei Gai and John Power, private communications (2006)
19. Y. Zhang, Ya. Derbenev and R. Li, Nucl. Instr. Meth. **A 507,** 459 (2003)
20. K. Robinson, Physical Review **111**, 373 (1958).
21. M.Cornacchia, and P. Emma, Phys. Rev. ST Accel. Beams **5**, 084001 (2002).
22. P. Emma, Z. Huang, K.-J. Kim and P. Piot, Phys. Rev. ST Accel. Beams **9**, 100702 (2006).
23. Y.-E Sun J. G. Power, K.-J. Kim, P. Piot, M. M. Rihaoui, Proceedings of PAC'07, 3441 (2007).
24. T. J. Maxwell, *Diffraction analysis of coherent transition radiation in electron linear accelerators*, Masters Thesis, Northern Illinois University (2007) available at http://nicadd.niu.edu/research/beams/main.html#theses
25. J. Ruan, H. Edwards, V. E. Scarpine, C.-Y. Tan, R. Thurman-Keup, YL. Li, J. G. Power, T. J. Maxwell, Proceedings of PAC'07, 470 (2007).
26. I. Haber et al., Nucl. Instr. Meth. **A 577** (2007) 150-156
27. B. Erdelyi, J. Maloney, J. Nolen, Phys. Rev. ST – AB, **10**, 064002 (2007)
28. B. Erdelyi, Int. J. of Pure and Appl. Math. **11(3):** 241-282 (2004)
29. B. Erdelyi, Int. J. of Pure and Appl. Math. **33(4):** 553-578 (2006)
30. B. Erdelyi, J. of Geom. and Symmetry in Physics, in print (2007)

5   Workshop and Conference Reports

5.1   Summary of the LARP Mini-Workshop on Beam-Beam Compensation 2007

5.1.1   Introduction

The LARP Mini-Workshop on Beam-Beam Compensation 2007 was held at SLAC, 2-4 July 2007. It was attended by 33 participants from 10 institutions in Asia, Europe, and America. 26 presentations were given, while more than one third of the time was allocated to discussions. The workshop web site is Ref. [1]. The workshop's main focus was on long-range and head-on beam-beam compensation, with a view towards application in the LHC. Other topics included the beam-beam performance of previous, existing and future circular colliders; beam-beam simulations; new operating modes, theory, and unexplained phenomena.

5.1.2   Performance of Circular Colliders, Simulations, Theory

The expected LHC beam-beam performance was presented by F. Zimmermann, CERN. In the nominal LHC there will be 4 experiments. In 3 of them the beams collide head-on, at the fourth they are separated by 5 σ. In each of the four interaction regions the bunches also experience 30 long-range interactions. Half of these are at an average separation of 9.5 σ, and are expected to have a significant impact on the beam dynamics. The other half is expected to have little impact. To alleviate the impact of long-range interactions, the LHC beams collide under a crossing angle of approximately 300 μrad. This puts the LHC in a new operating regime for hadron colliders, where the long-range interactions lead to the emergence of a "diffusive aperture", namely a threshold in the betatron amplitude at which the transverse diffusion rate increases by orders of magnitude. The total beam-beam induced tune spread is expected to be 0.010-0.012 for the nominal beam paramters (25% of this is contributed from long-range interactions), and up to 0.015-0.017 for the ultimate beam parameters. In light of the new challenges, the operating experience of other colliders was reviewed.

The B-factories KEKB and PEP-II were presented by K. Ohmi, KEK. These machines have delivered record luminosites above $10^{34} \mathrm{cm}^{-2} \mathrm{s}^{-1}$, and in both machines beam-beam effects are a dominant luminosity limit, typically leading to beam size blow-up. Beam-beam parameters of up to 0.132 have been reached in PEP-II, and up to 0.175 in KEKB. With such strong beam-beam interactions, the interplay with a number of other machine properties is important, such as working point (both machines operate near the half integer resonance), global linear optics errors, local optics errors at the IP, chromatic optics errors, sources of noise, static and dynamic offsets at the IP, feedback noise, and electron clouds.

A. Valishev, FNAL, summarized the Tevatron beam-beam performance. In this machine long-range beam-beam effects at injection cause 5-10% proton beam loss. At store, long-range interactions had caused beam lifetime deterioration and emittance increases. These effects could be reduced in 2006 through the implementation of a new

separation scheme ("helix"), leading to a 16% increase in luminosity lifetime. Currently the dominant beam-beam effects in stores are proton beam losses due to head-on interactions. The antiproton losses are almost entirely due to burn-off. The total beam-beam induced tune shift reached 0.026 for the antiprotons, and 0.016 for the protons. To increase the luminosity further, a working point near the half integer is considered, which does require a correction of the momentum dependency of the β-functions. Such a correction is also expected to be beneficial at the current working point.

In RHIC proton operation the total beam-beam induced tune spread reached 0.012, with 2 head-on collisions and no long-range interactions. (For heavy ions the beam-beam parameter is 2.5 times smaller.) With this about 10% of the luminosity decays exponentially with a lifetime of 0.3 h, the remainder has a lifetime of 12 h. A number of effects reduce the luminosity lifetime in conjunction with beam-beam effects. Nonlinear chromaticity induces a tune spread of approximately 0.003. A correction was implemented in 2007, but not yet tested with protons. 10 Hz triplet vibrations lead to offset modulations at the IP, for which an orbit feedback became operational in 2007. A modification of the triplet assemblies is under study to eliminate the 10 Hz vibrations at the source. A new 9 MHz rf system will become operational in 2008, allowing to match the proton bunches longitudinally at injection, leading to a smaller hour-glass effect (currently 23% at the beginning of stores). A new working point near the integer resonance will be tested in 2008, as presented by C. Montag, BNL. Simulations show a better dynamic aperture and a larger tolerance against tune errors. The implementation requires an improved orbit and beta-beat correction.

Simulations for hadron colliders are still challenging, since time scales of interest (hours) can still not easily be reached with large numbers of particles (tens of thousands) using a detailed model (like element-by-element with magnetic errors).

A. Kabel, SLAC, pursued the question of what we can learn from beam-beam simulations in proton machines, with examples from his code PLIBB. The code had been developed to calculate beam lifetimes for the Tevatron. He concluded that the calculation of observable quantities may now be within reach. A. Valishev, FNAL, showed simulations that explain and predict beam-beam effects in the Tevatron, using the code LIFETRACK [2]. Problems investigated were the bunch-by-bunch variations (due to the PACMAN effect) in orbit, tune, emittance growth, and chromaticity, as well as the effect of different helix settings. For time scales up to 5 min, the code has been shown to have predictive power, for longer time scales less so. J. Qiang, LBNL, showed strong-strong simulations for RHIC and the LHC obtained with his code BeamBeam3D, including emittance growth rates for different beam separations, and tunes in RHIC, and emittance growth rates for mismatched and offset beams in the LHC.

K. Ohmi, KEK, discussed the recent experience with crab crossing in KEKB, the first time such a scheme has been used in a collider. The KEKB beams meet under an angle of 22 mrad, and strong-strong simulations suggest that the beam-beam parameter can be increased by a factor 2 with crab crossing. So far the crab cavities were shown to actually tilt the beams in the expected manner, and they were operated at beam currents up to 1.3 A for the positrons, and 0.7 A for the electrons, although no absolue luminosity increase has been obtained yet (the specific luminosity did increase by about 15%). An rf phase fluctuation of 20 s period was observed in high current operation, and only with colliding beam.

Y. Alexahin, FNAL, reviewed coherent effects in hadron colliders. These are well established in e[+]e[-]-colliders but were not important in the SPS collider or the Tevatron

in the past (the ISR had seen some coherent effects but with their continuous beams of very high current and small beam-beam parameter the ISR situation was quite different from today's hadron colliders in a number of ways). About a decade ago, Alexahin and Gareyte had raised the possibility of an instability arising because the coherent π-mode tune created through the strong-strong beam coupling lies outside the incoherent beam-beam spectrum. π-mode tunes were observed later in RHIC, although only with an external excitation. Coherent beam-beam coupling lowered the TMCI threshold in LEP, and it leads to instability at low chromaticities in the Tevatron and RHIC. A number of suppression mechanisms were proposed including a break in the symmetry, and active damping.

Y.Cai, SLAC, presented unexplained phenomena in lepton machines. For example, currently it is not understood why the beam-beam parameter can be increased near the half integer working point to the values that have been observed. Some bunches, typically at the beginning of a PEP-II train "flipped" and were found to have very short lifetimes. The achieved vertical beam-beam parameter follows approximately a $\lambda^{-0.4}$ scaling, where λ is the damping decrements. While single bunch effects are generally well understood with simulations, this is less so with multiple bunches and in the presence of one or several other strong effects (such as ions, electron clouds, or other nonlinearities).

T. Pieloni, CERN and EPFL Lausanne, showed tune spectra calculated for the LHC, using COMBI. These are computed to predict bunch-by-bunch differences, and investigate beam-beam effects for different operational scenarios. In RHIC tune spectra were measured with colliding proton bunches, and compared to the calculated spectra. Taking into account that the RHIC BTFs are currently measuring predominantly the most intense bunches (i.e. bunches with only 1 head-on collision instead of 2 for most of the bunches), a good agreement for both the total tune spread, and the number of peaks in the spectrum was found.

5.1.3 Long Range Beam-Beam Compensation

Long-range beam-beam interactions are important in the Tevatron (70 per turn, distributed), and the LHC (30 per IR, localized). In RHIC there are nominally no long-range beam-beam interactions at store, but up to 12 can be generated for machine experiments. Long-range interactions, in conjunction with other effects, have also limited the performance of e+e- colliders such as DAΦNE (24 in main IR), KEKB (4 in IR), and PEP II (2 in IR). General strategies to mitigate the effect of long-range beam-beam interactions are a reduction of their number, or and increase in the beam separation. This can be done with early separation schemes using dipoles (as in RHIC, or an LHC upgrade scheme proposed by J.-P. Koutchouk and G. Sterbini, CERN), or via larger crossing angles. Another way to reduce long-range beam-beam effects is to compensate the field of the opposite beam by a magnetic field of opposite sign, that can be generated with either an electron beam (proposed for the Tevatron by V. Shiltsev) or a wire (proposed for the LHC by J.-P. Koutchouk). Such a compensation scheme appears to be practical only if the long-range interactions are localized around an IR, and a location for a compensator can be found with a phase advance only a few degrees away from the average betatron phase of the nearby long-range interactions. Space for long-range wire compensators is reserved in the LHC, and the compensation was shown to increase the dynamic aperture by about 2σ both for the nominal LHC and for a

possible upgrade, as shown by U. Dorda, CERN. A number of other important tests have been made so far.

Two wires were installed next to each other in the SPS in 2002 for beam test. Three types of signal were used in previous experiments: beam lifetime and background, final emittance, and scraper retraction. The beam lifetime scales with the 5th power of the distance between beam and wire. In 2004 two new movable units with three wires each were installed, only 2.6° away in betatron phase from the single-wire units, which is the same phase advance as between long-range collisions and wire in the LHC, to test the efficiency of the compensation, and different crossing schemes by means of two wires. Open questions from these tests were shown by F. Zimmermann, CERN. These include the scaling from the SPS to the LHC, discrepancies between measured and simulated dynamic aperture and beam lifetime, the breakdown of the 2-wire compensation at certain tunes, and the lifetime scaling with the wire distance to the beam (this is found to be different for the SPS, Tevatron and RHIC). Some of the SPS measurements were affected by the relatively short beam lifetime, which is only 5-10 min at 26 GeV/c.

In the e+e--collider DAΦNE the beam and luminosity lifetime could be improved with a combination of octupoles and long-range wire compensator, as shown by C. Milardi, LNF-INFN. This is the first time that long-range beam-beam compensation was demonstrated in an operating collider. In DAΦNE there are 24 long-range beam-beam interactions in the main IR. The compensating wires, built and installed in 2005, are outside the vacuum chamber, in-between the two beams, 4.9 m from the IP, and allow for a partial compensation of the long-range interactions. The observed beam lifetime improvements could be reproduced with the code LIFETRACK [2]. In the future a new vacuum chamber will be installed in the interaction region, by which all but two long-range interactions will be eliminated.

In RHIC there are nominally no long-range interactions in store, but up to 12 per turn can be generated for accelerator experiments. In the last two years the effect of a single long-range interaction was tested at injection and at store, where it was found that distances as small as 4 σ at store are needed to create visible beam losses under normal operating conditions. Last year, a vertically movable wire with an integrated strength of up to 125 A·m was installed in each of the RHIC rings. The experiments this year, presented by N. Abreu, BNL, measured loss rates of Au beams at 100 GeV/nucleon as a function of wire current and distance to the beam. The RHIC measurements complement the earlier SPS measurements, with the beam conditions of an actual collider ring and a good base beam lifetime. Simulations of the RHIC were done by U. Dorda, CERN, H.J. Kim and T. Sen, FNAL, and A. Kabel, SLAC. These aim to reproduce general features of the measured data, such as the onset of increased beam losses at certain wire distances and strengths. In some cases, a remarkably good agreement has been found but the simulation work is still ongoing. For next year, it is planned to test the compensation of a single long-range beam-beam interaction in RHIC with proton beams. In the LHC different bunches have different long-range interactions, and an optimum compensation requires that the wire current changes from bunch-to-bunch. This is technically challenging, and was discussed by U. Dorda, CERN.

5.1.4 Head-on Beam-Beam Compensation

The compensation of the head-on beam-beam effect can only be done with an electron beam that creates the same amplitude dependent force like the opposite beam, which typically has an approximately Gaussian profile.

A head-on compensation scheme was tested in DCI [3] with four beams (two e^+ and two e^- beams). However, due to coherent beam-beam effects, the space-charge compensation of the beam-beam effect did not work as expected. In hadron colliders, with much smaller beam-beam parameters, such strong coherent effects are not expected to be a problem. Head-on beam-beam compensation had been proposed for the SSC by E. Tsyganov, now at UT Southwestern, and his co-workers. E. Tsyganov reviewed this work at the workshop.

W. Scandale and F. Zimmermann, CERN, presented the possible LHC luminosity gain from an electron lens. Together with an injector upgrade an electron lens may be able to double the beam brightness under collision conditions. For the LHC ultimate beam parameters, and assuming no increase in the total beam intensity, this would result in 20% more average luminosity since the initial luminosity lifetime with head-on compensation would be only 7 h, half of the lifetime without the compensation. Head-on compensation would yield larger gains if the ultimate beam parameters had not yet been reached.

Much progress has been made with operating electron lenses in the Tevatron, presented by V. Kamerdzhiev, FNAL. The 2 Tevatron electron lenses were used for the compensation of beam-beam effects of colliding antiproton and, recently, in proton beams with energies of 980 GeV. They have been shown to improve the proton beam lifetime by us much as a factor of 2.3 under operating conditions. The compensation effect was most prominent in a few bunches (3-6 out of 36 total) having the largest tune shifts due to the PACMAN effect. Although this compensation is mostly due a fast tune shift, not a reduction in the tune spread needed for head-on compensation, it shows that electron lenses can improve the performance of an actual collider without creating emittance growth or other harmful effects for the beam.

At RHIC an effort has started, presented by Y. Luo, BNL, to investigate the benefits of an electron lens in simulations, and to define the hardware parameters of an electron lens, taking advantage of the EBIS [4] technology. The simulations aim to show by how much the beam-beam parameter can be increased with an electron lens. It is planned to conclude the simulation effort in about a year. With a positive outcome, a decision could be made for the construction of an electron lens at RHIC, which would then also become a test bed for such a device in the LHC.

The possible uses of electron lenses in the LHC were explored in more detail by V. Shiltsev, FNAL. Not only could these lenses be used as a head-on beam-beam compensator, potentially doubling the luminosity, they could also be used to create a stabilizing tune spread if needed, as a soft hollow collimator, and as a soft beam conditioner eliminating satellite bunches. By now a task has been created within LARP to investigate the configuration details of electron lenses, and to define the main parameters for possible electron lenses in the LHC.

5.1.5 References

1. Workshop website: http://www-conf.slac.Stanford.edu/larp/

2. D. Shatilov, Part. Acc. 52, 65 (1991).
3. G. Arzelia et al., Proc. 8th Int. Conf. High Energy Acc. (1971); H. Zyngier, AIP Proc. 57 (1979); Ya.S Derbenev, 3rd All Union Conf. On Acc. (1972); E. Keil, Proc. 3rd ICFA Beam Dyn. Workshop (1989).
4. J. Alessi et al., PAC07 (2007).

6 Forthcoming Beam Dynamics Events

6.1 40th ICFA Advanced Beam Dynamics Workshop on High Luminosity e^+e^- Factories (e^+e^- Factories 2008)

Eugene Levichev, BINP, Novosibirsk, Russia
Mail to: icfa08@inp.nsk.su, levichev@inp.nsk.su

The ICFA Workshop on Beam Dynamics at High Luminosity e^+e^- Factories will take place in Novosibirsk on April 14-16, 2008. The aim of this Workshop, supported by ICFA and Budker Institute of Nuclear Physics, is to exchange the experience and recent achievements at electron-positron factories. The workshop program covers the current trends for the available and future circular accelerators.

A preliminary schedule of the Workshop is as follows.

The first day: recent beam dynamics news from the main e+e- facilities and installations (KEK/KEKB, SLAC/PEPII, DAFNE, BEPCII, CESR, and VEPP2000).

The second day: the most intriguing issues of beam dynamics at e+e- colliders including the beam-beam effects, instabilities, electron clouds and feedbacks, high beam loading RF systems, background and collimation, dynamic aperture and beam polarization.

On the third day we plan to concentrate on the crab waist collision machines, mainly the Tor-Vergata SuperB project. However, other crab-waist collision proposals are also welcome.

The workshop will consist of plenary and poster sessions. The workshop website is under construction and will soon be available at: http://icfa08.inp.nsk.su.

6.2 Nanobeam 2008 Workshop

Nikolay Vinokurov
Budker Institute of Nuclear Physics, 11 Lavrentyev ave., Novosibirsk, Russia, 630090
Mail to: vinokurov@inp.nsk.su

Recently high quality beams with nanometer and sub-nanometer scale emittance and few-nanocoulomb charge per bunch became available. It opens great prospects for different applications. The first and the most ambitious is the linear collider. The numerous lower-scale projects cover the wide field from advanced x-ray sources to heavy-ion therapy. New challenges on beam quality, beam-optical systems, diagnostics, feedback, and stabilization of beam line components are under intensive investigation now. From the other hand, achievements of accelerator technology are used in nanoscience and nanotechnology, and number of such applications increases from year

to year. Two previous Nanobeam workshops took place at Lausanne (Switzerland) in 2002 and at Uji (Japan) in 2005.

The Nanobeam 2008 workshop is organized by the Budker Institute of Nuclear Physics. The scientific interests of this institution lie in the field of advanced accelerator techniques as round beam collider, free electron lasers and synchrotron radiation x-ray sources, energy recovery devices, electron coolers, linear colliders, advanced beam sources, etc. It will be reflected in the scientific program of the workshop, which will focus not only on the linear collider issues, but on the other advanced accelerator applications also.

Nanobeam 2008 will be held from 25 to 30 of May, 2008. The Nanobeam 2008 Workshop site is the Novosibirsk scientific center (Akademgorodok). For detailed information on the workshop please consult the workshop website http://ssrc.inp.nsk.su/NB08/.

6.3   ICFA Mini-Workshop on Deflecting/Crabbing RF Cavity

We are pleased to announce that an ICFA Mini-Wrokshop on Deflecting/Crabbing RF Cavity Research and Application in Accelerators will be held April 23-25, 2008 at the Shanghai Synchrotron Radiation Facility (SSRF) in Shanghai, China. The workshop is sponsored by the Shanghai Institute of Applied Physics (SINAP), Lawrence Berkeley National Labortory (LBNL) and Argonne National Laboratory (ANL).

Deflectingrabbing RF cavities have been proposed, designed and built for increasing luminosity by creating "head-on" collisions in high energy colliders, generating short x-ray pulses in synchrotron light sources, emittance exchange techniques and as a beam diagnostic. Much progress has been made in deflecting/crabbing cavity R&D following the recent successful commissioning and operation of the superconducting KEK-B crabbing cavity. The purpose of this workshop is to bring together researchers in various accelerator communities and discuss advances in delecting/crabbing RF cavity R&D. The workshop will cover delecting/crabbing cavity R&D in the application of:

1. High energy colliders (ILC, LHC, KEK-B, CLIC, …);
2. Generation of short x-ray pulses in synchrotron light sources;
3. Beam manipulations, emittance exchange and diagnostics.

Please contact Derun Li at DLi@lbl.gov if you have any question on the workshop. The workshop web site has been set up with more information on programs, registration, accommodation, transportation, Chinese visa application, local weather and attractions:

<div align="center">http://www.sinap.ac.cn/ICFA2008/index.hlm</div>

Please forward this announcement to anyone whom you think might be interested.

Derin Li (LBNL)
Zhentang Zhao (SINAP)
Ali Nassiri (ANL)
Jianfei Liu (SINAP)
On behalf of the Organizing and Program Committees

7 Announcements of the Beam Dynamics Panel

7.1 ICFA Beam Dynamics Newsletter

7.1.1 Aim of the Newsletter

The ICFA Beam Dynamics Newsletter is intended as a channel for describing unsolved problems and highlighting important ongoing works, and not as a substitute for journal articles and conference proceedings that usually describe completed work. It is published by the ICFA Beam Dynamics Panel, one of whose missions is to encourage international collaboration in beam dynamics.

Normally it is published every April, August and December. The deadlines are 15 March, 15 July and 15 November, respectively.

7.1.2 Categories of Articles

The categories of articles in the newsletter are the following:

1. Announcements from the panel.

2. Reports of beam dynamics activity of a group.

3. Reports on workshops, meetings and other events related to beam dynamics.

4. Announcements of future beam dynamics-related international workshops and meetings.

5. Those who want to use newsletter to announce their workshops are welcome to do so. Articles should typically fit within half a page and include descriptions of the subject, date, place, Web site and other contact information.

6. Review of beam dynamics problems: This is a place to bring attention to unsolved problems and should not be used to report completed work. Clear and short highlights on the problem are encouraged.

7. Letters to the editor: a forum open to everyone. Anybody can express his/her opinion on the beam dynamics and related activities, by sending it to one of the editors. The editors reserve the right to reject contributions they judge to be inappropriate, although they have rarely had cause to do so.

The editors may request an article following a recommendation by panel members. However anyone who wishes to submit an article is strongly encouraged to contact any Beam Dynamics Panel member before starting to write.

7.1.3 How to Prepare a Manuscript

Before starting to write, authors should download the template in Microsoft Word format from the Beam Dynamics Panel web site:

http://www-bd.fnal.gov/icfabd/news.html

It will be much easier to guarantee acceptance of the article if the template is used and the instructions included in it are respected. The template and instructions are expected to evolve with time so please make sure always to use the latest versions.

The final Microsoft Word file should be sent to one of the editors, preferably the issue editor, by email.

The editors regret that LaTeX files can no longer be accepted: a majority of contributors now prefer Word and we simply do not have the resources to make the conversions that would be needed. Contributions received in LaTeX will now be returned to the authors for re-formatting.

In cases where an article is composed entirely of straightforward prose (no equations, figures, tables, special symbols, etc.) contributions received in the form of plain text files may be accepted at the discretion of the issue editor.

Each article should include the title, authors' names, affiliations and e-mail addresses.

7.1.4   Distribution

A complete archive of issues of this newsletter from 1995 to the latest issue is available at

<div align="center">

http://icfa-usa.jlab.org/archive/newsletter.shtml.

</div>

This is now intended as the primary method of distribution of the newsletter.

Readers are encouraged to sign-up for electronic mailing list to ensure that they will hear immediately when a new issue is published.

The Panel's Web site provides access to the Newsletters, information about future and past workshops, and other information useful to accelerator physicists. There are links to pages of information of local interest for each of the three ICFA areas.

Printed copies of the ICFA Beam Dynamics Newsletters are also distributed (generally some time after the Web edition appears) through the following distributors:

Weiren Chou	chou@fnal.gov	North and South Americas
Rainer Wanzenberg	rainer.wanzenberg@desy.de	Europe[++] and Africa
Susumu Kamada	Susumu.Kamada@kek.jp	Asia[**]and Pacific

++ Including former Soviet Union.
** For Mainland China, Jiu-Qing Wang (wangjq@mail.ihep.ac.cn) takes care of the distribution with Ms. Su Ping, Secretariat of PASC, P.O. Box 918, Beijing 100039, China.

To keep costs down (remember that the Panel has no budget of its own) readers are encouraged to use the Web as much as possible. In particular, if you receive a paper copy that you no longer require, please inform the appropriate distributor.

7.1.5   Regular Correspondents

The Beam Dynamics Newsletter particularly encourages contributions from smaller

institutions and countries where the accelerator physics community is small. Since it is impossible for the editors and panel members to survey all beam dynamics activity worldwide, we have some Regular Correspondents. They are expected to find interesting activities and appropriate persons to report them and/or report them by themselves. We hope that we will have a "compact and complete" list covering all over the world eventually. The present Regular Correspondents are as follows:

Liu Lin	Liu@ns.lnls.br	LNLS Brazil
Sameen Ahmed Khan	Rohelakan@yahoo.com	SCOT, Middle East and Africa

We are calling for more volunteers as Regular Correspondents.

7.2   ICFA Beam Dynamics Panel Members

Name	eMail	Institution
Marica Biagini	marica.biagini@lnf.infn.it	LNF-INFN, Via E. Fermi 40, Frascati 00044, Italy
Yunhai Cai	yunhai@slac.stanford.edu	SLAC, 2575 Sand Hill Road, MS 26 Menlo Park, CA 94025, U.S.A.
Swapan Chattopadhyay	swapan@dl.ac.uk	The Cockcroft Institute, Daresbury Laboratory, Daresbury, Warrington WA4 4AD, U.K.
Weiren Chou (Chair)	chou@fnal.gov	Fermilab, MS 220, P.O. Box 500, Batavia, IL 60510, U.S.A.
Yoshihiro Funakoshi	yoshihiro.funakoshi@kek.jp	KEK, 1-1 Oho, Tsukuba-shi, Ibaraki-ken, 305-0801, Japan
Miguel Furman	mafurman@lbl.gov	Center for Beam Physics, LBL, Building 71, R0259, 1 Cyclotron Road, Berkeley, CA 94720-8211, U.S.A.
Jie Gao	gaoj@ihep.ac.cn	Institute for High Energy Physics, P.O. Box 918, Beijing 100039, China
Ajay Ghodke	ghodke@cat.ernet.in	RRCAT, ADL Bldg. Indore, Madhya Pradesh, India 452 013
Ingo Hofmann	i.hofmann@gsi.de	High Current Beam Physics, GSI Darmstadt, Planckstr. 1, 64291 Darmstadt, Germany
Sergei Ivanov	ivanov_s@mx.ihep.su	Institute for High Energy Physics, Protvino, Moscow Region, 142281 Russia
Kwang-Je Kim	kwangje@aps.anl.gov	Argonne Nat'l Lab, Advanced Photon Source, 9700 S. Cass Avenue, Bldg 401/C4265, Argonne, IL 60439, U.S.A.
In Soo Ko	isko@postech.ac.kr	Pohang Accelerator Lab, San 31, Hyoja-Dong, Pohang 790-784, South Korea
Alessandra Lombardi	Alessandra.Lombardi@cern.ch	CERN, CH-1211, Geneva 23, Switzerland
Yoshiharu Mori	mori@kl.rri.kyoto-u.ac.jp	Research Reactor Inst., Kyoto Univ. Kumatori, Osaka, 590-0494, Japan
Chris Prior	c.r.prior@rl.ac.uk	ASTeC Intense Beams Group, STFC RAL, Chilton, Didcot, Oxon OX11 0QX, U.K.
David Rice	dhr1@cornell.edu	Cornell Univ., 271 Wilson Laboratory, Ithaca, NY 14853-8001, U.S.A.
Yuri Shatunov	Yu.M.Shatunov@inp.nsk.su	Acad. Lavrentiev, prospect 11, 630090 Novosibirsk, Russia
Junji Urakawa	junji.urakawa@kek.jp	KEK, 1-1 Oho, Tsukuba-shi, Ibaraki-ken, 305-0801, Japan
Jiu-Qing Wang	wangjq@mail.ihep.av.cn	Institute for High Energy Physics, P.O. Box 918, 9-1, Beijing 100039, China
Rainer Wanzenberg	rainer.wanzenberg@desy.de	DESY, Notkestrasse 85, 22603 Hamburg, Germany
Jie Wei	wei1@bnl.gov	Institute for High Energy Physics, P.O. Box 918, 9-1, Beijing 100039, China

The views expressed in this newsletter do not necessarily coincide with those of the editors.
The individual authors are responsible for their text.